



UNIVERSITAT^{DE}
BARCELONA

Driven soft matter at the nanoscale

Sergio Granados Leyva



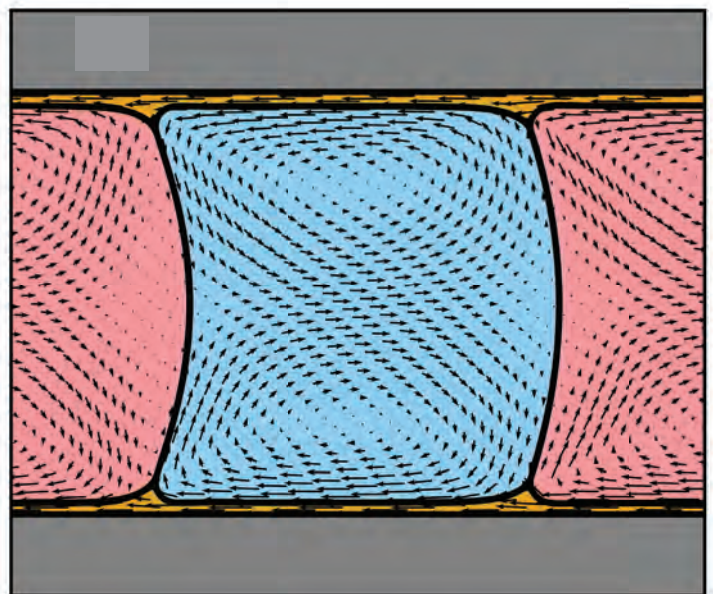
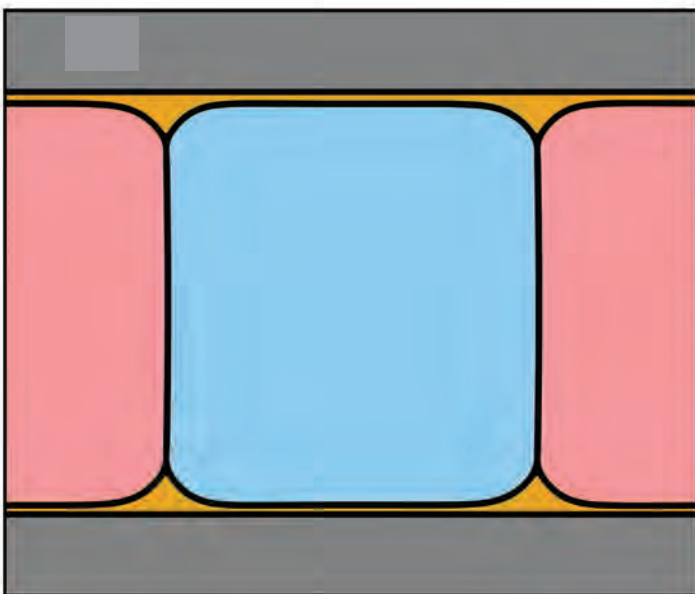
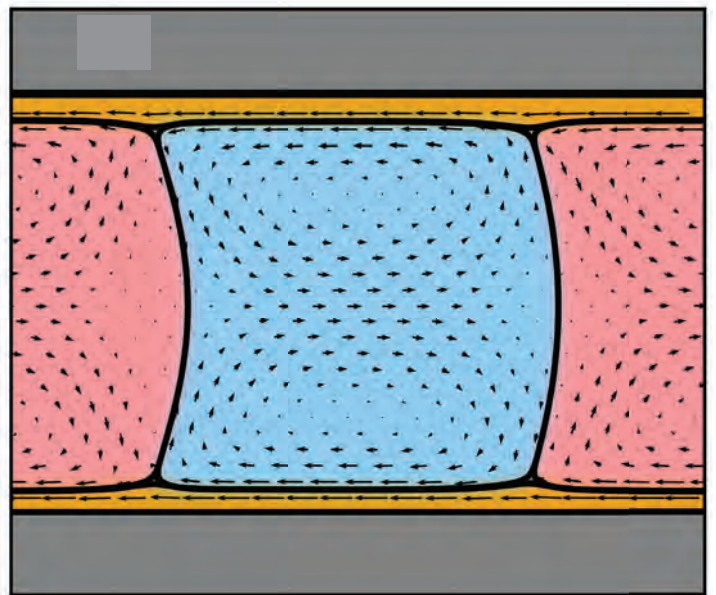
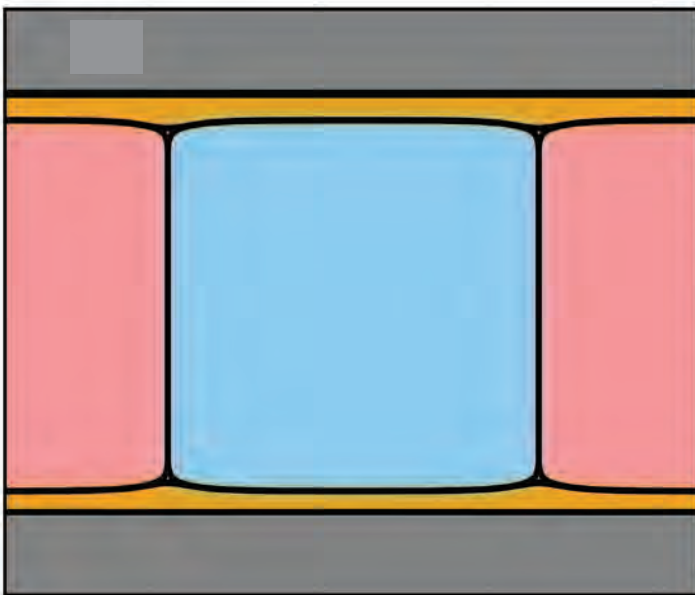
Aquesta tesi doctoral està subjecta a la llicència **Reconeixement 4.0. Espanya de Creative Commons.**

Esta tesis doctoral está sujeta a la licencia **Reconocimiento 4.0. España de Creative Commons.**

This doctoral thesis is licensed under the **Creative Commons Attribution 4.0. Spain License.**

Driven soft matter at the nanoscale

Sergi G. Leyva



Driven soft matter at the nanoscale

Programa de doctorat en Física

Autor/a: Sergi G. Leyva

Director/a: Ignacio Pagonabarraga, Aurora Hernández-Machado

Tutor/a: Giancarlo Franzese

Lloc on s'ha dut a terme la tesi: Universitat de Barcelona



UNIVERSITAT DE
BARCELONA

Abstract

This thesis will present a body of articles on the research topic of soft matter. The emphasis is put on the computational modelling of driven soft matter at length scales of micrometers and nanometers. We classify the presented works in two parts, the scientific approach of which differ notoriously. In the first part, experiments were available and the objective was to understand emergent responses reported in the lab. Since the outcome was already known, we used simple simulation methodologies that delved into the fundamental mechanisms that lead to the response of interest. The focus of the subjects, although diverse, was centered around dynamics of colloidal suspensions, hence a mixture of a majoritary liquid phase with a minority solid phase. In the second part of the thesis, we employed simulations that rigorously solved the hydrodynamics coupled to the physics of the free energy of interest. The goal was to investigate novel experimental setups, the outcome of which was unknown due to the early stage of the subject. With the simulation results, we built theories that explained the observed phenomena, setting the basis for future experimental explorations. This last part focused on two independent topics, namely, capillary driven spontaneous in lubricant infused surfaces and electrolytes in charge-patterned confined nanochannels.

Resumen

En esta tesis se presentarán una serie de artículos en el área de investigación de la materia blanda. La materia blanda es un subcampo de la materia condensada, en el que la energía típica de los sistemas es del orden de magnitud del de las fluctuaciones térmicas. Las escalas en las que se trabaja la materia blanda suelen ser la escala micrométrica (μm) y la nanométrica (nm), y en estas escalas la física de fluidos convive con la física de la vida y la de la materia interactuante. Esta mezcla de interacciones puede resultar en un alto grado de complejidad y en un sín fin de respuestas emergentes que aún quedan por entender. En estos últimos años, gracias al avance del poder computacional, se han desarrollado en la materia blanda muchas metodologías de simulación que ahora se pueden utilizar para estudiar muchas de las preguntas que aun quedan sin respuesta en la materia blanda. En esta tesis, haremos énfasis en la modelización computacional en este tipo de materia. Presentaremos un compendio de publicaciones, en las que hemos utilizado diferentes métodos de simulación para explicar experimentos y para postular nuevos desafíos experimentales. La tesis se divide en dos partes donde el enfoque científico varía: En la primera parte, mas centrada en coloides y micronadadores, se utilizan modelos computacionales simples para explicar efectos emergentes en experimentos de materia blanda. En la segunda parte, centrada en dinámica de fluidos, capilaridad y electrolitos se utilizan métodos mas sofisticados para intentar predecir, esta vez sin evidencia experimental alguna, los posibles escenarios a los que podría llevar una realización experimental. Tomada en su totalidad, esta tesis se puede entender como un enfoque práctico a la hora de escoger métodos de simulación en la micro y nanoescala.

Acknowledgements

I would like to thank my advisor, Ignacio, for all the years of research, discussions and collaborations, in which I have grown both scientifically and personally. I would like to thank him also for the funding of the initial years of my PhD, for trusting my intuition and for being always open to a new idea. I would also like to thank him for this unique opportunity of dedicating my life to science. I would like to thank my advisor Aurora also for the initial funding opportunity and for all the interesting and wonderful discussions in her office, and for all the coffees she offered me. I would like to thank Pietro for the opportunity to work with his group, collaborate with experimentalists and for his motivation and intuition for scientific endeavours. I would like to thank Rodrigo for all the tips for writing and drawing scientific content, and for his kindness and dedication when I stayed three months at the University Of Edinburgh. I would like to thank him also for all the discussions at the University of Edinburgh, which helped me drastically to advance my work. I would like to thank also his PhD's and postdoctoral researchers, and to all the people from the IMT for taking care of me during my time in Edinburgh, which resulted in one of the most wonderful experiences of my life. I would like to thank Tine for being such a scientific referent, a friend, and for the nights drinking beers and working late, in which I learnt more physics than in many months as a student.

I would like to thank too my PhD colleagues from the University of Barcelona for all the coffees and nights we have spent talking about physics, life, cinema and more. I would like to particularly thank Javi for all the coffees we had in the morning when things didn't seem to be working out. I would like to thank Zaida and Jurij for our informal meetings, which always lightened a tough week. I would like to thank my family for the support during all these years and the strength they have always transmitted to me, and which made possible my dedication to science. I would finally like to thank Ana for taking care of me, for trusting me, and for joining me in this fascinating journey that life is.

Contents

Abstract	ii
Resumen	iii
Acknowledgements	iv
Contents	v
List of Figures	vi
I General Introduction	1
0.1 Soft matter in a nutshell	2
0.2 Aims and structure	4
II Driving colloids at the microscale	8
1 Modelling colloidal particles	9
1.1 Modelling particles at low Re number	10
1.2 Magnetic triangles near a solid boundary and friction anisotropy	12
1.3 Hydrodynamic synchronisation in ratcheting colloidal matter .	18
1.4 Local clogging in ratcheting colloidal matter	21
1.5 Anomalous flows in disordered landscapes	23
1.6 Self-propelled active rafts by diffusiophoretic and diffusioos-	
motic flows	24
III Driving fluids at the microscale	28
2 Capillary driven multiphase fluids	29
2.1 Introduction	29
2.2 The Lattice-Boltzmann method	35
2.3 Ternary free energy model	39
2.4 Imbibition in lubricant coated surfaces	46
2.5 Dynamic contact angles in lubricant coated surfaces	50

3	Electrokinetically driven fluids in the nanoscale	61
3.1	Introduction	61
3.2	Lattice-Boltzmann coupled to electrokinetics	62
3.3	Electrostatics in the presence of a charged wall	62
3.4	Electrolyte flows in charge-patterned channels nanochannels	66
IV	Publications	68
4	Driven soft matter at the nanoscale	69
4.1	Friction Induces Anisotropic Propulsion in Sliding Magnetic Microtriangles	70
4.2	Hydrodynamic synchronization and clustering in ratcheting colloidal matter	78
4.3	Dynamics and clogging of colloidal monolayers magnetically driven through a heterogeneous landscape	88
4.4	Clogging transition and anomalous transport in driven suspensions in a disordered medium	98
4.5	Clustering induces switching between phoretic and osmotic propulsion in active colloidal rafts	109
4.6	Capillary imbibition in lubricant coated channels	124
4.7	Discontinuous transition in electrolyte flow through charge-patterned nanochannels	134
V	Conclusions	144
5	Conclusions and perspectives	145
	Bibliography	148

List of Figures

1.1	Some examples of synthetic microswimmers, classified by their swimming mechanism, with their corresponding characteristic speed. Figure extracted from <i>Soft Matter</i> , 2011 7 , 8169	13
1.2	Experimental realisation of a colloidal rotor, showing the relevant degrees of freedom, the angle θ and the height h . The rotation of θ is rectified into a translation motion thanks to the presence of the boundary. Figure extracted from <i>Phys. Rev. Lett.</i> 101 , 218304	14

1.3	Scheme showing the sliding motion observed in experiments and simulations. The permanent magnetic moment \mathbf{m} in this scheme points towards one of the tips of the triangle. However, in experiments the magnetic moment could point anywhere inside the plane of the triangle. In the simulations, we also varied systematically the orientation of the magnetic moment inside the triangle plane.	15
1.4	Summary of the behaviour of an isolated paramagnetic particle moving atop a garnet film with periodically inverted magnetisation. Figure extracted from our publication <i>Sci. Adv</i> , 2022 8 . A) shows the experimental setup, consisting of paramagnetic particles on a film of periodically inverted magnetisation, in the presence of an oscillating elliptical magnetic field. The red line represents the racter potential, which moves with speed wave $\nu_m = f\lambda$. B) Experimental observation of the potential landscape. C) Behaviour of an isolated paramagnetic particle moving upon actuation of an oscillating magnetic field. First, the particle is trapped at a minima of the potential and moves at a speed $v_x = \nu_m$. At a certain frequency threeshole, the viscous friction force, which is proportional to the velocity, overcomes the potential force, and the particle diminishes its velocity respect the travelling wave. D) Trajectory of a synchronous and asynchronous particles.	20
1.5	Example of a clogging transition for the passing of sheep through a bottleneck. A) Shows an image of the obstacle placed in front of the bottleneck. B) Shows an image of the recording used to characterise the power law exponent. C) Imaging as a function of time, showing how different events were separated. D) Number of sheep that pass the bottleneck as a function of time, with and without obstacle. E) Complementary (CDF) used for computation of the clogging characteristic exponent. F) Histogram of burst sizes of sheep. For more details see original text. Figure extracted from <i>Sci. Rep</i> , 2014, 4 , 7325	22
1.6	Example of a Janus particle. a) Shows a scanning electron microscopy image of a colloidal particle with a 20 nm thick gold cap (highlighted). b) Represents the trajectory of the particle after being actuated with light. Figure extracted from <i>Soft Matter</i> , 2011, 7 , 8810-8815	25
2.1	Dynamics of drops in lubricant-infused surfaces. a) Shows a scheme of a drop sliding in a surface inclined an angle α . b) and c) show highlight the meniscus of the drop. Figure d) shows the velocity of the drop as a function of $\sin\alpha$ when the viscosity of the drop is 50 times larger than that of the lubricant, which follows a linear behaviour, and is independent of the fraction of pillars in the texturised surface (ϕ). e) Shows the opposite case, where the lubricant viscosity is 50 times larger than than that of the drop. In this case, for small values of $\sin\alpha$ the velocity follows $V \sim \sin\alpha^{2/3}$, and for large values $V \sim \sin\alpha^3$. In the first regime, the fraction of pillars quantitatively influence the velocity. <i>Soft Matter</i> , 2017, 13 , 6981-6987	31

2.2	Schematic drawing of the Young law	33
2.3	Schematic drawing of hydrophilic vs hydrophobic surface	34
2.4	Results showing all six existing contact angles in the ternary free energy model, all of which can be tunned by means of κ_1, κ_2 and κ_3 parameters, along with h_1 and h_2 wetting parameters.	42
2.5	Comparison between analytical result and simulations for different contrast of viscosities and widths of the system. Figures a and b use a set of viscosities $\eta_1 = 1, \eta_2 = 0.5$ and $\eta_3 = 0.3$ for a channel width of 45 and 80 LB units respectively. Figures c and d use a set of viscosities $\eta_1 = 2, \eta_2 = 0.3$ and $\eta_3 = 1$ for a channel width of 45 and 80 LB units respectively.	44
2.6	Viscosity profile as a function of the concentration of phases	45
2.7	Concentration of each phase in x direction from Fig ??, near the lubricant contact line	45
2.8	Benchmark tests for contact angles. The figure on the left compares the theoretical angles (θ_t) with the measured contact angles in the interface (θ_m) in a liquid lense geometry when systematically varying the surface tensions. The figure on the right compares measure the solid-liquid contact angle for a fixed value of h_1 , when systematically varying the h_2 wetting potential. Both graphs together show the high accuracy of the ternary free energy model.	47
2.9	Simulation of a capillary spontaneous imbibition process using a ternary free energy, in the limit where one of the concentrations is set to 0 (no lubricant). The parameters correspond to a measured dynamic contact angle $\theta_d = 73.5$, invading fluid viscosity $\eta_1 = 1$, displaced fluid viscosity $\eta_2 = 0.01$, $\gamma_{12} = 1.033 \cdot 10^{-3}$ and channel width $H=42$. The simulations accurately follow the Lucas-Washburn law.	48
2.10	Simulation snapshot showing all the parameters to be considered in SLIPS simulations The blue color is the phase associated to the invading fluid, red to the displaced fluid and yellow to the lubricant. H_1 and H_2 refer to the widths of phase blue and red phase, respectively. H refers to the width of the channel. L is the length of the solid channel. $l(t)$ the instantaneous position of the front. θ is the dynamic contact angle.	48
2.11	$g(\theta)$ function	52
2.12	Dynamical angle as a function of Ca	52
2.13	Dynamical angle as a function of Ca in LB simulations	53
2.14	Left: Velocity field of a moving drop on top a of a solid Right: Velocity field of a moving drop on top a of a lubricant	54
2.15	Simulations showing a drop in equilibrium a lubricant-coated surface. Both simulations were performed with a uniform lubricant layer, with the same thickness. We show the equilibrium profiles of the drops for (a) a small ridge $\theta_l = 163$ b) a large ridge $\theta_l = 80$	55
2.16	(a) Matching Cox-Voinov when $\theta_l = 163, q=1$, advancing contact angle. (b) Matching Cox-Voinov when $\theta_l = 163, q=0.05$ receding contact angle. (c) Matching Cox-Voinov when $\theta_l = 80, q=1$,advancing contact angle. (d) Matching Cox-Voinov when $\theta_l = 80, q=0.05$,receding contact angle.	56

2.17 (a) Velocity as a function of the arc length (b) Normalised velocity as a function of the arc length.	57
2.18 Scheme corresponding to the geometrical configuration we use to relate the dissipation to the interface deformation.	59
2.19 (a) δ dependence on λ , for advancing angles and $q=1$ (b) δ dependence on λ , for advancing angles and $q=0.05$ (c) δ dependence on λ , for receding angles and $q=1$ (d) δ dependence on λ , for receding angles and $q=0.05$	60
3.1 Schematic double layer	64
3.2 Debye-Hückel and electroosmotic flow comparison between simulations and analytical results	65

PART I

General Introduction

0.1 Soft matter in a nutshell

In the last decade, soft matter has become one of the most important subfields of condensed matter, and its applications and research areas cover a broad range of topics. In colloidal and interfacial science, soft matter can benefit from classical methods of fluid dynamics to delve into the characteristic properties of emulsions and suspensions [1–4]. In capillaries, the energetic cost associated to increasing a surface area results in surface tension phenomena. Surface tension is the reason why drops, in equilibrium and in the absence of forces adopt a spherical shape. When subjected to external forces, drops can dynamically change their shape and deform depending on the nature and magnitude of the force. The physics of equilibrium and non-equilibrium drops have been a topic of research in soft matter for many years, and there are many books and a relevant body of articles [5–9] that delve into their properties, and highlight their importance. The interaction of a drop with a solid interface also gives rise to many responses of interest. The shape and dynamics of a drop are modified by the physical and chemical properties of the solid surface in which the drop lies [10]. In a solid micro-channel, surface tension can be used to spontaneously produce the invasion of a fluid into the channel without any use of external pumps [11–13]. When combined with electrokinetic and electrostatic models, flow equations are an important tool to understand ionic currents taking place across cells [14], activating cell mechanisms [15] and neuron communication [16]. Understanding such currents can, at the same time, lead to technological developments that imitate these biological responses, and apply them for harvesting energy from salinity gradients [17], or to build a transistor that relies solely in transport properties of electrolytes in confined nanochannels [18]. The latter are only a few examples of the promising technologies soft matter could contribute to by controlling the micro and nanoscales.

Closely related to biology, in soft matter there are many interacting systems that result in the emergence of complex responses, like self-organisation [19] or phase transitions [20]. The scales at which this phenomena take place is very close to the scale of biological matter, such as proteins, cells, bacteria and virus. However, this type of matter escapes the rules followed by conventional soft matter, since they are intrinsically out of equilibrium. The energy consumed by sub-units forming these systems can be transformed to motility and lead to spontaneous ordering, result in persistent defects and even in more complex degrees of organisation of matter. Soft matter has advanced towards the characterisation of these systems, studying biological matter in controlled environments to gain insight about this complexity observed in living matter. This topic of soft matter receives the name of active matter. By exploiting simple interaction rules, complex emergent behaviours can be modelled to investigate bacteria motility [21–23], cellular filaments inside the cell [24], birds [25], school of fishes [26] and more. Efforts are being made to generalise fluid models to approximate the behaviour and transport properties of motile cancer cells [27], and distinguish healthy cells from cancerigenous cells. When combined with chemistry and biology, cell organoids can be simulated with a realistic cell media to underpin the role of a precise biological structure and understand how it is integrated in the vast majority of processes that a cell can do [28]. In summary, the latter examples exhibit the capability to invert energy in motion or deformation, which can result in self-propulsion, self-assembly and aggregation

phenomena [29]. Active matter can be synthesised too in a laboratory benefiting from chemical interactions, in order to design experimental realisations that simplify the complexity found in nature. Particularly important are Janus particles, which exploits an asymmetry in the surface of the sphere to produce diffusio-phoretic flux that self-propells the particle [30].

As the reader might have noted, it seems quite difficult to enclose soft matter in a simple definition. The usual definition fails to capture the complexity of the situations in which soft matter is focused and the emergent behaviours it can give rise to. The mentioned studies contain both alive and inert matter, micro and macro sized systems, systems where fluid dynamics is important and systems where fluid dynamics is irrelevant. This heterogeneity of topics in soft matter is precisely one of its core values, and the most powerful one: Multidisciplinarity. In soft matter, physicists work together with chemists. Engineers and biologists, both in its theoretical and experimental aspects, collaborate to understand principles, design devices and create new methodologies that can help overcome the challenges of this century.

However, there is a common ground for the mentioned research topics in soft matter. First, the ability of the media to deform in the presence of external forces, compared to other subfields of condensed matter. Second, the components of soft matter systems are typically in the micro/nano scale, where quantum effects are not determinant, but thermal fluctuations might influence the system behaviour, since the energy scale is comparable to that of room temperature energy, $k_B T$. However, soft matter does not focus solely in matter at the micro and nano-scales. Some matter composed by macrosopic units such as birds or fish schools are also a subject of study for soft matter. In these systems, similar methodologies can be used, and phenomenology can be similar compared to its microscopic counterparts, like bacteria. The microscopic emergence of a macroscopic temperature is also modelled in these systems as a noise contribution, similarly to other models of colloidal suspensions [31], capturing random contributions to the motion in living organisms. Such properties make soft matter systems particularly appealing to some of the classical statistical mechanics approaches. These systems can be surrounded by a fluid media, and hydrodynamic interactions might be relevant in some situations, which might lead to consider the Navier-Stokes equations from hydrodynamics. Distinguishing between equilibrium processes and non-equilibrium processes is also important in order to accurately consider the phenomenology involved in the behaviour of interest. Driven soft matter is often out of equilibrium, which can complicate the modelling of the phenomena involved in the area of research. Continuum models can help modelling non-equilibrium phenomena from thermodynamic principles. The standard Cahn-Hilliard equation is an example of the latter which models phase separation of a binary mixture. This equation is based in a free energy that depends on a concentration c that has two minima. By means of introducing a term of the type ∇c the increase of surface area is penalised, resulting in surface tension. Hence, if the initial configuration at a certain domain consists of a random distribution of concentrations, the system will phase separate in two phases, corresponding to the two minima configured by the bulk. In conclusion, there are a set of tools that are susceptible to be applied to soft matter systems, which have been a source of novel and interesting results in the recent years.

Due to the complexity of some of the phenomena of interest in soft matter

systems, computational approaches have become extensively used in the field. In the last decades, the increasing computational capacity of modern computers multiplied the amount of simulation methodologies to model fluids in the micro and nanoscale [32–34] for fluid mixtures [35–37], realistic models of water interacting with complex proteins [38–40], nucleation [41], overdamped colloidal aggregates [42] and microswimmers [43–46], just to quote some examples. Many advances in this research areas have benefited from such computational approaches to explore some experimentally inaccessible measurements and to test and validate hypothesis to understand the responses of complex media. While a lot of research is still being conveyed to develop new simulation methodologies, a lot of standardised simulation procedures already exist for soft matter research, and rarely one needs to start from scratch to focus on a problem of interest. The rising of standardised versions of codes based on simulation methodologies has also lead to different approaches to model phenomena. For example, one could seek to include all the possible existing effects to model a behaviour in the most realistically rigorous way possible. This approach can be useful to test whether the simplifications leading to an analytical result could hold in a more realistic situation. The objective could be to determine what are the role of other contributions that can come at play. For example, in one of the works presented in this thesis, we derived a simple analytical model to predict the spontaneous imbibition of a front in a lubricant coated channel. This simple model neglected some contributions that could rise due to the lubricant covering the solid channel, like the varying lubricant thickness near the front, or the lubricant ridge arising at the triple contact line. The simulations considered in detail hydrodynamics of all three phases, along with the surface tension interactions. We were able to determine that the dynamic regimes identified in the analytical model still held.

A different approach to simulations can be summed up in a quote attributed to Einstein: *Everything should be made as simple as possible, but not simpler.* By using simple computational methodologies, the path towards the minimum ingredients to derive an analytical model are clearer, and a deep fundamental understanding of the problem can be achieved. Of course, these two approaches are complementary to describe a broad view of a phenomena. When there are experimental results and the goal is to understand the principles governing an emergent response, then a simple computational approach is a good idea. For example, clogging of particles through a bottleneck is an emergent response, which arise from the steric interactions between particles when forced through a narrow constriction. By modelling some aspects of this transition and comparing them to the experimental results, we can understand which combination of interactions leads to the emergent response. We will benefit from this two approaches depending on the goal of our research and the starting point of the investigation.

0.2 Aims and structure

In this thesis, we have used different simulation methodologies, which differ in complexity and computational performance. There are two main parts constituting this work. Both have computational and theoretical components. The first part is focused on non-equilibrium colloidal suspensions and active

matter, and is more aligned towards the *keep it simple* principle. It benefited from experimental results obtained in Prof. Pietro Tierno's group. With our simulation modelling and theoretical analysis we wanted to determine the principles leading to the emergent responses observed in experiments. The methodologies used in this part are simple to implement in codes, like Brownian Dynamics (BD) and Molecular Dynamics (MD), and have been programmed from scratch to simulate colloidal suspensions of spherical objects. Some additions had to be made in some cases compared to the standard algorithms. For instance, Ref. [47] incorporated far-field hydrodynamic interactions, leading to the conclusion that these interactions were responsible for the resynchronization of particles with the moving landscape. We will delve deeper into the particularities of each simulation methodology in the following sections.

The second part pursued completely different challenges. We focus on understanding different scenarios in the context of a different kind of mesoscopic simulations. The absence of experimental and theoretical results was overcome by means of well-established simulation methodologies, based on the Lattice-Boltzmann (LB) method. The first chapter is dedicated to a series of simulations that delve into accurate capillary flows in lubricant-coated surfaces, and use this simulations to build an analytical framework. On one side, spontaneous imbibition is a classical problem, the first theoretical solution of which was reported a century ago [11]. Experimental results are also very common, and a large amount of simulation methodologies have been developed to understand its origin both microscopically [48–50] and mesoscopically [51–53], reproducing the well known classical results. On the other side, there is an increasingly popular experimental approach to eliminate surface roughness and thus hysteresis in the contact angle of a drop [54–56]. The solid surface is typically treated to be imbibed by a lubricant, which always stays attached to the solid surface due to its preferential wettability. What would be the properties of a front moving in a confined channel where the walls are covered by such a lubricant? Neither experimental results nor theoretical calculations were available for this realisation. We built up from a Lattice-Boltzmann (LB) open source code [57] to incorporate a three-phase fluid with tunable contact angles. We used this methodology to probe different scenarios and build a theoretical model that reproduced our observations and provided a framework to understand the mechanism that changed the dynamics of the front. Some properties related to the dissipation due to the interface deformation were not clearly understood, which lead us to compare the lubricant-coated scenario to a conventional dry surface. The second chapter of this part is dedicated to a publication where we combined the Lattice-Boltzmann method with an electrokinetic model to simulate the effect of a charge pattern in electrolytes confined in nanochannels. The results showed a flow transition as a function of the pressure gradient, which we complimented with a Dissipative Particle Dynamics (DPD) explicit ion methodology. Both simulation results agreed with the predicted onset of the transition obtained by means of a mean-field model.

To conclude this introduction, I will briefly sum up the content of the chapters and sections of this thesis. The different subsections will serve as a build up to a series of publications presented in the last part. The reader will be introduced to the context and novelty of the results by providing and commenting the relevant literature. The computational and theoretical details

will be sketched, in order to facilitate the reading of the published works. In the publications the reader will find the bulk of the scientific work, the place it occupies in the present research topic, the precise goals of each and the conclusions. We will avoid repeating content that is already present in the article. We will elaborate on the simulation methodologies and in the main research field concepts when the article lacks comprehensive information about the prior research leading to the publication.

The two aforementioned parts are independent, so that any ordering of these two might look arbitrary. However, we have decided to start with the part where MD and BD simulations have been used, since these computational approaches are more intuitive. In part II, we will start in Sec. 1.1 introducing the peculiarities of the hydrodynamic equations and suspensions in the microscale, where objects are typically of the order of $1\mu\text{m}$. Most of the presented publications here are combined with experimental results, or are motivated by previous experiments. In Sec. 1.2 we present Pub. 4.1, a publication consisting in MD simulations of a triangular microswimmer modelled by three beads linked together, which can swim due to friction anisotropy present in the vicinity of a solid wall. In Sec. 1.3, we will introduce Pub. 4.2, a paper where we aim to study the colloidal transport in modulated ratchet potentials and the far-field hydrodynamic contribution to the dynamics. In section 1.4 we will present Pub. 4.3, a work where we investigate the local clogging properties of ratcheted motion of colloidal particles, where bottlenecks are configured by a distribution of pinned spherical particles. After this, we will present a general characterisation of clogging of particles driven by a constant force in section 1.5. This new approach, explained in Pub. 4.4 characterises clogging in arbitrary landscapes and allows to identify a new flowing regime that will be explained in detail in the paper, and will help us to probe active matter moving through arbitrary disordered landscape. Finally, in section 1.6 we will present Pub. 4.5, a work where we investigated the motion of an active raft, configured by an apolar active particle interacting with silica particles through diffusio-phoretic means.

In the second part, called Driving fluids at the microscale we will deal with the research that benefited from the LB methodology. The main goal of this first chapter of the second part has been to investigate capillary driven spontaneous imbibition of fronts in lubricant coated channels. In the introduction, Sec. 2.1, we will explain basic concepts of surface tension. In order to understand the novelty of the work, we will build up on these basic concepts to briefly summarise the famous results obtained by Washburn, which have been observed experimentally multiple times. We will also dedicate a chapter to describe the basis of the LB method in Sec. 2.2. The ternary free energy mixture model we used to simulate surface tension with tunable solid-liquid contact angles is introduced in Sec. 2.3. We will end this chapter presenting Pub 4.6, the work on capillary driven spontaneous imbibition in lubricant coated surfaces. A second section of this chapter will deal with the deformation of an interface between two fluids, 2.5. The theory for this latter topic when the interface moves on top of solid surface has been already established [58, 59] We will introduce the results of this theory to the reader, and highlight how it can be extended to capture the deformation of an interface between two fluids when the interface moves on top of a thin lubricant layer.

In chapter 3, we will present Pub. 4.7, a contribution to the field of

electrolytes in confinement. First we will introduce some basic results from the literature in section 3.1 to provide intuition about characteristic lengthscales of electrolyte fluids near a charged wall. We will also introduced briefly how the LB method is coupled to an electrokinetic free energy model in section 3.2. In Sec. 3.4 we summarise the context of the presented publication and the results.

Part IV will present all the publications in the same order as they have been presented in the index of contents. Finally, part V will summarise the conclusions of this thesis from a broad perspective.

PART II

Driving colloids at the microscale

CHAPTER 1

Modelling colloidal particles

The term colloid is of broad use in soft matter science. In general, colloidal matter can refer to any mixture of two or more phases of matter. One phase is in a larger proportion, and is defined to be the continuous phase, while the other phase is in smaller proportion and is referred to as dispersed phase. Here we will model colloidal systems comprised of a fluid continuous phase, and a suspension of solid particles as the dispersed phase. The size of the solid particles of the dispersed phase considered here will be of the order of the micrometer (10^{-6} m) size. However, in fluid-solid suspensions the solid particles might be as small as a nanometer nm (10^{-9} m). The characteristic scales of the solid particles impact significantly the behaviour of the dispersed phase and its physical properties. In the nanoscale, solid particles are subjected to larger thermal fluctuations, which can hinder emergent collective responses of the solid subunits. Additionally, in the nanoscale the no-slip boundary condition, which imposes that the fluid velocity at a solid boundary is strictly zero, does not hold anymore. Instead, a slip velocity emerges at the solid interface, which will also impact the dynamics of colloidal suspensions near solid walls [60]. There is no need to worry about these effects here, since the typical size of the colloidal particles considered in this part are of the order of $1 \mu\text{m}$. Hence, the no-slip boundary condition holds and thermal fluctuations will not be determinant, though they still exist in such a scale, and we will account them in the models.

When solid particles in a suspension move due to the action of external forces they perturb the flow around them, which will also affect other surrounding solid particles. Fully solving the Navier-Stokes equation numerically in the general case is a difficult task that requires vast computational resources. However, some simplifications can be made from the particular scale we are using. In the Navier-Stokes equation, there is a dimensionless parameter that accounts for the ratio of inertial force to viscous forces. This number can be written as $\text{Re} = \rho u / L \eta$, where ρ is the fluid density, u is the characteristic flow velocity, η is the viscosity of the fluid, and L the characteristic length of the system. In a system of a characteristic size of $L \sim 1 \mu\text{m}$, considering water as the characteristic fluid, we obtain that $\text{Re} \sim 11.23v$, where v is given in SI units. Bacteria are among the fastest microswimmers in the microscale, moving at speeds of the order of $10 \mu\text{m}$, which means that the typical Re number in colloidal suspensions will not grow over $\text{Re} \sim 10^{-4}$, and inertia will be negligible. This means that the equation for hydrodynamics in colloidal suspensions will be the Stokes equation

$$\rho \frac{d\mathbf{u}}{dt} = -\nabla p + \eta \nabla^2 \mathbf{u} + \rho \mathbf{F}, \quad (1.1)$$

where $\mathbf{u}(\mathbf{r}, t)$ is the solvent velocity field, t is time, p is pressure, ρ is the fluid density and \mathbf{F} is the external force. In the next section, we will explain the general approach to model colloidal particles. We will seek and develop simulation models that compromise computational cost with an accurate description of the responses we have encountered in experimental realisations.

1.1 Modelling particles at low Re number

The Stokes equation has some peculiarities we are not used to in our macroscopic world, where typically $\text{Re} \gg 1$. An important feature is the time reversibility of Stokes flows. This implies, for example, that a mixing of two immiscible phases of fluids at $\text{Re} \ll 1$ by a force $\mathbf{F}(\mathbf{r}, \mathbf{t})$ is reversible by means of reverting the applied force for the same amount of time $-\mathbf{F}(\mathbf{r}, \mathbf{t})$. In a viscous media where $\text{Re} \ll 1$, friction is all there is. If one imagines himself throwing a tennis ball in such a medium, the ball would immediately stop at the same exact time our racket stops touching the ball due to the inability to sustain inertia. This has important implications for biological entities that are known to swim in the microscale and to any effort of moving particles at such scale.

One needs to seriously consider the implications of Eq. 1.1. When a particle moves in a viscous medium, it generates a flow that will act on other particles due to the fluid drag. Additionally, the microscopic motion of the molecules of the liquid induce a random fluctuation of the particle position in time. We start by describing the general equation for particles in a fluid medium that considers all these effects, including inertia. This fundamental equation is the Langevin equation

$$\mathbf{m} \frac{d^2 \mathbf{r}}{dt^2} = \mathbf{F}^H + \mathbf{F}^I + \mathbf{F}^P \quad (1.2)$$

where \mathbf{m} is the generalised mass/moment of inertia matrix, of dimension $6N \times 6N$, being N the number of particles considered. The first term on the right, \mathbf{F}^H is the drag exerted in the particles due to their motion relative to the fluid. Its expression is

$$\mathbf{F}^H = -\boldsymbol{\nu}(\mathbf{v} - \mathbf{v}_f(\mathbf{r})) \quad (1.3)$$

where $\boldsymbol{\nu} = \boldsymbol{\mu}^{-1}$ is the resistance matrix, which is the inverse of the mobility matrix $\boldsymbol{\mu}$. The terms of this matrix depend on the spatial configuration of particles, which generally changes in a simulation. This implies calculating the resistance matrix each time-step.

The second term on the right, \mathbf{F}^I represents all the internal and external forces of the particles, like interparticle potential, dipolar interactions, or the force due to a magnetic field. The last term represents a stochastic force. It is a noise term that includes the motion of the particle due to the collision of fluid molecules with the solid particle, leading to fluctuations of the particle position. Thus, it is the term that explains the random motion of a colloidal particle in a fluid, which is typically referred to as Brownian motion. The Brownian contribution is generally characterised by

$$\langle \mathbf{F}^B \rangle = 0 \quad \text{and} \quad \langle \mathbf{F}^B(0) \mathbf{F}^B(t) \rangle = 2k_B T \boldsymbol{\mu} \delta(t). \quad (1.4)$$

where $\boldsymbol{\mu}$ is the configuration dependent resistance matrix that gives the hydrodynamic force due to their motion relative to the fluid [61]. The amplitude of the noise in Eq. 1.4 can be derived from the fluctuation-dissipation theorem for a N-body system. It is important to note that the Langevin equation is valid as long as the spatial configuration of the particles does not change drastically during the time scale of the Brownian fluctuations, which is satisfied by all the cases of interests presented in this thesis. Otherwise it would mean that the characteristic time of the collisions between liquid molecules and the relaxation time of the colloidal particle are comparable. In such cases, other simulation methodologies that explicitly consider the solvent such as Molecular Dynamics, would be more appropriate.

Fully solving this stochastic differential equations numerically, even when the solvent is considered implicitly through the drag exerted on the particles by the fluid, is still very expensive computationally. There are different reasons for this. First, one needs to consider the lubrication between the surface of the particles. Due to the no-slip boundary condition, when two particles come close enough, the relative motion between them tends to stop due to the drag that rises from this condition. Furthermore, the long-range hydrodynamic interaction between two particles go as $1/r^2$, meaning that no cut-off distances can be imposed to sum the drag forces of all particles in the system. However, the most expensive computation is due to the many body hydrodynamic interactions, since calculating its contribution to the motion requires inverting the mobility matrix, a computational bottleneck that requires $O(N^3)$.

In the models we will present in this chapter, when hydrodynamics are considered, we will overcome this computational bottleneck by considering simplified versions of the mobility matrices. We will consider that particles induce a flow at the Oseen level, while the thermal fluctuations will be sampled from a Gaussian distribution, as it is the case for an isolated particle. Additionally, we will consider the Langevin equation in the overdamped limit, neglecting the inertial term. The latter limit is often known as the Brownian dynamic limit. In this limit Eq. 1.2 reads

$$\mathbf{F}^H + \mathbf{F}^i = -\gamma \frac{d\mathbf{r}}{dt} + \boldsymbol{\xi}(t), \quad (1.5)$$

where \mathbf{F}^H will be the hydrodynamic drag calculated using far field hydrodynamics at the Oseen level, or at the Blake level if a solid boundary is present. The term *boldsymbol{\xi}* represents the force due to the random fluctuations for a single particle

$$\langle \boldsymbol{\xi}(t)\boldsymbol{\xi}(t') \rangle = 2k_B T \gamma \delta(t - t') \mathbf{I}, \quad (1.6)$$

where \mathbf{I} is the identity matrix. In the following sections, we will describe a series of simulations the purpose of which was to understand the underlying mechanism of a experimental emergent response. For each publication, the simulation methodology has been tailored carefully to imitate in the most straightforward manner the experiments, when available, while keeping as low as possible the computational cost. We will introduce the topic of research and justify how we modelled the system in order to obtain realistic outcomes that represent the relevant physics. The publications we show use either Brownian Dynamics or Molecular Dynamics in the limit where acceleration is negligible, reducing the dynamics to that of the Brownian methodology. This latter method

can be useful when one needs to impose constrictions on the distance between two particles by means of some computational algorithm [62]. Hence, our objective will be to sketch how we approach the challenge of modelling different experimental systems, trying to reduce the complexity of the problem as much as possible in order to rationalise the results.

1.2 Magnetic triangles near a solid boundary and friction anisotropy

This publication pertains to the topic of the physics of swimmers in the microscale, a fascinating topic that highlights how some organisms have adapted to swim at small Re . By a swimmer we mean an object or an organism that is able to self-propel in a fluid medium, whatever the mechanism might be. This research topic was born because of a striking consequence of the laws of hydrodynamics at low Re in the micro and nanoscale: The scallop theorem. This theorem states that at $Re \ll 1$, in a fluid bulk, no motion is possible by means of periodic oscillations of a single degree of freedom of a swimmer. In other words, a scallop cannot swim at $Re \ll 1$ in the bulk of a fluid, since it has only one degree of freedom, namely, the aperture angle between the shells, which oscillates periodically in time [63]. At least two degrees of freedom are required, in order to describe a closed trajectory in phase space that avoids reciprocity. This means that the swimming mechanisms developed in the sea by fish and aquatic mammals are rendered useless, along with all the knowledge of friction reduction we have gathered in aerodynamics. Their mechanisms of locomotion have evolved to overcome very efficiently the limitations of the scallop theorem and achieve fast swimming speeds without relying on inertia. Examples of this are spermatozoa, which can move due to long flexible tails [64]. The specific swimming locomotion of bacteria can differ between different species. For example, there are bacteria that swim with flagella, which consists of long filaments attached to some part of the bacteria. Different species can differ on the number of these flagella and where they are attached to, and can have different swimming modes, like pull or push the fluid around them, or tumbling motion to change direction [65].

The physics of microswimmers have been subject of study for almost fifty years now, since E.M Purcell stated the scallop theorem [63]. One of the challenges associated to this discovery has been, since that time, to be able to design synthetic microswimmers, to understand better which designs can lead to propulsion and which ones could potentially be used for medical applications. A plethora of simple designs of synthetic microswimmers which can move freely in a fluid bulk have been proposed and tested experimentally. Relevant examples include the corkscrew magnetic swimmer, which relies in the chirality of an object that moves in a corkscrew fashion [66], or magnetic swimmers consisting of a head and a non-flexible tail, which can move due to the friction asymmetry between the head and the tail in a periodic cycle [67].

The presence of a solid boundary introduces an additional degree of freedom, which facilitates locomotion and results in new swimming modes. For example, a stick rotating with a constant angular velocity, with an angular momentum pointing towards one direction inside the solid plane will move, similarly to a wheel. This is a consequence of the no-slip boundary condition at the wall,

1.2. Magnetic triangles near a solid boundary and friction anisotropy

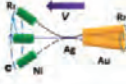
Type of Propellers	Schematic/Micrograph	Maximum dimensional speed U_{\max} ($\mu\text{m/s}$)	Maximum dimensionless speed $\tilde{U}_{\max} = U/Lf$ ($\times 10^{-3}$)
<i>Escherichia coli</i>		$U \approx 30 \mu\text{m/s}$	$L = 10 \mu\text{m}$ $f = 100 \text{Hz}$ $\tilde{U} \approx 30$
Flexible propeller			$\tilde{U}_{\max} \approx 94$ $L = 24 \mu\text{m}$ $f = 10 \text{Hz}$ $U \approx 22 \mu\text{m/s}$
Flexible propeller		$U_{\max} = 6 \mu\text{m/s}$	$L = 6.5 \mu\text{m}$ $f = 15 \text{Hz}$ $\tilde{U} = 62$ $\tilde{U}_{\max} = 77$ $L = 6.5 \mu\text{m}$ $f = 7 \text{Hz}$ $U = 3.5 \mu\text{m/s}$
Flexible propeller		$U_{\max} = 21 \mu\text{m/s}$	$L = 5.8 \mu\text{m}$ $f = 35 \text{Hz}$ $\tilde{U} = 103$ $\tilde{U}_{\max} = 164$ $L = 5.8 \mu\text{m}$ $f = 15 \text{Hz}$ $U = 14.3 \mu\text{m/s}$
Helical propeller		$U_{\max} = 18 \mu\text{m/s}$	$L = 38 \mu\text{m}$ $f = 30 \text{Hz}$ $\tilde{U} = 16$ $\tilde{U}_{\max} = 21$ $L = 38 \mu\text{m}$ $f = 10 \text{Hz}$ $U = 8 \mu\text{m/s}$
Helical propeller		$U_{\max} = 40 \mu\text{m/s}$	$L = 2 \mu\text{m}$ $f = 150 \text{Hz}$ $\tilde{U} = 133$
Surface walker		$U_{\max} = 3.5 \mu\text{m/s}$	$L = 4 \mu\text{m}$ $f = 15 \text{Hz}$ $\tilde{U} = 58$ $\tilde{U}_{\max} = 80$ $L = 4 \mu\text{m}$ $f = 10 \text{Hz}$ $U = 3.2 \mu\text{m/s}$
Surface walker		$U_{\max} = 12 \mu\text{m/s}$	$L = 3 \mu\text{m}$ $f = 32 \text{Hz}$ $\tilde{U} = 125$
Surface walker		$U_{\max} = 37 \mu\text{m/s}$	$L = 12 \mu\text{m}$ $f = 35 \text{Hz}$ $\tilde{U} = 88$ $\tilde{U}_{\max} = 90$ $L = 4 \mu\text{m}$ $f = 47 \text{Hz}$ $U = 17 \mu\text{m/s}$

Figure 1.1: Some examples of synthetic microswimmers, classified by their swimming mechanism, with their corresponding characteristic speed. Figure extracted from *Soft Matter*, 2011 **7**, 8169

which produces an additional degree of freedom, namely, the motion parallel and perpendicular to the wall, due to the difference between friction in these two directions. This leads to locomotion near a boundary [68]. On Shun Pak *et al* summarised and classified accurately some of the synthetic microswimmers that have been realised in the last decades, emphasising the swimming mechanism and the characteristic speed [69]. Fig. 1.1, show a rich variety of mechanisms that can be used both in nature and synthetically in the lab to break the scallop theorem.

Here we will focus on a particular implementation of a surface walker actuated by a time dependent magnetic field. Fig.1.2 shows a scheme of a experimental realisation of a magnetically actuated rotor. This microswimmer has certain similarities to the one we will study in this section. Two paramagnetic particles are attached with a DNA bridge, and when an oscillating magnetic field is

1.2. Magnetic triangles near a solid boundary and friction anisotropy

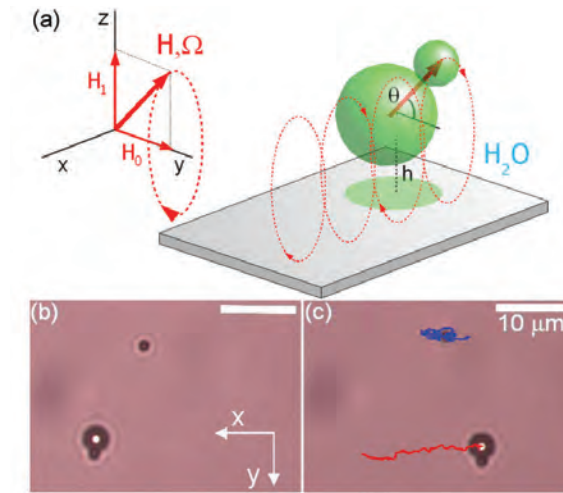


Figure 1.2: Experimental realisation of a colloidal rotor, showing the relevant degrees of freedom, the angle θ and the height h . The rotation of θ is rectified into a translation motion thanks to the presence of the boundary. Figure extracted from Phys. Rev. Lett. **101**, 218304

applied, the pair aligns with the magnetic field and oscillates. The vector linking the two particles describes a circular motion, which is rectified into a translation due to the additional degree of freedom introduced by the boundary. Since there is only two degrees of freedom, namely the motion perpendicular and parallel to the wall, the magnetic actuated rotor results only in two directions of motion, namely, forward and backward, depending on the chirality of the magnetic field. Upon inversion of the y component of the magnetic field, the direction does not change.

The magnetic swimmer we will characterise moves when actuated with the same type of magnetic field as that shown in Fig. 1.2. However, this magnetic microswimmer has the particularity of a swimming mode in which the triangle does not describe full rotations in relation to the solid plane. Instead, it slides along the solid plane with the lower surface of the triangle laying close to the solid boundary. By switching the magnetic field chirality (clockwise and counterclockwise) and the sign of the y component of the magnetic field, we demonstrate that friction anisotropy can produce four different directions of motion, allowing full control of the swimmer directionality.

The goal of this publication was to understand the experimentally-reported propulsion mechanisms of a magnetic triangle. In particular, the sliding propulsion mechanism, sketched in Fig 1.3 seemed to differ to the other two, which were in essence closer to that of magnetic actuated rotors [68]. The experimental triangles were formed by magnetised nanobeads, which were molded into a triangular shape. The shape was typically isosceles, but some defects in the shape existed, since the nanobeads added rugosity to the surface. The triangle had a permanent moment contained pointing towards some direction inside the triangle planar surface. Additionally, different experimental realisations of the triangles had different moments pointing towards different

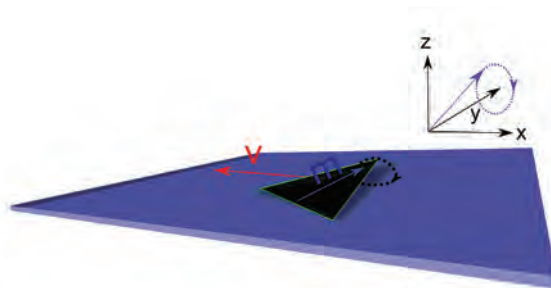


Figure 1.3: Scheme showing the sliding motion observed in experiments and simulations. The permanent magnetic moment \mathbf{m} in this scheme points towards one of the tips of the triangle. However, in experiments the magnetic moment could point anywhere inside the plane of the triangle. In the simulations, we also varied systematically the orientation of the magnetic moment inside the triangle plane.

directions, leading to a distribution of magnetic moment orientations.

We wanted to model the minimum ingredients that would account for the different propulsion mechanisms, and in particular, for the aforementioned novel propulsion mechanism where the triangle was observed to swim in four directions, making it suitable for surface exploration in the micro-scale. Thus, we proposed a coarse-grained model of a triangle formed by three beads, and introduced hydrodynamics in a simplified way that accounted for the solid boundary, and determined if such a simple model could reproduce the experimental observations. The algorithm we used was Molecular Dynamics, since we needed to keep fixed the distances between the beads by means of a constraint algorithm [62]. We will now present the algorithm and the conclusions of the work.

The Molecular Simulations model used was similar to that to simulate a filament of beads interacting hydrodynamically [70]. The simplest version of Molecular Dynamics consists on solving Newton's equation of motion for a set of particles that interact through different forces. These forces may arise from external fields, or from the repulsion when two particles come and interact closely enough. In our case, we will also introduce hydrodynamic interactions in a simplified way, as the force friction exerted by the particles due to the wall interaction, and due to the fluid flow that a bead generates in other beads when it moves. The algorithm consists in the following steps

1. Update positions:

$$r_i(t + \Delta t) = r_i(t) + v_i(t)\Delta t + \frac{1}{2}a_i(t)(\Delta t)^2$$

2. Calculate forces based on new positions:

$$a_i(t + \Delta t) = \frac{F_i(r(t + \Delta t))}{m_i}$$

1.2. Magnetic triangles near a solid boundary and friction anisotropy

3. Update velocities:

$$v_i(t + \Delta t) = v_i(t) + \frac{1}{2} (a_i(t) + a_i(t + \Delta t)) \Delta t$$

Given the initial conditions of the position and velocity for each particle, at each new time step we will need to compute all the forces exerted on each particle in order to update the acceleration, and then update the velocity we will need on the following step. We will now highlight which forces we chose to simulate the magnetic triangle.

For the sake of simplicity, we proposed a three bead model. The beads are connected by means of a MILC SHAKE algorithm [62] that ensures that the distance between beads is kept constant. The equation of motion for each bead is

$$m \frac{d^2 \mathbf{r}_i}{dt^2} = \mathbf{F}_i^m + \mathbf{F}_i^g + \mathbf{F}_i^{LJ} + \mathbf{F}_i^H \quad (1.7)$$

where subindex $i = 1, 2, 3$ refers to a bead. The first term \mathbf{F}_{ij}^m is the force due to the interaction of the triangle magnetic moment with the magnetic field. Distributing the forces on the beads to generate a torque implies taking into account the geometric constraints involved in the triangle. In our model the torque applied to the center of mass is

$$\tau = (\mathbf{r}_1 - \mathbf{r}_{\text{CM}}) \times \mathbf{F}^c_1 + (\mathbf{r}_2 - \mathbf{r}_{\text{CM}}) \times \mathbf{F}^c_2 + (\mathbf{r}_3 - \mathbf{r}_{\text{CM}}) \times \mathbf{F}^c_3 \quad (1.8)$$

where \mathbf{r}_{CM} is the center of mass of the triangle, and \mathbf{F}_i^c refers to the force of constraint of particle i , in order to exert the torque τ . As the torque does not induce any net force in the three-bead system, there is the extra constraint $\mathbf{F}^c_1 + \mathbf{F}^c_2 + \mathbf{F}^c_3 = 0$, that allows to rewrite Eq 1.8 as

$$\tau = (\mathbf{r}_1 - \mathbf{r}_3) \times \mathbf{F}^c_1 + (\mathbf{r}_2 - \mathbf{r}_3) \times \mathbf{F}^c_2 \quad (1.9)$$

There is 3 equations, one of each component x , y and z , and 6 variables left, corresponding to the components of \mathbf{F}^c_1 and \mathbf{F}^c_2 . The rest of constraints can be obtained imposing that the torque does not produce any local tensions along lines joining i and j between beads in the triangle, hence

$$(\mathbf{r}_1 - \mathbf{r}_2) \cdot (\mathbf{F}^c_1 - \mathbf{F}_1) = 0 \quad (1.10a)$$

$$(\mathbf{r}_1 - \mathbf{r}_3) \cdot (\mathbf{F}^c_1 - \mathbf{F}_3) = 0 \quad (1.10b)$$

$$(\mathbf{r}_2 - \mathbf{r}_3) \cdot (\mathbf{F}^c_2 - \mathbf{F}_3) = 0 \quad (1.10c)$$

Note that \mathbf{F}^c_3 can be rewritten in terms of \mathbf{F}^c_1 and \mathbf{F}^c_2 so that we are left with 3 equations, and the linear system can be solved. The system of equations 1.9 and 1.10 was solved numerically performing a LU decomposition combined with a backward and a forward substitution algorithm [71].

The second rhs in Eq. 1.7, $\mathbf{F}_i^{LJ}(z_i)$ accounts for the steric interactions between the beads and a wall placed at $z_i = 0$, which is of the Lennard-Jones type. This interaction is required for avoiding the triangle beads to keep falling

1.2. Magnetic triangles near a solid boundary and friction anisotropy

forever in the absence of gravity. The LJ interaction keeps $z_i > 0$, and is of the form

$$\mathbf{F}_i^{LJ}(z_i) = \frac{u_0}{r^{13}} \mathbf{e}_z \quad (1.11)$$

The last term \mathbf{F}_i^H takes into account the hydrodynamic interactions. In the vicinity of a stationary wall, a bead moving in a viscous fluid creates a velocity field that interacts with with its own image respect the wall, the other moving particles, and the images of the moving particles. The hydrodynamic velocity produced by a point-like bead subject to a force \mathbf{F}_i in the presence of a stationary wall is given by the Blake tensor [72]. The expression for the hydrodynamic force in this case is

$$\mathbf{v}_{iH} = \Delta\nu_i \mathbf{F}_i + \sum_{j \neq i} \mathbf{G}(\mathbf{r}_i, \mathbf{r}_j) \mathbf{F}_j, \quad (1.12)$$

where $\mathbf{F}_i = \mathbf{F}_i^m + \mathbf{F}_i^g + \mathbf{F}_i^{LJ}$ is the total force acting on a particle. The first term in the right side of Eq. 1.12 gives the self interaction contribution of the particle with its own image on the stationary wall. The tensor $\Delta\nu$ captures this interaction $\Delta\nu = \nu(\mathbf{1} - \hat{\mathbf{z}}\hat{\mathbf{z}}) + 2\nu\hat{\mathbf{z}}\hat{\mathbf{z}}$, where $\nu = -\frac{3}{16}\frac{a}{z_i}$, a is the hydrodynamic radius of the bead, and z_i its z coordinate distance to the stationary wall [73]. The second term in the right side provides the cross hydrodynamic interactions between different beads: $\mathbf{G}(\mathbf{r}_i, \mathbf{r}_j) \equiv \mathbf{G}_{ij}$ which takes into account the hydrodynamic flux contribution between a bead j , its image, and bead i . Due to this velocity field, particles experience a hydrodynamic drag that can be approximated, to lowest order as $\mathbf{F}_{iH} = -\gamma(\dot{\mathbf{r}}_i - \mathbf{v}_{iH})$, so that the final expression for the force is

$$\mathbf{F}_{iH} = -\gamma_0^\parallel \left(\hat{\mathbf{n}}\hat{\mathbf{n}} \frac{\gamma_0^\perp}{\gamma_0^\parallel} + \hat{\mathbf{p}}\hat{\mathbf{p}} \right) \left[\dot{\mathbf{r}}_i - \Delta\nu_i \mathbf{F}_i - \frac{1}{8\pi\eta} \sum_j \mathbf{F}_j \mathbf{G}_{ij} \right] \quad (1.13)$$

The first right hand term in brackets in Eq. 1.13 is the asymmetric friction tensor $\hat{\gamma}$, which takes into account the difference in friction of beads when they move parallel to the plane containing the three beads, or perpendicular to it. The terms $\hat{\mathbf{n}}\hat{\mathbf{n}}$ and $\hat{\mathbf{p}}\hat{\mathbf{p}}$ are tensors that determine the hydrodynamic friction normal ($\hat{\mathbf{n}}$) or perpendicular ($\hat{\mathbf{p}}$) to the triangle plane. The scalars γ_0^\perp , γ_0^\parallel denote the bead friction perpendicular and parallel to the triangle plane. This difference in friction accounts for the planar geometry of the triangle. By comparing with experiments, we determined that this friction difference had to be accounted to reproduce accurately the different swimming modes. The explanation for this is very intuitive, since it is reasonable to imagine that the triangle experiences a smaller friction when its a \mathbf{p} vector that rotates while \mathbf{n} is constant.

Now we will rewrite the dynamic equations in rescaled units to reduce the number of independent parameters. We address the equation in scalar form for simplicity. Rewriting Eq. 1.13 in terms of a characteristic length of the triangle, r_c , and characteristic time $\tau = \gamma_0^\parallel r_c^2 / |m||B|$ leads to

$$\frac{t_a}{\tau} \ddot{\tilde{\mathbf{r}}}_i = -\hat{\gamma} \dot{\tilde{\mathbf{r}}}_i + (\tilde{\mathbf{F}}_i^m - \xi \hat{\mathbf{e}}_z)(\mathbf{1} + \hat{\gamma} \Delta\nu_i) + \frac{3}{4} \frac{a}{r_c} \sum_j \tilde{\mathbf{F}}_j \tilde{\mathbf{G}}_{ij} \quad (1.14)$$

1.3. Hydrodynamic synchronisation in ratcheting colloidal matter

Here, $t_a = \frac{m}{\gamma}$ is the inertial time. Since the motion is overdamped, we will use $t_a \sim 0$. The magnetic field has the expression

$$\mathbf{B}_{rot} = B_x \sin(2\pi ft) \hat{\mathbf{x}} + B_y \hat{\mathbf{y}} + B_z \cos(2\pi ft) \hat{\mathbf{z}}, \quad (1.15)$$

where B_x, B_y, B_z refers to each coordinate in space and f is the applied frequency to the magnetic field. The relation between the modulus of the rotating magnetic field \mathbf{B}_{rot} and the constant component B_y also have a profound impact on the dynamics. A dimensionless $\xi \equiv r_c mg / |m| |\mathbf{B}|$ accounts for the relative gravity compared with the torque. A large torque compared to the triangle weight, induced by $|\vec{B}| |\vec{m}| / r_c \gg mg$ implies a negligible ξ . Experimentally this scalar can only be controlled through the applied magnetic field.

In the Blake tensor there is another characteristic length, a , which comes from rewriting the contribution $1/8\pi\eta$ in terms of the Stokes drag force expression $\gamma = 6\pi\eta a$, and hence is a length associated to the bead hydrodynamic radius. The factor a/r_c is associated to the non-dimensional thickness of the triangular swimmer. In the simulations define $\tau \equiv 1$ and $r_c \equiv 1$.

To sum up: The parameters of the model are $a/r_c, \frac{\gamma_0^\perp}{\gamma_0^\parallel}, B_y/|\vec{B}_{rot}|, \xi, f$. The three first parameters are to be tuned in the simulations. As characteristic values, we take the hydrodynamic radius to be close to triangle thickness, $a \simeq 0.15$, $\gamma_0^\parallel = 1$ and $\frac{\gamma_0^\perp}{\gamma_0^\parallel} = 2$. The rest of the parameters, $B_y/|\vec{B}_{rot}|, \xi, f\tau$ will be varied to characterise the different dynamic regimes in simulations. The force due to the magnetic torque $\tilde{\mathbf{F}}_m \equiv \|\mathbf{F}_m\| |\mathbf{r}| / |\mathbf{m}| |\mathbf{B}|$ has no dimensions, and we set this parameters to $|\vec{m}| = |\vec{B}| = r_c = 1$ in simulations for simplicity, and will vary the ratio between the magnetic field components.

For integrating Eq. 1.14 we use an implicit, two step Velocity-Verlet algorithm in matrix notation to deal with different tensorial elements. With this simple simulation methodology, we were able to observe the three swimming modes of the magnetic triangle. Furthermore, we also observed the synchronous-asynchronous rotational dynamics of the triangle, obtaining a quantitative agreement. The underlying mechanism was observed to be anisotropic motion of the triangle due to the misalignment of the magnetic moment of the triangle respect the symmetric axis. The results and details of the work and comparisons with experiments are shown in Pub.4.1.

1.3 Hydrodynamic synchronisation in ratcheting colloidal matter

Transport of matter at the micro and nanoscale is complex and can give rise to emergent responses. If the goal is to collectively move particles in the presence of a solid boundary, hydrodynamic interactions might alter both the dynamics and the resulting pattern morphology observed in experiments [74]. In this section, we present a publication that delved in the dynamical and morphological properties of a suspension of colloidal particles driven by a magnetic field. The system consisted of paramagnetic colloidal particles moving above a solid substrate, composed by a garnet film of periodically inverted magnetisation. It can be proven theoretically and experimentally that a single paramagnetic particle in such a substrate, in the presence of an oscillating magnetic field, is transported by a energy landscape that corresponds to a travelling periodic

1.3. Hydrodynamic synchronisation in ratcheting colloidal matter

wave [75]. These particles have diameters close to $1 \mu\text{m}$ and are embedded in a viscous fluid, which means that they move in a highly viscous medium where acceleration does not play any relevant role. The velocity of the travelling wave can be tuned by increasing the frequency of the external magnetic field, which should translate into a faster velocity of the paramagnetic particle. However, increasing the particle speed also means increasing the friction exerted by the viscous medium, which follows the Stoke's law $\nu = 6\pi\eta r v$. Eventually, the friction force overcomes the force exerted by the minima of the energy landscape, which translates into complex sliding dynamics, where particles jump between minima of the travelling potential in the opposite direction to that of the travelling wave. Thus, there is a frequency threshold f_c , referred as the critical frequency, below which individual particles translate with the same speed as the energy potential travelling wave, and above which particles move slower compared to the travelling wave speed. The critical frequency f_c was already analytically calculated in [75] and compared to the experiments. In Fig. 1.4 we reproduce a summary of the described dynamics of these paramagnetic particles.

Strikingly, experiments showed that when the density of paramagnetic particles increased, the critical frequency increased too, suggesting a collective speed-up effect. Furthermore, particles arranged forming local rhomboidal shapes, suggesting that the speed up could be correlated to a morphological change. Since the initial theory was written only for a single particle, no influence of the colloidal density on f_c could be expected [75]. Explicitly simulating the solvent and the paramagnetic particles at the same time would be computationally very expensive. In these case, we develop a computational model that carefully picked which aspect of the experiment wants to be understood. We accounted for the solvent by means of Brownian Dynamics simulations, in order to account for the different collective effects that can emerge between these paramagnetic particles embedded in a fluid due to its interactions.

Thus, we take the Langevin equation in the overdamped limit, Eq. 1.5. The forces will now be different compared to the previous section. Here, three main forces contribute to the motion and morphology of the particles. First, the magnetic force $\mathbf{F}_i^{\text{ext}}$ that results in the travelling ratchet, which was already obtained in previous works [75]. In the presence of a magnetic field, paramagnetic particles have a magnetic moment directed towards the instantaneous magnetic field, and this magnetic dipoles will result in dipolar interactions between the particles, accounted by a pair force interaction $\mathbf{F}_{ij}^{\text{dip}}$. A third contribution is the flow perturbation induced by the motion of a particle in the rest of the particles. These are what we refer to as the hydrodynamic interactions, which we account by means of a velocity contribution to the particle i due to the motion of the rest of the particles, $F_h = \gamma \mathbf{v}_i^H$. This velocity is given, again, by the Blake-Green tensor, j , to particle i , thus $\mathbf{v}_i^H = \sum_{j \neq i} \mathbf{G}(\mathbf{r}_i, \mathbf{r}_j) \mathbf{F}_j$. Compared to the previously presented publication, in this experimental realisation there is no need to include an asymmetry in the friction tensor since the motion is purely 2D and contained inside a plane parallel to that of the solid surface.

Additionally, we introduce a repulsive steric force to avoid overlapping of the

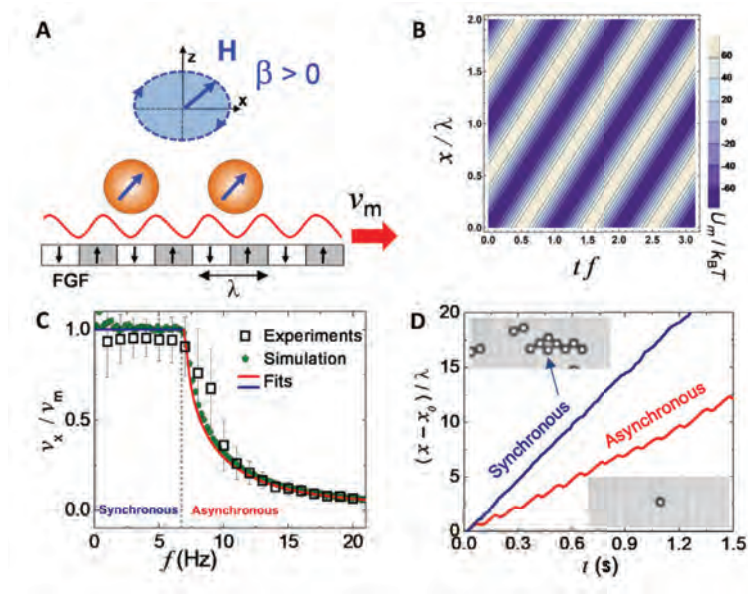


Figure 1.4: Summary of the behaviour of an isolated paramagnetic particle moving atop a garnet film with periodically inverted magnetisation. Figure extracted from our publication *Sci. Adv.*, 2022 **8**. A) shows the experimental setup, consisting of paramagnetic particles on a film of periodically inverted magnetisation, in the presence of an oscillating elliptical magnetic field. The red line represents the ratchet potential, which moves with speed wave $\nu_m = f\lambda$. B) Experimental observation of the potential landscape. C) Behaviour of an isolated paramagnetic particle moving upon actuation of an oscillating magnetic field. First, the particle is trapped at a minima of the potential and moves at a speed $v_x = \nu_m$. At a certain frequency threshold, the viscous friction force, which is proportional to the velocity, overcomes the potential force, and the particle diminishes its velocity respect the travelling wave. D) Trajectory of a synchronous and asynchronous particles.

particles, $\mathbf{F}_{ij}^{\text{int}}$. The final Brownian Dynamics equation is

$$\gamma \frac{d\mathbf{r}_i}{dt} = \mathbf{F}_i^{\text{ext}} + \sum_{j \neq i} \mathbf{F}_{ij}^{\text{dip}} + \sum_{j \neq i} \mathbf{F}_{ij}^{\text{int}} + \gamma \mathbf{v}_i^H + \boldsymbol{\xi} \quad (1.16)$$

which we integrate by means of the Euler algorithm

$$\mathbf{r}_i(t + dt) = \mathbf{r}_i(t) + dt \frac{\mathbf{F}_i(t)}{\gamma} \quad (1.17)$$

More details of the forces for the integration algorithm and results of this study are shown in Pub. 4.2. The simulations demonstrated that the re-synchronisation of the particles with the travelling wave was purely induced by far field hydrodynamics. This resulted from comparisons between simulations where far field hydrodynamics was introduced, observing the corresponding speed-up, with simulations where there was no far-field hydrodynamics. In

the latter case, both including and neglecting dipolar interactions lead to a decrease in the particle speed with increasing density in the asynchronous region. By turning on far field hydrodynamics, we observed a quantitative agreement between simulations and experiments considering the velocity as a function of the frequency. However, the characteristic morphology of rhombic clusters was not observed with hydrodynamic interactions alone. Dipolar interactions need to be included to observe this rhombical structures. The reason for this was due to the attraction induced by two nearby magnetic moments, which tends to alineate particles one in front of the other. However, the distance between two minima of the ratchet potential was smaller than the diameter of the particle, resulting in diagonal resynchronised clusters all along the garnet film.

1.4 Local clogging in ratcheting colloidal matter

In this section, we use the same experimental setup of the previous section, namely, the paramagnetic particles in the film with periodically inverted magnetisation. However, here we focus in their motion through an heterogenous medium. When a bunch of particles move through a narrow constriction, it might happen that a certain geometric arrangement of the particles results in a clog. For a certain time, no flow takes place through the constriction, and the clog could remain for an indefinite period of time. This phenomena does not belong to any particular length-scale. Clogging takes place in our daily life, when we use a salt shaker and whenever granular media is forced through a racked texture. It takes place too whenever a silo containing rice or any granular media is discharged. Understanding clogging is relevant beyond soft matter and it can be observed in larger scales, e.g sheep [76,77] and pedestrians [78].

In micro-scale systems, clogging is particularly important, since particles in colloidal suspensions can clog microfluidic circuits and difficult lab-on-a-chip implementations. In the presented publication, we investigated clogging of particles driven by a modulated ratchet potential through narrow constrictions. These constrictions were experimentally designed by attaching a random distribution of spherical solid silica particles to the substrate. The particles configured an obstacle landscape, and some random placement of several obstacles could constitute a bottleneck where clogging could be observed for certain frequencies. We use the same Brownian Dynamics methodology described in the previous section for the simulations. Additionally, we included a second different kind of particles, corresponding to the silica particles, which remained pinned through the simulation, and mimicked the same exact experimental geometries, obtained in experiments by image processing.

To characterise the clogging transition, we followed the standard procedure published by Zuriguel *et al* [79]. This procedure is based on the fact that the complementary cumulative distribution function of passing time between particles in the constriction follows a power-law distribution $t^{-\alpha}$. If $\alpha < 2$, the average passing time between particle diverges, which states that there is a finite probability that the clog persists at an arbitrary large time. This notion is used to say that, for an experimental or simulation time-series with a certain election of parameters, the system is clogged if $\alpha < 2$, and unclogged if $\alpha > 2$. Using this procedure, it has been shown that clogging is a very local phenomena that strongly depends on the interactions involved and the geometrical properties of

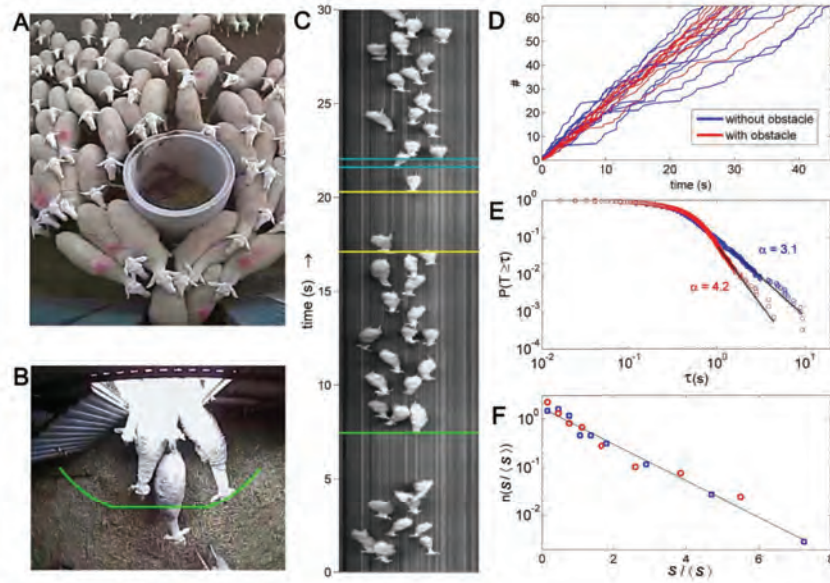


Figure 1.5: Example of a clogging transition for the passing of sheep through a bottleneck. A) Shows an image of the obstacle placed in front of the bottleneck. B) Shows an image of the recording used to characterise the power law exponent. C) Imaging as a function of time, showing how different events were separated. D) Number of sheep that pass the bottleneck as a function of time, with and without obstacle. E) Complementary (CDF) used for computation of the clogging characteristic exponent. F) Histogram of burst sizes of sheep. For more details see original text. Figure extracted from *Sci. Rep.*, 2014, **4**, 7325

the constriction. For example, in Fig. 1.5 it is shown that placing an obstacle in front of the bottleneck drastically changes the clogging exponent, and results in enhanced flow.

In the experiments, we observed two main features we were interested in understanding: First, the complementary cumulative distribution function exhibited periodic plateaus that seemed to be correlated to the external magnetic field frequency. Second, for increasing frequency of the magnetic field, the cumulative distribution function collapsed in a clogged state where $\alpha \sim 2$, meaning that larger exponents were never observed. To elucidate this mechanisms, we systematically compared the simulations of three different important factors to clogging, namely, the presence of hydrodynamic interactions, the capability of obstacles to move a certain distance from the equilibrium position and vibrate, and the distance between obstacles in the constriction, which could not be precisely determined due to the resolution of the microscope. Additionally, we also characterised the correlation of clogging events when two constrictions were placed together. The results showed that hydrodynamics tend to enhance clogging processes, while vibration of the obstacles were responsible for the saturation of the clogging exponent. The results can be read in Pub. 4.3.

1.5 Anomalous flows in disordered landscapes

In the previous section, we focused on the local aspects of clogging for a particular driving potential and a geometrical configuration of particles that constituted a bottleneck. The main goal was to compare the experimental realisations with a minimum simulation model that captured the relevant interactions inducing the clogging transition in experiments. In the publication introduced in this section, we moved our scope to a broader point of view. We considered a general, arbitrary landscape of obstacles, with no particular or defined bottleneck. This random distribution of pinned particles in a region of space has an area fraction of ϕ_{pin} . If moving particles are randomly initialised with a certain density ϕ_{mov} , carefully avoiding overlap with the obstacles, and are then driven by an external force in a viscous overdamped suspension, they interact with the obstacles. At small $\phi_{\text{pin}} \sim 0$, the average velocity of moving particles will be the same of free moving individual particles. As ϕ_{pin} increases, some particles might get trapped for a while, decreasing the average velocity of the system. This decrease of particle velocity is gradual, and eventually, when ϕ_{pin} is large enough the average velocity becomes zero.

This is a standard problem the interest of which lays in moving matter across porous media, as it happens in filtration processes [80]. The ϕ_{pin} at which the average velocity becomes zero is typically referred to as the clogging density ϕ_{pin}^c [81], since most particles remain trapped in arrangements of obstacles. However, this notion of clogging across porous media must not be confused with the local notion of clogging considered in the previous section. The approach is different to the local constriction one, since no precise bottleneck locations can be defined. For a given obstacle configuration, it consists in determining the concentration of pinned colloids, ϕ_{pin}^c , above which the system will be in a fully clogged state characterised by a null average velocity [81,82]. In contrast, when looking at the detailed dynamics of particles between $\phi_{\text{pin}} = 0$ and ϕ_{pin}^c , a rich mixture of dynamical states is observed. For example, the velocity distribution at small and intermediate densities shows a double peak, one centered around zero, the other around the characteristic velocity of the particles, which suggests the idea of a separation between arrested particles, and free flow particles. Looking at visualisation of simulations, it can be seen for intermediate ϕ_{pin} that clogging is also observed locally, even when the average velocity is not fully zero, suggesting the idea of an anomalous notion of flow, where the flux of particles is only allowed through certain regions of the landscape.

The focus of this work was to relate the observed clogging taking place locally, at some regions of space crowded with obstacles, to dynamical properties such as the the velocity distributions of particles, and geometrical properties like the cluster distribution. It was already stated that ϕ_{pin}^c remains mostly constant regarding the total area fraction $\phi = \phi_{\text{pin}} + \phi_{\text{mov}}$, which indicates that the average spacing of obstacles, l_c is the relevant lengthscale that impedes the flow of moving particles through the system [81]. Is there a similar length-scale that sets the appearance of local clogs, while there is still flow across the landscape in the system?

To describe this dynamical properties, we propose a measurement method in the simulations, which is the time τ required for a particle to move its own diameter d . Each time a particle move its own radius, it will be considered an event of the random variable τ_i . If all particles are moving in a landscape

1.6. Self-propelled active rafts by diffusiophoretic and diffusioosmotic flows

with no obstacles, at small ϕ_{mov} all events will correspond to $\tau_i = d/v_d$. If obstacles are introduced, then larger measures of τ_i will be observed. If the same procedure as in local clogging is followed [79] and the complementary cumulative distribution function of this measurement is computed, one finds that this distributions follow a power law, $t^{-\alpha}$, analogous to the local case. By means of computing the exponent α , the same criteria can be used to determine whether the time particles remain clogged in obstacles diverge or not. When $\alpha > 2$, particles flow and clogs do not form persistently, and we refer to this dynamical state as normal flow. When $\alpha < 2$, clogs form in the landscape, some of which can persist for most of the simulation time, coexisting with regions where flow takes place freely. We define this dynamical state of the system as an anomalous flow, since a general notion of flow is not well defined. Furthermore, we defined a local notion of clogging, similar to the local measurements performed in bottlenecks, in order to determine the relation between clogging measured in local regions of the landscape and clogging looking through the passing time of particles τ .

In summary, in this work we wanted to model a suspension of colloidal particles driven across an heterogeneous landscape. We wanted to imitate a feasible experimental realisation, such as that from Pub. 4.3, in order to develop a methodology to bridge concepts between local clogging and particles driven through porous media. However, since in this case there was no experimental realisation, we chose to study particles driven by a constant force, since this facilitated the understanding of the observed responses and velocity distributions. The motivation for such a study was to find a standard, comprehensive methodology of characterising clogging given a certain force and a certain geometrical configuration consisting of an indefinite number of bottlenecks. We found that local clogging and clogging defined as we have briefly described in this section follow the same qualitative trends and even coincide qualitatively in the limit of large densities. This confirms the apparently intuitive observation that abnormal flow is dominated by local clogging events, which influence the morphology and velocity distribution of the colloidal particles.. We hope the presented work in Pub. 4.4 will be useful to perform comparative studies quantitatively, between different type of driven colloidal particles, including active matter, and its ability to hinder or enhance clogging of the porous media.

1.6 Self-propelled active rafts by diffusiophoretic and diffusioosmotic flows

We end this chapter with an incursion to a different topic, the interest of which has increased exponentially in the last decade. Active matter systems are composed by units that can consume energy, which can be extracted from the media, or due to internal metabolic processes of a living organism, in order to self-propel or deform [83]. This has striking consequences for their theoretical understanding: Detailed balance is broken locally [84], which means that active matter is intrinsically out of equilibrium. This challenges the use and utility of most statistical tools. Furthermore, the active nature of these forces can result in non-reciprocity between different types of particles or interactions, breaking the 3rd Newton's law of physics. The interest on this type of matter, while proceeding from different research fields and areas, such as cell motility in

1.6. Self-propelled active rafts by diffusiophoretic and diffusioosmotic flows

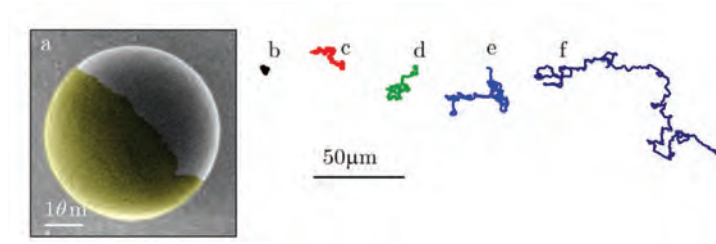


Figure 1.6: Example of a Janus particle. a) Shows a scanning electron microscopy image of a colloidal particle with a 20 nm thick gold cap (highlighted). b) Represents the trajectory of the particle after being actuated with light. Figure extracted from *Soft Matter*, 2011, **7**, 8810-8815

biology, self-assembly of herds like schools of fish or birds, and colloidal science, has resulted in a common framework to think, simulate, and model this systems. This diverse body of knowledge has evolved into a distinct field of study in its own right. It represents a collaborative effort across various disciplines, working together to unravel the underlying causes of complex behaviors observed in nature.

The most famous colloidal synthetic active system consists of a suspension of particles called Janus particles [85]. As shown in Fig. 1.6a, asymmetric coating of a sphere can result in a self-propelled persistent motion, in Fig 1.6b. In general, these synthetic particles have two faces with two different chemical properties, one of which can catalyse a reaction of a substance in the media when the sample is homogeneously illuminated. These particles, when isolated, self-propel following a persistent random walk [86]

$$\langle \Delta r^2 \rangle = 4D_0t + \frac{v^2}{2D_r} [2D_r t + e^{-2D_r t} - 1], \quad (1.18)$$

where the first term corresponds to the conventional diffusion coefficient D_0 and the second term is the active contribution. The velocity v is the colloid swimming speed and D_r its rotational diffusion coefficient. At short times, this persistent random walk follows $\langle \Delta r^2 \rangle \sim 4D_0t + (vt)^2$, which results in a ballistic motion at small times. When a suspension of such particles is illuminated the system can phase-separate in a large density phase and small density phase [86], in agreement with theoretical predictions [87].

The previous active particles are polar, since they have a fixed persistent direction of motion. Active apolar particles, on the other hand, do not directly transform activity into motion [88]. These active apolar matter, like hematite particles, when illuminated with a blue light, produce a concentration field that induces diffusiophoretic interactions on the surfaces of other particles. An isolated active apolar particle will not move upon light actuation, since the diffusio-phoretic flow generated at the surface of the particle is symmetric respect the particle center. However, in the presence of a passive silica particle, non-reciprocal interactions in the surface of both particles will lead to a pair formation that will self-propel. The hematite, in a mixture of water and hydrogen peroxide (H_2O_2), decomposes the peroxide in oxygen and water, which produce a gradient in the chemical concentration around the particle and induces

1.6. Self-propelled active rafts by diffusiophoretic and diffusioosmotic flows

diffusiophoretic flows [88]. In order to consider the dynamical mechanism that drives the particles, let us write the decomposition of H_2O_2 in water. The diffusion of the chemical field of the products of the reaction in the surface of a particle can be well described by the Laplace equation

$$\nabla c(r, \theta, \psi) = 0. \quad (1.19)$$

The production/consumption of chemicals enters the equations through parameter α in the Neumann boundary conditions

$$D_c \partial_r c(r)|_\sigma \propto \alpha, \quad (1.20)$$

where D_c is the diffusion constant of c , and σ the surface of the particle. The solution to Eq. 1.19 of an active colloid i in the presence of a second colloid j , in spherical coordinates, is described by the expression

$$c_i(r, d, \theta) = \frac{\alpha_i \sigma_i^2}{4D_c} \frac{1}{r} + c_{i,j}(r, d, \theta) \quad (1.21)$$

where d is the distance between the particles $d = |\mathbf{r}_i - \mathbf{r}_j|$, σ_i is the radius of particle i , and $c_{i,j}$ are the terms coming from the disturbance of the chemical field due to the presence of a second particle j . These terms can be obtained, e.g., from a multipolar expansion, and differ depending on whether the interaction is between two active particles, or an active and a passive pair. A sphere in the presence of a chemical field gradient experiences a tangential diffusiophoretic velocity $\mathbf{v} = \mu_d \nabla_{||} c(\mathbf{r})$, where μ_d is the diffusiophoretic velocity. Momentum conservation on the sphere leads to

$$\mathbf{V} = -\frac{1}{\pi\sigma^2} \int_\sigma dS \mathbf{v}(r, \theta) = (\pi\sigma^2)^{-1} \mu_d \int_\sigma dS \nabla_{||} c(r, \theta) \quad (1.22)$$

where the integral is over the surface of the sphere σ . Combining these expressions together, one finds that an active particle imposes a velocity in the passive particle

$$v^{a \rightarrow p} = -\frac{\alpha \mu^p d}{12D_c} \left(\frac{\sigma_a}{d}\right)^2, \quad (1.23)$$

where μ^p is the diffusiophoretic mobility. On the other hand, a passive particle imposes the following velocity on the active

$$v^{p \rightarrow a} = \frac{\alpha \mu^a d}{12D_c} \left(\frac{\sigma_p}{\sigma_a}\right)^3 \left(\frac{\sigma_a}{d}\right)^5. \quad (1.24)$$

where μ^a is the diffusiophoretic mobility. Interestingly, these two velocities have two qualitatively different dependences as a function of the distance. Passive particles are attracted towards an active particle following $v \propto 1/d^2$, while active particles are attracted towards the passive ones following a weaker velocity $v \propto 1/d^5$. Hence, action-reaction is broken, and this expression predicts that a pair of an active and a passive particle will move with the active particle at the front, since the passive interaction will be typically stronger and directed towards the passive particle.

In the work presented in this section, Pub. 4.5, we were interested in the response of a single active particle in the presence of a bath of passive particles.

1.6. Self-propelled active rafts by diffusiophoretic and diffusioosmotic flows

In the experiments, it was observed that the active hematite particle nucleated a dense packed raft, which moved with a large persistent length l_c , while sweeping particles in its motion. We implemented the non-reciprocal interactions from Eq. 1.23 and Eq. 1.24 in a Brownian-Dynamic model. Besides these velocities, particles interact with a WLC potential to avoid overlap when passive particles get attracted towards the active ones. In experiments, the active particles had an ellipsoidal shape. To simulate an ellipsoid, we consider a dumbbell model, where two particles were linked with a strong harmonic spring to constitute one active particle. As in the experiments, the active particle got surrounded by passive particles that constituted a raft. However, comparing the simulations and the experiments reveals that in the simulations, the active raft moved towards the opposite direction compared to the experiments. In the simulations, the raft moved towards the direction where angularly a smaller number of particles were accumulated, since the regions of larger passive particle density pushed the raft following Eq. 1.23. Eventually, the raft swept enough particles to change its direction again, resulting in a small persistence length. This is in accordance with the behaviour of a dimer formed by an active and a passive particle, which was observed in experiments. The pair is observed to move with the active particle at the front. However, experiments predicted that the raft direction of motion correlated towards the direction in which an angular larger accumulation of particles was present. In the presented work, we will show that this contradiction is solved when we consider theoretically the role of the diffusio-osmotic flow taking place at the solid boundary below the active raft.

PART III

Driving fluids at the microscale

CHAPTER 2

Capillary driven multiphase fluids

2.1 Introduction

In this third part of the thesis, we will focus on a different type of transport. In the previous sections, the particular details of the hydrodynamic coupling to the embedding fluid was not determinant. When required, far-field hydrodynamics were introduced in BD and MD simulations to account for the flow contribution in a specific point of space by a force singularity.

Here we will study fluids under confinement. Confinement will refer to a fluid or a combination of fluids in a channel of width of the order of $w \sim 50 \mu\text{m}$. The fluid equations that govern the dynamics of the liquids inside these channels are, again, Stokes equations, also referred to as creeping flow equations

$$\begin{aligned}\eta \nabla^2 \mathbf{v} &= \nabla p, \\ \nabla \cdot \mathbf{v} &= 0,\end{aligned}\tag{2.1}$$

where the first equation is the simplified Navier-Stokes equation for $\text{Re} \ll 1$, when advective terms are negligible, and the second equation states the flow incompressibility. Besides the time reversibility already mentioned at the beginning of the last part, these equations have some other interesting peculiarities. In the microscale the no-slip boundary condition in solid interfaces has a strong impact in the flow profile, in contrast to our daily life experience with fluids. This condition strongly affects the velocity field of the embedded fluid. Furthermore, flows in confined microchannels and drops are very sensitive to interfacial phenomena, since the bulk of the fluid is comparable to the fluid area. Surface tension is one of the most important interfacial phenomena in the microscale and will be the focus of this chapter.

Surface tension is responsible for the Lucas-Washburn law, which states that a viscous fluid can spontaneously invade a channel occupied by a gas without any external energy supply. According to the Lucas-Washburn law, the front position will follow a dependence $h \sim t^{1/2}$. The Lucas-Washburn law has been the start point for a plethora of works where different effects are included to increase the accuracy of the predictions. In the early stages of the imbibition, when the channel is filled with air, the friction forces of the invading fluid are negligible and inertial effects dominate the dynamics, following $l \propto t$ in the early stage [89]. The effect of viscosity in the displaced fluid has also been subject of study [90]. An important contribution can be explained by the contact angle dynamics: When the channel starts to invade the front, the measured contact

angle as a function of time does not exactly coincide with the equilibrium angle θ_e , since the balance at the contact line is not zero. The interface deformation depends on the speed of the front by means of the Cox-Voinov equations [58], which quantifies the dissipation involved in the interface deformation. These effects can be studied altogether numerically and compared with the simulations to obtain high accuracy comparisons with experiments [12]. Furthermore, some works have analysed how the long-time diffusive exponent, t^α , changes with the geometrical and physical properties of the channel. Channels with axial variations have been characterised [91] to determine the optimum shape that allows a faster invasion speed. Capillary advance between elastic sheets have also been subject of study [92–94].

One of the experimental limitations of spontaneous capillary imbibition in solid surfaces is the roughness of the surface. Solid surfaces are not completely smooth, but have a certain rugosity that can pin the interface of drops [95], and make them resistant to motion. This additional friction can be quantified by means of the hysteresis of the equilibrium contact angle. Indeed, in regular solid surfaces, drops do not immediately start to flow. Instead, it is observed that the static contact angle reaches a maximum value, above which the drop starts to move. The difference between the minimum and maximum equilibrium contact angle is referred to as contact angle hysteresis [96] and quantifies the resistance to the onset of drop motion. This pinning effect also affects fronts in spontaneous imbibition and modifies the front speed [97,98]. The surface roughness can suddenly stop the spontaneous imbibition and pin the front, drastically stopping the invasion. Efforts have been made to avoid the pinning effects of conventional solids. There are superhydrophobic surfaces that benefit from a texturised structure and a dynamic state of drops where between pillars of the texture, air bags are formed, reducing the friction. These superhydrophobic surfaces reduce pinning effects, but they cannot withstand pressure [99], seriously limiting their capabilities in real situations. Other solid surfaces such as slippery omniphobic covalently attached liquid-like (SOCAL) consist in microbrushes that can prevent pressure to destroy the surface hydrophobicity in order to repel drops [100]. However, these surfaces are designed to repel drops and spontaneous imbibition requires that the surface is hydrophilic.

A different strategy consists in designing surfaces that are prone to be spontaneously imbibed by a lubricant that covers the whole surface. Slippery Liquid Porous Surfaces (SLIPS) [55] and Liquid Infused Surfaces (LIS) [56] are lubricant coated surfaces inspired by the plant *Nepenthes* [101]. The texturised surface of this plant, when wet, is inescapable to insects, which fall inside the pitch and get digested. SLIPS and LIS also make use of texturisation to favour the embedding of a lubricant film. These surfaces are resistant to applied pressures, and when the layer of lubricant is disrupted, it heals due to the combined wetting properties of the solid and the lubricant. Furthermore, the election of the lubricant allows tuning of the wetting and viscous properties with respect the target fluid. The lubricant viscosity also plays a determinant role on drop dynamics, as shown in Fig. 2.1. It has been determined that when the viscosity of the lubricant (η_s) is larger than that of the drop (η), the drop follows a velocity law $v \propto (\sin \alpha)^{3/2}$ as a function of the tilted angle α for small inclinations, and $v \propto (\sin \alpha)^3$ for larger inclinations. In the opposite case, when $\eta \ll \eta_s$ the velocity law changes the exponent and follows $v \propto (\sin \alpha)^1$ [56]. We this results from the original paper in Fig. 2.1. The explanation for this

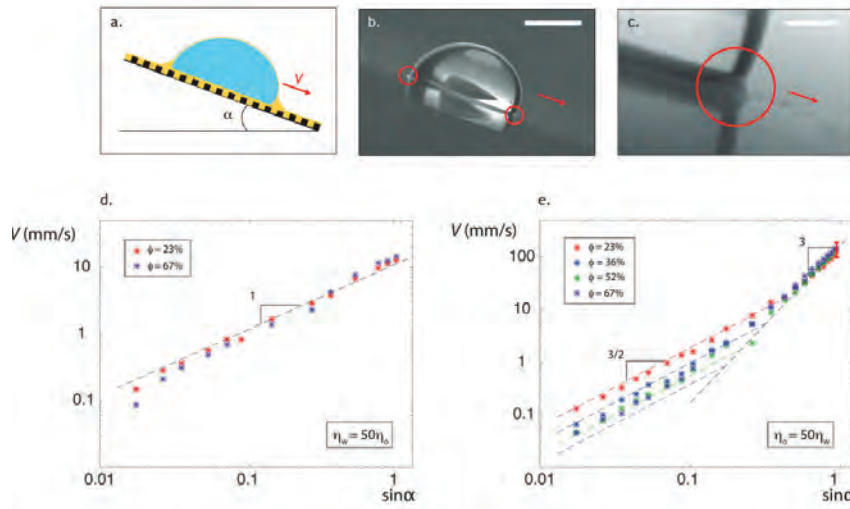


Figure 2.1: Dynamics of drops in lubricant-infused surfaces. a) Shows a scheme of a drop sliding in a surface inclined an angle α . b) and c) show highlight the meniscus of the drop. Figure d) shows the velocity of the drop as a function of $\sin\alpha$ when the viscosity of the drop is 50 times larger than that of the lubricant, which follows a linear behaviour, and is independent of the fraction of pillars in the texturised surface (ϕ). e) Shows the opposite case, where the lubricant viscosity is 50 times larger than than that of the drop. In this case, for small values of $\sin\alpha$ the velocity follows $V \sim \sin\alpha^{2/3}$, and for large values $V \sim \sin\alpha^3$. In the first regime, the fraction of pillars quantitatively influence the velocity. *Soft Matter*, 2017, **13**, 6981-6987

change of the drop dynamics can be found in the dissipation mechanism of the drop, which changes depending on the viscosity contrast η/η_s . These results suggests that a lubricant-coated channel could also trigger a different dissipation mechanism depending on the lubricant viscosity, unveiling new dynamics of spontaneous imbibition. The first publication of this part, Pub. 4.6 consists in simulations of spontaneous imbibition in lubricant coated channels. The goal was to probe different dynamical regimes by systematically changing the lubricant viscosity. Since this problem is theoretically very complex to treat in a fully analytical way we developed a simulation methodology to study the properties of lubricant coated surfaces. In the next subsections, we briefly introduce the reader to surface tension phenomena. Later we describe the basis for the simulation methodology we used, the Lattice-Boltzmann method, the ternary fluid free energy model we used to simulate surface tensions and how we coupled together these two approaches to simulate lubricant coated surfaces. After presenting this publication, we will introduce the dynamics of contact line for interfaces moving atop of solids. This introduction will serve as a build-up to a section where we will explore the role of the lubricant viscosity in in the contact line dynamics of a drop.

Surface Tension

Surface tension is one of the dominant interfacial phenomena existing in the microscale, exploited by nature and industrial applications. In a water-air interface, water minimises its surface area by acquiring a spherical shape. In this spherical geometry, water molecules in the interface will maximise the neighboring particles of water, while minimising the neighbouring air molecules, minimising the surface energy. In general, increasing the area of an interface between two liquids requires an energy per unit area γ which needs to be supplied [9]

$$\delta W = \gamma dA. \quad (2.2)$$

Surface tension is also the reason why bubbles and drops experience an a pressure drop across the interface. The Young-Laplace equation states that an increase in hydrostatic pressure takes places across any interface between two fluids

$$\Delta p = \gamma \left(\frac{1}{R} + \frac{1}{R'} \right) \quad (2.3)$$

where R and R' are the principal radii of curvature of the interface. This equation is the reason why smaller drops get adsorbed by larger drops: Smaller drops have a larger curvature, which results in a larger pressure inside. The resulting pressure gradient drives the fluid inside the smaller drop to the biggest one [9].

When an interface between two liquids is in contact with a solid surface, additional contributions to the surface tension need to be considered. Indeed, each of the two liquid-solid interfaces will also have a different interfacial tension, which will quantify the affinity of each liquid to the solid surface. These different contributions result in the phenomena of wettability and spreading of drops and fronts in contact with solid surfaces. We consider three interfaces, which we will refer to as liquid (l), gas (g) and solid (s), as shown in Fig. 2.2. Each interface will have a surface tension, and we will refer to γ_{sl} for the solid-liquid interface, γ_{sg} for the solid-gas interface, and γ_{lg} for the liquid-gas interface. The spreading parameter, S , characterises whether a drop will wet and expand all over a solid surface or not

$$S = \gamma_{sg} - (\gamma_{sl} + \gamma_{lg}). \quad (2.4)$$

This parameter quantifies the difference between surface energy when the substrate is dry, which corresponds to the first term in the rhs of Eq. 2.4, and the energy when there is no gas around, which are the terms inside brackets. If $S > 0$, the liquid spreads completely to minimise the surface energy, since the gas-solid interface has a larger energy cost. If $S < 0$, it is said that the drop is in partial wetting. The drop does not spread, but instead it forms an equilibrium contact angle with the solid surface. Since the surface tension can also be interpreted as a force per unit length, we can write down the equations to find the equilibrium contact angle. As drawn in the schematic diagram in Fig. 2.2, in the presence of a solid, equating the forces leads to the Young equation

$$\gamma_{lg} \cos \theta_e = \gamma_{sg} - \gamma_{sl} \quad (2.5)$$

The contact angle $\theta_e = 90^\circ$ is a special limit case, referred to as neutral wetting condition. In this case, both fluids, liquid and gas, have the same affinity to

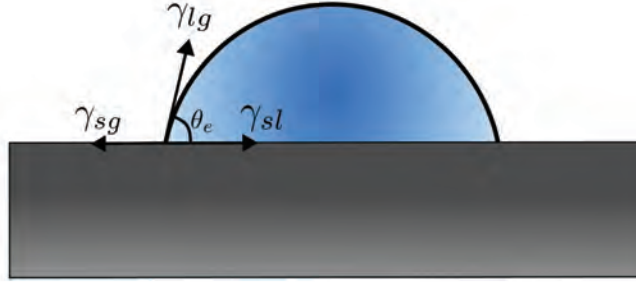


Figure 2.2: Schematic drawing of the Young law

the solid $\gamma_{sg} = \gamma_{sl}$. If $\theta_e > 90^\circ$ it is said that the liquid fluid is hydrophobic with respect to that surface, since the larger $\gamma_{sl} > \gamma_{sg}$ implies a preferential wettability of the gas phase for the solid to minimise the surface energy. If $\theta_e < 90^\circ$, the liquid phase is said to be hydrophylic, since $\gamma_{sl} < \gamma_{sg}$ implies a preferential wettability of the liquid for the solid respect the gas phase to minimise the surface energy.

Distinguishing between hydrophobic and hydrophylic contact angles becomes extremely important when considering the effect of introducing a solid surface in a bath of liquid. As we show in Fig. 2.3a), a hydrophobic contact angle produces a spontaneous invasion of the liquid phase in the channel, which is compensated by the gravity. Oppositely, an hydrophobic contact angle produces an invasion of the gas phase in the channel, lowering the water level below the reservoir level. Let's write down the equations at equilibrium conditions by looking at Fig. 2.3. First, we relate the curvature to the contact angle using the Young-Laplace equations Eq. 2.3. Considering that the channel consists in two parallel plates, the liquid-gas interface will form a meniscus which will be a portion of a sphere. In this case, the curvature will correspond to the radius of the sphere, which can be computed using the simple trigonometrical relation $\cos \theta_e = H/2R$. Here, H is the distance between the two plates. The pressure change across the solid-gas interface will be

$$\Delta p = \frac{2\gamma_{lg} \cos \theta_e}{H} \quad (2.6)$$

On the other hand, the hydrostatic pressure of a column h of liquid with density ρ is $p_h = p_0 + \rho gh$, where g is gravity. By equating this two terms, we get Jurin's law, which relates the height of the column with the surface tension and contact angle,

$$h = \frac{2 \cos \theta_e \gamma_{lg}}{H \rho g} \quad (2.7)$$

Hence, when placing a hydrophylic tube in a water reservoir, we will observe how initially a water front starts to invade the channel, and eventually it equilibrates at a certain height h and equilibrium angle θ_e .

What would happen in the absence of gravity? In this case, since the pressure drop cannot be compensated, the fluid front will continue to advance and eventually fill the channel. This is what we refer to as an spontaneous

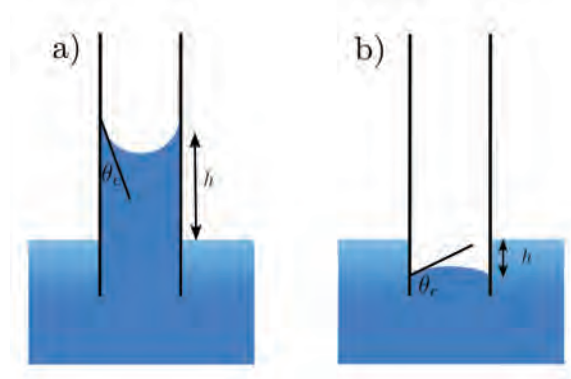


Figure 2.3: Schematic drawing of hydrophilic vs hydrophobic surface

imbibition. Let us consider the dynamical equation to predict the position of the front as a function of time. We know that the driving force corresponds to the pressure gradient across the interface in Eq. 2.6. We need to find the friction exerted by the channel on the fluid.

To find this friction, the Stokes equation Eq.2.1 must be solved for the considered geometry. In our case, this geometry will consist in two infinite, parallel plates. The viscous contribution by the gas phase will be neglected in this derivation. We will consider that the liquid invades the channel generating a laminar flow between the two infinite parallel plates, with the same cross section as depicted in Fig. 2.3. We consider that the front moves in the x direction, while the plates are placed at $y=0$ and $y=H$. We make the approximation that the velocity profile does not depend on x , hence $\mathbf{v} = v_x(y)\mathbf{e}_x$, where \mathbf{e}_x is the unit vector in the x direction. To calculate the friction imparted by the solid, we need to evaluate the shear stress at the wall $\tau_{xy} = dv/dx|_{y=0}$ and integrate it from the start of the channel to the front position $l(t)$. We start with the solution to the first differential equation Eqs. 2.1

$$v_x(y) = \frac{1}{\eta} \frac{\partial p}{\partial x} y^2 + Ay + C. \quad (2.8)$$

The constants can be determined with the no-slip boundary conditions, $v_x(0) = 0$ and $v_x(H) = 0$. The solution for the flow profile in this case is

$$v_x(y) = \frac{1}{\eta} \frac{\partial p}{\partial x} (y^2 - Hy) \quad (2.9)$$

We will now write the pressure gradient in terms of the mean velocity of the fluid. The mean velocity over a width w is computed as

$$u = \frac{1}{A} \int_0^w dz \int_0^H v_x(y) = \frac{\partial p}{\partial x} \frac{H^2}{12\eta} \quad (2.10)$$

Where A corresponds to the integral surface area, $A = Hw$. Note that we integrate in z over an arbitrary width w for units riguroosity, but this arbitrary width is cancelled after integration. After the pressure gradient in Eq. 2.10 in

2.2. The Lattice-Boltzmann method

terms of u , we evaluate the shear stress and compute the force exerted by the solid surface

$$F_v = \int_0^l dx \frac{12u\eta}{H} = \frac{12u\eta l}{H} \quad (2.11)$$

This is the friction resulting from the no-slip boundary condition, exerted by the solid on the fluid. The dynamic equation of imbibition is a balance between the force in Eq. 2.11 and the force resulting from the Young pressure drop, $F_c = \Delta p H = 2\gamma_{lg} \cos \theta_e$. Note that both F_c and F_v are forces per unit length, since these forces do not depend on the z coordinate. The last step to obtain the dynamical equation consists in assuming that the average velocity u corresponds to the front velocity $u = dl/dt$. Equating the two forces, we get to the differential equation

$$l \frac{dl}{dt} = \frac{\gamma_{lg} \cos \theta_e H}{6\eta}, \quad (2.12)$$

Integration of the latter equation leads to the imbibition law

$$l(t) = \sqrt{\frac{\gamma_{lg} \cos \theta_e H}{3\eta} t}. \quad (2.13)$$

The latter equation states that since the pressure gradient is constant and the most viscous phase invades the channel increasing the dissipation, front advance slows down with the front penetration following diffusive dynamics. This result is widely known in imbibition dynamics as the Lucas-Washburn (LW) law [11]. The derived law in this section is an idealised situation, where the surface is smooth and has a constant cross section, the gas phase has negligible viscosity, the contact angle is constant and equal to the equilibrium contact angle and no inertial effects are considered. In a real imbibition experiment, none of these simplifications are exact, which typically causes deviations and other exponents different to the predicted by the Lucas-Washburn law, $l \propto t^{1/2}$.

2.2 The Lattice-Boltzmann method

We will start describing the fundamentals of the LB method. We will introduce the kinetic approach that serves as a basis for LB simulations, in order to grasp why the LB method can accurately capture the Navier-Stokes equation. This approach is based in the Boltzmann equation, a kinetic equation derived in statistical physics that describes microscopically out-of-equilibrium processes. It is possible to derive analytically macroscopic properties of a fluid, like thermal conductivity and viscosity, from the microscopic description of the Boltzmann equation. This analysis is referred to as the Chapman-Enskog theory [102], and provides the basis for utilisation of a discretised version of the Boltzmann equation to simulate fluids accurately. We will present the discrete version of the Boltzmann equation for a lattice, the Lattice-Boltzmann equation, and we will comment on some general aspects of the implementation. To properly describe in detail the LB method would require an entire thesis dedicated to it. There are already many books and papers about the LB method, how to derive it analytically and how to implement it [57, 103, 104], so we will skip a detailed discussion on these technicalities. Instead, we will focus on a broad view of the concepts of the method and why it is advantageous.

The LB method has many advantages over other fluid simulation implementations. Computationally, it is a method that can be implemented at local level, which facilitates parallel implementation for high performance. From the physics point of view, it allows to implement solid boundaries in arbitrary geometries in a very straightforward manner. This solid boundaries can fulfil the no-slip boundary condition, or can be relaxed to allow for a slip length. More importantly for our purposes, this simulation methodology allows the coupling of the LB equation to a thermodynamic free-energy that contains additional physics of interest. For characterising lubricant-coated surfaces, the LB method will be coupled to a free energy that derives from a Ginzburg-Landau approximation. This free energy accurately captures the physics of surface tension. Furthermore, it can be extended for analytically setting the solid-liquid equilibrium contact angles as a boundary condition with a solid.

We will introduce the viscosity model used to impose a different viscosity in each phase, which is essential to capture Lucas-Washburn law. The criteria to compute the interfaces will also be commented and the methodology to extract the contact angle from locating the interface. Benchmarking tests will be shown prior to presenting the publications. We will also show some other previous simulations that paved the way towards the final spontaneous imbibition results in lubricant-coated surfaces. For example, the equilibrium properties of the drops and the comparison with the quantities analytically derived from the free energy framework.

The Boltzmann equation

As we have already mentioned, the core of the LB method lays in microscopic statistical analysis tools to describe macroscopic properties of matter. We will highlight here the fundamentals before describing the LB equation. The reader interested in the details is redirected to the reference [103]. The Boltzmann equation describes the evolution of the particle distribution function $f(\mathbf{x}, \boldsymbol{\xi}, t)$. This function represents at time t , the density of particles with velocity (ξ_x, ξ_y, ξ_z) at position \mathbf{x} . A remarkable property of this microscopic function is that it allows to recover the macroscopic physical quantities of a fluid composed by microscopic particles, such as the macroscopic local density

$$\rho(\mathbf{x}, t) = \int \int \int f(\mathbf{x}, \boldsymbol{\xi}, t) d\xi_x d\xi_y d\xi_z, \quad (2.14)$$

and the momentum density

$$\rho(\mathbf{x}, t) \mathbf{u}(\mathbf{x}, t) = \int \int \int \boldsymbol{\xi} f(\mathbf{x}, \boldsymbol{\xi}, t) d\xi_x d\xi_y d\xi_z. \quad (2.15)$$

Other physical quantities can be obtained from upper moments of the distribution function. The evolution of the distribution function depends on how particles collide, and how they exchange momentum. In dilute gases, one typically assumes that collisions happen on a one to one basis, and for monoatomic gases, that such collisions are elastic, so that translational energy is conserved. The collisions tend to even out angular distribution of particle velocity around the mean velocity value \mathbf{u} . Therefore, at large times the distribution function will equilibrate and reach the equilibrium distribution

function $f^{eq}(\mathbf{x}, \boldsymbol{\xi}, t)$. The Boltzmann equation describes how the distribution function is advected in the presence of a source term, $\Omega(f)$, that represents the collisions. Considering the total differential leads to

$$\frac{\partial f}{\partial t} + \xi_\beta \frac{\partial f}{\partial x_\beta} + \frac{F_\beta}{\rho} \frac{\partial f}{\partial \xi_\beta} = \Omega(f). \quad (2.16)$$

The first two terms describe the advection of the particles with velocity $\boldsymbol{\xi}$. The third term represents velocities being advected by the forces. The term on the rhs is a source term that accounts for the collision between particles. There are many different collision operators depending on the type and outcome of collision between particles. The collision operator must satisfy a set of conservation rules in order to reproduce physical constraints. We will not dig further into the details of obtaining and analysing collision operators.

In the LB method, the Bhatnagar, Gross and Krook (BGK) collision operator is typically used

$$\Omega(f) = -\frac{1}{\tau}(f - f^{eq}) \quad (2.17)$$

which simply relaxes the distribution function towards the equilibrium one at a relaxation time τ . The expression of this equilibrium distribution function f^{eq} can be analytically determined by means of some arguments, like isotropy and assuming a separated variable type of function [103]. It can be proved theoretically that this equilibrium distribution function is unique, and hence, is the only state to which particles can relax to in equilibrium. Here we have presented the BGK collision operator to highlight how the most simple version of the collision operator looks like. However, we will not use the BGK operator. Instead, we will use a multi-relaxation time (MRT) collision operator that enhance the stability of fluid phases with different viscosities in binary and ternary mixtures .

The Lattice-Boltzmann method

The basis for using the Boltzmann equation for fluid dynamics simulations lies in the fact that the same conservation laws as in fluid dynamics can be analytically found on a macroscopic scale. However, obtaining a numerical expression for the Boltzmann equation is not trivial and straightforward. The equation needs to be discretised in velocity space first, and then in space and time. The velocity discretisation is done through Hermitian series expansion, and in space and time through the method of characteristics. This discretisation introduces a set of weighted scalars that need to be computed in order to recover physical behaviours and conserved quantities. The discretisation of the velocities introduces a choice for the set of directions to which the distribution function can be advected. This discretisation is referred to as a velocity set, $\{\mathbf{c}_i\}$. Each velocity set has a name, depending on the number of dimensions and the number of velocities it has been computed to work for. These are typically referred to as DkQl, where k is the spatial dimension of the lattice, and l the number of discretised velocities in a set $\{\mathbf{c}_i\}$, which corresponds to the lattice connectivity. The possible sets one can construct via discretisation of the Boltzmann equation are D1Q3, D2Q7, D2Q9, D3Q15, D3Q19 and D3Q27. A larger number of discretised velocities in a set will result in a larger computational cost. The

D3Q19 is a good compromise between accuracy and computational performance for laminar flows, and it is the set we use in our simulations.

After discretisation of the Boltzmann equation, the Lattice-Boltzmann equation is

$$f_i(\mathbf{r} + \mathbf{c}_i \Delta t; t + \Delta t) = f_i(\mathbf{r}; t) + \sum_j L_{ij}(f_i(\mathbf{r}; t) - f_i^{eq}(\mathbf{r}; t)) \quad (2.18)$$

where Δt is the discrete time step, and L_{ij} is the collision operator that provides the way by which the distribution function evolves towards its equilibrium value. The Eq. 2.18 is solved at each position of a lattice, referred to as fluid nodes. At each time step, the collision operator is computed and the particle distribution is advected according to the discretisation of the velocity set. Our implementation of the LB method is based in the open source code "*Ludwig*" [57]. This implementation uses a multiple relaxation time algorithm (MRT) in moment space, to relax each moment towards its equilibrium distribution. Compared to the BGK algorithm, where all moments are relaxed using the same relaxation time, the MRT algorithm is more stable and accurate, although it is more complex to implement. However, this algorithm was already implemented in "*Ludwig*". Physical quantities can be obtained by computing moments of the distribution function, similar to Eqs. 2.14 and 2.15, but summing over the discretised velocity set

$$\rho(\mathbf{r}; t) = \sum_i f_i(\mathbf{r}; t), \quad \rho u_\alpha(\mathbf{r}; t) = \sum_i f_i(\mathbf{r}; t) c_{i\alpha}, \quad \Pi_{\alpha\beta}(\mathbf{r}; t) = \sum_i f_i(\mathbf{r}; t) c_{i\alpha} c_{i\beta} \quad (2.19)$$

where ρ corresponds to the local density, $\rho \mathbf{u}_\alpha$ to the local momentum, and $\Pi_{\alpha\beta}$ to the stress tensor. The non-slip boundary conditions are implemented by means of the bounce-back algorithm [103]. This algorithm identifies, locally at each fluid node, if there is a neighbouring solid node. If there is, it reflects every distribution in the direction where the solid node is. This results in the the no-slip boundary condition. The bounce-back algorithm allows to define solid nodes locally, to define solid channels with arbitrary shapes.

As already mentioned, the most important property of the LB method is that it can be proven using the Chapman-Enskog analysis that the NS equation is recovered in the macroscopic limit. A legitimate question to be asked is: Why should we use a method based in the Boltzmann equation to simulate the NS equation? There are several different reasons. The first one is that solving numerically the LB equation is much more easier than solving the NS equations. Interaction between nodes in the LB equation are linear, while the non-linearities are accounted for in the collision operator. Hence, it is a highly efficient parallelizable algorithm. The bounce-back algorithm allows for arbitrary geometries that can be defined just by choosing the solid nodes at which the velocities will be reflected. This, together with the fact that any free energy is relatively easy to couple with the LB equation makes it a very competitive and efficient algorithm for solving the NS equations with high accuracy and a variety of different physical problems where hydrodynamics need to be accounted for. There are some details that need to be considered when programming the LB methodology. Here we only wanted to sketch and revisit the basics of the method. For additional details, like force implementation, specific calculations

of velocity sets, rigorous demonstrations and implementation of the bounce-back algorithm, the reader is referred to [103].

2.3 Ternary free energy model

Here we will describe the free energy we have used to couple to the LB method and obtain accurate simulations of ternary mixtures for lubricant coated surfaces. Following a general Landau expansion for a binary free-energy functional, it is possible to generalise its form adding an additional phase to reproduce a ternary mixture [105]

$$F = \int_{\Omega} \left\{ \frac{\kappa_1}{2} C_1^2 (1 - C_1)^2 + \frac{\kappa_2}{2} C_2^2 (1 - C_2)^2 + \frac{\kappa_3}{2} C_3^2 (1 - C_3)^2 + \frac{\kappa'_1}{2} (\nabla C_1)^2 + \frac{\kappa'_2}{2} (\nabla C_2)^2 + \frac{\kappa'_3}{2} (\nabla C_3)^2 \right\} dV \quad (2.20)$$

where C_1, C_2 and C_3 are the concentrations of the three fluids, and the integral takes place over the volume Ω . In this free energy functional, we want to have three minima, each of which will correspond to a fluid phase. The terms with κ_1, κ_2 and κ_3 can describe the three required minima. However, to ensure that only these minima exist, a hard constraint has to be imposed $C_1 + C_2 + C_3 = 1$. The terms with κ'_1, κ'_2 and κ'_3 penalise the existence of a liquid-liquid interface, such that the free energy is minimised when the surface area between fluids is minimal. Hence, the gradient terms are responsible for the emergence of surface tension in the model. Further insight about the properties of this free-energy functional can be obtained if one of the fluids concentrations is set to 0, and we focus on the coexistence of two fluids, C_m and C_n . Since in this case $C_n + C_m = 1$, the chemical potential of specie m can be defined as as

$$\mu_m = \frac{\delta F}{\delta C_m} \quad (2.21)$$

Imposing thermodynamical equilibrium $\nabla \mu_m = 0$ and locating the interface between fluid n and m in $x=0$, we can obtain the interfacial profile along the x axis

$$C_m = \frac{1 + \tanh \frac{x}{2\alpha}}{2} \quad (2.22)$$

where α is a parameter that depends on the free-energy coefficients

$$\alpha = \sqrt{(\kappa'_m + \kappa'_n) / (\kappa_m + \kappa_n)} \quad (2.23)$$

Parameters κ and κ' can be arbitrarily tuned to achieve the desired surface tensions. The two coexisting minima at $C_m = 0$ and $C_m = 1$ however require that $\kappa_m > 0$ and $\kappa'_m + \kappa'_n > 0$. In order to reduce the degrees of freedom of the system, we follow [106] and define $\kappa' = \alpha^2 \kappa$. Using this constrain the surface tension now has the expression

$$\gamma_{mn} = \frac{\alpha}{6} (\kappa_m + \kappa_n) \quad (2.24)$$

Surface thermodynamics

Modelling lubricant-coated surfaces require an additional boundary for the components on the fluid that interact with solid nodes. Such additional boundaries have to account for the different affinities of the fluids to the walls and reproduce the physics of contact angles, characterised by the contact angles and the surface tensions. In other words we want this free energy model to reproduce the Young equation 2.5. The surface free energy contributions can be described by

$$\int_{\partial\Omega} [\Psi_1]_s + [\Psi_2]_s + [\Psi_3]_s \quad (2.25)$$

where $\partial\Omega$ is the solid boundary in which the fluid is embedded. The surface free-energy density for each component corresponds to

$$\Psi_m|_s = -h_m C_m|_s \quad (2.26)$$

where $C_m|_s$ is the value of the order parameter at the surface. Functional minimization for the component m at the solid boundary leads to

$$\alpha^2 \kappa_m \nabla_{\perp} C_m|_s = \left. \frac{d\Psi_m}{dC_m} \right|_s = -h_m \quad (2.27)$$

The contribution from the majority phase m, and the contributions from the minority phases n can be calculated separately using Noether's theorem to obtain an analytical expression of the interfacial tension γ_{sm} . To sum up, in the simulations the parameters h_1, h_2 and h_3 are an input in the simulation that are used as a Neumann boundary condition, and such condition allows to calculate analytically the surface tensions, which at the same time allows to obtain the contact angles θ_{12} , θ_{23} and θ_{31} .

Auxiliary variables

From the computational point of view it is much more easier to work with the following auxiliary variables

$$\rho = C_1 + C_2 + C_3, \quad \phi = C_1 - C_2, \quad \Psi = C_3 \quad (2.28)$$

Such variables allow us to work straightforward with the mass density ρ , since Navier-Stokes equation can be also written in terms of such mass density as usual. With this change of variables, the wetting boundary conditions take the form

$$\nabla_{\perp} \rho|_s = -\frac{h_1}{\alpha^2 \kappa_1} - \frac{h_2}{\alpha^2 \kappa_2} - \frac{h_3}{\alpha^2 \kappa_3} \quad (2.29)$$

$$\nabla_{\perp} \phi|_s = -\frac{h_1}{\alpha^2 \kappa_1} + \frac{h_2}{\alpha^2 \kappa_2} \quad (2.30)$$

$$\nabla_{\perp} \Psi|_s = -\frac{h_3}{\alpha^2 \kappa_3}. \quad (2.31)$$

2.3. Ternary free energy model

There is a redundancy in these parameters. A good requirement is that the gradient of the density has to be zero at the surface, $\nabla_{\perp}\rho|_s = 0$ such that

$$\frac{h_1}{\kappa_1} + \frac{h_2}{\kappa_2} + \frac{h_3}{\kappa_3} = 0. \quad (2.32)$$

Following this constraint h_1, h_2 and h_3 can be uniquely determined for a prescribed set of contact angles.

The simulations use the auxiliary variables ρ , ϕ and ψ . However, for determining the position of the interface between the different fluids its more intuitive to work with the original concentrations C_i . The auxiliary variables can be related to the concentrations inverting the relations in Eq 2.28 and follows

$$C_1 = \frac{\rho + \phi - \psi}{2}, C_2 = \frac{\rho - \phi - \psi}{2}, C_3 = \psi \quad (2.33)$$

Determining the contact angles

Following [107], to obtain the angle between the three fluids in absence of a solid boundary, from mechanical equilibrium in the triple contact line between the fluids, we can write the two following equations

$$\gamma_{12} + \gamma_{23} \cos \theta_2 + \gamma_{31} \cos(\theta_2 + \theta_3) = 0 \quad (2.34)$$

$$\gamma_{31} + \gamma_{23} \cos \theta_3 + \gamma_{12} \cos(\theta_2 + \theta_3) = 0 \quad (2.35)$$

whose solution leads to the cosine rule

$$\cos \theta_2 = \frac{\gamma_{13}^2 - \gamma_{23}^2 - \gamma_{12}^2}{2\gamma_{23}\gamma_{12}} \quad (2.36)$$

which can also be applied also to obtain angles θ_1 and θ_2 .

The contact angle relations θ_{mn} with the solid surface depending on h_n , h_m and κ_m and κ_n can be derived analytically [106] to give

$$\cos \theta_{mn} = \frac{(\alpha\kappa_n + 4h_n)^{3/2} - (\alpha\kappa_n - 4h_n)^{3/2}}{2(\kappa_m + \kappa_n)(\alpha\kappa_n)^{1/2}} - \frac{(\alpha\kappa_m + 4h_m)^{3/2} - (\alpha\kappa_m - 4h_m)^{3/2}}{2(\kappa_m + \kappa_n)(\alpha\kappa_m)^{1/2}} \quad (2.37)$$

The three contact angles from this calculations are not actually independent, since

$$\gamma_{12} \cos \theta_{12} = \gamma_{2s} - \gamma_{1s} \quad (2.38)$$

$$\gamma_{23} \cos \theta_{23} = \gamma_{3s} - \gamma_{2s} \quad (2.39)$$

$$\gamma_{31} \cos \theta_{31} = \gamma_{1s} - \gamma_{3s} \quad (2.40)$$

Summing the three equations the Grifalco-Good relation is obtained

$$\gamma_{12} \cos \theta_{12} + \gamma_{23} \cos \theta_{23} + \gamma_{31} \cos \theta_{31} = 0 \quad (2.41)$$

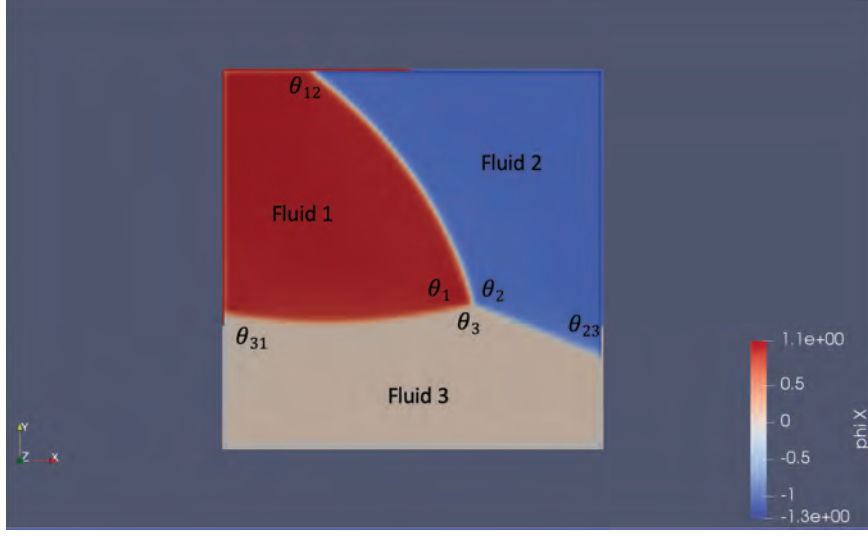


Figure 2.4: Results showing all six existing contact angles in the ternary free energy model, all of which can be tuned by means of κ_1, κ_2 and κ_3 parameters, along with h_1 and h_2 wetting parameters.

LB method coupled to the Cahn-Hilliard equations

To couple the ternary free energy with the Lattice-Boltzmann method, two additional ingredients are required. First, the order parameters ϕ and ψ have to be evolved in time, according to the diffusion of each phase, and the advection by the fluid velocity. This temporal evolution is introduced by means of the Cahn-Hilliard equation for each order parameter

$$\frac{\partial \phi}{\partial t} + \partial_\beta (\phi v_\beta) = M_\phi \nabla^2 \mu_\phi \quad (2.42)$$

$$\frac{\partial \psi}{\partial t} + \partial_\beta (\psi v_\beta) = M_\psi \nabla^2 \mu_\psi \quad (2.43)$$

where M_ϕ and M_ψ are the mobility parameters for the ϕ and ψ order parameters, respectively. The Cahn-Hilliard equations allow to locally couple the order parameters to the velocity fields at each node. However, we still need to couple the order parameters with the fluid flow, since existence of an interface will also modify the velocity field. In our implementation of the ternary free energy we use a forcing approach. A force at each node resulting from the chemical gradient derived from the ternary free energy is introduced. We employ the standard forcing algorithm by Guo [108] to introduce the force in the LB algorithm. There are two different equivalent ways to introduce the external forcing, since the ternary free energy satisfies

$$\partial_\beta \sigma_{\alpha\beta} = \partial_\alpha p + \rho \partial_\alpha \mu_\rho + \phi \partial_\alpha \mu_\phi + \psi \partial_\alpha \mu_\psi. \quad (2.44)$$

where $\sigma_{\alpha\beta}$ is the pressure tensor. The right side of the equation computes the force as the divergence of the stress tensor, while the left side computes the force through the gradients of the chemical potential [106]. In simulations,

these two methodologies are not entirely equivalent since the choice between divergence or the gradient will result in different discretisation errors. Here we will stick to the gradient of the chemical potential for each phase, $F_\beta^\phi = \mu \partial_\beta \phi$ and $F_\beta^\psi = \mu \partial_\beta \psi$, where $\beta = x, y, z$.

In our implementation, the Laplacian in the Cahn-Hilliard model is discretised by means of a 27 point stencil in 3 dimensions and gradients are approximated in each direction by a central difference scheme.

Viscosity model

In this subsection we discuss how to introduce tunable viscosities for each fluid phase. Two different viscosity models are compared and discussed to apply to the LB algorithm coupled to the ternary free energy. The viscosity models in this work pursue to produce a viscosity contrast between the three immiscible fluid phases, as would happen generally in a experimental system. The most straightforward way to achieve this viscosity contrast is to assume the viscosity to be a function of the bulk phases $\eta(c_1, c_2, c_3)$, where the concentrations C_i are taken locally. The models should fulfil the condition $\eta(c_1, 0, 0) = \eta_1, \eta(0, c_2, 0) = \eta_2$ and $\eta(0, 0, c_3) = \eta_3$. As the order parameter already has a dependence when changing from one fluid to another that approximately follows an hyperbolic tangential function, a legitimate election could be a linear function

$$\eta(c_1, c_2, c_3) = c_1 \eta_1 + c_2 \eta_2 + c_3 \eta_3 \quad (2.45)$$

Another feasible equation to model the viscosity contrast consists in assuming an exponential, factorised expression

$$\eta(c_1, c_2, c_3) = \eta_1^{c_1} \cdot \eta_2^{c_2} \cdot \eta_3^{c_3} \quad (2.46)$$

referred to as the Arrhenius viscosity model. To test the different viscosity models we solve the equation of motion for a mixture of three fluids. The system is considered to be infinite in the x direction, and have a certain width, b, in the y direction. The fluid phases are placed such that initially $c_1 = 1$ for $y < b/3$, $c_2 = 1$ for $b/3 < y < 2b/3$ and $c_3 = 1$ for $y > 2b/3$. As the flow is considered to be laminar and inertial effects not important, we will consider the creeping flow equations 2.47, in which we approximate that the problem only depends on the y direction $u_x(y)$

$$\eta_i \frac{\partial^2 u_x}{\partial y^2} + f_x = 0 \quad (2.47)$$

where $i=1,2,3$ depending on which phase of the fluid we solve the equation. In general, the velocity field in this geometry can be obtained from Eq 2.47 and is a parabola

$$u_i = -\frac{f_x c_x^2}{2\eta_i} + c_{i,1}x + c_{i,2} \quad (2.48)$$

To solve the equations in the mentioned geometry, the six coefficients in the previous equation have to be determined and hence six boundary conditions are required. These conditions are the non-slip boundary condition at the solid walls positioned at the bottom y_b and top y_t of the system, hence $u_1(y_b) = u_3(y_t) = 0$.

Furthermore, the velocity field must be continuous in the interface between liquids, thus, interface between first and second phase located at y_{12} and second and third phase, at y_{23} . Hence, $u_1(y_{12}) = u_2(y_{12}), u_2(y_{23}) = u_3(y_{23})$. Finally, the tangential stresses in the interface between the two fluids must also be the same $\eta_1 \partial u_1 / \partial y = \eta_2 \partial u_2 / \partial y$ in y_{12} and $\eta_2 \partial u_2 / \partial y = \eta_3 \partial u_3 / \partial y$ in y_{23} . The resulting system is tedious but linear and can be exactly solved using linear algebra algorithms. The simulation results, comparing with the analytical results for two different sets of viscosities are shown in Fig 2.5. The results show

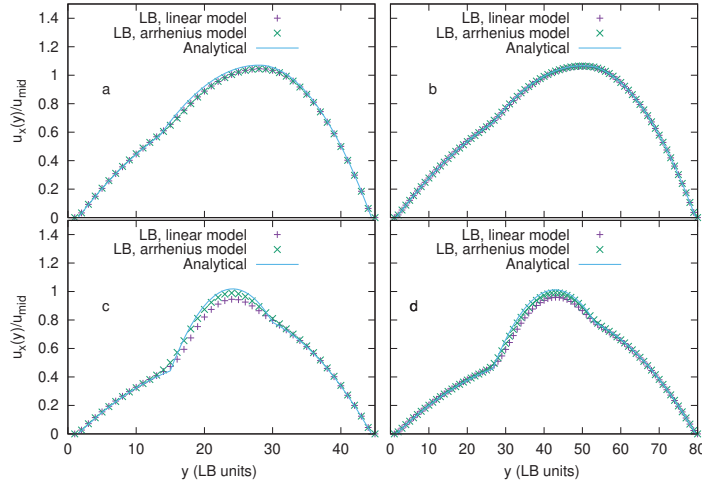


Figure 2.5: Comparison between analytical result and simulations for different contrast of viscosities and widths of the system. Figures a and b use a set of viscosities $\eta_1 = 1$, $\eta_2 = 0.5$ and $\eta_3 = 0.3$ for a channel width of 45 and 80 LB units respectively. Figures c and d use a set of viscosities $\eta_1 = 2$, $\eta_2 = 0.3$ and $\eta_3 = 1$ for a channel width of 45 and 80 LB units respectively.

quantitative agreement between the simulation and the analytical result. It is seen that when the viscosities are comparable both linear and Arrhenius viscosity models are equivalent as the jump of viscosity in the interface is small. Widening the length of the system improves relevantly the quantitative agreement. However, as the viscosity contrast increases, the Arrhenius model seems to produce a better agreement, both for $b=45$ and $b=80$. The velocity profile for figure 2.5c is shown in 2.6. We observe that in the Arrhenius model, from η_1 to η_2 , and from η_3 to η_2 the viscosity changes faster towards the η_2 value. Hence, the Arrhenius model basically reduces the distance from two bulk faces where the viscosity have an intermediate value, following more accurately the conditions imposed in the analytical solution.

Defining the interface

At some point in the interface following Eq 2.22 the concentrations between C_1 and C_3 coincide such that $C_1 = C_3 = 0.5$ and that point where both concentrations are the same can be defined as the interface position. In Fig. 2.7

2.3. Ternary free energy model

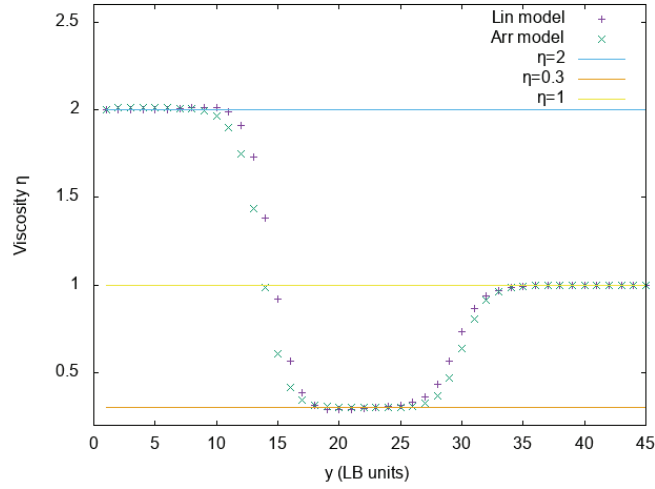


Figure 2.6: Viscosity profile as a function of the concentration of phases

we show the concentration profiles along the direction x , where there is a change from a majoritary phase of concentration c_1 to a majoritary phase of concentration c_3 . However, there is the interface of fluid c_2 nearby, since we observe that this concentration is not zero, and remains constant. The question is how to find an algorithm that correctly identifies in each direction each interface. As imposed in the model, the total sum of the three components is 1

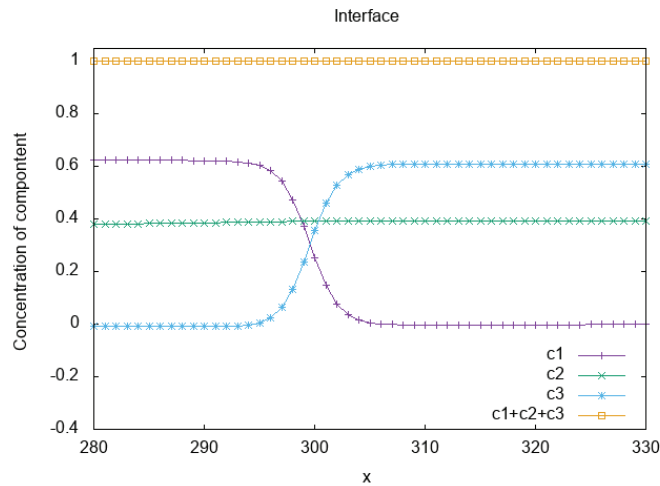


Figure 2.7: Concentration of each phase in x direction from Fig ??, near the lubricant contact line

and does not vary. The concentration profile for the lubricant, C_2 , is constant along the x axis, and also the sum of the components C_1 and C_3 . Moreover, it can be seen that in this case C_1 and C_3 have the same concentration for a

certain x coordinate x in which the concentration equals $C^* = (C_1 + C_3) \cdot 0.5$. Hence, we will define the interface of fluid 1-3 as the exact x position where the concentration profiles for both C_1 and C_3 equals C^* . We can extend this for a certain node, in all directions of the node, to find the interface in every possible direction. This same criteria can also be used to determine the position of the interface between fluid 2 and fluid 1, and 2 and 3, hence the lubricant contact lines.

Measuring the contact angle

Once the interface profile is obtained, a systematic measurement method for obtaining the contact angle between fluids is required to characterise the properties of the moving interface. In geometries such as liquid lenses with three phases, fitting spheres using a least-squared algorithm for each fluid interphase yields to accurate results. Each interface is fitted to a circle and then the intersection between interfaces is analytically calculated. From this intersection point the implicit derivative of a circle is used to calculate the contact angle.

Benchmarking tests

Using the described methodology, we obtain Fig. 2.4, as reproduced originally in Ref. [106]. In the figure, we show the order parameter ϕ , which is correspond to C_1 phase when $\phi = 1$, C_2 phase when $\phi = -1$, and C_3 phase when $\phi = 0$ following Eqs. 2.33. We observe six different angles: θ_1, θ_2 and θ_3 are the contact angles between the fluids, which are independent of the wetting potential, h , and are determined by the surface tensions, using Eq 2.36 for each contact angle (only two are independent). The other three contact angles, θ_{12}, θ_{23} and θ_{31} account for the affinity of the fluids to the solid boundary and are determined by the surface tensions and the h wetting boundary via Eq 2.37. In Fig. 2.8 we show the benchmarking tests, comparing the theoretical and measured contact angles, both for fluid-fluid (left) and fluid-solid (right) interfaces. The high accuracy on the predictions validate the ternary free energy model as an accurate model to simulate three fluids with tunable contact angles.

2.4 Imbibition in lubricant coated surfaces

In this section we finally introduce the results from Pub. 4.6. During the first sections of this chapter we have introduced a series of concepts to highlight that surface tension related phenomena is still an active research area. Deeper understanding of the properties of solid surfaces leads to industrial innovations, which results in constant critical revisions of the theory to design new ways of dealing with drops in solid surfaces and transport of fluids. After the last sections, the reader should be aware that the simulation of capillary surface tension phenomena is not straightforward, and requires of a solid machinery to tackle the coupling between hydrodynamic equations and interfacial stress. In our case, we have chosen the Lattice-Boltzmann method and a thermodynamic free energy which allows to tune contact angles. Our goal when working with this computational approach has been to develop a technique by which we could simulate spontaneous invasion of fronts by capillarity effects in lubricant coated surfaces. A reason to use this approach lies in the fact that in a binary mixture,

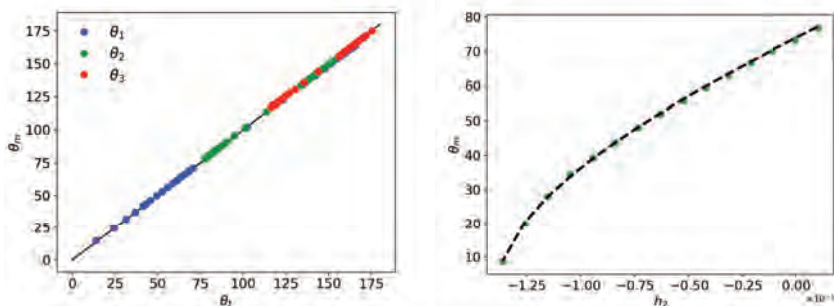


Figure 2.8: Benchmark tests for contact angles. The figure on the left compares the theoretical angles (θ_t) with the measured contact angles in the interface (θ_m) in a liquid lense geometry when systematically varying the surface tensions. The figure on the right compares measure the solid-liquid contact angle for a fixed value of h_1 , when systematically varying the h_2 wetting potential. Both graphs together show the high accuracy of the ternary free energy model.

the long-stage Lucas-Washburn law has been shown to be reproduced very easily [109]. The most interesting possible outcome of spontaneous imbibition in lubricant-coated surfaces would be a change in the exponent $h \sim t^{1/2}$. Hence, our first step was to reproduce the Lucas-Washburn law from Eq. 2.13, initialising to 0 the lubricant concentration phase $C_l = 0$.

To explore the outcome of the spontaneous imbibition, we set a geometry consisting in two reservoirs, one of invading liquid on the left, and one of displaced fluid on the right. Each reservoir has a length L_r larger than the solid channel length L , $L_r = 2L$. The two reservoirs are connected by the channel, of length L , and the interface between the fluids is placed at $l(0) = 0.05L$. We have to take into account that it takes some time for the interface to relax towards a curved shape by capillarity effects. Indeed, initially the interface is a straight line with contact angle $\theta = 90^\circ$. The gradients of the chemical potential induce flows which deform the interface in accordance to the combination of surface tensions, curving the interface, which at the same time induce a pressure drop. During this time, where the interface is being deformed by capillary forces, the front initially moves a distance $l \sim H/2$ before starting to move following the Lucas-Washburn. This distance has to be subtracted from the simulation results to compare with the Lucas-Washburn law. In Fig. 2.9 we show the comparison between a simulation and the Eq. 2.13, demonstrating that the ternary model captures very accurately the spontaneous imbibition of a viscous front.

For spontaneous imbibition simulations in lubricant coated surfaces, we use the same geometry as the described for reproducing the Lucas-Washburn law. But this time we introduce a third phase, the lubricant, which covers the solid surface. Simulations show that indeed, if the invading fluid has hydrophylic properties with respect the solid lubricant and the solid channel, it will spontaneously invade the channel. Some important considerations need to be accounted for succesful simulations of lubricant-coated surfaces. As in the LW law, the pressure drop in the interface between invading and displaced phase sets a velocity field that forces the hydrophylic liquid to invade the channel.

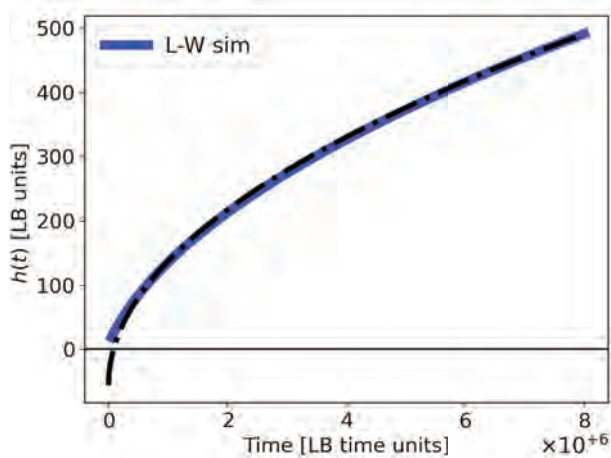


Figure 2.9: Simulation of a capillary spontaneous imbibition process using a ternary free energy, in the limit where one of the concentrations is set to 0 (no lubricant). The parameters correspond to a measured dynamic contact angle $\theta_d = 73.5$, invading fluid viscosity $\eta_1 = 1$, displaced fluid viscosity $\eta_2 = 0.01$, $\gamma_{12} = 1.033 \cdot 10^{-3}$ and channel width $H=42$. The simulations accurately follow the Lucas-Washburn law.

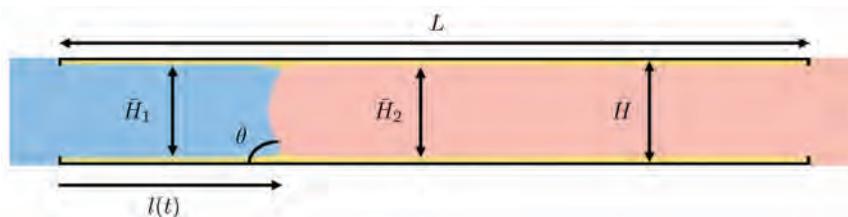


Figure 2.10: Simulation snapshot showing all the parameters to be considered in SLIPS simulations. The blue color is the phase associated to the invading fluid, red to the displaced fluid and yellow to the lubricant. \bar{H}_1 and \bar{H}_2 refer to the widths of phase blue and red phase, respectively. H refers to the width of the channel. L is the length of the solid channel. $l(t)$ the instantaneous position of the front. θ is the dynamic contact angle.

However, in this case the velocity field drags the lubricant. The dragging of lubricant can eventually lead to the breaking of the lubricant layer, and consequent drop formation of the lubricant, stopping the spontaneous imbibition. Two important conditions can be imposed to avoid this failure of the lubricant layer. First, the spreading parameter S has to be positive for both the invading fluid and lubricant, $S_{1l} > 0$ and lubricant and displaced fluid $S_{2l} > 0$, so that the equilibrium contact angle with the lubricant is $\theta_e = 0$, and it preferentially wets the whole solid surface. This is not only a simulation requirement, but also a requirement of SLIPS and LIS in experiments. The second condition consists in placing pillars at the start and end of the solid channel, as can be observed in Fig. 2.10. The corners prevent the lubricant to get out of the channel, but more

important, they impose an average lubricant viscosity $u_l = 0$. This condition is also important for SLIPS and LIS, since experiments show that flows on lubricant coated surfaces do not erode the lubricant width. The strong wetting properties of the lubricant keeps the lubricant width constant even after many experimental realisations. Thus, by placing the pillars and avoiding lubricant loss we are closer to experimental realisations of SLIPS and LIS surfaces.

We comment also on the measurement of the contact angle. Fig. 2.10 shows a snapshot of the simulation, where all the characteristic parameters of the model are defined. The width of the invading fluid and displaced phase are \bar{H}_1 and \bar{H}_2 , respectively, while the channel width is H . The lubricant width at each phase away from the interface is $h_1 = H - \bar{H}_1$ and $h_2 = H - \bar{H}_2$ for the invading and displaced phase, respectively. The lubricant width is initially uniform. However, the fluid-fluid surface tensions lead to the appearance of a small ridge in the triple fluid contact line. The combination of this ridge with the motion of the front leads h_1 and h_2 to not be uniform, specially close to the triple contact line. However, from the interface, these two lubricant widths are very similar. Comparing the theoretical model we derive in Pub. 4.6 with the simulations we observe that the asymmetries near the ridge do not affect significantly the quantitative comparison.

Finally, we comment on the the driving force in the capillary imbibition. This driving force, as in the Lucas-Washburn law, is caused by the pressure drop due to the curvature of the interface. To calculate this pressure drop, we use

$$\Delta p = \frac{2\gamma_{12} \cos \theta_s}{H} \quad (2.49)$$

where θ_s is extracted from fitting the interface to a circle, and interpolating the circle shape to the solid, calculating the contact angle at the intersection between the fitted circle and the solid surface. By measuring the contact angle in this way, we can use the channel width H , instead of the width of the displacing fluid H_1 . Note that the pressure drop depends on the curvature of the interface, which do not depend on where the contact angle is computed. The same pressure drop would be obtained if \bar{H}_1 and θ_t were to be used in Eq. 2.49, where θ_t is the contact angle computed at the triple contact line.

Our results, presented in Pub. 4.6 show that indeed, the lubricant coated surface qualitatively changes the dynamics of imbibition. In the limit of large lubricant viscosities, we recover the LW result, where $h \sim t^{1/2}$. In the limit of small lubricant viscosity, we observe a new dynamic regime where $h \sim t^1$, suggesting a qualitatively different dissipation mechanism. We demonstrate with a simple theoretical model, based in the same derivation of the LW equation sketched in this thesis, that this qualitative change can be explained by the change of the velocity flow profile in the bulk of the fluid phases. In the LW, the flow profile follows a Poiseuille flow, while in the linear regime, the flow profile approximates a plug flow, where all the dissipation takes place in the lubricant layer. We use the theoretical model to predict that in the presence of an external forcing, the invasion of the front will take place exponentially in time, and validate this results with the simulations, obtaining good agreement. Our results sets a framework to characterise experimental spontaneous imbibition of lubricant coated surfaces.

2.5 Dynamic contact angles in lubricant coated surfaces

The work described in the previous chapter was focused on the dynamical properties of a front invading a lubricant coated channel spontaneously due to capillary forces. Since we were mainly interested in the overall invasion dynamics and the possible scenarios for the imbibition exponent, our model considered only the minimal ingredients to reproduce qualitatively and quantitatively the imbibition curves. Some important questions were left for follow-up studies. For example, the contact angle dynamics of the front can play a significant role in the dynamics of the front. It has been mentioned that when the front invades the channel, the measured contact angle does not exactly coincide with the equilibrium contact angle. In fact, it is larger. This is not surprising: If the dynamic contact angle was the equilibrium one, the front would not move. In this case, the forces at the contact line would be balanced and no invasion could take place. To improve the accuracy of prediction of the model, a full description should delve into how the dynamic contact angle depends on the equilibrium contact angle and the contact line speed when invading the channel.

When the lubricant is absent, a rigorous mathematical model exists which explains how the contact angle depends on the capillary number, the surface tension, and the equilibrium contact angle. The Cox-Voinov theory [58] describes how dissipation in the liquid-liquid interface relates to the deformation of the contact line in the presence of a solid wall, as a function of the capillary number. The main goal of this section was to determine if the Cox-Voinov model could capture the deformation of the liquid-liquid interface, when moving atop of a lubricant. More specifically, we were interested in systematically measuring the dynamic contact angle from the simulations, for a range of Ca , and for a set of different viscosities, and compare the obtained curves of $\theta_d(Ca)$ with the Cox-Voinov model. Capturing how the liquid-liquid interface deforms with the Ca allows to quantify the dissipation associated to that dynamic contact angle, which can later be included in the equation of imbibition dynamics. However, the influence of this dissipation on the dynamics of imbibition is still to be analysed. Here we will only focus on determining the dynamic contact angle when the contact line moves on top of a lubricant.

In this section, we briefly summarise the Cox-Voinov theory, what does it predict, and the obtained curves of $\theta_d(Ca)$. Then we will present the simulations results comparing the Cox-Voinov equations with the deformation of the interface in lubricant-coated channels. Simulations show that the Cox-Voinov theory captures accurately the interface deformation. Finally, we will derive a semi-analytical model that allows to predict the deformation of the interface as a function of the lubricant viscosity.

The Cox-Voinov theory: Moving contact line on top of a solid

The dynamics of the contact line is a classical hydrodynamic problem, that involves the breakdown of the no-slip boundary condition in solid channels. Solving the creeping flow equations with the no slip boundary condition produce stresses and viscous dissipation that diverges at the contact line [110]. In other words, if the no slip boundary condition holds then there can be no contact line motion. Yet such motion takes place physically. Such problem is intrinsic to any sharp interface mathematical model. Experimentally, the problem was studied

2.5. Dynamic contact angles in lubricant coated surfaces

by Hoffman *et al* [111], and they determined that the dynamic contact angle was correlated to the Ca number plus a shift factor. Moreover, this shift factor was determined solely by the static contact angle, θ_0 . Mathematically, some intuitive arguments were given to reproduce the behaviour observed by Hoffman in the particular case of complete wetting $\theta_{eq} \simeq 0$ and negligible displaced fluid viscosity [10]. The problem was studied for an arbitrary viscosity contrast and static angle by Cox [58], who used matching asymptotic expansions to solve for each region of the interface. The derived equations are referred to as the Cox-Voinov equations, as the results were also shown independently by Voinov [59].

More recently, some other works focused on a computational characterisation comparing the results obtained by Cox, solving the Navier-Stokes equation numerically, and obtaining good agreements [112]. Such studies have provided a further understanding of the break-down of the no slip boundary condition. Other computational approaches, as the Lattice-Boltzmann method [113], have become increasingly popular to study this problem as they provide accurate description of the hydrodynamic behaviour combined with a natural solution to the divergence problem at the contact line. The free energy employed earlier in this chapter is a diffusive-interface model, that does not require of an explicit slip length, since the order parameters can diffuse along the interface, giving rise to an effective slip at the contact line.

In the context of the LB simulations, it has been stated that the Cox-Voinov equations are fulfilled with these diffusive models [114]. Also the mechanisms for the motion of the contact line in such cases have been studied and the slipping mechanism falls into the general-class of Navier slip models [115].

The main mathematical expressions obtained by Cox [58] can be written as

$$g(\theta) = g(\theta_0) + \text{Ca} \ln(L_y/l_s) \quad (2.50)$$

where L_y is a characteristic macroscopic length, l_s is a microscopic length, Ca is the capillary number that depends on the viscosity η and the surface tension γ

$$g(\theta) = \int_0^\theta d\phi [f(\phi)]^{-1} \quad (2.51)$$

where

$$f(\phi) = \frac{2 \sin \phi [q^2(\phi^2 - \sin^2 \phi) + 2q[\phi(\pi - \phi) + \sin^2 \phi] + (\pi - \phi)^2 - \sin^2 \phi]}{q(\phi^2 - \sin^2 \phi)[(\pi - \phi) + \sin \phi \cos \phi] + (\phi - \sin \phi \cos \phi)[(\pi - \phi)^2 - \sin^2 \phi]} \quad (2.52)$$

where $q = \eta_2/\eta_1$ is the contrast viscosity, and η_2, η_1 the viscosities of the displaced and displacing fluid, respectively.

Figure 2.11 on the following page shows the integral function in Equation 2.51 plotted for three different values of the contrast viscosity, q, matching the results in [58]. Note that from this figure, given any static angle θ_0 we can estimate graphically the dynamic angle using Equation 2.50 by adding the term $\text{Ca} \ln(L_y/l_s)$ in the x-axis and seeking where the curve $g(\theta)$ falls for the given added term. It is possible to obtain an approximated analytical expression. Expanding the function $f(q, \phi)^{-1}$ in power series for small angles, hence $\theta \simeq 0$ it can be seen that the first non zero term is second order $f(\phi)^{-1} \simeq \theta^2/3 + O[x]^3$. Hence, Equation 2.50 in this case can be expressed as

$$\theta^3 = \theta_0^3 + 9\text{Ca} \ln(\delta^{-1}), \quad (2.53)$$

2.5. Dynamic contact angles in lubricant coated surfaces

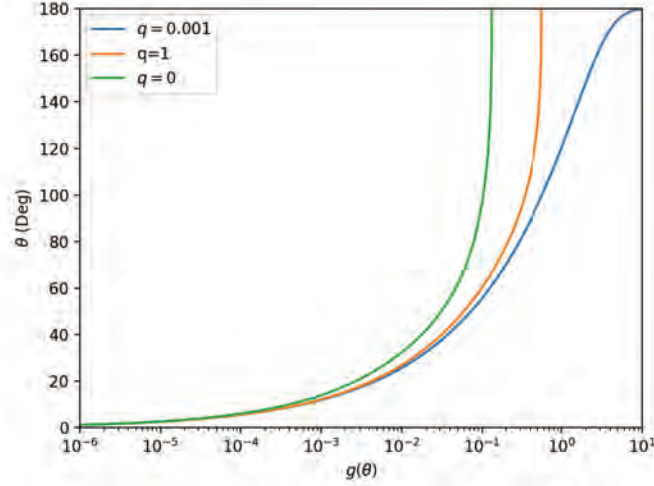


Figure 2.11: Representation of function $g(\theta)$ in Equation Equation (2.51) on the preceding page using numerical integration.

where $\delta^{-1} = L/l_s$ is the ratio between the characteristic macroscopic length of the system and l_s a microscopic length. Note that for this expression to hold, not only θ has to be small, but also θ_0 to provide an accurate value of the integral expression 2.51. The latter equations corresponds to a simplification of the Cox-Voinov model widely used in experiments. Furthermore, Eq.2.53 is very similar to the equation derived considering that the dissipation in the wedge of a liquid is employed in deforming the interface, in the limit $\theta_0 \simeq 0$ [10]. To validate the range of application of this approximation we have obtained numerically the angle θ using Eq. 2.50 and compared to Eq. 2.53, benchmarking the numerical expression.

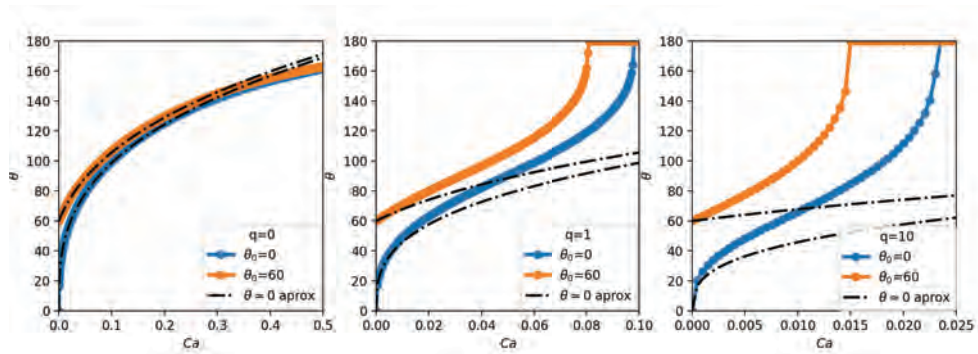


Figure 2.12: Dynamical angle as a function of Ca for the exact expression and analytical approximation for three viscosity contrasts.

The results in Figure 2.12 show that expression 2.53 only holds for a large range of Ca if the viscosity contrast q is approximately 0. Increasing the static

2.5. Dynamic contact angles in lubricant coated surfaces

angle still produces an accurate description of Equation 2.50. However, for increasing q and increasing static angle Equation 2.53 breaks down and doesn't produce an accurate description of the dynamic angle.

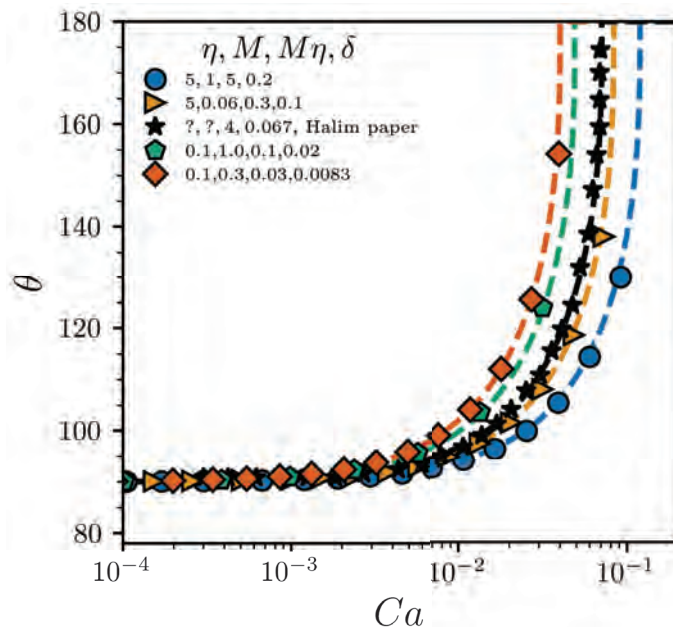


Figure 2.13: Dynamical angle as a function of Ca for LB simulations with different parameters. The dotted lines correspond to simulations extracted from the paper by Kusumaatmaja et al *Journal of Fluid Mechanics*, 2016, **788**, 209-227

We now show the results of the dynamic contact angle, as a function of the Ca obtained with our LB in the solid case. We use the ternary free energy but restrict the initial state to only two liquids, without a lubricant, effectively reducing the equations to the binary mixture model. We compare our results to those obtained for the binary mixture model [116], benchmarking our simulation methodology in this problem. It has been shown that the moving of the contact line in the binary mixture model is controlled by a slip length l_s that arises from the diffusive model. This slip length can be defined in many ways. A possible definition is to use the term $\mathbf{v}\nabla\phi = M\nabla^2u$ to estimate this slip length, where M is the mobility of the order parameter [116]. Specifically, the slip length can be defined to be the distance from the wall to the local maxima of the previously defined quantity. The slip length mainly is controlled by the viscosities, the mobilities and the interfacial width of the fluids. The scaling of the slip length is observed to behave differently depending on the value of this three parameters. Two regimes can be encountered: First, the diffusive regime when $M\eta/l^2 \ll 1$. In this case it is observed that the slip length scales with the interfacial width l and the diffusive length scale $l_d = (M\eta)^{1/2}$. The slip length follows $l_s \sim (l_d l)^{1/2}$. Second, the sharp interface regime can be found when $M\eta/l^2 \gg 1$ and they find $l_s \sim M\eta/l^2$. In all regimes the general Cox-Voinov relation Eq.2.50 is satisfied. A smaller slip length translates in

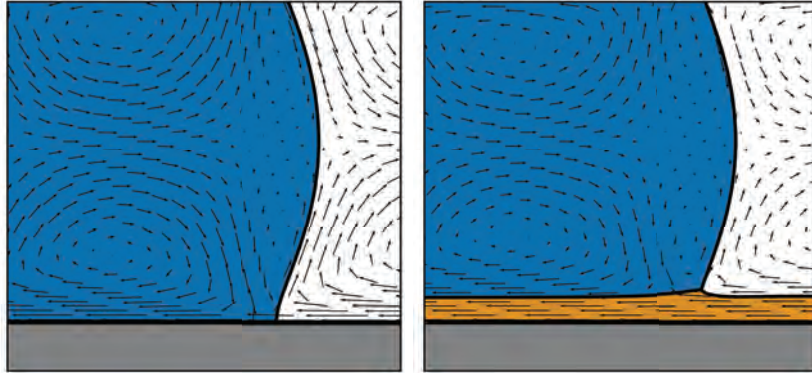


Figure 2.14: Left: Velocity field of a moving drop on top of a solid Right: Velocity field of a moving drop on top of a lubricant

a larger dissipation according to the Cox-Voinov model, leading to a larger angle deformation at smaller Ca . In Fig. 2.13 we compare one of the simulation results from Kusumaatmaja *et al* [116] with simulations we obtained with our LB methodology and observe the same trends when varying the mobility and the viscosity.

In the results we will present now we will show parameters in the sharp interface limit, which is the most similar to experimental conditions. We will show how the lubricant viscosity affects the deformation of the contact angle with the Ca and provide a framework for experiments to predict the microscopic lengthscale as a function of the lubricant viscosity.

Moving contact line in lubricant-coated surfaces

We first start by comparing the fluid profiles inside the drop when there is a drop moving on top of a solid, and a drop moving on top of a lubricant Fig. 2.14. We observe that both velocity profiles follow the same trends, already shown by Briant *et al* [113]. Hence, we expect that the deformation of the contact angle will not deviate much from the Cox-Voinov results, when the contact angle is measured at the top of the ridge, respect the horizontal solid channel. In Fig. 2.14b) we note the existence of a ridge in the contact line between the lubricant (yellow), the blue fluid (drop), and the white fluid (gas). This ridge is a consequence of the Neumann angles of the liquids, controlled by the surface tensions of the fluids. It is characterised by the angle of the lubricant θ_l at the triple contact line. In Fig. 2.15 we show the morphological difference between a small ridge and a large ridge. In Fig. 2.15a), the small ridge translates into an almost constant width of the lubricant layer. Instead, in Fig. 2.15b) we observe that the large ridge results in an accumulation of fluid near the contact line, and a thin layer of lubricant near the bulk of the drops.

An interesting question we will explore here is whether the ridge affects qualitatively the apparent dynamic contact angle. For this reason we will characterise the measured contact angle θ as a function of the Ca , for three different ridges: A large ridge $\theta_l = 80$, a medium ridge $\theta_l = 134$ and a small

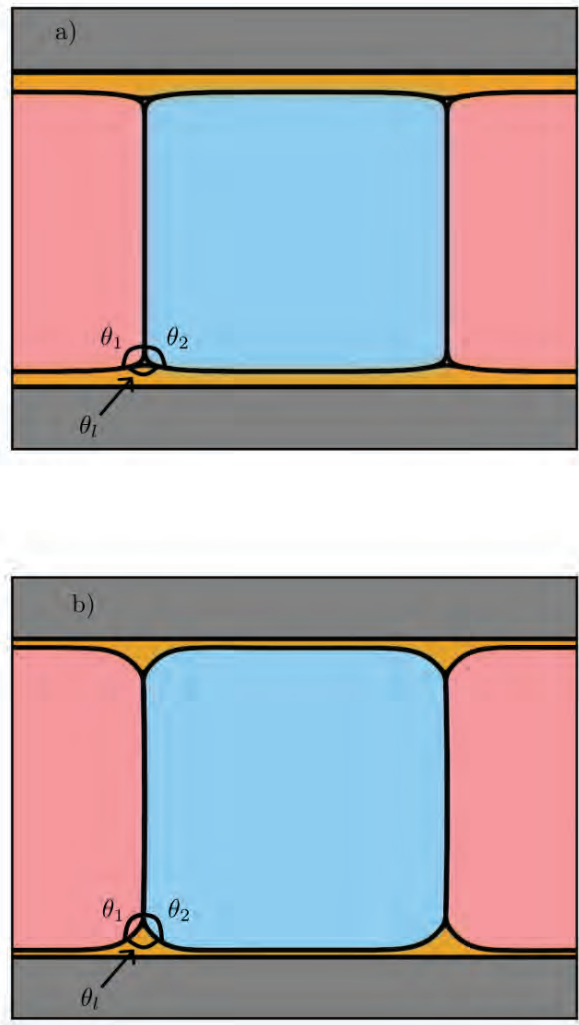


Figure 2.15: Simulations showing a drop in equilibrium on a lubricant-coated surface. Both simulations were performed with a uniform lubricant layer, with the same thickness. We show the equilibrium profiles of the drops for (a) a small ridge $\theta_l = 163^\circ$ (b) a large ridge $\theta_l = 80^\circ$

ridge $\theta_l = 160^\circ$. The final motivation was to compare the outcome with the Cox-Voinov theory, and test if it holds in lubricant-coated surfaces.

We first show the results of the LB simulations. We systematically vary the lubricant viscosity for different sizes of the ridge, and compare it to the case where the drop contacts directly the solid surface. We define the ratio of viscosities $\lambda = \eta_s/\eta_l$, which will be the main parameter to vary. Our first results consist on fitting the Cox-Voinov equations to the lubricant-coated simulation results. More specifically, we fit the parameter $\delta^{-1} = L_y/l_s$ in Eq. 2.50 to the measured contact angles as a function of Ca. In Fig. 2.16 we summarise the

2.5. Dynamic contact angles in lubricant coated surfaces

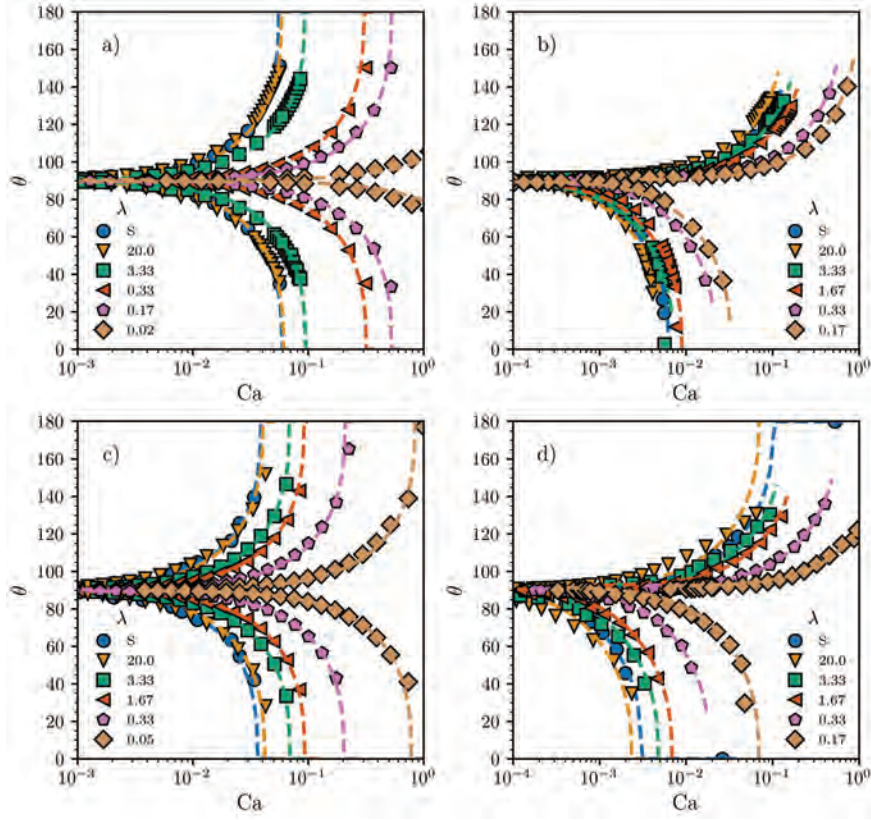


Figure 2.16: (a) Matching Cox-Voinov when $\theta_l = 163$, $q=1$, advancing contact angle. (b) Matching Cox-Voinov when $\theta_l = 163$, $q=0.05$ receding contact angle. (c) Matching Cox-Voinov when $\theta_l = 80$, $q=1$, advancing contact angle. (d) Matching Cox-Voinov when $\theta_l = 80$, $q=0.05$, receding contact angle.

comparisons for advancing and receding contact angles, for small ($\theta_l=163$) and large ($\theta_l=80$) wetting ridge. For each case, we have systematically varied the lubricant viscosity while fixing the viscosity contrast of the other two liquids and the angle of the ridge θ_l . Values larger than 90° correspond to advancing angles, while smaller ones correspond to receding angles. Fig 2.16a and b shows the contact angle dynamics for two viscosity contrasts $q = 1$ and $q = 0.05$ when $\theta_l = 163$, while Fig 2.16c and d) show $\theta_l = 80$ for $q = 1$ and $q = 0.05$ respectively. We observe that fitting δ^{-1} using Eq. 2.50 in general captures the behaviour of the dynamic contact angle as a function of Ca for more than three orders of magnitude. Interestingly, in Fig. 2.16 we observe for a large lubricant viscosity, the lubricant-coated case approaches the case in which lubricant is absent. Thus, effectively the lubricant layer acts as a solid. In $q = 0.05$, increasing η_s also approaches the points to the solid case, but eventually the most viscous lubricant surpasses the solid, suggesting a larger dissipation in large viscosity lubricant layer. We observe that the larger deviation from the Cox-Voinov theory corresponds to Fig. 2.16d), $\lambda = 20$, to a viscosity mismatch between

2.5. Dynamic contact angles in lubricant coated surfaces

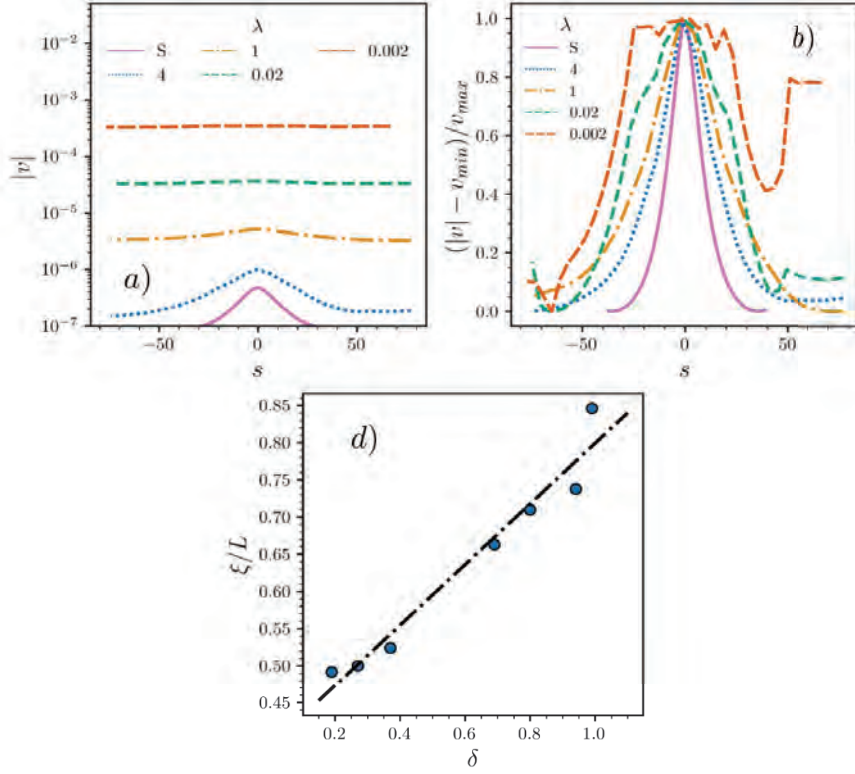


Figure 2.17: (a) Velocity as a function of the arc length (b) Normalised velocity as a function of the arc length.

drops when the lubricant ridge is large. Another interesting result is that decreasing the lubricant viscosity is correlated to deformations of the dynamic angle at larger Ca . In other words, decreasing the lubricant viscosity makes the interface of the drop less prone to deform. Since δ^{-1} is inversely correlated to the microscopic slip length, l_s , this result indicates that the lubricant can effectively act as a slip length that reduces the deformation of the interface.

To test this hypothesis, we track the velocity at the interface close to the fluid triple contact line, as a function of the integrated arc length $s = \int \Omega(s) ds$, where Ω is the interface contour, and $ds^2 = dx^2 + dy^2$. We observe that the width of the peak, ξ , of the velocity across the interface arc length is close to the solid case for large λ , which explains why large λ tends to the solid case. From Figs. 2.17a and 2.17b we learn that decreasing λ does not only decrease the peak, but additionally, the velocity does not decrease to zero. Instead, the whole layer is increasing its speed, moving at a rather constant velocity. By normalising the speeds by its maximum value, we can observe in further detail how the peak broadens as λ is decreased. We observe that the width of this peak correlates to l_s , which indicates that our hypothesis goes in the right direction.

Theoretical model for contact angles in lubricant-coated surfaces

Now we know that the Cox-Voinov equations are fulfilled in lubricant-coated surfaces. We also know that the lubricant layer has an impact in the slip length that determines the deformation of the contact angle in the Cox-Voinov relation. Now we will derive a simple model to predict some aspects of the dynamic contact angle, as a function of the lubricant viscosity. We follow a similar argument to that used by De Gennes to obtain an estimate of the dynamic contact angle behaviour as a function of Ca [10]. We note that the expression obtained by this method only recovers the correct dependence in the limit where the dynamic contact angle tends to zero. However, this expression contains useful information about the dependence of Ca with the contact angle. Therefore, this theoretical model will provide physical insight on the impact of a lubricant layer on the dependence of the dynamic contact angle. Following [10], the dissipation at the wedge of the fluid is equated to the dissipation resulting from the mismatch between the equilibrium contact angle and the dynamic contact angle, thus

$$T\dot{S} = \int_{x_0}^{L_x} dx \int_0^h \eta_s \left(\frac{dv_l(y)}{dy} \right)^2 dy + \int_h^{l(x)} \eta \left(\frac{dv(y)}{dy} \right)^2 dy \quad (2.54)$$

where η_s , η corresponds to the lubricant and drop viscosities, and $v_s(y)$, $v(y)$ to the lubricant and drop velocity profiles, respectively. As shown in Fig. 2.18 the velocity profile can be approximated to a straight line at the lubricant and a parabola in the liquid wedge, to simplify the calculations, similar to the calculation shown in the supplementary material from 4.6. After solving the flow profile, and integrating Eq. 2.54 we find

$$T\dot{S} = \frac{3\eta U^2}{\tan \theta} \ln \frac{\lambda(L_y - h) + 3h}{\epsilon\lambda + 3h} \quad (2.55)$$

where h is the lubricant width and ϵ is a microscopic parameter that recovers the solid case when $h = 0$ and prevents the divergence when there is no lubricant. The force associated to the contact line can be written as $F = \gamma(\cos \theta - \cos \theta_e)$. The rate of energy associated to the moving of the contact line, can be equated to the rate of dissipation previously calculated $FU = T\dot{S}$, to obtain

$$U\gamma(\cos \theta - \cos \theta_e) = \frac{3\eta U^2}{\tan \theta} \ln \frac{\lambda(L_y - h) + 3h}{\epsilon\lambda + 3h} \quad (2.56)$$

In the limit of small θ , for $\theta_e = 0$ we get the final relation

$$\theta^3 = 6\text{Ca} \ln \frac{\lambda(L_y - h) + 3h}{\epsilon\lambda + 3h} \quad (2.57)$$

which is very similar to Eq. 2.53, but now

$$\delta^{-1} = \frac{\lambda(L_y - h) + 3h}{\epsilon\lambda + 3h} \quad (2.58)$$

It is interesting to take the limits of Eq. 2.58 to understand the dependence of the term inside the logarithm. In the limit where $\epsilon \rightarrow 0$, the lubricant

2.5. Dynamic contact angles in lubricant coated surfaces

regularise the slip length from Eq. 2.53¹ such that there is no divergence when $\varepsilon \rightarrow 0$. In other words, there is no need of a cutoff distance to regularise the dissipation since it is well defined. When the lubricant viscosity is large compared to the drop, $\eta_s/\eta_l \rightarrow \infty$, we find the expected expression for the solid, $\delta^{-1} = (L_y - h)/\varepsilon$, where in this particular case $\varepsilon = l_s$. In the opposite limit, $\eta_s/\eta_l \rightarrow 0$, we find $\delta^{-1} \rightarrow 1$, which means that the effective slip length becomes comparable to the length of the wedge. As a consequence, a wedge can move at much more larger capillary numbers without further deformation of the interface. Furthermore, this expression predicts that δ^{-1} goes as $\eta/\eta_s = \lambda$ in the limit of small ε .

In the next section we will compare the δ^{-1} fitted factors to the theory prediction as a function of λ . Although the relation here has been derived in the limit $\theta_e = 0$ and $\theta \sim 0$, we assume that the relation inside the logarithm should still hold in the general case, for arbitrary viscosity contrasts of the drop and surrounding liquid.

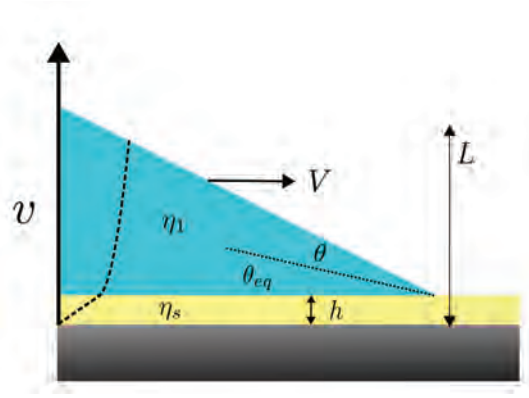


Figure 2.18: Scheme corresponding to the geometrical configuration we use to relate the dissipation to the interface deformation.

Comparisons between the theory and the simulations

To test the derived model, we now use Eq. 2.58 to find whether its possible to predict δ^{-1} . We approximate $\varepsilon \sim 0$, and use L_y as a fitting parameter. The results are shown in Fig. 2.19. The theory captures quite well the qualitative trend in all the cases, for receding and advancing angles, and both viscosity contrasts q . We observe some interesting features between the different cases. First, in the insets we observe that all cases follow accurately the dependence 2.58 when λ is small. The small ridge, $\theta_s = 160$, seems to accurately follow the expression in Figs.2.19a), b), and c), while $q = 0.5$ and receding angles in Fig. 2.19d) seem to have the larger deviations even for a quasi-planar ridge. Another consistent trend is the following: The angles with larger ridge deviate

¹Note that we now rename l_s as ε , since these quantities are not equivalent in the lubricant coated setup.

2.5. Dynamic contact angles in lubricant coated surfaces

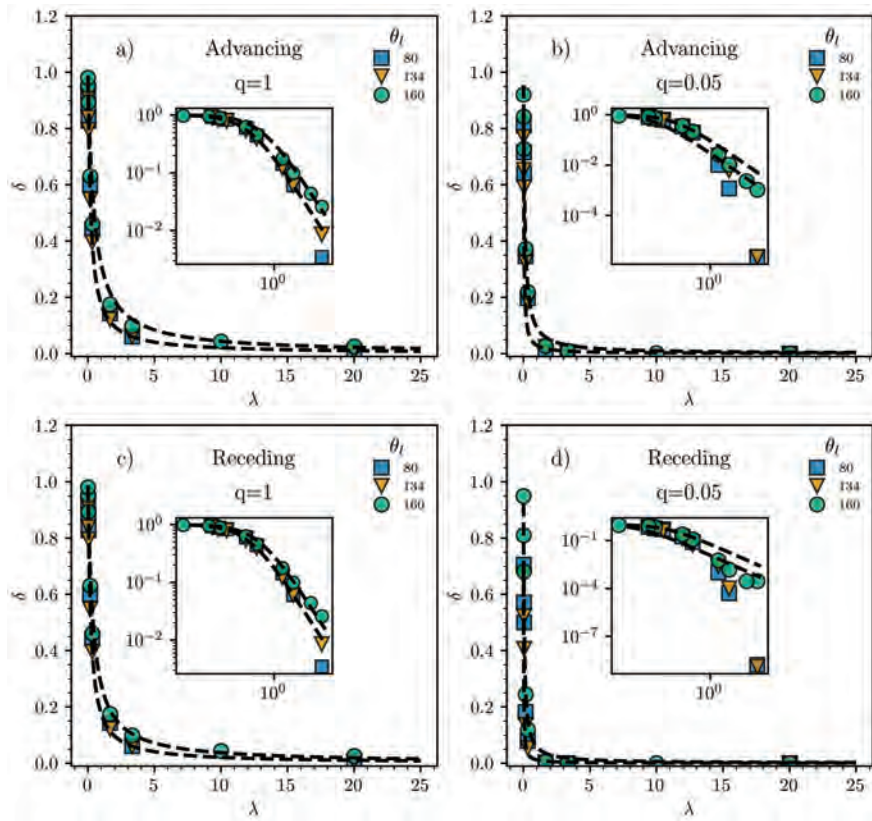


Figure 2.19: (a) δ dependence on λ , for advancing angles and $q=1$ (b) δ dependence on λ , for advancing angles and $q=0.05$ (c) δ dependence on λ , for receding angles and $q=1$ (d) δ dependence on λ , for receding angles and $q=0.05$

for smaller λ and a larger deviation is observed, suggesting that the ridge has an important contribution to the dissipation.

To conclude, we observe that Cox-Voinov captures the essence of the contact angle dynamics in lubricant coated faces. Interestingly, a good model can be obtained from very simple assumptions. This model qualitatively reproduces the trends, but fails quantitatively for large viscosities and for large bridges. The reason for this deviations are still subject of scientific consideration.

CHAPTER 3

Electrokinetically driven fluids in the nanoscale

3.1 Introduction

In the previous chapter we have described a surface driven phenomena, namely surface tension, which dominates capillary flows. This is only one possibility available in the broad range of interactions that can exist in micro and nanoscales. Here we will focus on a different venue. We will explore electrolytes, hence, fluids that contain ionic species that are coupled hydrodynamically. This topic is of fundamental interest across many fields. In biology and neuroscience, electrolyte fluids are a key ingredient to trigger signals, control the salinity concentration inside cells and counter-act any possible source of external pressure, just to quote some examples. In engineering, controlling the transport of electrolytes is a key ingredient to design new renewable energy sources [17] and even replicate neuronal behaviors [18]. The fact that electrolytes play a determinant role in controlling the behaviour of cells, resulting in chemical and mechanical responses has been known since the last century [117], when Huxley and Hodgkins studied the giant axon of a species of squid at different salinities. Here the goal will be to determine the properties of a electrolyte embedded charge-patterned nanochannel. We will explain how this patterned channels can be used to control electrolyte flows and result in responses similar to complex emergent responses found in nature [117].

Before this, we need to present some of the fundamental results of electrolytes in the presence of charged surfaces. In electrolytes, one of the fundamental equations that controls the local distribution of ions in equilibrium is the Poisson equation

$$\nabla^2 \psi = -\frac{\rho_e}{\varepsilon}, \quad (3.1)$$

which relates the electrostatic potential ψ to the local charge ρ_e and the permittivity of the medium ε . When integrated, the Poisson equation determines how a charge distribution sets the electric potential. At the same time, a electric potential gradient sets an electric field that will act on every charged specie

$$\mathbf{E} = -\nabla\psi. \quad (3.2)$$

Finally, if a ionic charge distribution in a medium is not in equilibrium, ionic fluxes will inevitably appear. The equation for the transport of ions

is fundamental to any non-equilibrium process, as the one we studied in the publication we will present in this chapter. The transport equations can be written by considering the local continuity equations. Three different contributions are generally to be considered, namely, diffusion, advection and migration due to electric fields. This transport equation is often referred to as the Nernst-Planck equation, and follows

$$\frac{\partial c}{\partial t} = \nabla \cdot \left[D \nabla c - c \mathbf{v} + \frac{Dze}{k_B T} c \mathbf{E} \right]. \quad (3.3)$$

The terms on the rhs correspond to diffusion, advection and electromigration, respectively. Note that the advection term relates the ion transport to the local velocity, such that a velocity field will result ionic transport.

3.2 Lattice-Boltzmann coupled to electrokinetics

Coupling the Lattice-Boltzmann method to an electrokinetic model is not trivial and requires a combination of different computational techniques [118]. For solving electrokinetic problems we use "*Ludwig*" open source code [57]. The core of the LB method remains the same as explained in Sec. 2.2. However, now the LB method will be coupled to the electrokinetic model by means of the Maxwell tensor. The force will be calculated as the divergence of this tensor, and at each step will be included in the streaming of the distribution function following the standard method by Guo [108]. At each time step, the Poisson equation will be solved in order to determine the instantaneous potential. The Nernst-Planck equations will be used to calculate the flux of ions and update the concentrations of each specie at each node. To update the ionic concentration following the Nernst-Planck equations require evaluating at every step each of the three contributions from Eq. 3.3, namely the diffusive contribution, the advection by the fluid velocity and the electromigration produced by the internal and external electric field. The fluid velocity obtained from the first moment of the distribution in the advection term of the Nernst-Planck equation, coupling the electrokinetic model hydrodynamically to the LB method.

We have also used an implementation that allow for a slip length, since in the nanoscale the no-slip boundary condition does not hold, leading to a slip velocity that depends on the interaction between molecules and the solid surface. The existence of a slip length can strongly alter the flow when a pressure gradient or an electric field is applied, as we will see in the presented publication.

3.3 Electrostatics in the presence of a charged wall

We will now study some of the most famous solution to the equilibrium distribution of a symmetric charge electrolyte in presence of an infinite charged plate. This problem is known as the electric double layer. By a symmetrical charge electrolyte we mean that each ionic specie has the same charge $z_- = z_+ = z$. From thermodynamics it is possible to derive an expression for the chemical potential $\mu(\mathbf{r})$ of ions and counter-ions,

$$\mu(\mathbf{r}) = \mu_0 + k_B T \ln \left(\frac{c_{\pm}(\mathbf{r})}{c_0} \right) \pm Ze\psi(\mathbf{r}). \quad (3.4)$$

3.3. Electrostatics in the presence of a charged wall

The thermodynamic equilibrium implies that there is no chemical potential gradient. This, together with the condition that away from the surface the concentration is constant $c_{\pm}(\infty) = c_{\pm,0}$ and the electric potential at infinity is constant and defined to be 0, $\psi(\infty) = 0$, leads to the following equation for the charge distribution

$$c_{\pm}(\mathbf{r}) = c_{\pm,0} \exp\left(\frac{\psi(\mathbf{r})Ze}{k_B T}\right) \quad (3.5)$$

Note that to this point, the shape of the electric potential is not specified, and the problem is not solved. However from this equation, we can extract the electric local density, ρ_e , which we can use to compute the potential. The electric density can be obtained as the difference between ions c_+ and counter-ions c_- ,

$$\rho_e(\mathbf{r}) = Ze[c_+(\mathbf{r}) - c_-(\mathbf{r})] = -2Zec_0 \sinh\left[\frac{\psi(\mathbf{r})Ze}{k_B T}\right] \quad (3.6)$$

In the limit of strong thermal fluctuations, $\psi(\mathbf{r})Ze/k_B T \sim 0$, the hyperbolic sine function can be expanded around zero, so that $\sinh[\psi(\mathbf{r})Ze/k_B T] \sim \psi(\mathbf{r})Ze/k_B T$. This approximation is often referred to as the Debye-Hückel approximation. With this approximation, we can easily solve the Poisson equation 3.1. Since the charged plate is infinite, the electrostatic potential will only depend on one dimension, the coordinate of which we will refer to as x . The differential equation is

$$-2c_0 \frac{\psi(\mathbf{r})(Ze)^2}{\epsilon k_B T} = \frac{d^2\psi}{dx^2}. \quad (3.7)$$

The solution to this differential equation is an exponential function. As a boundary condition, we define the electrostatic potential at the surface, $x = 0$, to be $\psi(0) = \xi$, and we finally obtain

$$\psi(x) = \xi \exp\left(-\frac{x}{\lambda_D}\right), \quad (3.8)$$

where

$$\lambda_D = \sqrt{\frac{\epsilon k_B T}{2(Ze)^2 c_0}}, \quad (3.9)$$

is the Debye length, and is one of the most important characteristic lengths in problems of electrolytes in confined media. The Debye length can be related by means of the the electrolyte concentration to the Bjerrum length $l_B = e^2/(4\pi\epsilon k_B T)$. This a complementary important characteristic length in electrokinetics, which quantifies at which distance the attraction force between two ions is comparable to the thermal energy. Its importance lies in relating the physical properties of the electrolyte solution to the screening length at which thermal fluctuations blur the influence of the charged plate.

When an external field is applied parallel to the plate, in the presence of a charged plate that follows Eq. 3.8, we can compute the flow profile using the Stokes equation. In the absence of a pressure gradient, the only force will be that of the external electric field. Hence

$$\eta \frac{d^2 u_x}{dx^2} = -\rho_e(x) E_z \quad (3.10)$$

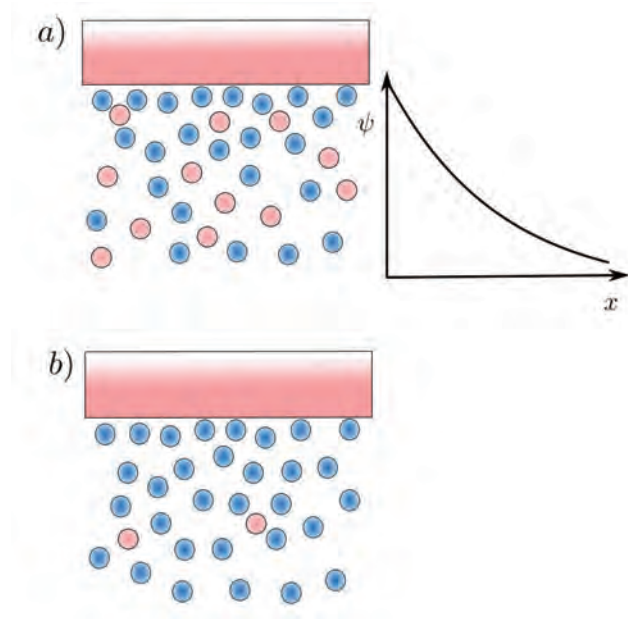


Figure 3.1: Electric potential when a) the screening length is small compared to the size of the system, so that the Debye-Hückel is a good approximation and b) in the case where the screening length is large compared to the size of the system.

Substituting Eq. 3.6 and Eq. 3.8 in the latter equation we obtain

$$v(x) = v_{eo} e^{-\frac{x}{\lambda_D}} \quad (3.11)$$

where $v_{eo} = \varepsilon \xi E_z / \eta$ is the electroosmotic velocity. This phenomenon is referred to as electroosmotic flow, and it is an important result of electrokinetic theory. In contrast to a typical Poiseuille flow, electroosmotic flows are forced near the wall, where local charge electroneutrality is broken due to the charged surface. Hence, most of the shear takes place near the charged boundary, while there is essentially no shear at the center.

The order of magnitude of the Debye length in a standard electrolyte solution is around 10 nm. If two equal charged plates are faced against each other at a distance $d \gg \lambda_D$, then the problem can be approximated with the Debye-Hückel approximation applying the corresponding boundary conditions, and analytical solutions can be found.

However, if these two characteristic distances are of the same order of magnitude, or the Debye length is larger, $d \leq \lambda_D$, the two screening lengths overlap and there is no screening layer. Instead, counterions can accumulate in the charged region due to the strong electric confinement. In the general case, for inhomogeneous channels, finding analytical solutions can be very difficult. Computational approaches can help to determine which mechanisms come at play and set the electric potential and ion concentrations. The solutions discussed in this section correspond to the simplified situation of the Debye-

3.3. Electrostatics in the presence of a charged wall

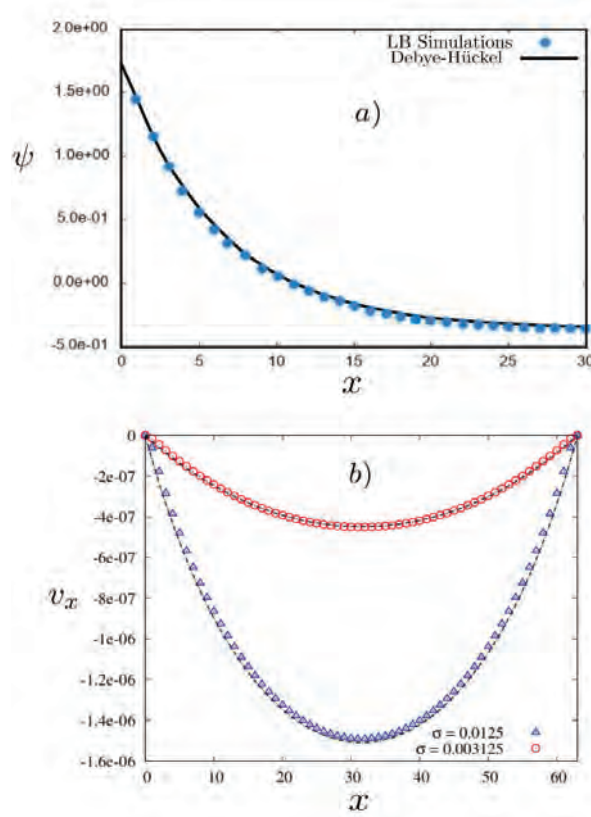


Figure 3.2: a) Comparison between the electric potential predicted by the Debye-Hückel and the one obtained with LB simulations. b) Comparison between the electrokinetic flow in a electrolyte confined by two equally charged plates, for two different charge densities σ each the solid plate. All units are in written in LB units, which are explained in the publication.

Hückel approximation, but is very useful to build intuition about electrostatic and eletrokinetics of ionic solutions.

We now compare the obtained analytical expressions with simulations obtained with the model described in the previous section. Fig. 3.2a) shows a simulation where parameters have been chosen in the Debye-Hückel limit. The walls, defined at $x = 0$ and $x = L$ have a uniform, constant surface charge σ . We chose L large enough, $L=100$ so that we can approximate each plate as an infinite plate the electric double layer of which has fully developed. The electrolyte is initialised at a certain uniform concentration $c_{\pm,0}$ that ensures that the whole system is electroneutral, hence that the sumation of all the charges in the bulk of the fluid and surface plate is zero. The surface charge in this case was $\sigma = 0.0006$. Simulations are run until a steady state is reached. We look at the equilibrium potential from the plate located at $z=0$ and compare the analytical solution, obtaining an excellent agreement.

For benchmarking purposes, we introduce the general solution for the electrosmotic flow, without assuming the Debye-Hückel approximation, which

3.4. Electrolyte flows in charge-patterned channels nanochannels

can be obtained in the case of two parallel plates with uniform and constant surface charge. In the following solution, only counter-ions are considered. The electrostatic potential in this case can be solved analytically [119]

$$c(x) = \frac{c_0}{\cos^2(Kx)}, \quad (3.12)$$

where $\rho_0 = K^2/2\pi l_b$, K is the solution of the transcendental equation,

$$\frac{KL}{2} \tan\left(\frac{KL}{2}\right) = \pi L_b \sigma, \quad (3.13)$$

The electroosmotic flow can then be obtained

$$v_y(x) = \frac{eE_z c_0}{\eta K^2} \log\left[\frac{\cos(Kx)}{\cos\left(\frac{KL}{2}\right)}\right] \quad (3.14)$$

where L is the width of the channel. In Fig. 3.2b) we compare the simulation results for two different surface charges and obtain a quantitative agreement in both cases. Hence, we validate that the developed LB method also works far from the Debye-Hückel regime.

3.4 Electrolyte flows in charge-patterned channels nanochannels

The last section has been dedicated to create a framework to understand the context of electrokinetic problems. Many promising technologies, such as blue energy [17] or iontronics [18] rely on controlling electroosmotic flows at the nanoscale level. Knowing the response of the flow in advance to a pressure gradient or an electric field is a difficult task and experiments and simulations are mandatory, specially when theoretical models are not available. Particularly appealing are the channels that have the ability to response asymmetrically to either a pressure gradient or an electric field. In the case of the pressure gradient assymetry, this is known as gating mechanism, and is essential to cells. The lipidic membrane of cells are plagued with ionic channels that selectively let ions pass. Furthermore, this asymmetric, selective response can result in a hysteresic loop when a oscillating electric field is applied. This hysteresic loop, often refered to as the memristor effect, is a key ingredient to fabricate electrolyte based transistors. Hence, ionic channels can result in a response that is analogous to the electronic transistor, but purely based in ionic transport. The framework to building such devices based in ionic responses is referred to iontronics, and is a promising research topic, since it would allow computational operations with a high energetic efficiency.

Channels that exhibit rectification have existed for quite a long time [120–126], and those with a conical shape are one of the most popular [127]. The surface charge typically is held constant and uniform. Interestingly, the assymetry shape introduces an assymetry in the response of the fluid depending on the side of the applied electric field or pressure gradient [123]. This is because more counter ions are accumulated around the small tip of the cone, resulting in a force upon action of an external field.

3.4. Electrolyte flows in charge-patterned channels nanochannels

In the publication introduced in this section, we identify a different mechanism that also leads to rectification. We explore the flow response to pressure gradients in a straight charge-patterned nanochannel. The charge-patterned is symmetric, meaning that two patches of equal length but opposite signs are put in the channel, one next to the other. Hence, the electrolyte inside the channel is electroneutral, as opposed to the conical geometry. We observe a discontinuous flow transition as a function of the pressure gradient. At low pressure gradients, a small diffusive flow is observed. At a certain threshold, the order of magnitude of the flow increases orders of magnitude, and the velocity profile transitions to a parabolic flow. The details are explained in the presented publication Pub. 4.7.

PART IV

Publications

CHAPTER 4

Driven soft matter at the nanoscale

Publication 1:
Friction Induces Anisotropic Propulsion in Sliding
Magnetic Microtriangles

Gaspard Junot¹, Sergi G. Leyva^{1,2}, Christoph Pauer³, Carles Calero^{1,4},
Ignacio Pagonabarraga^{1,2,5}, Tim Liedl³, Joe Tavaoli³, and Pietro
Tierno^{1,2,4}

¹Departament de Física de la Matèria Condensada, Universitat de Barcelona, 08028 Barcelona,
Spain

²Universitat de Barcelona Institute of Complex Systems (UBICS), Universitat de Barcelona,
08028 Barcelona, Spain

³Faculty of Physics and Center for Nano Science, Ludwig-Maximilians-Universität,
Geschwister-Scholl-Platz 1, München 80539, Germany

⁴Institut de Nanociència i Nanotecnologia, IN²UB, Universitat de Barcelona, 08028 Barcelona,
Spain

⁵CECAM Centre Européen de Calcul Atomique et Moléculaire, École Polytechnique Fédérale de
Lausanne, Batochime, Avenue Forel 2, 1015 Lausanne, Switzerland

Nano Letters (2022), **22**, 18, 7408-7414

Friction Induces Anisotropic Propulsion in Sliding Magnetic Microtriangles

Gaspard Junot,[▽] Sergi G. Leyva,[▽] Christoph Pauer, Carles Calero, Ignacio Pagonabarraga, Tim Liedl, Joe Tavaoli, and Pietro Tierno*



Cite This: <https://doi.org/10.1021/acs.nanolett.2c02295>



Read Online

ACCESS |

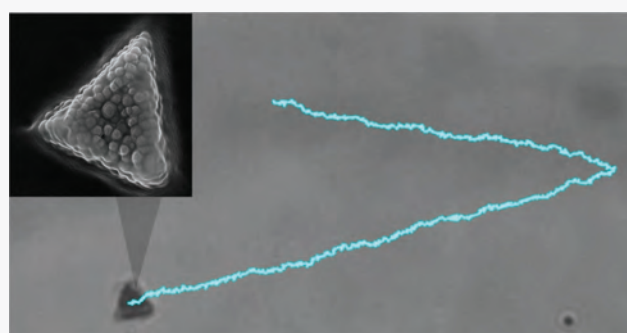
Metrics & More

Article Recommendations

Supporting Information

ABSTRACT: In viscous fluids, motile microentities such as bacteria or artificial swimmers often display different transport modes than macroscopic ones. A current challenge in the field aims at using friction asymmetry to steer the motion of microscopic particles. Here we show that lithographically shaped magnetic microtriangles undergo a series of complex transport modes when driven by a precessing magnetic field, including a surfing-like drift close to the bottom plane. In this regime, we exploit the triangle asymmetric shape to obtain a transversal drift which is later used to transport the microtriangle in any direction along the plane. We explain this friction-induced anisotropic sliding with a minimal numerical model capable to reproduce the experimental results. Due to the flexibility offered by soft-lithographic sculpturing, our method to guide anisotropic-shaped magnetic microcomposites can be potentially extended to many other field responsive structures operating in fluid media.

KEYWORDS: Active Colloids, Micromotors, Magnetism, Soft-lithography, Shape-anisotropy



Shape anisotropy plays an important role in magnetic systems, since it creates a demagnetizing field and a preferred direction for magnetization.¹ Anisotropy is also an intrinsic property of many biological systems, from elongated bacteria² to epithelial cells in tissue sheets³ and vertebrate bodies,⁴ while being of crucial importance for the behavior of nanoscale systems.^{5–9} In colloidal science, shape anisotropy affects the fundamental behavior of microscopic particles dispersed in liquid media, from Brownian motion¹⁰ to crystal frustration,¹¹ packing^{12,13} and glassy behavior.^{14,15} Anisotropic colloids can be easily manipulated via external fields,¹⁶ and their controlled motion has been used in several applications to date, such as probing the viscoelastic properties of complex fluids,^{17–19} or stirring and mixing liquids in confined microfluidic systems.^{20–22} For self-propelling particles systems,²³ where injected or environmental energy is directly converted into directed motion, the anisotropic shape may induce curved trajectories,^{24,25} or be responsible for emergent collective behaviors different from those of isotropic ones.^{26–28}

Here we realize isosceles magnetic microtriangles and demonstrate their propulsion in a viscous fluid when subjected to a time-dependent, conical precessing field. Depending on the field parameters, i.e. the amplitudes and driving frequency, we observe three distinct regimes of motion, where the triangles perform rolling or tumbling-like dynamics, and a sliding mode characterized by an average static planar orientation. In the latter

case, the triangles hold their surface quasi parallel to the bounding wall and we show that, when the direction of the magnetic moment does not coincide with the long side of the triangle, friction asymmetry between the two short sides induces a nonzero transversal drift. Under such conditions, one can transport the triangle along different directions across the plane, even performing closed orbits. In contrast, such trajectory reduces to a line when the magnetic moment is aligned with the long side. We explain these observations with a minimal simulation scheme which considers three linked ferromagnetic particles close to a stationary bounding wall, avoiding the complexity of considering a continuous triangular shape. We demonstrate with our simulation model that such transverse drifts take place due to the coupling of the shape anisotropy and magnetic misalignment of the triangle moment with respect to the symmetric axes. Thus, our results show how magnetic misalignment can lead to new microswimmers capabilities including the realization of very specific trajectories and their operations near solid surfaces.

Received: June 7, 2022

Revised: August 22, 2022

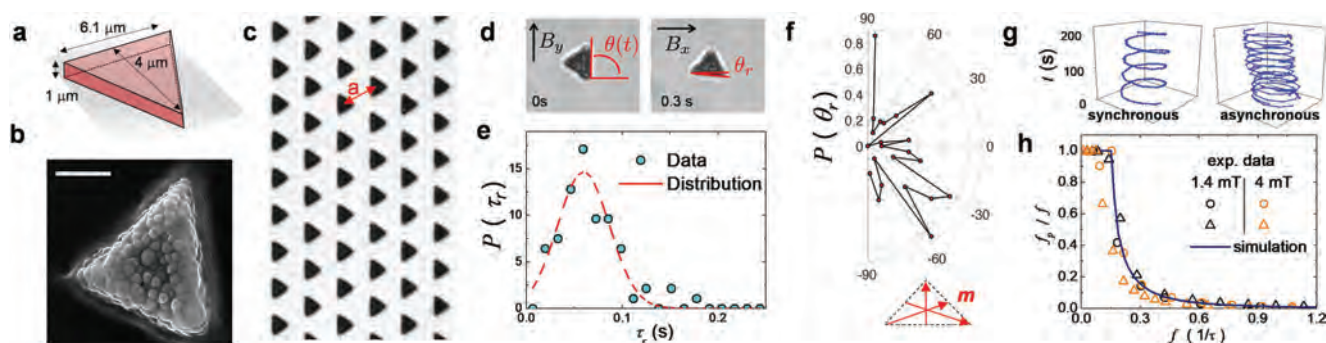


Figure 1. (a) Schematic of a ferromagnetic microtriangle with the corresponding sizes. (b) Scanning electron microscope image showing the embedded ferromagnetic nanoparticles (size 400 nm), scale bar is 2 μm . (c) Optical microscope image of an array of microtriangles before its extraction, lattice constant is $a = 12.4 \mu\text{m}$. (d) Microscope images showing the reorientation when a static field along the \hat{y} -direction ($B_y = 1 \text{ mT}$) is suddenly switched along the \hat{x} direction ($B_x = 1 \text{ mT}$). See also SI Video S1. (e) Distribution $P(\tau_r)$ of the relaxation time τ_r of the microtriangles measured respect to the x -axis. Symbols are experimental data, continuous line is a Gaussian function with mean $\langle \tau_r \rangle = 60 \text{ ms}$. (f) Top: Angular distribution $P(\theta_r)$ of the reorientation angle θ_r . Bottom: schematic showing the three main directions of \mathbf{m} within a microtriangle. (g) Position in the (\hat{x}, \hat{y}) plane versus time (vertical axis) of the tip of one magnetic triangle under a rotating magnetic field (amplitude $B_0 = 1.4 \text{ mT}$) in the synchronous (left, driving frequency $f = 1 \text{ Hz}$) and asynchronous (right, $f = 7 \text{ Hz}$) regimes. (h) Normalized rotational frequency of the triangle f_p/f versus f for two different triangles (circles and triangles) and field amplitudes (black and orange). The frequency is measured with respect to the reduced time τ (see text), the continuous line results from numerical simulations.

The ferromagnetic microtriangles are realized by filling polydimethylsiloxane molds with a suspension of silica magnetic nanoparticles (400 nm diameter) dispersed in a monomer matrix, see Figure 1a,b and Section S1 in the Supporting Information (SI) for more details. The triangles are $\sim 1 \mu\text{m}$ thick and isosceles, with two equal sides of length $5.1 \mu\text{m}$, and a longer one equal to $6.1 \mu\text{m}$. After cross-linking the monomer and extracting the triangles from the mold, Figure 1c, we disperse the obtained particles in highly deionized water, and insert the solution in a glass microchannel of height $100 \mu\text{m}$ and width $\sim 2 \text{ mm}$. The triangles sediment close to the bottom of the channel due to density mismatch, and there they display small thermal fluctuations in both the translational and orientational degrees of freedoms.

Free triangles display magnetic attraction due to the presence of a permanent magnetic moment \mathbf{m} . To measure the amplitude and direction of \mathbf{m} within these structures, we investigate the triangle reorientation under a static field $B_y = 1 \text{ mT}$. First, the field is applied along one direction (\hat{y} -axis) and then is suddenly switched along the perpendicular one (\hat{x} -axis), see Figure 1d and SI Video S1. One can describe this reorientation in terms of a balance between the applied magnetic torque $\tau_m = |\mathbf{m} \times \mathbf{B}| = mB \sin \theta$ with the viscous one $\tau_v = -\zeta_r \dot{\theta}$. Here θ describes the angle between the direction of \mathbf{m} within the triangle and the applied field, and ζ_r is the rotational friction coefficient. In the overdamped limit, $\tau_m + \tau_v = 0$ and the resulting solution, $\tan(\theta/2) = \exp(-t/\tau_r)$ determines the relaxation time, $\tau_r = \zeta_r / (mB)$. As shown in Figure 1e, after studying the reorientation of 73 triangles, we find that the distribution of relaxation times $P(\tau_r)$ is nearly Gaussian, centered around a mean value of $\langle \tau_r \rangle = 60 \text{ ms}$ with a standard deviation $\sigma_{\tau_r} = 27 \text{ ms}$. Using $\zeta_r \sim 8\pi\eta V_v$ with $\eta = 10^{-3} \text{ Pa}\cdot\text{s}$ the viscosity of water and $V_v = 1.22 \times 10^{-17} \mu\text{m}^3$ the triangle volume, we obtain a permanent moment of $m = 6.4 \times 10^{-21} \text{ A m}^2$.

Further, the reorientation experiments provide information on the direction $\theta_r \in [-\pi/2, \pi/2]$ subtended by the magnetic moment with the long side of the triangle, which in turn allows to identify the corresponding direction of \mathbf{m} within the triangle. As shown in Figure 1f, the permanent moment is oriented along three main directions, $\theta_r = -45^\circ, 45^\circ$ and 90° , see also the

schematic at the bottom of Figure 1f. As we show below, depending on the location of \mathbf{m} one can obtain different types of trajectories by changing the field parameters.

The magnetic properties of the microtriangles can alternatively be characterized by monitoring its response to a circularly polarized, in plane rotating magnetic field, $\mathbf{B} = B_0(\cos(2\pi ft)\hat{x} - \sin(2\pi ft)\hat{y})$ being f the driving frequency and $B_0 = B_x = B_y$ the field amplitude. The rotating field applies a magnetic torque τ_m which induces a rotational motion around a central axis. One can identify two dynamic regimes that emerge when tracking the position of one tip of the triangle as a function of time, Figure 1g. Below a critical frequency f_c the triangle rotates synchronously with the driving field, the phase-lag angle φ between \mathbf{m} and \mathbf{B} is constant and the rotational frequency $f_p = f$. In contrast, for higher frequencies, $f > f_c$ the motion becomes asynchronous and the spatiotemporal plot displays small kinks where \mathbf{m} loses its phase with \mathbf{B} and f_p decreases as f increases. Such regime can be described in terms of the Adler equation,²⁹ which gives in the deterministic limit $f_p/f = 1 - \sqrt{1 - (f_c/f)^2}$.

Here $f_c = f_c(\zeta_r, \mathbf{m}, \mathbf{B})$ and thus triangles with different magnetic moments \mathbf{m} will be characterized by a different critical frequencies. However, all data can be rescaled by plotting f_p/f versus the driving frequency measured in terms of a reduced time, $\tau = 1/(2\pi f_c)$. This reduced time compares the magnetic torque with the viscous one. When $f(1/\tau) \gtrsim (2\pi)^{-1}$, the viscous torque resistance is larger than the magnetic one, which gives rise to the asynchronous regime. Figure 1h shows f_p/f against f/τ for two different types of triangles (circles and triangles) and at two amplitudes of the rotating field, $B_0 = 1.4$ and 4 mT . This scaling also leads to excellent quantitative agreement with numerical simulations of a minimal model of the microtriangles, more details will be given later.

We induce propulsion of the microtriangle in water by applying a magnetic modulation that precesses with frequency f around an axis parallel to the glass substrate (\hat{x}, \hat{y}) . A field that precesses around the \hat{y} -axis is given by

$$\mathbf{B} = B_x \sin(2\pi ft)\hat{x} + B_y \hat{y} + B_z \cos(2\pi ft)\hat{z} \quad (1)$$

This type of magnetic modulation has been used in the past as a convenient means to transport other types of anisotropic objects, including paramagnetic doublets,³⁰ ribbons,³¹ or composite particles.^{32,33} When this modulation is applied to a microtriangle, it tries to align its moment with the precessing field, which would induce a conical rotation, similar to a gyroscope spinning. However, due to the complex shape of the triangle, the relative large aspect ratio (area to thickness) and the steric interaction with the bounding wall, we find three types of transport modes, depending on the different field parameters, Figure 2a. For low amplitude of the static, in-plane component

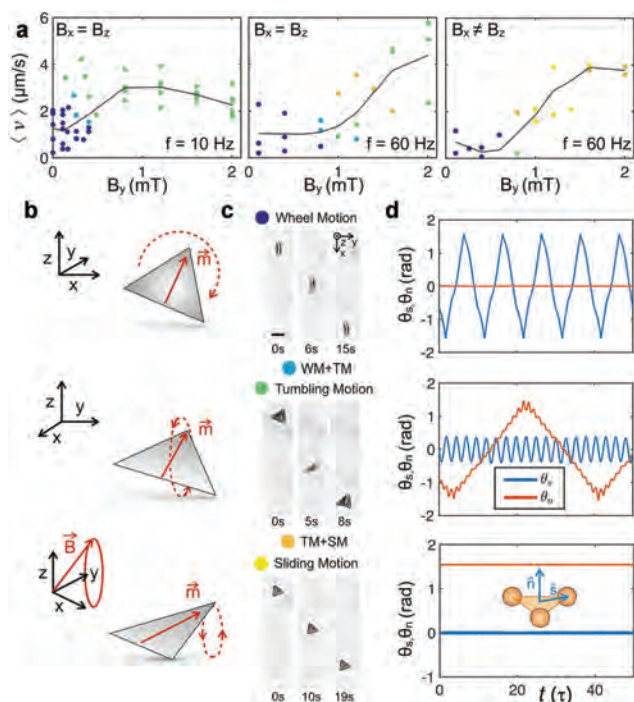


Figure 2. (a) Mean speed $\langle v \rangle$ with $v = \sqrt{v_x^2 + v_y^2}$ versus static component B_y of the precessing field for two different frequencies $f = 10$ Hz and $f = 60$ Hz at $B_x = B_z = 1.6$ mT (first and second panel) and at amplitudes $B_x = 1.4$ mT and $B_z = 1.27$ mT (third panel). (b,c) Schematic (b) and sequence of images (c) taken at three different instants of times of a propelling microtriangle in the three regimes: wheel (top, $B_x = B_z = 1.6$ mT, $B_y = 0$ mT, $f = 10$ Hz), tumbling (middle, $B_x = B_z = 1.6$ mT, $B_y = 0.32$ mT, $f = 10$ Hz) and sliding (bottom, $B_x = 1.4$ mT, $B_z = 1.27$ mT, $B_y = 1.2$ mT and $f = 60$ Hz). The scale bar in the top image is $5 \mu\text{m}$, the number of observed events are 33 for the wheel, 37 for the tumbling and 30 for the sliding mode. The corresponding videos illustrating these experimental situations are deposited as Supporting Information (Videos S2, S3, and S4). (d) Results from numerical simulations: normal (θ_n) and vector (θ_s) angles versus rescaled time for three situations corresponding to the experimentally observed regimes of motion. The small schematic in the bottom panel shows the modeled three particle system with the unit vectors \mathbf{n} and \mathbf{s} .

B_y , ($B \lesssim 0.5$ mT), Figure 2a left, middle, and right, the microtriangle rotates perpendicularly to the bounding wall, and it moves as a microscopic wheel, see first row of Figure 2b, Figure 2c and the SI Video S2. This transport mode is observed for a wide range of frequencies ($f \in [10, 60]$ Hz). The triangle transport is induced by the rotational-translational coupling, resulting from the dependence of the friction with the fluid on the distance to the bounding wall.³⁴ Due to the relative small thickness of the triangles, the wheel motion is usually

characterized by a small translational speed of the order of $\langle v \rangle \in [0.5, 2] \mu\text{m/s}$.

Increasing the static component B_y , forces the triangle to lay parallel to the bounding wall. However, for larger values of B_y ($B_y \gtrsim 0.5$ mT) the triangle still tries to follow as a whole the field modulation, and the resulting mode is a tumbling-like translation where the triangle continuously flips, second row of Figure 2b and Figure 2c. In this situation, increasing B_y destabilizes the in-plane rotation, and the permanent moment follows the field modulation but it features some wobbling of the microtriangle, see the SI Video S3. As shown in Figure 2a left and middle, this transport mode usually displays an higher average translational speed, $\langle v \rangle \in [2, 6] \mu\text{m/s}$.

At high frequencies ($f = 60$ Hz) and large values of B_y ($B_y \gtrsim 0.5$ mT) and for an elliptically polarized field ($B_x \neq B_z$), we find that the tumbling mode transits to a surfing like propulsion, where the microtriangle is observed to translate without flipping, with an intermediate speed of $\langle v \rangle \in [2, 4] \mu\text{m s}^{-1}$, third row of Figure 2b and Figure 2c. By carefully analyzing the experimental videos, we observed that in this mode the microtriangle shape laid almost parallel to the bounding plane while displaying a fast rotational movement of the tips. These rotations have a very small amplitude, that impede to characterize them experimentally and resolve the full three-dimensional dynamics of the tips. Instead, we have used numerical simulations (details are given later) to clarify the mechanism of motion in this regime. We found that the rotations of the tips produce unequal displacements along and perpendicular to the bounding wall, which induce asymmetric dissipations capable to break the time reciprocity of the fluid flow at low Reynolds number.³⁵ As shown in the SI Video S4, the microtriangles literally surf on top of the plane displaying a small wobbling. The orientation θ_r of the magnetic moment \mathbf{m} with respect to the long triangle side varies from triangle to triangle and so does the orientation of the long triangle side with respect to the transverse direction (\hat{y} -axis). In particular, when $\theta_r = 0^\circ$, \hat{x} is an axis of symmetry of the triangle whereas when $\theta_r \neq 0^\circ$ it is not. Thanks to these three modes, a triangle can adapt its locomotion to the environment. In an open environment, one can use the fastest mode (tumbling). However, when required to pass through a small orifice or pore, one can easily switch to the wheel or sliding modes which could enable the triangle to pass through these constrictions.

To confirm the experimental observations, we have developed a numerical model to gain insight in the mechanisms of the different transport modes. We represent the microtriangle as three beads, $i = 1, \dots, 3$ of equal mass m and located at a fixed distance away from each other. The equation of motion for each particle follows

$$m \frac{d^2 \mathbf{r}_i}{dt^2} = \mathbf{F}_i^m + \mathbf{F}_i^g + \mathbf{F}_i^{LJ} + \mathbf{F}_i^H \quad (2)$$

The first term on the right side, \mathbf{F}_i^m , accounts for the net force acting on bead i as a result of the constraint that keeps the three beads at constant separation from each other, and to the torque due to the coupling between the magnetic moment of the microtriangle \mathbf{m} (aligned with a prescribed axis rigidly fixed to the triangular plane) and the external magnetic field \mathbf{B} . \mathbf{F}_i^g corresponds to the gravitational force, while \mathbf{F}_i^{LJ} accounts for the steric interactions between the beads and the solid bounding wall. Finally, \mathbf{F}_i^H denotes the force acting on the bead i due to hydrodynamic interactions. These forces are described in detail in the Section S2 in SI. This minimal model captures the

essential mechanisms leading to rectification and thus net transport, which emerges from the coupling between the object geometry, the symmetry of the external driving and the plane mediated hydrodynamic interactions.

As shown in the small scheme at the bottom of Figure 2d, to characterize the three regimes of motion we define two unit vectors, \hat{n} and \hat{s} which define the direction perpendicular to plane of the triangle and from the center to one of the three particles, respectively. Thus, we describe the three translating modes in terms of the angles $\theta_n = \arcsin(\hat{n} \cdot \hat{z})$ and $\theta_s = \arcsin(\hat{s} \cdot \hat{z})$. For the wheel motion (top panel in Figure 2d) θ_n remains constant and the three-particle system performs rolling only in the (\hat{x}, \hat{z}) plane, with θ_s periodically varying within the range $[-\pi, \pi]$ similar to the propulsion of magnetic rollers.³⁶ The tumbling transport (middle panel in Figure 2d) features periodic oscillations of both angles θ_n and θ_s . The θ_s conical precession produces a slow rotation of θ_n , which periodically flips the microtriangle. The propulsion by flipping of the microtriangle is analogous to the motion of actuated rotors under the effect of a conical precessing field.³⁷ Finally, the last panel of Figure 2d corresponds to the surfing like transport. The simulations show that the ratio between the gravitational attraction and the magnetic force plays a key role in avoiding the flipping of θ_n , stabilizing the average planar oscillations when the triangle slides. This motion is characterized by almost constant values of both angles with small oscillations. The simulations allow to visualize the bead trajectories which represents the triangle tips. Small and fast asymmetric oscillations are observed for each tip in each period, resulting in a net propulsion, see SI Video 9.

The model also allows a deep exploration of the parameter space which unveils the different degrees of freedom that allow propulsion in the sliding mode. In particular, for a microtriangle with $\theta_r = 90^\circ$, Figure 3 displays how θ_s varies parametrically as a function of $\theta_l = \arcsin(\hat{s} \cdot \hat{y})$, which corresponds to the trajectory where the vertex \hat{s} points to. As the static field component B_y increases, both the rectification velocity of the sliding triangle and the area contained by the corresponding trajectory decrease, and eventually the trajectory does not contain a finite area,

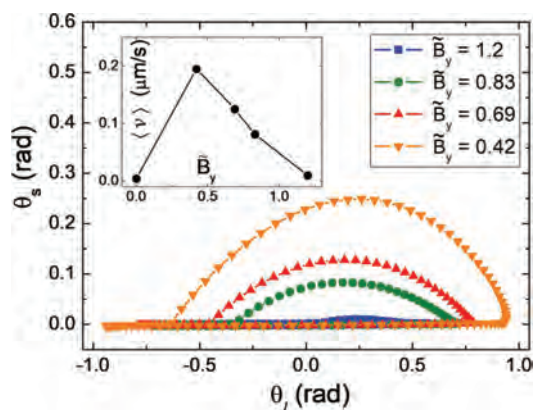


Figure 3. Trajectories of the angle θ_s as a function of θ_l for a simulated microtriangle with $\theta_r = 90^\circ$. Here \tilde{B}_y refers to the constant component of the magnetic field normalized by the radius of the rotating field, $\tilde{B}_y = B_y / (B_x + B_z)$. The inset shows the average translational velocity of each trajectory. The frequency is set to $f = 2.56$ Hz. In this specific set of simulations, \hat{s} is parallel to the magnetization.

corresponding to the regime where the triangle does not slide. Now the tips' oscillations are parallel to the boundary wall surface with a vanishing area. Hence, the parallel and perpendicular motion of the triangle vertex in the presence of the solid bounding wall provide the two independent degrees of freedom required by Purcell scallop theorem to break the time reversal symmetry and produce a translational motion.³⁵

We now focus on the sliding mode, where the microtriangle translates almost parallel to the close bounding wall. In this regime we find that microtriangles characterized by a permanent moment $\theta_r \neq 0$, exhibit a net propulsion along the axis of precession (y axis) in addition to the motion along the perpendicular direction. As shown in Figure 4a, see also

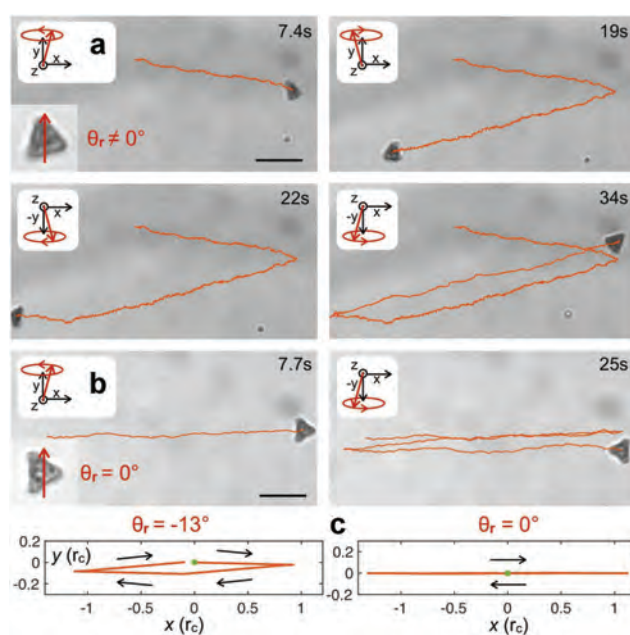


Figure 4. (a) Sequence of images showing a two-dimensional trajectory of a microtriangle in the sliding regime when the permanent moment is inclined with respect to its long side ($\theta_r = -17^\circ$). The change in the horizontal transport direction ($v_x \rightarrow -v_x$) is realized by inverting the chirality of the rotating field ($B_x \rightarrow -B_x$), while the change in the vertical direction is obtained by inverting the static component ($B_y \rightarrow -B_y$). The corresponding video is SI Video S3. (b) One dimensional trajectory showing the back and forward motion of a sliding microtriangle with symmetric orientation of the two short sides along the transport direction ($\theta_r = 0^\circ$). (c) Corresponding results from numerical simulations of a sliding microtriangle for $\theta_r = -13^\circ$ (left) and $\theta_r = 0^\circ$ (right).

VideoS5 in the Supporting Information, this effect is robust, and reproducible, and can be used to rectify the motion of sliding triangles to bring them to any point of the plane by simply switching the chirality of the rotating field (here inverting B_x) and the static field B_y . In contrast, microtriangles whose magnetization is parallel to their long side ($\theta_r = 0^\circ$) do not display such asymmetric friction and the corresponding transversal drag, Figure 4b. Consequently, those triangles can only be driven along a line (here the \hat{x} -axis). As shown in Figure 4c, we observe the same behavior in simulation i.e. triangles exhibit transversal motion only when $\theta_r \neq 0$. Magnetic misalignment allows for each set of magnetic field configurations to produce a different orientation of the tips' oscillations with respect to the laboratory frame, leading to the four transversal

directions, as can be observed in SI Video S6. The sliding propulsion mode that we report does not involve complete rotations of the micro-object. In this case, the rectification of its motion into net displacement requires both the anisotropy of friction due to the presence of the solid wall and, at least, two degrees of freedom to define the particle configuration. Hence, we expect that any anisotropic object will, generically, be able to slide under the appropriate external actuating field. For example, a disk can exhibit wheel, tumbling and sliding. However, the sliding propulsion will have the same direction as the wheel and tumbling motion, depending only on the chirality of the magnetic field. This is because there cannot be misalignment in a planar magnetic moment contained in a disk. Hence, the degree of anisotropy has a strong impact in the possibility to manipulate and control the direction of motion of the object.

At large area fractions, our ferromagnetic microtriangles can interact and assemble due to dipolar forces. As shown in the top inset of Figure 5a, already in the absence of any applied field, the

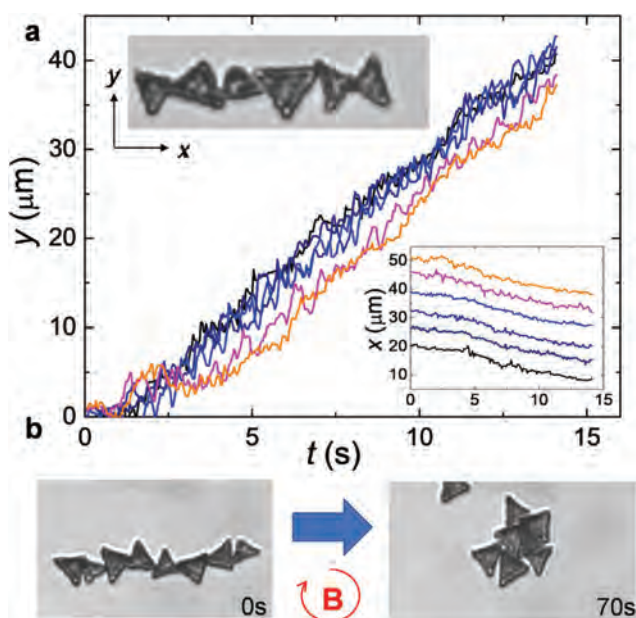


Figure 5. (a) Position versus time of the center of mass of 6 triangles that collectively translate via the tumbling mode at a constant speed $\langle v_y \rangle = 3.1 \mu\text{ms}^{-1}$. The applied precessing field has amplitudes $B_z = B_x = 1.6$ mT and $B_y = 1.22$ mT (static field) and frequency $f = 10$ Hz. Top inset displays a microscope image of the initial assembly ($B = 0$), see also SI Video S7. Bottom inset shows the transversal trajectory with a constant separation distance between the particles. (b) Microscope image showing the initial (0s) and final (70s) configuration of 8 triangles that are assembled in a compact structure due to an in-plane rotating magnetic field with $f = 10$ Hz and $B_x = B_y = 1$ mT.

particles tend to aggregate forming linear chains where the internal orientation of the individual triangles depends on the orientation of their permanent moments. Once they adopt an elongated structure, the triangles display weak thermal fluctuations and the structure is practically fixed, but they can be readily transported and redispersed in the water via an external field. For example, Figure 5a and the corresponding SI Video S7, shows the propulsion of the chain when it is subjected to a precessing field. The particles show a relative displacement advancing one with respect to the other during a field cycle, which lead to fluctuations along the y -position. In contrast, they

tend to keep their separation distance constant, as shown by the bottom inset (x -position). Thus, one can translate the magnetic chain at a constant speed, and their collective motion could be used to transport other non magnetic cargoes dispersed in the fluid medium.

Apart from collective transport, the magnetic triangles could be assembled in more compact structures, starting from a linear aggregate. This feature is demonstrated in Figure 5b, where the microtriangles are subjected to an in-plane, circularly polarized rotating field. The rotating field creates a torque on the particles and induce time-averaged attractive dipolar interactions.³⁸ Such compact structure forms due to the competition between dipolar forces and excluded volume, while assemble the particles to reduce the free space thus maximizing packing. We note that the assembly of few microtriangles is the starting point to investigate the field-induced aggregation of more complex structures that can be easily designed with our lithographic technique.

In conclusion, we have demonstrated that lithographically made soft magnetic microtriangles display a rich series of transport modes when subjected to a conically precessing magnetic field. We find that, depending on the field parameters, these complex particles may either translate as microwheel, tumble or even display a surfing like dynamics where they slide close to the bounding wall. In the sliding mode, we find that anisotropy in friction and magnetic misalignment may be used to generate a transversal particle motion, and the microtriangle can be driven across the full plane by switching the static component of the applied field and the field chirality. Those different modes enable the triangle to adapt its locomotion to different situations, giving the triangle an advantage with respect to more simple isotropic particles. All these dynamical modes can be explained by considering a simple model of three linked ferromagnetic spheres interacting with a bounding plane. We finally stress that transport of isotropic magnetic colloids and their collective dynamics have been matter of much research so far. However, using particles with complex shapes may further unveil novel transport modes which could be used to create more complex functional operations in fluid based applications. We have demonstrated this concept with a microtriangle, but our results are rather general, as any anisotropic shaped object with a magnetic misalignment could result in a sliding propulsion with different transversal motions.

■ ASSOCIATED CONTENT

Supporting Information

The Supporting Information is available free of charge at <https://pubs.acs.org/doi/10.1021/acs.nanolett.2c02295>.

More details on experimental system and numerical simulation (PDF)

Videoclip illustrating the reorientation dynamics of two magnetic microtriangles initially aligned by a static field of amplitude 1 mT along the vertical (y) direction which is subsequently switched along the horizontal (x) direction (AVI)

Videoclip illustrating the wheel motion of a magnetic microtriangle which is driven first towards top and later towards bottom by inverting the chirality of the precessing field (AVI)

Tumbling motion of a magnetic microtriangle which is driven first toward top and later toward bottom by inverting the chirality of the precessing field (AVI)

Video showing the surfing-like propulsion of a magnetic microtriangle which is driven first toward top and later toward bottom by inverting the chirality of the precessing field (AVI)

Videoclip showing how a microtriangle performs a close trajectory by acquiring a transversal speed due to friction anisotropy (AVI)

Video showing position of the three tips of a microtriangle in the sliding mode obtained from numerical simulation (AVI)

Videoclip showing collective transport of six microtriangles initially assembled to form a chain (AVI)

AUTHOR INFORMATION

Corresponding Author

Pietro Tierno – Departament de Física de la Matèria Condensada, Institut de Nanociència i Nanotecnologia, and Universitat de Barcelona Institute of Complex Systems (UBICS), Universitat de Barcelona, 08028 Barcelona, Spain; orcid.org/0000-0002-0813-8683; Email: ptierno@ub.edu

Authors

Gaspard Junot – Departament de Física de la Matèria Condensada, Universitat de Barcelona, 08028 Barcelona, Spain

Sergi G. Leyva – Departament de Física de la Matèria Condensada, Universitat de Barcelona, 08028 Barcelona, Spain; Universitat de Barcelona Institute of Complex Systems (UBICS), Universitat de Barcelona, 08028 Barcelona, Spain

Christoph Pauer – Faculty of Physics and Center for Nano Science, Ludwig-Maximilians-Universität, München 80539, Germany

Carles Calero – Departament de Física de la Matèria Condensada, Universitat de Barcelona, 08028 Barcelona, Spain; Institut de Nanociència i Nanotecnologia, Universitat de Barcelona, 08028 Barcelona, Spain; orcid.org/0000-0002-1977-1724

Ignacio Pagonabarraga – Departament de Física de la Matèria Condensada, Universitat de Barcelona, 08028 Barcelona, Spain; Universitat de Barcelona Institute of Complex Systems (UBICS), Universitat de Barcelona, 08028 Barcelona, Spain; CECAM, Centre Européen de Calcul Atomique et Moléculaire, École Polytechnique Fédérale de Lausanne (EPFL), 1015 Lausanne, Switzerland

Tim Liedl – Faculty of Physics and Center for Nano Science, Ludwig-Maximilians-Universität, München 80539, Germany; orcid.org/0000-0002-0040-0173

Joe Tavaoli – Faculty of Physics and Center for Nano Science, Ludwig-Maximilians-Universität, München 80539, Germany

Complete contact information is available at:

<https://pubs.acs.org/10.1021/acs.nanolett.2c02295>

Author Contributions

[†]G.J. and S.G.L. contributed equally to this work.

Notes

The authors declare no competing financial interest.

ACKNOWLEDGMENTS

We thank Helena Massana-Cid and Antonio Ortiz-Ambriz for experimental advice. This work has received funding from the European Research Council (ERC Consolidator Grant Contract

No. 811234). I.P. acknowledges support from MCIU (No. PGC2018-098373-B-100 AEI/FEDER-EU), AGAUR (No. 2017SGR-884), and Swiss National Science Foundation (No. 200021-175719). J.T., T.L. and C.P. acknowledges support from the German Research foundation (DFG) for funding under Project No. TA 1375/1-1 (J.T.) and through the SFB1032 “Nanoagents,” Project A6 (T.L. and C.P.). P.T. acknowledge support from MCIU (No. PID2019-108842GB-C21) and the Program “ICREA Acadèmia”.

REFERENCES

- (1) Vereda, F.; de Vicente, J.; Hidalgo-Álvarez, R. Physical properties of elongated magnetic particles: magnetization and friction coefficient anisotropies. *ChemPhysChem* **2009**, *10*, 1165–1179.
- (2) Wadhwa, N.; Berg, H. C. Bacterial motility: machinery and mechanisms. *Nat. Rev. Microbiol.* **2022**, *20*, 161–173.
- (3) Herrera-Perez, R. M.; Kasza, K. E. Biophysical control of the cell rearrangements and cell shape changes that build epithelial tissues. *Curr. Opin. Genet. Dev.* **2018**, *51*, 88–95.
- (4) Mongera, A.; Rowghanian, P.; Gustafson, H. J.; Shelton, E.; Kealhofer, D. A.; Carn, E. K.; Serwane, F.; Lucio, A. A.; Giammona, J.; Campàs, O. A fluid-to-solid jamming transition underlies vertebrate body axis elongation. *Nature* **2018**, *561*, 401–405.
- (5) Cozzoli, P. D.; Snoeck, E.; Garcia, M. A.; Giannini, C.; Guagliardi, A.; Cervellino, A.; Gozzo, F.; Hernando, A.; Achterhold, K.; Ciobanu, N.; Parak, F. G.; Cingolani, R.; Manna, L. Colloidal Synthesis and Characterization of Tetrapod-Shaped Magnetic Nanocrystals. *Nano Lett.* **2006**, *6*, 1966–1972.
- (6) Szymura, M.; Wojnar, P.; Klopotoski, L.; Suffczynski, J.; Goryca, M.; Smoleński, T.; Kossacki, P.; Zaleszczyk, W.; Wojciechowski, T.; Karczewski, G.; Wojtowicz, T.; Kossut, J. Spin Splitting Anisotropy in Single Diluted Magnetic Nanowire Heterostructures. *Nano Lett.* **2015**, *15*, 1972–1978.
- (7) Hudait, B.; Dutta, S. K.; Bera, S.; Pradhan, N. Introducing B-Site Cations by Ion Exchange and Shape Anisotropy in CsPbBr₃ Perovskite Nanostructures. *Nano Lett.* **2021**, *21*, 5277–5284.
- (8) Burks, E. C.; Gilbert, D. A.; Murray, P. D.; Flores, C.; Felner, T. E.; Charnvanichborikarn, S.; Kucheyev, S. O.; Colvin, J. D.; Yin, G.; Liu, K. 3D Nanomagnetism in Low Density Interconnected Nanowire Networks. *Nano Lett.* **2021**, *21*, 716–722.
- (9) Almeida, T. P.; Lequeux, S.; Palomino, A.; Sousa, R. C.; Fruchart, O.; Prejbeanu, I.-L.; Dieny, B.; Masseboeuf, A.; Cooper, D. Quantitative Visualization of Thermally Enhanced Perpendicular Shape Anisotropy STT-MRAM Nanopillars. *Nano Lett.* **2022**, *22*, 4000–4005.
- (10) Han, Y.; Alsayed, A. M.; Nobili, M.; Zhang, J.; Lubensky, T. C.; Yodh, A. G. Physical properties of elongated magnetic particles: magnetization and friction coefficient anisotropies. *Science* **2009**, *314*, 626–30.
- (11) Grason, G. M. Perspective: Geometrically frustrated assemblies. *J. Chem. Phys.* **2016**, *145*, 110901.
- (12) Manoharan, V. N.; Elsesser, M. T.; Pine, D. J. Dense Packing and Symmetry in Small Clusters of Microspheres. *Science* **2003**, *301*, 483–487.
- (13) Baule, A.; Mari, R.; Bo, L.; Portal, L.; Makse, H. A. Mean-field theory of random close packings of axisymmetric particles. *Nat. Commun.* **2013**, *4*, 2194.
- (14) Donev, A.; Cisse, I.; Sachs, D.; Variano, E. A.; Stillinger, F. H.; Connelly, R.; Torquato, S.; Chaikin, P. M. Improving the density of jammed disordered packings using ellipsoids. *Science* **2004**, *303*, 990–3.
- (15) Zheng, Z.; Ni, R.; Wang, F.; Dijkstra, M.; Wang, Y.; Han, Y. Structural signatures of dynamic heterogeneities in monolayers of colloidal ellipsoids. *Nat. Commun.* **2014**, *5*, 3829.
- (16) Tierno, P. Recent advances in anisotropic magnetic colloids: realization, assembly and applications. *Phys. Chem. Chem. Phys.* **2014**, *16*, 23515–23528.

- (17) Anguelouch, A.; Leheny, R. L.; Reich, D. H. Application of ferromagnetic nanowires to interfacial microrheology. *Appl. Phys. Lett.* **2006**, *89*, 111914.
- (18) Dhar, P.; Cao, Y.; Fischer, T. M.; Zasadzinski, J. A. Active Interfacial Shear Microrheology of Aging Protein Films. *Phys. Rev. Lett.* **2010**, *104*, 016001.
- (19) Choi, S. Q.; Steltenkamp, S.; Zasadzinski, J.; Squires, T. M. Active microrheology and simultaneous visualization of sheared phospholipid monolayers. *Nat. Commun.* **2011**, *2*, 1–6.
- (20) Terray, A.; Oakey, J.; Marr, D. W. M. Microfluidic Control Using Colloidal Devices. *Science* **2002**, *296*, 1841.
- (21) Sawetzki, T.; Rahmouni, S.; Bechinger, C.; Marr, D. W. M. In situ assembly of linked geometrically coupled microdevices. *Proc. Natl. Acad. Sci. U. S. A.* **2008**, *105*, 20141–20145.
- (22) Kavcic, B.; Babic, D.; Osterman, N.; Podobnik, B.; Poberaj, I. Magnetically actuated microrotors with individual pumping speed and direction control. *Appl. Phys. Lett.* **2009**, *95*, 023504.
- (23) Bechinger, C.; Di Leonardo, R.; Löwen, H.; Reichhardt, C.; Volpe, G.; Volpe, G. Active particles in complex and crowded environments. *Rev. Mod. Phys.* **2016**, *88*, 045006.
- (24) DiLuzio, W. R.; Whitesides, G. M.; Stone, H. A. Swimming in Circles: Motion of Bacteria near Solid Boundaries. *Appl. Phys. Lett.* **2006**, *90*, 400–412.
- (25) Kümmel, F.; ten Hagen, B.; Wittkowski, R.; Buttinoni, L.; Eichhorn, R.; Volpe, G.; Löwen, H.; Bechinger, C. Circular Motion of Asymmetric Self-Propelling Particles. *Phys. Rev. Lett.* **2013**, *110*, 198302.
- (26) Elgeti, J.; Winkler, R. G.; Gompper, G. Physics of microswimmers—single particle motion and collective behavior: a review. *Prog. Phys.* **2015**, *78*, 056601.
- (27) Zöttl, A.; Stark, H. Emergent behavior in active colloids. *J. Phys.: Cond. Matter* **2016**, *28*, 253001.
- (28) Pauer, C.; du Roure, O.; Heuvingh, J.; Liedl, T.; Tavaoli, J. Programmable Design and Performance of Modular Magnetic Microswimmers. *Adv. Mater.* **2021**, *33*, 2006237.
- (29) Adler, R. A. Study of Locking Phenomena in Oscillators. *Proc. IRE* **1946**, *34*, 351.
- (30) Tierno, P.; Golestanian, R.; Pagonabarraga, I.; Sagués, F. Controlled Swimming in Confined Fluids of Magnetically Actuated Colloidal Rotors. *Phys. Rev. Lett.* **2008**, *101*, 218304.
- (31) Casic, N.; Quintero, N.; Alvarez-Nodarse, R.; Mertens, F. G.; Jibuti, L.; Zimmermann, W.; Fischer, T. M. Propulsion Efficiency of a Dynamic Self-Assembled Helical Ribbon. *Phys. Rev. Lett.* **2013**, *110*, 168302.
- (32) Gao, W.; Sattayasamitsathit, S.; Manesh, K. M.; Weihs, D.; Wang, J. Magnetically Powered Flexible Metal Nanowire Motors. *J. Am. Chem. Soc.* **2010**, *132*, 14403–14405.
- (33) Pak, O. S.; Gao, W.; Wang, J.; Lauga, E. High-speed propulsion of flexible nanowire motors: Theory and experiments. *Soft Matter* **2011**, *7*, 8169–8181.
- (34) Goldman, A. J.; Cox, R. G.; Brenner, H. Low viscous motion of a sphere parallel to a plane wall—I Motion through a quiescent fluid. *Chem. Eng.* **1967**, *22*, 637.
- (35) Purcell, E. M. Life at low reynolds number. *Am. J. Phys.* **1977**, *45*, 3.
- (36) Martinez-Pedrero, F.; Navarro-Argemí, E.; Ortiz-Ambriz, A.; Pagonabarraga, I.; Tierno, P. Emergent hydrodynamic bound states between magnetically powered micropropellers. *Sci. Adv.* **2018**, *4*, No. eaap9379.
- (37) Tierno, P.; Sagués, F. Steering trajectories in magnetically actuated colloidal propellers. *Eur. Phys. J. E* **2012**, *35*, 71.
- (38) Tierno, P.; Muruganathan, R.; Fischer, T. M. Viscoelasticity of Dynamically Self-Assembled Paramagnetic Colloidal Clusters. *Phys. Rev. Lett.* **2007**, *98*, 028301.

Publication 2:
Hydrodynamic Synchronisation And Clustering In
Ratcheting colloidal Matter

Sergi G. Leyva^{1,2}, Ralph L. Stoop¹, Ignacio Pagonabarraga^{1,2,3}, and Pietro
Tierno ^{1,2,4}

¹Departament de Física de la Matèria Condensada, Universitat de Barcelona, 08028 Barcelona,
Spain

²Universitat de Barcelona Institute of Complex Systems (UBICS), Universitat de Barcelona,
08028 Barcelona, Spain

³CECAM Centre Européen de Calcul Atomique et Moléculaire, École Polytechnique Fédérale de
Lausanne, Batochime, Avenue Forel 2, 1015 Lausanne, Switzerland

⁴Institut de Nanociència i Nanotecnologia, IN²UB, Universitat de Barcelona, 08028 Barcelona,
Spain

Science Advances (2022), **8**, 23

PHYSICS

Hydrodynamic synchronization and clustering in ratcheting colloidal matter

Sergi G. Leyva^{1,2†}, Ralph L. Stoop^{1†}, Ignacio Pagonabarraga^{1,2,3}, Pietro Tierno^{1,2,4*}

Ratchet transport systems are widespread in physics and biology; however, the effect of the dispersing medium in the collective dynamics of these out-of-equilibrium systems has been often overlooked. We show that, in a traveling wave magnetic ratchet, long-range hydrodynamic interactions (HIs) produce a series of remarkable phenomena on the transport and assembly of interacting Brownian particles. We demonstrate that HIs induce the resynchronization with the traveling wave that emerges as a “speed-up” effect, characterized by a net raise of the translational speed, which doubles that of single particles. When competing with dipolar forces and the underlying substrate symmetry, HIs promote the formation of clusters that grow perpendicular to the driving direction. We support our findings both with Langevin dynamics and with a theoretical model that accounts for the fluid-mediated interactions. Our work illustrates the role of the dispersing medium on the dynamics of driven colloidal matter and unveils the growing process and cluster morphologies above a periodic substrate.

INTRODUCTION

The directional transport of microscopic entities in fluid media occurs in several physical and biological processes ranging from the nanoparticle delivery in a microfluidic network (1, 2) to liquid sliding across topographic surfaces (3, 4), translocation of proteins (5), molecular motors (6, 7), or enzymes (8). At the microscale, thermal fluctuations can be converted into directed motion via the ratchet effect, which uses spatial or temporal asymmetries in the system to generate a preferred direction of motion (9, 10). Technological progresses in engineering external potentials have shown that colloidal particles represent an experimentally accessible model system to investigate ratchet transport effects (11–16). Beyond the colloidal domain, realizing particle-based ratchets may also be of interest for other research fields, since a similar transport scheme can be extended to other systems on different length scales (17–20). However, many experimental realizations have focused on proposing scheme for single particles, or few interacting ones, neglecting the effect of the dispersing medium. Such effect may become important in many-body systems, affecting the particle transport and also leading to unexpected emergent phenomena.

The dynamics of microscopic particles in liquid media often occurs at low Reynolds number (Re), where inertial forces are negligible and fluid mechanic laws become time reversible. Under such conditions, hydrodynamic interactions (HIs), namely, fluid-mediated long-range interactions, may become important since they are excited by the diffusive or driven motion of the dispersed particles. These interactions have been invoked as essential in many physical and biological systems and lead to several fascinating phenomena from the spontaneous formation of vortex colonies (21) or the circular path of the bacteria *Escherichia coli* (21), to the synchronized beating of cilia (22). Apart from biological systems, there are several

examples where HIs play a crucial role in the organization (23–25) and dynamics (26–28) of micrometer-scale particles. When considering particles driven via a ratchet effect, the role of HIs has been often overlooked, giving more emphasis on other types of interactions such as steric (29), optic (30), electrostatic (31), or geometric (32) ones. Thus, understanding the role of HIs often hidden in such systems, although challenging, will shed light on novel physical effects that could occur in other soft or biological systems on similar length scales.

Here, we investigate the collective dynamics and the effect of HIs in a ratcheting colloidal system based on a magnetic traveling wave. We show that, by raising the particle density, these interactions modify the particle dynamics, leading to a series of emerging phenomena. These include a “speed-up” effect characterized by a substantial raise of the particle speed due to the resynchronization with the translating potential and a synchronized clustering during transport. In the latter case, we find a novel mechanism for cluster growth and morphology originated by the underlying symmetry of the substrate.

To elucidate the fundamental physical mechanisms in our system, we complement the experimental results with theory and numerical simulations.

RESULTS

The magnetic ratchet

Our driven colloidal system is based on a ferrite garnet film (FGF), which displays at zero applied field a pattern of parallel ferromagnetic domains with alternating up and down magnetization, and a spatial periodicity of $\lambda = 2.6 \mu\text{m}$ (Fig. 1A). On the surface of the FGF, the stray field generates a sinusoidal-like magnetic potential composed of a series of equispaced minima located at a distance λ . Above this platform, we deposit paramagnetic polystyrene microspheres with diameter $d = 2.8 \mu\text{m}$ and magnetic volume susceptibility $\chi \sim 0.4$ (Dynabeads M-270, Invitrogen). These particles are doped with nanoscale iron oxide grains, and they feature a paramagnetic behaviour acquiring an induced moment $\mathbf{m} = V\chi\mathbf{H}_{\text{tot}}$ under an external field \mathbf{H}_{tot} , where $V = (\pi d^3)/6$. Once above the film, the particles form a two-dimensional (2D) monolayer with negligible out-of-plane motion due to the magnetic attraction toward the Bloch

Copyright © 2022
The Authors, some
rights reserved;
exclusive licensee
American Association
for the Advancement
of Science. No claim to
original U.S. Government
Works. Distributed
under a Creative
Commons Attribution
NonCommercial
License 4.0 (CC BY-NC).

Downloaded from <https://www.science.org> on November 30, 2023

¹Departament de Física de la Matèria Condensada, Universitat de Barcelona, Barcelona, Spain. ²Universitat de Barcelona Institute of Complex Systems (UBICS), Universitat de Barcelona, Barcelona 08028, Spain. ³CECAM, Centre Européen de Calcul Atomique et Moléculaire, École Polytechnique Fédérale de Lausanne, Batochime, Avenue Forel 2, 1015 Lausanne, Switzerland. ⁴Institut de Nanociència i Nanotecnologia, IN²UB, Universitat de Barcelona, Barcelona, Spain.

*Corresponding author. Email: ptierno@ub.edu

†These authors contributed equally to this work.

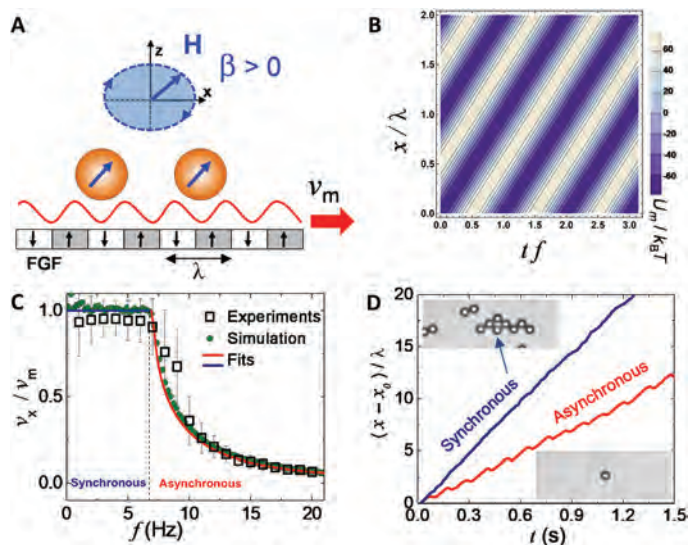


Fig. 1. The magnetic ratchet system. (A) Schematic of the magnetic traveling wave: A sinusoidal potential (wavelength $\lambda = 2.6 \mu\text{m}$) is generated above the surface of an FGF. The potential translates at a speed $v_m = \lambda f$ under the action of an elliptically polarized rotating field H with frequency f and ellipticity β . (B) Calculated energy landscape of one driven particle showing the time evolution of low (high) energy corridors in blue (white). (C) Normalized single-particle speed v_x versus frequency f from experiments (open symbols) and numerical simulation (filled symbols). Continuous lines are fit to the synchronous (blue) and sliding (red) regimes. (D) Normalized position $(x - x_0)/\lambda$ versus time t of a single particle (red line, bottom image) and a particle in a rhombic cluster (blue line, top image). In both cases, $f = 8 \text{ Hz}$ and $\beta = -0.4$, which corresponds to asynchronous regime for the individual particle, and x_0 is the position at time $t = 0 \text{ s}$. The movement of pair of particles in the asynchronous regime is shown in movie S1.

walls. Further details on the preparation of the FGF film are given in Materials and Methods.

We manipulate and transport the particles above the FGF by applying an external rotating field elliptically polarized in the (x, z) plane with frequency f

$$\mathbf{H}(t) \equiv [H_x \cos(2\pi ft) \mathbf{e}_x - H_z \sin(2\pi ft) \mathbf{e}_z] \quad (1)$$

Here, H_x, H_z are the amplitudes along the x, z axis, where $H_0 = \sqrt{(H_x^2 + H_z^2)}/2$ is the total amplitude. The elliptical polarization of the applied field is controlled by the parameter $\beta = (H_x^2 - H_z^2)/(H_x^2 + H_z^2)$, which will be used to tune the dipolar interactions. Here, $\beta > 0$ ($\beta < 0$) corresponds to $H_x > H_z$ ($H_x < H_z$), i.e., a higher in-plane (out-of-plane) field component. This time-dependent field modulates the stray magnetic field on the FGF surface and leads to a translating spatially periodic magnetic energy landscape, $U_m = -U_0 \cos\left[\frac{2\pi}{\lambda}(x - v_m t)\right]$ as shown in Fig. 1B. Here, U_0 is the potential amplitude (see later) and $v_m = \lambda f$ is the speed of the traveling wave. As a consequence of this modulation, the magnetic landscape transports colloidal particles that are trapped in its energy minima.

Figure 1C illustrates the main feature of the single-particle transport and combines experiments and simulation data (see later), demonstrating the quantitative agreement between both. By raising the driving frequency, we find two dynamic regimes, separated by a

critical frequency $f_c = 6.7 \text{ Hz}$. The first regime is a phase-locked motion ($f < f_c$) where the particle moves with the speed of the traveling wave, $v_x = v_m$. For $f > f_c$, the particle desynchronizes with the traveling wave (sliding regime), and its average speed decreases as $v_x = v_m(1 - \sqrt{1 - f_c^2/f^2}) < v_m$ (Fig. 1C). In the latter regime, the traveling wave becomes too fast and the loss of synchronization results from the viscous drag that overcomes the magnetic driving. As we are interested in the collective resynchronization effect due to HIs, we drive our particles above f_c , fix for all experiments the total amplitude $H_0 = 850 \text{ A m}^{-1}$, and vary mainly β and the normalized surface density $\tilde{\rho} = N\pi(d/2)^2/A$, where N is the number of particles located in area A . An illustrative example of the difference between synchronous and asynchronous regimes is shown in Fig. 1D (see also movie S1), which shows the evolution of the position along the driving direction for a single particle and a particle in a rhombic-like cluster. In both cases, the driving frequency is $f = 8 \text{ Hz}$ ($\beta = -0.4$) so that the position of the individual particle (image at the bottom) displays a series of characteristic oscillations due to the loss of synchronization with the traveling wave. These small delay leads to a reduction of the mean speed and thus of the slope. As we will discuss in the next section, we find that a particle in a cluster displays a speed-up effect for frequencies $f > f_c$ that enhances synchronization with the traveling wave, reaching a maximum speed equal to v_m .

Particle interaction and speed-up

Above the FGF, the paramagnetic colloids interact mainly via dipolar forces and HIs. The first types of interactions (we come back to HIs later) can be tuned by varying the parameter β (33). For two particles above the FGF plane, the threshold ellipticity that separates the dipolar interactions from attractive to repulsive is given by $\beta_c = -1 + 2/(3 \cos^2 \vartheta)$, where ϑ is the polar angle that connects the x axis with the distance r between the particle centers. As shown in Fig. 2A, when particles are aligned along the x axis ($\vartheta = 0$), magnetic attraction (repulsion) arises for $\beta > -1/3$ ($\beta < -1/3$), and close to $\beta_c = -1/3$, such interactions are minimized. This dependence of dipolar interactions on β allows to manifest the effect of HIs in both attractive and repulsive scenarios.

Figure 2B shows the results of a series of experiments where we systematically vary the surface density $\tilde{\rho}$ and measure the collective particle speed along the driving direction (x), \bar{v}_x , for different values of β , all in the asynchronous regime ($f = 8 \text{ Hz} > f_c$). We find that for $\tilde{\rho} > 0.2$, the colloidal particles resynchronize with the traveling wave reaching the maximum speed of $v_m = 20.8 \mu\text{m s}^{-1}$, much higher than that of a single particle, for example, $v_x = 7 \mu\text{m s}^{-1}$ for all $\beta > 0$. This remarkable speed-up effect is rather robust, spanning a wide range of densities $\tilde{\rho} \in [0.2, 0.65]$. Further, this speed-up is observed for both attractive and repulsive dipolar interactions $\beta \in [-0.6, 0.6]$, which leads us to exclude magnetic dipolar interactions as the main reason for the observed resynchronization. Collective velocities of the order $\bar{v}_x \in [6, 20.8] \mu\text{m s}^{-1}$ correspond to relatively large Péclet numbers $Pe \in [84, 291]$; thus, the generated hydrodynamic flow becomes progressively more important and must inevitably affect the particle motion. Here, we calculate the Péclet number Pe as the ratio between the Brownian time τ_B required by the particle to diffuse its own radius and the driven time τ_D required to move its radius due to the magnetic landscape. Here, $\tau_D = d^2/(4D_{\text{eff}})$, where $D_{\text{eff}} = 0.14 \mu\text{m}^2 \text{ s}^{-1}$ is the effective diffusion coefficient of the paramagnetic colloid, and $\tau_D = d/(2v_x)$. We further note that for $\beta > 0.2$, the collective speed

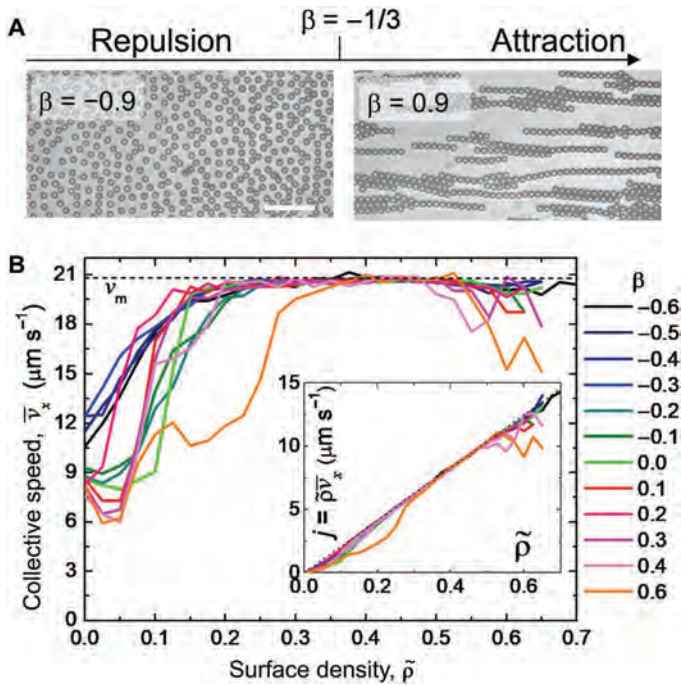


Fig. 2. Experimental current density diagram. (A) Experimental images showing translating repulsive particles ($\beta = -0.9 < 1/3$) and chains ($\beta = 0.9 > 1/3$) in the sliding regime with $f = 8$ Hz. Scale bar, $20 \mu\text{m}$ (left). See also corresponding movies S2 and S3. (B) Collective particle speed \bar{v}_x versus normalized surface density $\tilde{\rho}$ for different values of β . Dashed line corresponds to $v_m = 20.8 \mu\text{m s}^{-1}$. Inset shows the corresponding linear raise of the particle flux $j = \tilde{\rho} \bar{v}_x$ versus $\tilde{\rho}$.

decreases at large densities, $\tilde{\rho} > 0.5$ (Fig. 2B). In this situation, the strong dipolar forces induce the formation of elongated and compact trains (Fig. 2A, right), where HIs are weakened because of the reduced space between the particles. In this situation, the chains recover the asynchronous regime and the system displays an overall reduction of the average speed. We note that in our system, we never observe a reverse of the particle current due to the spatial symmetry of the translating periodic potential. However, a current reversal could be realized by either preparing a special magnetic modulation that would produce a spatially asymmetric potential (34) or adding a bias force against the flow that would tilt the potential.

DISCUSSION

Numerical simulation

The emerging dynamics observed in our driven colloidal system result from the combined action of different interactions, including magnetic dipolar and hydrodynamics ones. To understand their relative role in the system, we perform Brownian dynamic simulations (see Fig. 1C). For each particle i at position \mathbf{r}_i , we integrate the overdamped equation of motion

$$\gamma \frac{d\mathbf{r}_i}{dt} = \mathbf{F}_i^{\text{ext}} + \sum_{j \neq i} \mathbf{F}_i^{\text{dip}} + \sum_{j \neq i} \mathbf{F}_i^{\text{int}} + \gamma \mathbf{v}_i^H + \xi \quad (2)$$

where γ is the friction coefficient, $\mathbf{F}_i^{\text{ext}}$ is the external driving force resulting from the traveling wave, $\mathbf{F}_i^{\text{dip}}$ is the total force due to magnetic dipolar interactions, $\mathbf{F}_i^{\text{int}}$ accounts for the steric force with the rest of the particles, and ξ is a Gaussian white noise. These forces

reproduce the isolated particle experimental speed, as shown in Fig. 1C. More details on $\mathbf{F}_i^{\text{ext}}$, $\mathbf{F}_i^{\text{dip}}$, and $\mathbf{F}_i^{\text{int}}$ and the parameters used are given in Materials and Methods. To model HIs, we assume that the particles are embedded in a solvent and dragged by the fluid flow of velocity \mathbf{v}_i^H , generated by the net force acting on the rest of the suspended particles, $\mathbf{F}_i(\mathbf{r}_i) = \mathbf{F}_i^{\text{ext}}(\mathbf{r}_i) + \sum_{j \neq i} [\mathbf{F}_{ij}^{\text{dip}}(\mathbf{r}_{ij}) + \mathbf{F}_{ij}^{\text{int}}(\mathbf{r}_{ij})]$. We account for this effect with

$$\mathbf{v}_i^H = \sum_{j \neq i}^N \mathbf{G}_{ij}(\mathbf{r}_i, \mathbf{r}_j) \mathbf{F}_j(\mathbf{r}_j) \quad (3)$$

where $\mathbf{G}_{ij}(\mathbf{r}_i, \mathbf{r}_j)$ stands for the Blake-Oseen mobility tensor (35), which considers the effect of the close proximity of the substrate in the far-field approximation. Last, ξ represents a random force due to thermal fluctuation, with zero mean, $\langle \xi \rangle = 0$, and delta correlated, $\langle \xi(t) \xi(t') \rangle = 2k_B T \gamma \delta(t - t')$.

By integrating Eq. 2, we find that the quantitative agreement with the experimental data can be obtained only by including HIs, even in the absence of dipolar forces. As a representative case, we show in Fig. 3A the collective speed \bar{v}_x for $\beta = -0.3$, where dipolar interactions are slightly repulsive. If we disregard the induced flow, $\mathbf{v}_i^H \approx 0$, and account only for steric and/or magnetic dipolar interactions, the average colloidal speed decreases with the particle density, $\tilde{\rho}$, in contrast to the experimental observations. We note that at large densities, we identify numerically the transition to the asynchronous regime when $\bar{v}_x \sim 0.95 v_m$. When magnetic interactions are weak ($\beta = -0.3$), increasing $\tilde{\rho}$ raises the speed-up effect and thus f_c due to the hydrodynamic coupling between the particles. The effect is such that at $\tilde{\rho} = 0.6$, the new critical frequency $f_c = 10.3$ Hz almost doubles that of a single particle (see Fig. 3B, bottom line). Increasing the magnetic coupling instead reduces the speed-up effect: For attractive interactions ($\beta > -0.3$), the formation of chain weakens HIs, reducing the net particle speed. In the repulsive case ($\beta < -0.3$), particles are forced to span a larger region and this reduces both the hydrodynamic coupling and f_c , as shown in Fig. 3B (top line). We also note that commensurability between the particle size and the wavelength of the underlying pattern in 1D is also important for the synchronization with the moving landscape. By running the simulation along 1D with particles larger than λ , we find that full synchronization was not achieved in opposition to our 2D experimental setup. Thus, a smaller diameter allows the particles to be accommodated in consecutive minima and to be more easily driven by the magnetic landscape.

Theoretical model

To explain the observed synchronization effect, we consider a pair of aligned colloids displacing perpendicular to the FGF and take into account the interplay between the external potential and the HIs. We assume negligible thermal noise and start from the overdamped equation of motion of one particle i

$$\gamma \dot{x}_i = F^e(x, t) + \gamma v_i^H \quad (4)$$

where the force due to the magnetic potential on such particle at position x_i is

$$F^e(x_i, t) = -16 \frac{U_0 H}{\lambda M_s} e^{-2\pi z_0/\lambda} \sin \left[2\pi \left(\frac{x_i}{\lambda} - ft \right) \right] \quad (5)$$

Here, z_0 is the particle elevation fixed by the balance between gravity and steric repulsion from the solid substrate, $U_0 = \pi d^3 \chi \mu_0 M_s^2 / 6$ is the characteristic magnetic energy, μ_0 is the vacuum permeability,

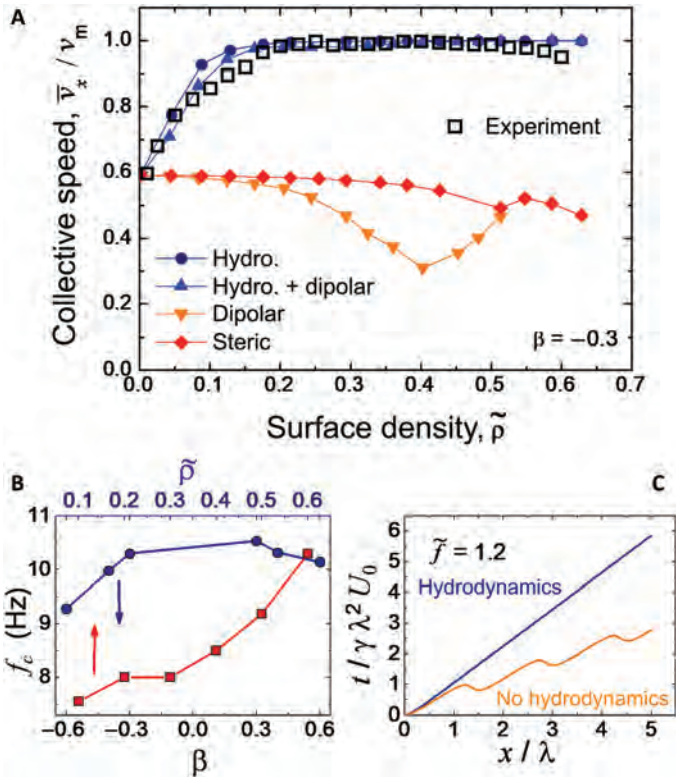


Fig. 3. Experiment and simulation results. (A) Normalized collective speed \bar{v}_x versus surface density $\tilde{\rho}$ from experiments, empty squares ($\beta = -0.3$ and $f = 8 \text{ Hz} > f_c$), and numerical simulation (Eq. 2) with HIs (filled circles), hydrodynamic and dipolar interactions (upper triangles), only dipolar interactions (lower triangles), and only steric interactions (diamonds). (B) Simulations: Critical frequency f_c versus surface density $\tilde{\rho}$ (squares) field ellipticity β (circles) for $\beta = -0.3$ ($\tilde{\rho} = 0.6$). (C) Numerical integration of Eq. 9 with and without hydrodynamics for $\tilde{f} = 1.2$.

and $M_s = 1.3 \cdot 10^4 \text{ A m}^{-1}$ is the saturation magnetization of the FGF film (36). We rewrite the equation of motion by rescaling length and time with λ and $\gamma\lambda^2/U_0$, respectively, and moving to the reference frame of the traveling wave via the change of variables $q(t) = -x(t)/\lambda + ft$

$$\dot{q}_i(t) = \tilde{f} - \tilde{f}_c \left[\sin [2\pi q_i] + \frac{3d}{8\lambda} \sum_{j \neq i}^N \tilde{G}(q_i, q_j) \sin [2\pi q_j] \right] \quad (6)$$

where $\tilde{G}(q_i, q_j) = 8\pi\eta\lambda \mathbf{e}_x \cdot \mathbf{G}(q_i, q_j) \cdot \mathbf{e}_x$, and we have introduced the dimensionless parameters $\tilde{f}_c \equiv 16H_0 e^{-2\pi z_0}/M_s$ and $\tilde{f} \equiv f\gamma\lambda^2/U_0$, where $\gamma = 3\pi\eta d$ is the viscous friction in a medium of viscosity η . We note that the essence of the role played by the hydrodynamic coupling is captured already with the Oseen tensor; the substrate contributes quantitatively to the ratio \tilde{f}_h/\tilde{f}_c . For the Oseen-Blake tensor

$$\tilde{G}(q_i, q_j) = \frac{2}{\Delta_{ij}} \left[1 - \frac{1 + \epsilon_{ij} + \frac{3}{4}\epsilon_{ij}^2}{(1 + \epsilon_{ij})^{5/2}} \right] \quad (7)$$

where $\Delta_{ij} \equiv |q_i - q_j|$ and $\epsilon_{ij} \equiv \left(\frac{2h}{\Delta_{ij}}\right)^2$, while for the Oseen tensor, $\tilde{G}(q_i, q_j) = \frac{2}{\Delta_{ij}}$. In Eq. 6, the contribution of the HIs appears from the second term in the right hand side, while in the absence of HIs, we obtain the single-particle behavior characterized in Fig. 1C. In this case, the solution $\dot{q} = 0$ is only possible when $\tilde{f} < \tilde{f}_c$, where the

particle is synchronized with the traveling wave. To analyze the impact of HIs, for simplicity, we assume that the particles are equidistantly distributed above the traveling wave with periodicity λ , which allows factorizing Eq. 6 as

$$\dot{q}_i(t) = \tilde{f} - \tilde{f}_c \sin [2\pi q_i] \left[1 + \frac{3d}{8\lambda} \sum_{j \neq i}^N \tilde{G}(q_i, q_j) \right] \quad (8)$$

Synchronous motion, $\dot{q} = 0$, occurs when $\sin [2\pi q_i] = \tilde{f}/\tilde{f}_c \left[1 + \frac{3d}{8\lambda} \sum_{j \neq i}^N \tilde{G}(q_i, q_j) \right]$, which is allowed for frequencies $\tilde{f} < \tilde{f}_h \equiv \tilde{f}_c \left[1 + \frac{3d}{8\lambda} \sum_{j \neq N/2}^N \tilde{G}(q_{N/2}, q_j) \right]$. Since $\tilde{G}(q_i, q_j) > 0$, $\tilde{f}_h > \tilde{f}_c$, HIs increase the frequency range where the synchrony with the traveling wave is sustained. In particular, HIs displace the critical frequency of an amount $\delta\tilde{f} = \tilde{f}_h - \tilde{f}_c$, which increases with the number N of colloidal particles. The confinement due the solid substrate decreases \tilde{f}_h monotonously as the colloids approach the wall; at contact, $\delta\tilde{f} = 0$.

We further note that the momentum exchange with the substrate can alter qualitatively the range of frequencies over which the synchronization is sustained. For example, \tilde{f}_h doubles its magnitude when the colloids come into contact with a slip substrate with respect to its magnitude in an unbounded medium. For a slip planar interface, we find that the Oseen-Blake tensor is given by $\tilde{G}(q_i, q_j) = \frac{2}{\Delta_{ij}} \left[1 + \frac{1}{(1 + \epsilon_{ij})^{1/2}} \right]$.

Colloidal synchronization and assembly

The hydrodynamic-induced synchronization is due to the net drag generated by the flow of the rest of the colloidal particles as they are propelled by the magnetic traveling wave. The underlying mechanism is already apparent when analyzing the motion of a pair of driven colloids, where Eq. 8 reduces to

$$\dot{q}_i = \tilde{f} - \tilde{f}_c \sin [2\pi q_i] - \tilde{f}_c \frac{F_h \sin [2\pi q_j]}{|q_i - q_j|}, i, j = 1, 2 (i \neq j) \quad (9)$$

with $F_h = 3d/4\lambda$ the normalized strength of the HIs, and where, for simplicity, we disregard the effect of the substrate. Accordingly, in this case, $\tilde{G}(q_i, q_j) = \frac{2}{|q_i - q_j|}$ and a pair of particles a distance Δ away will displace synchronously up to $\tilde{f}_h = \tilde{f}_c(1 + F_h/\Delta)$. Figure 3C shows the trajectories for two colloids initially at a distance equal to $\Delta = \lambda$, for which $\tilde{f}_h/\tilde{f}_c = 3/2$. Above \tilde{f}_c , the colloids slip with respect to the underlying moving substrate in the absence of HI, while they move synchronously due to the additional hydrodynamic drag until \tilde{f}_h .

Equation 9 not only shows that already a pair of particles produces hydrodynamic synchronization but also suggests a growing mechanism for colloidal clusters. Aggregates formed by synchronized particles travel faster than asynchronous colloids. After a collision, the particles attach to the synchronous cluster and increase their velocity to lock with the traveling wave. We can also apply our model to other driven colloidal systems that display HIs. For example, Lutz *et al.* (37) reported that optically trapped colloids subjected to a constant force on a toroidal potential display a speed enhancement due to HIs. As shown in the Supplementary Materials, if we apply our model to such situation, we find that HIs lead to an increase of the particle velocity, but only when the particles surmount the energetic barrier of the optical potential.

HIs also play a determinant role in the emerging colloidal morphologies. When $\beta > -1/3$, attractive dipolar interactions induce

chain formation along the direction of motion, x , due to the effective repulsion that the particles experience when moving transversally. However, we experimentally observe that, up to $\beta \sim 0.7$, the particles self-assemble into traveling clusters with a characteristic rhombic-like ordering spanning both directions; a typical case is shown in Fig. 4A with $\beta = 0.4$.

We characterize the aggregation process in terms of the cluster variance along the driving direction, $\sigma_x = \frac{1}{N_c} \sum_{i=1}^{N_c} (x_{cm} - x_i)^2$, where x_{cm} is the center of mass and N_c is the number of particles in the cluster. Figure 4C displays σ_x , normalized by σ_t , the latter being the variance of a perfect chain, when N_c particles are in close contact moving along a straight line. In the absence of HIs, $\sigma_x/\sigma_t \sim 1$ for most of the cluster length, which corresponds to the situation depicted in Fig. 4D. Similarly, as shown in the inset of Fig. 4B, the cluster anisotropy parameter $\phi = |\sigma_x - \sigma_y| / (\sigma_x + \sigma_y)$ is maximal in absence of HIs, while it vanishes by increasing N_c with HIs. These results highlight that, in the presence of a periodic substrate, HIs and dipolar forces promote the formation of colloidal aggregates, with sizes and symmetries not allowed on a simple plane.

The rhombic-like ordering results from the competition between the size of the colloidal particles and the periodicity of the magnetic landscape, in the presence of dipolar and HIs. Dipolar interactions attract particles and set them in contact at a distance d . HIs synchronize

the particles at a distance λ along the driving direction (x). Thus, particles at close contact have a transverse distance $l_d = \sqrt{d^2 - \lambda^2}$ (see small inset in Fig. 4B). Thus, the contribution of HIs to the cluster morphology consists of a drag force that synchronizes particles, placing them at a characteristic distance λ along the x direction. In the experimental system, we find that the ratio $d/\lambda = 0.92$, which sets a transversal length between particles in the cluster of $l_d \approx 0.28$. Now, decreasing the ratio d/λ gives a larger transversal length and a larger area covered by the clusters along the transverse direction. In contrast, increasing d/λ to unity leads to the formation of synchronized particles that travel in the form of trains of particles. In such case, even at large $\beta > 0$, the synchronicity with the traveling wave is not lost due to the presence of HIs. We further note that rhombic ordering is reminiscent of the equilibrium structure predicted for 2D colloidal systems, with interactions that compete with the symmetry of an underlying substrate (38). However, the morphologies we observe develop from the interplay between the ratchet potential coupled to HIs and the magnetic dipolar interactions, as unveiled by our numerical simulations in Fig. 4B. The exclusion of HIs by setting $\mathbf{v}_i^H = 0$ leads to the formation of traveling chains, as shown in Fig. 4C.

To conclude, we have investigated the role of HIs on the collective dynamics of microscopic particles driven above a translating magnetic

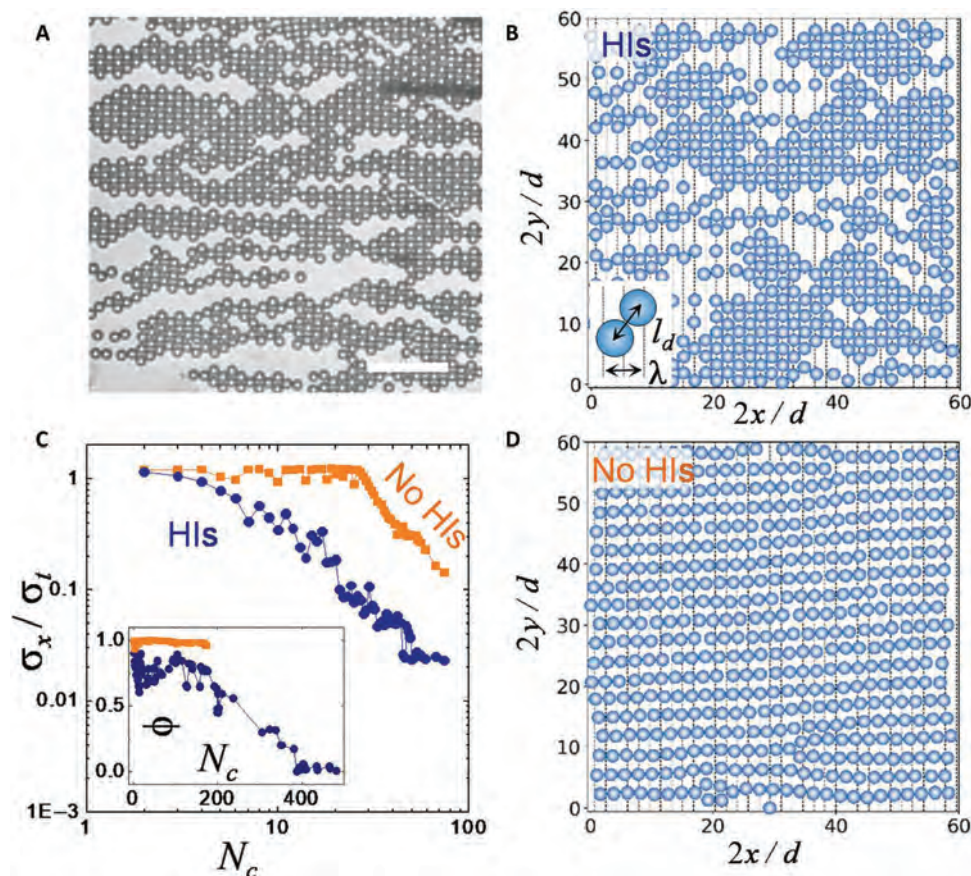


Fig. 4. Collective propulsion and assembly. Experimental (A) and simulation (B and D) snapshots of anisotropic clusters propelled by a rotating field with $\beta = 0.4$. Scale bar, $20 \mu\text{m}$ (A). Bottom scheme in (B) illustrates the transverse distance l_d . See movie S4. In (B) [(D)], the simulation was run with [without] HIs. (C) Simulations: Relative cluster dispersion σ_x/σ_t versus number of particles in the cluster N_c with (blue) and without (orange) HIs. Inset shows the corresponding cluster anisotropy ratio $\phi = |\sigma_x - \sigma_y| / (\sigma_x + \sigma_y)$ versus N_c .

potential. We find that such interactions lead to a substantial raise of the particle speed and favor colloidal arrangements congruent with the periodicity of the underlying substrate. We experimentally observe that such arrangement promotes the emergence of compact rhombic clusters along the potential domains. We rationalize the experimental observations with both theory and numerical simulations. Thus, our system leads to a variability of the morphology of synchronized clusters due to the interplay between the substrate symmetry, hydrodynamic, and dipolar interactions.

Traveling wave ratchets where directed transport is achieved via a sliding periodic potential are present in several soft and condensed matter systems. Examples with microscopic colloids, apart from our garnet film, include electrophoretic (39) or magnetically (40) driven particles above patterned substrates, and in other field include active particles (41), chemotactic fronts (42), defects and asperities in frictional sliding (43), or magnetic flux quanta (44). Thus, with our work, we investigate the role of the dispersing media on the collective particle dynamics and show that it can lead to unexpected phenomena, which could have been overlooked in similar ratchet systems at high density. We also mention that recently, Belovs *et al.* (45) reported numerically the synchronization of puller type magnetotactic bacteria under a rotating magnetic field. This work confirms the general nature of the phenomena of synchronization due to HIs (46, 47), which we have experimentally observed here with a driven ratchet system.

Ratchet transport schemes have been invoked as simplified models to explain the complex dynamics that occur in many physical and biological systems (48), including micro- and nanomachines (49–52), intracellular transport (53, 54), and even as a way to rectify active matter (55–58). With our colloidal model system, we show the importance of considering HIs and their crucial role in the collective organization of driven microscopic matter.

MATERIALS AND METHODS

Magnetic film and coating

The FGF was grown by dipping liquid-phase epitaxy on a gadolinium gallium garnet substrate; more details can be found in a previous work (59). Before the experiments, we coat the FGF film with a 1-μm-thick layer of a photoresist (AZ-1512 Microchem, Newton, MA) to prevent adhesion of the paramagnetic particles on the substrate. This process was performed via combination of spin coating and backing, following previous work (60). We wash the FGF in highly deionized water (MilliQ, Millipore) before each experiment.

Details of the numerical simulation

In our simulation scheme, we integrate the set of Eq. 2 where the remaining terms on the right hand side, apart from the fourth one (HIs), are described below. The external driving force that is produced by the traveling wave (36) is given by

$$\mathbf{F}^{\text{ext}}(x, t) = F_M \left[u_1(t) \sin\left(\frac{2\pi x}{\lambda}\right) - u_2(t) \cos\left(\frac{2\pi x}{\lambda}\right) \right] \mathbf{e}_x \quad (10)$$

where $u_1(\beta, t) = \sqrt{1 + \beta} \cos(2\pi ft)$, $u_2(\beta, t) = \sqrt{1 - \beta} \cos(2\pi ft)$, and $F_M = 16H_0 e^{-2\pi z} U_0 / M_s \lambda$.

$\mathbf{F}_i^{\text{dip}}$ is the dipolar interaction between the paramagnetic particles. For two point dipoles ($\mathbf{m}_i, \mathbf{m}_j$) located at position (i, j), it is given by

$$\mathbf{F}^{\text{dip}}(\mathbf{r}_{ij}) = \frac{3\mu_0}{4\pi |\mathbf{r}_{ij}|^4} ((\hat{\mathbf{e}}_{ij} \times \mathbf{m}_i) \times \mathbf{m}_j + (\hat{\mathbf{e}}_{ij} \times \mathbf{m}_j) \times \mathbf{m}_i) - 2\hat{\mathbf{e}}_{ij}(\mathbf{m}_i \cdot \mathbf{m}_j) + 5\hat{\mathbf{e}}_{ij}((\hat{\mathbf{e}}_{ij} \times \mathbf{m}_i) \cdot (\hat{\mathbf{e}}_{ij} \times \mathbf{m}_j)) \quad (11)$$

where $\hat{\mathbf{e}}_{ij}$ is the unitary vector between particle i and j , $\mathbf{r}_{ij} = \mathbf{r}_i - \mathbf{r}_j$, and $\mu_0 = 4\pi \cdot 10^{-7}$ H m. Further, we consider induced point dipoles; thus, for a particle i , the magnetic moment is given by $\mathbf{m}_i = V\chi \mathbf{H}_{\text{tot}}(\mathbf{r}_i)$, where the instantaneous total magnetic field is given by the sum of the external magnetic field and the contribution from the FGF film, $\mathbf{H}^{\text{tot}} = \mathbf{H} + \mathbf{H}^{\text{sub}}$, i.e.

$$\mathbf{H}^{\text{tot}} = (H_x \cos(2\pi ft), 0, -H_z \sin(2\pi ft)) + \frac{4M_s}{\pi} e^{-2\pi z/\lambda} \left(\cos\left(\frac{2\pi x t}{\lambda}\right), 0, -\sin\left(\frac{2\pi x t}{\lambda}\right) \right) \quad (12)$$

Further, $\mathbf{F}_i^{\text{int}}$ is the interaction force between the particles that we derive from a Yukawa-like potential, which accounts for both a short-range repulsion due to electrostatic interactions and the finite particle size. The force between two particles at positions \mathbf{r}_i and \mathbf{r}_j can be written as

$$\mathbf{F}^{\text{int}}(\mathbf{r}_{ij}) = \frac{U_Y}{\lambda_Y} \sum_{i \neq j}^N \left[\frac{\sigma}{r_{ij}} \left(\frac{\sigma}{r_{ij}} + \frac{\sigma}{\lambda_Y} e^{-\frac{r_{ij}}{\lambda_Y}} \right) - B \right] \mathbf{e}_{ij} \quad (13)$$

The parameter U_Y quantifies the strength, and λ_Y the characteristic decay length of the Yukawa potential between the interaction of a pair of particles, and $\sigma = d/2$ denotes the radius of the particles. The parameter B is a constant ensuring that the force is zero at the cutoff interaction radius r_c

$$B = \frac{\sigma}{r_c} e^{-\frac{r_c}{\lambda_Y}} \left(\frac{\sigma}{\lambda_Y} + \frac{\sigma}{r_c} \right) \quad (14)$$

Last, ξ represents a random force due to thermal fluctuation, with zero mean, $\langle \xi \rangle = 0$, and delta correlated, $\langle \xi(t) \xi(t') \rangle = 2k_B T \gamma \delta(t - t')$.

To minimize the number of parameters used in the numerical simulation, we rescale length in terms of the radius of the particles $\sigma = d/2$, time in terms of $\tau_D = \gamma d / (2F_M)$, and the magnetic field components in terms of the amplitude H_0 . Thus, Eq. 2 can be divided by the characteristic velocity F_M/γ , and Eq. 11 in this dimensional units reduces to

$$\bar{\mathbf{F}}^{\text{dip}} = \frac{F^d}{|\bar{\mathbf{r}}_{ij}|^4} f(\bar{\mathbf{r}}_{ij}, h^{\text{tot}}(\bar{\mathbf{r}}_i), h^{\text{tot}}(\bar{\mathbf{r}}_j)) \quad (15)$$

where F^d is the dipolar strength $F^d = \frac{3\mu_0}{F_M \mu_0 4\pi} (V\chi)^2$ and $f(\bar{\mathbf{r}}_{ij}, h^{\text{tot}}(\bar{\mathbf{r}}_i), h^{\text{tot}}(\bar{\mathbf{r}}_j))$ is a function that contains the dependences in Eq. 11 involving only the total magnetic field contributions on each particle and the unit vector between two particles. Further, we use a radius of $r_d \approx 4.5\sigma$ as dipolar cutoff radius is defined, which corresponds to a distance large enough so that contributions of the dipolar interactions are of the order $|\bar{\mathbf{F}}^{\text{dip}}| \approx 0.05$. As the dipolar force depends not only on distance but also on the joining direction between two particles, the force is imposed to be 0 at r_d using

$$\bar{\mathbf{F}}^{\text{dip}} = F^d \left(\frac{f(\hat{\mathbf{r}}_{ij}, h_i, h_j)}{|\bar{\mathbf{r}}_{ij}|^4} - \frac{f(\hat{\mathbf{r}}_{ij}, h_i, h_j)}{|r_d|^4} \right) \quad (16)$$

Equation 2 can be finally rewritten in reduced units as

$$\frac{d\bar{\mathbf{r}}_i}{dt} = \frac{U_Y}{\lambda_Y F_M} \sum_{j \neq i} \bar{\Psi}(\bar{\mathbf{r}}_{ij}) + \bar{\mathbf{F}}^{\text{ext}}(\bar{x}_i, \bar{t}) + \bar{\mathbf{F}}^{\text{dip}}(\bar{\mathbf{r}}_{ij}, h_i, h_j) + \frac{1}{F_M} \frac{3}{4} \sum_{j \neq i} \bar{\mathbf{G}}_{ij}(\bar{\mathbf{r}}_i, \bar{\mathbf{r}}_j) \bar{\mathbf{F}}(\bar{\mathbf{r}}_j) + \sqrt{\frac{2}{Pe}} \frac{\tau_D}{dt} \bar{\xi} \quad (17)$$

Here, $\bar{\mathbf{r}} = \mathbf{r}/\sigma$, $\mathbf{G}(\mathbf{r}_i, \mathbf{r}_j) = \frac{3}{4\gamma} \bar{\mathbf{G}}(\bar{\mathbf{r}}_i, \bar{\mathbf{r}}_j)$, and Pe is the Péclet number. In turn, $\bar{\Psi} = \Psi(\bar{\mathbf{r}}_{ij})$ is the dimensionless Yukawa force between particles i and j .

As typical experimental values, we use $\gamma = 2.6 \times 10^{-8} \text{ m N}^{-1} \text{ s}^{-1}$ and $F_M = 0.1 \text{ pN}$. The simulation parameters are estimated to be $h_{\text{sub}} = 15.3$, $F^d = 56.1$, Yukawa force strength $U_0/\lambda F_M = 300$, $Pe = 150$, and $\lambda_Y = 1$. Further, comparing the simulations for a single particle and the experiments (Fig. 1C) as a function of the frequency, we can estimate the characteristic time as $\tau_D = 0.075 \text{ s}$.

SUPPLEMENTARY MATERIALS

Supplementary material for this article is available at <https://science.org/doi/10.1126/sciadv.abo4546>

REFERENCES AND NOTES

- S. Matthias, F. Müller, Asymmetric pores in a silicon membrane acting as massively parallel Brownian ratchets. *Nature* **424**, 53–57 (2003).
- M. J. Skaug, C. Schwemmer, S. Fringes, C. D. Rawlings, A. W. Knoll, Nanofluidic rocking Brownian motors. *Science* **359**, 1505–1508 (2018).
- I. U. Vakarelski, N. A. Patankar, J. O. Marston, D. Y. C. Chan, S. T. Thoroddsen, Stabilization of Leidenfrost vapour layer by textured superhydrophobic surfaces. *Nature* **489**, 274–277 (2012).
- S. Feng, P. Zhu, H. Zheng, H. Zhan, C. Chen, J. Li, L. Wang, X. Yao, Y. Liu, Z. Wang, Three-dimensional capillary ratchet-induced liquid directional steering. *Science* **373**, 1344–1348 (2021).
- H. Mazal, M. Iljina, I. Riven, G. Haran, Ultrafast pore-loop dynamics in a AAA+ machine point to a Brownian-ratchet mechanism for protein translocation. *Sci. Adv.* **7**, eabg4674 (2021).
- R. D. Astumian, Thermodynamics and kinetics of a Brownian motor. *Science* **276**, 917–922 (1997).
- D. Keller, C. Bustamante, The mechanochemistry of molecular motors. *Biophys. J.* **78**, 541–556 (2000).
- J. W. McCausland, X. Yang, G. R. Squyres, Z. Lyu, K. E. Bruce, M. M. Lamanna, B. Söderström, E. C. Garner, M. E. Winkler, J. Xiao, J. Liu, Treadmilling FtsZ polymers drive the directional movement of spG-synthesis enzymes via a Brownian ratchet mechanism. *Nat. Commun.* **12**, 609 (2021).
- P. Reimann, Brownian motors: Noisy transport far from equilibrium. *Phys. Rep.* **361**, 57–265 (2002).
- P. Hänggi, F. Marchesoni, Artificial Brownian motors: Controlling transport on the nanoscale. *Rev. Mod. Phys.* **81**, 387–442 (2009).
- J. Rousselet, L. Salome, A. Ajdari, J. Prost, Directional motion of Brownian particles induced by a periodic asymmetric potential. *Nature* **370**, 446–447 (1994).
- L. P. Faucheux, L. S. Bourdieu, P. D. Kaplan, A. J. Libchaber, Optical thermal ratchet. *Phys. Rev. Lett.* **74**, 1504–1507 (1995).
- K. Gunnarsson, P. E. Roy, S. Felton, J. Pihl, P. Svedlindh, S. Berner, H. Lidbaum, S. Oscarsson, Programmable motion and separation of single magnetic particles on patterned magnetic surfaces. *Adv. Mater.* **17**, 1730–1734 (2005).
- B. Yellen, O. Hovorka, G. Friedman, Arranging matter by magnetic nanoparticle assemblers. *Proc. Natl. Acad. Sci. U.S.A.* **102**, 8860–8864 (2005).
- A. Ros, R. Eichhorn, J. Regtmeier, T. T. Duong, P. Reimann, D. Anselmetti, Absolute negative particle mobility. *Nature* **436**, 928 (2005).
- S.-H. Lee, K. Ladavac, M. Polin, D. G. Grier, Observation of flux reversal in a symmetric optical thermal ratchet. *Phys. Rev. Lett.* **94**, 110601 (2005).
- J. Frank, R. K. Agrawal, A ratchet-like inter-subunit reorganization of the ribosome during translocation. *Nature* **406**, 318–322 (2000).
- C. C. de Souza Silva, J. V. de Vondel, M. Morelle, V. V. Moshchalkov, Controlled multiple reversals of a ratchet effect. *Nature* **440**, 651–654 (2006).
- C. J. O. Reichhardt, C. Reichhardt, Ratchet effects in active matter systems. *Annu. Rev. Condens. Matter. Phys.* **8**, 51–75 (2017).
- S. Park, J. Song, J. S. Kim, In silico construction of a flexibility-based DNA Brownian ratchet for directional nanoparticle delivery. *Science* **5**, eaav4943 (2019).
- I. H. Riedel, K. Kruse, J. Howard, A self-organized vortex array of hydrodynamically entrained sperm cells. *Science* **309**, 300–303 (2005).
- A. Vilfan, F. Jülicher, Hydrodynamic flow patterns and synchronization of beating cilia. *Phys. Rev. Lett.* **96**, 058102 (2006).
- M. Baron, J. Bławdziewicz, E. Wajnryb, Hydrodynamic crystals: Collective dynamics of regular arrays of spherical particles in a parallel-wall channel. *Phys. Rev. Lett.* **100**, 174502 (2008).
- Y. Goto, H. Tanaka, Purely hydrodynamic ordering of rotating disks at a finite Reynolds number. *Nat. Commun.* **6**, 5994 (2015).
- K. Yeo, E. Lushi, P. M. Vlahovska, Collective dynamics in a binary mixture of hydrodynamically coupled microrotors. *Phys. Rev. Lett.* **114**, 188301 (2015).
- T. M. Squires, M. P. Brenner, Like-charge attraction and hydrodynamic interaction. *Phys. Rev. Lett.* **85**, 4976–4979 (2000).
- J. Santana-Solano, J. L. Arauz-Lara, Hydrodynamic interactions in quasi-two-dimensional colloidal suspensions. *Phys. Rev. Lett.* **87**, 038302 (2001).
- A. Grimm, H. Stark, Hydrodynamic interactions enhance the performance of Brownian ratchets. *Soft Matter* **7**, 3219–3227 (2011).
- P. K. Ghosh, V. R. Misko, F. Marchesoni, F. Nori, Self-propelled janus particles in a ratchet: Numerical simulations. *Phys. Rev. Lett.* **110**, 268301 (2013).
- A. V. Arzola, M. Villasante-Barahona, K. Volke-Sepúlveda, P. Jákl, P. Zemánek, Omnidirectional transport in fully reconfigurable two dimensional optical ratchets. *Phys. Rev. Lett.* **118**, 138002 (2017).
- C. Marquet, A. Buguin, L. Talini, P. Silberzan, Rectified motion of colloids in asymmetrically structured channels. *Phys. Rev. Lett.* **88**, 168301 (2002).
- B. H. Wunsch, J. T. Smith, S. M. Gifford, C. Wang, M. Brink, R. L. Bruce, R. H. Austin, G. Stolovitzky, Y. Astier, Nanoscale lateral displacement arrays for the separation of exosomes and colloids down to 20 nm. *Nat. Nanotechnol.* **11**, 936–940 (2016).
- A. V. Straube, P. Tierno, Tunable interactions between paramagnetic colloidal particles driven in a modulated ratchet potential. *Soft Matter* **10**, 3915–3925 (2014).
- F. Martínez-Pedrero, H. Massana-Cid, T. Ziegler, T. H. Johansen, A. V. Straube, P. Tierno, Bidirectional particle transport and size selective sorting of Brownian particles in a flashing spatially periodic energy landscape. *Phys. Chem. Chem. Phys.* **18**, 26353–26357 (2016).
- J. R. Blake, A note on the image system for a stokeslet in a no-slip boundary. *Proc. Camb. Philos. Soc.* **70**, 303–310 (1971).
- A. V. Straube, P. Tierno, Synchronous vs. asynchronous transport of a paramagnetic particle in a modulated ratchet potential. *Europhys. Lett.* **103**, 28001 (2013).
- C. Lutz, M. Reichert, H. Stark, C. Bechinger, Surmounting barriers: The benefit of hydrodynamic interactions. *Europhys. Lett.* **74**, 719–725 (2006).
- T. Neuhaus, M. Marechal, M. Schmiedeberg, H. Löwen, Rhombic preordering on a square substrate. *Phys. Rev. Lett.* **110**, 118301 (2013).
- H. Kawamoto, K. Seki, N. Kuromiya, Mechanism of travelling-wave transport of particles. *J. Phys. D Appl. Phys.* **39**, 1249–1256 (2006).
- B. B. Yellen, R. M. Erb, H. S. Son, R. Hewlin, H. Shang, G. U. Lee, Traveling wave magnetophoresis for high resolution chip based separations. *Lab Chip* **7**, 1681–1688 (2007).
- C. Sándor, A. Libál, C. Reichhardt, C. J. O. Reichhardt, Collective transport for active matter run-and-tumble disk systems on a traveling-wave substrate. *Phys. Rev. E* **95**, 012607 (2017).
- R. E. Goldstein, Traveling-wave chemotaxis. *Phys. Rev. Lett.* **77**, 775–778 (1996).
- M. Hirano, K. Shinjo, Atomistic locking and friction. *Phys. Rev. B Condens. Matter* **41**, 11837–11851 (1990).
- D. Cole, S. Bending, S. Savel'ev, A. Grigorenko, T. Tamegai, F. Nori, Ratchet without spatial asymmetry for controlling the motion of magnetic flux quanta using time-asymmetric drives. *Nat. Mater.* **5**, 305–311 (2006).
- M. Belovs, R. Livanovics, A. Cebers, Hydrodynamic synchronization of pairs of puller type magnetotactic bacteria in a high frequency rotating magnetic field. *Soft Matter* **15**, 1627–1632 (2019).
- J. Kotar, M. Leoni, B. Bassetti, M. Lagomarsino, P. Cicuta, Hydrodynamic synchronization of colloidal oscillators. *Proc. Natl. Acad. Sci. U.S.A.* **107**, 7669–7673 (2010).
- N. Uchida, R. Golestanian, Generic conditions for hydrodynamic synchronization. *Phys. Rev. Lett.* **106**, 058104 (2011).
- B. Lau, O. Kedem, J. Schwabacher, D. Kwasnieski, E. A. Weiss, An introduction to ratchets in chemistry and biology. *Mater. Horiz.* **4**, 310–318 (2017).
- R. D. Astumian, M. Bier, Fluctuation driven ratchets: Molecular motors. *Phys. Rev. Lett.* **72**, 1766–1769 (1994).
- F. Jülicher, A. Ajdari, J. Prost, Modeling molecular motors. *Rev. Mod. Phys.* **69**, 1269–1282 (1997).
- P. Maggaretti, I. Pagonabarraga, D. Frenkel, Running faster together: Huge speed up of thermal ratchets due to hydrodynamic coupling. *Phys. Rev. Lett.* **109**, 168101 (2012).

52. S. Kassem, T. van Leeuwen, A. S. Lubbe, M. R. Wilson, B. L. Feringa, D. A. Leigh, Artificial molecular motors. *Chem. Soc. Rev.* **46**, 2592–2621 (2017).
53. C. Appert-Rolland, M. Ebbinghaus, L. Santen, Intracellular transport driven by cytoskeletal motors: General mechanisms and defects. *Phys. Rep.* **593**, 1–59 (2015).
54. C. Hepp, B. Maier, Kinetics of DNA uptake during transformation provide evidence for a translocation ratchet mechanism. *Proc. Natl. Acad. Sci. U.S.A.* **113**, 12467–12472 (2016).
55. P. Galajda, J. Keymer, P. Chaikin, R. Austin, A wall of funnels concentrates swimming bacteria. *J. Bacteriol.* **189**, 8704–8707 (2007).
56. M. B. Wan, C. J. Olson Reichhardt, Z. Nussinov, C. Reichhardt, Rectification of swimming bacteria and self-driven particle systems by arrays of asymmetric barriers. *Phys. Rev. Lett.* **101**, 018102 (2008).
57. L. Angelani, R. Di Leonardo, G. Ruocco, Self-starting micromotors in a bacterial bath. *Phys. Rev. Lett.* **102**, 048104 (2009).
58. R. D. Leonardo, L. Angelani, D. Dell’Arciprete, G. Ruocco, V. Iebba, S. Schippa, M. P. Conte, F. Mecarini, F. De Angelis, E. Di Fabrizio, Bacterial ratchet motors. *Proc. Natl. Acad. Sci. U.S.A.* **107**, 9541–9545 (2010).
59. P. Tierno, F. Sagués, T. H. Johansen, T. M. Fischer, Colloidal transport on magnetic garnet films. *Phys. Chem. Chem. Phys.* **11**, 9615–9625 (2009).
60. P. Tierno, Magnetically reconfigurable colloidal patterns arranged from arrays of self-assembled microscopic dimers. *Soft Matter* **8**, 11443 (2012).

Acknowledgments: We thank T. H. Johansen for providing us the FGF film. **Funding:** This work has received funding from the European Research Council (ERC) under the European Union’s Horizon 2020 Research and Innovation Programme (grant agreement no. 811234). S.G.L. and I.P. acknowledge support from Horizon 2020 program through 766972-FET-OPEN-NANOPHLOW. R.L.S. acknowledges support from the Swiss National Science Foundation (grant 180729). I.P. acknowledges support from Ministerio de Ciencia, Innovación y Universidades (grant no. PGC2018-098373-B-I00 AEI/FEDER-EU) and from Generalitat de Catalunya under project 2017SGR-884 and Swiss National Science Foundation project no. 200021-175719. P.T. acknowledges support from Ministerio de Ciencia, Innovación y Universidades (PID2019-108842GB-C21) and the Generalitat de Catalunya (ICREA Acadèmia). **Author contributions:** S.G.L. performed numerical simulations and theory. R.L.S. carried out the experiments. I.P. and P.T. supervised the work. All authors discussed and interpreted the result of the manuscript. **Competing interests:** The authors declare that they have no competing interests. **Data and materials availability:** All data needed to evaluate the conclusions in the paper are present in the paper and/or the Supplementary Materials.

Submitted 4 February 2022

Accepted 19 April 2022

Published 8 June 2022

10.1126/sciadv.abo4546

Hydrodynamic synchronization and clustering in ratcheting colloidal matter

Sergi G. Leyva, Ralph L. Stoop, Ignacio Pagonabarraga, and Pietro Tierno

Sci. Adv. **8** (23), eabo4546. DOI: 10.1126/sciadv.abo4546

View the article online

<https://www.science.org/doi/10.1126/sciadv.abo4546>

Permissions

<https://www.science.org/help/reprints-and-permissions>

Use of this article is subject to the [Terms of service](#)

Science Advances (ISSN 2375-2548) is published by the American Association for the Advancement of Science, 1200 New York Avenue NW, Washington, DC 20005. The title *Science Advances* is a registered trademark of AAAS.

Copyright © 2022 The Authors, some rights reserved; exclusive licensee American Association for the Advancement of Science. No claim to original U.S. Government Works. Distributed under a Creative Commons Attribution NonCommercial License 4.0 (CC BY-NC).

Publication 3:
Dynamics and clogging of colloidal monolayers
magnetically driven through a heterogeneous landscape

Sergi G. Leyva^{1,2}, Ralph L. Stoop¹, Pietro Tierno^{1,2,3}, and Ignacio Pagonabarraga^{1,2,4}

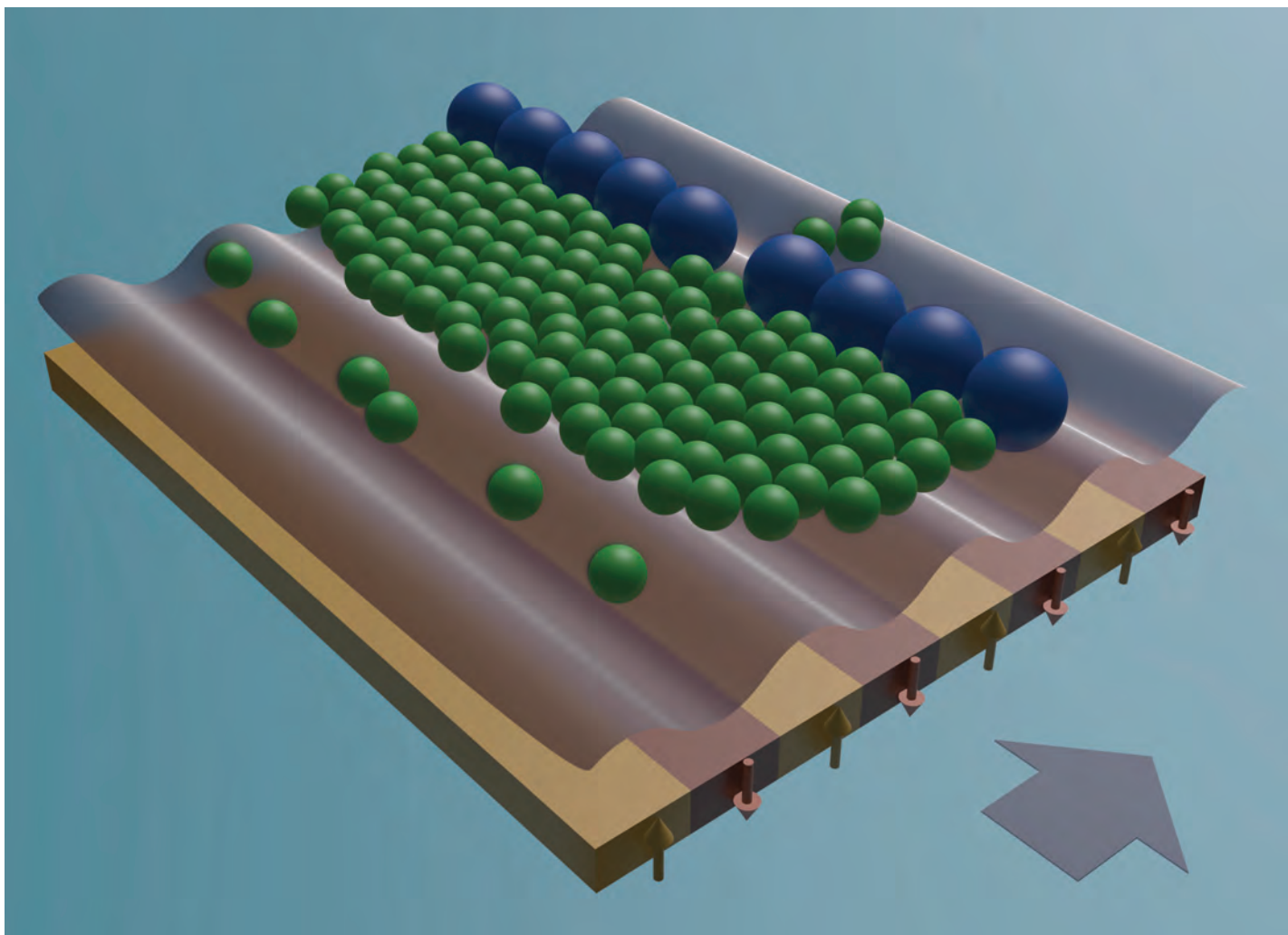
¹Departament de Física de la Matèria Condensada, Universitat de Barcelona, 08028 Barcelona, Spain

²Universitat de Barcelona Institute of Complex Systems (UBICS), Universitat de Barcelona, 08028 Barcelona, Spain

³Institut de Nanociència i Nanotecnologia, IN²UB, Universitat de Barcelona, 08028 Barcelona, Spain

⁴CECAM Centre Européen de Calcul Atomique et Moléculaire, École Polytechnique Fédérale de Lausanne, Batochime, Avenue Forel 2, 1015 Lausanne, Switzerland

Science Advances (2022), **8**, 23



Highlighting research from Sergi Granados Leyva and Ralph Lukas Stoop at the Department of Condensed Matter Physics, University of Barcelona.

Dynamics and clogging of colloidal monolayers magnetically driven through a heterogeneous landscape

An ensemble of paramagnetic colloids is driven against a barrier made of larger silica obstacles with a narrow opening. Here we combine experiments and numerical simulations to shed light on the role of flexibility in the obstacle displacements and the effect of hydrodynamic interactions between the particles. This colloidal model system is used to investigate the emergence of clogging in microscale matter.

As featured in:



See Ignacio Pagonabarraga *et al.*,
Soft Matter, 2020, **16**, 6985.



Cite this: *Soft Matter*, 2020,
16, 6985

Dynamics and clogging of colloidal monolayers magnetically driven through a heterogeneous landscape†

Sergi Granados Leyva,^a Ralph Lukas Stoop,^a Pietro Tierno ^{abc} and Ignacio Pagonabarraga ^{*abd}

We combine experiments and numerical simulations to investigate the emergence of clogging in a system of interacting paramagnetic colloidal particles driven against a disordered landscape of larger obstacles. We consider a single aperture in a landscape of immobile silica particles which are irreversibly attached to the substrate. We use an external rotating magnetic field to generate a traveling wave potential which drives the magnetic particles against these obstacles at a constant and frequency tunable speed. Experimentally we find that the particles display an intermittent dynamics with power law distributions at high frequencies. We reproduce these results by using numerical simulations and show that clogging in our system arises at large frequency, when the particles desynchronize with the moving landscape. Further, we use the model to explore the hidden role of flexibility in the obstacle displacements and the effect of hydrodynamic interactions between the particles. We also consider numerically the situation of a straight wall and investigate the range of parameters where clogging emerges in such case. Our work provides a soft matter test-bed system to investigate the effect of clogging in driven microscale matter.

Received 16th May 2020,
Accepted 3rd July 2020

DOI: 10.1039/d0sm00904k

rsc.li/soft-matter-journal

Introduction

Understanding the transport properties of microscopic particles through heterogeneous media^{1,2} is important for several technological processes, including filtration,^{3,4} particle sorting,^{5,6} microfluidics^{7,8} and many others across materials and engineering science. From a fundamental point of view, there are several fascinating nonequilibrium phenomena that emerge when such particles are driven across disordered landscapes such as depinning, jamming, plastic flow and rectification effects.⁹ These phenomena are also common to other physical systems across different length scales, from vortex matter driven across type II superconductors,¹⁰ to electrons on liquid helium,¹¹ active matter^{12,13} and skyrmions.¹⁴ The simple case of an

ensemble of particles forced to pass through a single constriction may give rise to different complex effects, such as intermittency in the particle flow, clogging and complete blockage *via* formation of arches and particle bridges.¹⁵ This effect has been investigated in the past on different length scales,¹⁶ from humans,¹⁷ to sheep,¹⁸ granular particles^{19,20} and biological systems.^{21–23} While most of the works have been focused on clogging in macroscopic systems, only few studies have addressed the case of microscopic particles dispersed in fluid media.^{16,24,25} At such length scale the presence of thermal fluctuations and hydrodynamic interactions between the particles may alter the system dynamics reducing or favoring the effect of clogging.

In this context, some of us²⁶ investigated recently the collective dynamics of paramagnetic colloidal particles that were driven across a disordered landscape of obstacles, namely non magnetic particles fixed at random positions above a substrate. While this work focused on the global transport properties in the presence of several obstacles, it did not include the detailed study of a single aperture, where the particle flow is not perturbed by the presence of several openings. Moreover, investigating a single aperture could provide many insights toward understanding the occurrence of clogging in microscale matter, and has a direct connection to the systems mentioned previously. Thus, in this work, we investigate the emergence of clogging when colloidal particles are forced to pass through a single, narrow opening. Starting from

^a *Departament de Física de la Matèria Condensada, Universitat de Barcelona, Av. Diagonal 647, 08028, Barcelona, Spain. E-mail: ptierno@ub.edu; Tel: +34 934034031*

^b *Universitat de Barcelona Institute of Complex Systems (UBICS), Universitat de Barcelona, Barcelona, Spain*

^c *Institut de Nanociència i Nanotecnologia, IN²UB, Universitat de Barcelona, Av. Diagonal 647, 08028, Barcelona, Spain*

^d *Centre Européen de Calcul Atomique et Moléculaire, École Polytechnique Fédérale de Lausanne (EPFL), Batochime, Avenue Forel 2, Lausanne, Switzerland*

† Electronic supplementary information (ESI) available: Two video clips, one from the experiments and the other from numerical simulation illustrating the dynamics of the driven magnetic colloids. See DOI: 10.1039/d0sm00904k

our experimental system, we demonstrate the occurrence of clogging, characterized by a power-law decay of the statistical distribution of the passage time of the particles. We complement our experimental findings with Brownian dynamic simulations which unveil relevant mechanisms that determine the anomalous flow of the forced colloids. In particular, we analyze the role of hydrodynamic interactions and the flexibility of the obstacles at the opening. Finally, we extend the numerical simulations to consider also the situation of a narrow opening in a planar wall of non magnetic particles. While such case is difficult to realize experimentally *via* direct particle sedimentation, it is similar to many other situations present in *e.g.* microfluidics systems, which are characterized by fixed and straight PDMS channels.

Methods

Experimental system

We use commercially available paramagnetic colloidal particles (Dynabeads, M-270, Thermo Fisher Scientific) characterized by a diameter of $d = 2.8 \mu\text{m}$ and a magnetic volume susceptibility of $\chi \sim 0.4$. The particles are composed of a polystyrene matrix with surface carboxylic groups, and are doped with nanoscale iron oxide grains. The particles are dispersed in highly deionized water (MilliQ, Millipore) and deposited above the surface of a uniaxial ferrite garnet film (FGF). The FGF was previously synthesized *via* dipping liquid phase epitaxy²⁷ and it is characterized by parallel stripes of ferromagnetic domains with alternating up and down magnetization. In the absence of an external field, the wavelength of the FGF pattern is $\lambda = 2.6 \mu\text{m}$, and the saturation magnetization $M_s = 1.3 \times 10^4 \text{ A m}^{-1}$, see Fig. 1(a). Before the experiments, the FGF is coated with a thin layer ($\sim 1 \mu\text{m}$ thick) of a photoresist (AZ-1512 Microchem, Newton, MA) using spin coating and backing procedures.²⁸

The particles are transported against fixed obstacles made of silica dioxide microspheres (44054-5ML-F, Sigma-Aldrich) with diameter $d = 5 \mu\text{m}$ (standard deviation $\sigma \lesssim 0.35 \mu\text{m}$). Before the experiments, the silica particles are irreversibly attached above the FGF surface with the following procedure. First, the silica particles are diluted in highly deionized water at different concentrations and deposited above the FGF surface. After their sedimentation which lasts few minutes, the particles float above the FGF due to their negative surface charge. Sticking on the substrate is induced by the addition of a salt, namely a solution of 10 mM NaCl in water. The NaCl ions of the salt screen the electrostatic interactions favoring permanent linkage of the silica particles to the FGF *via* attractive van der Waals interactions. After that, the salt solution was removed and was replaced by a water dispersion containing the paramagnetic colloids. As a result, the magnetic particles float on a substrate composed of a quenched disorder of silica obstacles, Fig. 1(b).

Transport mechanism

We start by describing the particle motion in the absence of obstacles. Once placed above the FGF surface, the particles are

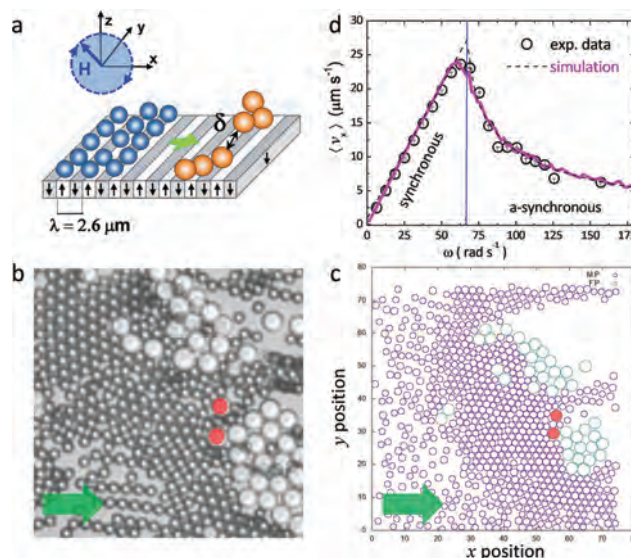


Fig. 1 (a) Schematic showing the experimental system composed of a monolayer of paramagnetic colloids (blue) driven against larger silica particles (orange) and arranged to form one opening of width δ . The particles are located above a ferrite garnet film of wavelength λ and are driven toward right by a rotating magnetic field elliptically polarized in the (\hat{x}, \hat{z}) plane. (b and c) Experimental (b) and simulation (c) images showing a portion of the whole system where the silica particles (larger colloids) form a constriction of width δ . The direction of motion is indicated by a green arrow. See Videos S1 and S2 in the ESI.† (d) Mean particle speed $\langle v_x \rangle$ along the direction of motion versus angular frequency ω in the absence of obstacles. Scattered circles are experimental data, while continuous magenta line are results from numerical simulation. The continuous blue line at $\omega_c = 68.8 \text{ rad s}^{-1}$ separates the synchronous (left) and the asynchronous (right) regimes. Dashed lines are fit following the equations in the text.

attracted by the magnetic domain walls, and form a two-dimensional monolayer above the (\hat{x}, \hat{y}) plane. We induce directed particle transport by using an external rotating magnetic field elliptically polarized in a perpendicular plane (\hat{x}, \hat{z}) , see Fig. 1(a). The applied field, with amplitude H_0 and angular frequency ω is given by, $\mathbf{H} \equiv (H_x \cos(\omega t), 0, H_z \sin(\omega t))$, where $H_0 = \sqrt{(H_x^2 + H_z^2)}/2$, and (H_x, H_z) are the two field components. Since the field is elliptically polarized, it can be characterized also by the ellipticity $\beta = (H_x^2 - H_z^2)/(H_x^2 + H_z^2)$, where $\beta \in [-1, 1]$ and $\beta = 0$ corresponds to the circular polarization. For all the experiments we keep fixed the amplitude to $H_0 = 800 \text{ A m}^{-1}$ and the ellipticity parameter to $\beta = -0.4$. The latter choice ensures that dipolar interactions are negligible along the propulsion direction²⁹ and the particles can be considered, in first approximation, as hard-spheres.

The external magnetic field modulates the stray field of the FGF surface, and it generates a two-dimensional sinusoidal-like potential which continuously translates along one direction (\hat{x}) perpendicular to the magnetic stripes. The potential moves at a constant and frequency tunable speed $v_p = \omega\lambda/(2\pi)$, and drags with it the paramagnetic colloids located in its minima. As shown in Fig. 1(d), depending on the driving frequency one can identify two dynamic regimes.³⁰ Below a critical frequency ω_c , the particles are trapped in the potential minima and move with these minima (synchronous regime) at a constant average

speed $\langle v_x \rangle = v_p$. When $\omega > \omega_c$, the motion of the particles desynchronizes with the moving landscape, and the average speed decreases as $\langle v_x \rangle = v_p(1 - \sqrt{1 - (\omega_c/\omega)^2})$ (asynchronous regime). As shown in Fig. 1(d), we find $\omega_c = 68.8 \text{ rad s}^{-1}$ for the experimental parameters used here, a value which is in excellent agreement with the numerical simulations (see later) for an obstacle free system. Further, in the synchronous regime the particles acquire a translational speed $\langle v_x \rangle \in [2, 23] \mu\text{m s}^{-1}$ which corresponds to a Péclet number $\text{Pe} \in [20, 230]$. We estimate the latter by considering the ratio between the Brownian time $\tau_B = d^2/(4D_{\text{eff}})$ required by the particle to diffuse its own radius ($d/2$), and the driven time $\tau_D = d/(2\langle v_x \rangle)$ required to move its radius due to the magnetic landscape. Here we use the value of the effective diffusion coefficient $D_{\text{eff}} = 0.14 \mu\text{m}^2 \text{ s}^{-1}$ which was estimated in a previous work.³¹

Simulation scheme

We complement the experimental results by using Brownian dynamic simulation with periodic boundary conditions. We consider a system composed of moving paramagnetic colloids, of size r_p , and silica obstacles, of size r_o . All particles are characterized by their positions, \mathbf{r}_i with $i = 1 \dots N_p + N_o$. Initially, we consider obstacles fixed on the substrate, $\mathbf{r}_i = \mathbf{r}_{i, \text{eq}}$, $i = N_p \dots N_p + N_o$, while the magnetic particles evolve following the overdamped dynamics:

$$\frac{1}{\mu} \frac{d\mathbf{r}_i}{dt} = \sum_j \mathbf{F}^{\text{int}}(\mathbf{r}_{ij}) + \mathbf{F}^{\text{ext}}(\mathbf{r}_i) + \mathbf{F}^{\text{T}}(\mathbf{r}_i), \quad (1)$$

where $i = 1, \dots, N_p$, μ is the particle mobility, \mathbf{F}^{int} is the pair interaction between the colloids, \mathbf{F}^{ext} the external driving force and \mathbf{F}^{T} accounts for the force exerted by the thermal bath. The interparticle forces derive from a Yukawa potential, and account effectively for the colloidal electrostatic short range repulsion and finite particle size. The force between a particle i of type a , of radius r_a , and a particle j of type b , of radius r_b , can be written as:

$$\mathbf{F}^{\text{int}}(\mathbf{r}_{ij}) = \frac{U_{ab}}{\lambda_{ab}} \sum_{i \neq j}^N \left[\frac{\sigma_{ab}}{r_{ij}} \left(\frac{\sigma_{ab}}{r_{ij}} + \frac{\sigma_{ab}}{\lambda_{ab}} e^{-\frac{r_{ij}}{\lambda_{ab}}} \right) - B_{ab} \right] \mathbf{e}_{r_{ij}}, \quad (2)$$

where $\mathbf{e}_{r_{ij}}$ a unit vector along the two considered particles, and $\mathbf{r}_{ij} = \mathbf{r}_i - \mathbf{r}_j$. The parameter U_{ab} quantifies the strength, and λ_{ab} the characteristic decay length, of the Yukawa potential between the interaction of a particle of type a and one of type b , $\sigma_{ab} = (r_a + r_b)/2$ denotes the radius of the interaction between the pair. The parameter B_{ab} is a constant ensuring that the force is zero at the cutoff interaction radius r_c ,

$$B_{ab} = \frac{\sigma_{ab}}{r_c} e^{-\frac{r_c}{\lambda_{ab}}} \left(\frac{\sigma_{ab}}{\lambda_{ab}} + \frac{\sigma_{ab}}{r_c} \right). \quad (3)$$

We neglect the magnetic dipolar interactions since it was previously shown²⁹ that these interactions become negligibly small along the propulsion direction for applied fields with $\beta = -1/3$, similar to our case. The external force results from the magnetically modulated landscape and it is given by²⁹

$$\mathbf{F}^{\text{ext}}(x, t) = F_M \left[u_1(t) \sin\left(\frac{2\pi x}{\lambda}\right) - u_2(t) \cos\left(\frac{2\pi x}{\lambda}\right) \right] \hat{\mathbf{x}} \quad (4)$$

where $u_1(\beta, t) = \sqrt{1 + \beta} \cos(\omega t)$, $u_2(\beta, t) = \sqrt{1 - \beta} \cos(\omega t)$ and $F_M = 16H_0 e^{-2\pi z/\lambda} / (\lambda M_s)$ is a prefactor that considers the particle elevation (z) from the substrate. The last term in eqn (1) is a random force associated to the temperature. Integration of this term over one time step, Δt , gives a random displacement $\Delta \mathbf{r}^r$ characterized by a Gaussian distribution, of magnitude $\Delta \mathbf{r}^r = \mu \mathbf{F}_i^{\text{T}} \Delta t$ and $\langle (\Delta \mathbf{r}^r)^2 \rangle = 4D_0 \Delta t$, being D_0 the particle diffusion coefficient.

For computational convenience, we make eqn (1) adimensional using the magnitude of the external force F_M , the colloid radius r_p , the characteristic speed $v_c = F_M \mu$ and the time $\tau_D = d/2\mu F_M$ scales, which identify the relevant Péclet number, $\text{Pe} = v_c r_p / D_0 = \mu F_M \sigma / D_0$. Accordingly, we can rewrite eqn (1) as:

$$\frac{d\mathbf{r}_i}{dt} = \frac{U_{ab}}{\lambda_{ab} F_M} \sum_{j \neq i} \psi(\mathbf{r}_{ij}) + \mathbf{F}^{\text{ext}}(\bar{x}, \bar{t}) + \sqrt{\frac{4}{\text{Pe}} \frac{\tau_D}{\Delta t}} \zeta \quad (5)$$

where $\bar{\mathbf{r}} = \mathbf{r}/r_p$, $\bar{\omega} = \omega \tau_D$, $\bar{\Delta t} = \Delta t / \tau_D$. In turn, $\bar{\psi} = \bar{\psi}(\bar{\mathbf{r}})_{ij}$ is the dimensionless Yukawa force between particles i and j ,

$$\psi(\mathbf{r}_{ij}) = \left[\frac{\bar{\sigma}_{ab}}{\bar{r}_{ij}} \left(\frac{\bar{\sigma}_{ab}}{\bar{r}_{ij}} + \frac{\bar{\sigma}_{ab}}{\bar{\lambda}_{ab}} e^{-\frac{\bar{r}_{ij}}{\bar{\lambda}_{ab}}} \right) - B_{ab} \right] \mathbf{e}_{r_{ij}} \quad (6)$$

where $\bar{\sigma}_{ab} = \sigma_{ab}/r_p$, and $\bar{\lambda}_{ab} = \lambda_{ab}/r_p$. Finally, $\bar{\mathbf{F}}^{\text{ext}}(\bar{x}, \bar{t})$ corresponds to the dimensionless form of the external, driving force, eqn (4).

We integrate eqn (5) using a time step $\Delta t / \tau_D = 1 \times 10^{-4}$, $r_p = 1$, $r_o = 1.78$, $\lambda_p = 1$, $\lambda_{op} = 1.39$, $U_{pp}/\lambda_{pp} F_M = 300$, $U_{op}/\lambda_{op} F_M = 150$ and $\text{Pe} = 150$. Further parameters were extracted by fitting the results from the experimental data to the one obtained from numerical simulation of an obstacle free system, see Fig. 1(d). From this benchmarking, we estimate the mobility $\mu \simeq 1/6\pi\eta r_a$ of the paramagnetic particles in water as $\mu = 3.79 \times 10^7 \text{ N s m}^{-1}$ and the magnitude of the force of the traveling wave potential as $F_M = 0.1 \text{ pN}$. With these values we calculate the characteristic time of the particle motion as $\tau_D = 0.04 \text{ s}$. Having demonstrated a good agreement between the simulations and the experiments in the absence of obstacles, we introduce the obstacles to our simulations. As shown in Fig. 1(c), we map the experimental situation (Fig. 1(b)) to our simulations by using the same spatial distribution of the obstacles.

In the numerical simulations, the obstacles are considered as rigidly attached to the substrate, and N runs only over the paramagnetic colloids. Careful inspection of the experimental videos reveals very small oscillations of the silica particles around their equilibrium position upon collisions. These oscillations may result from a combination between steric interactions of the silica particles with the polymer coated film and weak van der Waals attractions. Quantifying these interactions is a difficult task, and we consider them as an effective spring constant which accounts for the fact that the silica particles are not pulled away when subjected to forces coming from the driven colloids. Experimentally, it is difficult to quantify these oscillations since they are very small, and their amplitude is smaller than the error bars associated to the tracking. To account for this effect, we take into account the possibility that the obstacles are slightly displaced due to the forces exerted by the moving paramagnetic colloids. In this case we include

the obstacles as part of the N moving particles, which evolve according to the equation:

$$\frac{d\mathbf{r}_i}{dt} = \sum_{j \neq i} \frac{U_{ab}}{\lambda_{ab} F_M \mu} \psi(\mathbf{r}_{ij}) + \frac{k r_p}{\mu F_M} (\bar{\mathbf{r}}_i - \bar{\mathbf{r}}_{i,eq}), \quad (7)$$

with $i = N_p + 1, \dots, N_p + N_o$. The particles are subject to a spring of strength k when the obstacle is displaced from its equilibrium position, $\bar{\mathbf{r}}_{i,eq}$. The competition between the external driving frequency and the frequency related with the elastically displaced particles can lead to different and significant results.

Since the colloids are embedded in a solvent, we have also generalized the Brownian dynamics of the paramagnetic colloids to account for the impact that hydrodynamic interactions mediated by the solvent have in the clogging kinetics. Each particle is dragged by the fluid flow, \mathbf{v}_i^H , generated by the rest of the colloids due to the forces they are subject to, an effect that can be captured generalizing eqn (1) to

$$\frac{1}{\mu} \frac{d\mathbf{r}_i}{dt} = \sum_j \mathbf{F}^{\text{int}}(\mathbf{r}_{ij}) + \mathbf{F}^{\text{ext}}(\mathbf{r}_i) + \mathbf{F}^T(\mathbf{r}_i) + \frac{\mathbf{v}_i^H}{\mu}, \quad (8)$$

where we take into account the impact that the close proximity of the wall, and express the induced velocity in the point particle approximation as:

$$\mathbf{v}_i^H = \sum_{j \neq i} \mathbf{G}(\mathbf{r}_{ij}) \mathbf{F}^{\text{int}}(\mathbf{r}_{ij}). \quad (9)$$

Here $\mathbf{G}(\mathbf{r}_{ij})$ stands for the Blake-Oseen mobility tensor³² which considers the effect of the close proximity of the substrate in a far field approximation. We note that a sample with finite size could produce a screening of the hydrodynamic interactions between the particles. However, in our case, the experimental cell is wide enough that this screening develops over length scales that are long compared with the distances over which the particles interact and move through the obstacles.

Discussion

Clogging: experimental results

Introducing obstacles to the substrate completely changes the behavior of the driven particles as they are now forced to interact with the silica spheres which induces a deviation of their trajectories. As shown in Fig. 1(b) and (c), we consider the case of obstacles which create a narrow gap of width δ . We find that the presence of the opening strongly reduces the average speed of the monolayer eventually even leading to complete blockage, $\langle v_x \rangle = 0$, for $\delta < 3 \mu\text{m}$. For larger values of the distance, $3 \mu\text{m} < \delta < 4 \mu\text{m}$, we find an intermittent flow of the magnetic colloids which arises from the simultaneous arrival of the particles at the aperture, and their accumulation in a close packed state, which is locally jammed.

The appearance of clogging, namely the blockage of the particle flow, can be characterized by measuring the distribution $P(t_p)$, that quantifies when the time lapse between the passage of consecutive particles through the aperture is larger than a given time t_p . This distribution is also known as the

complementary cumulative distribution function. It has been previously shown that in the presence of an intermittent flow such distribution is expected to display asymptotically an universal behavior, *i.e.* a power law decay at high values of t_p ($P \sim t_p^{-\alpha}$) as a function of its exponent, α .^{19,33} This exponent can be used to distinguish the regime of normal flow, $\alpha > 2$, *i.e.* when the average flow rate is finite, from intermittency and clogging, $\alpha < 2$, *i.e.* when the average time lapse between consecutive passing elements through the aperture diverges. Hence, we can use $\alpha = 2$ to identify the transition to clogging, where it cannot be specified whether or not there is flow at a given time.¹⁶ Indeed a clogged state it is not fully blocked, as some material can be briefly released.

We use video microscopy to precisely track the positions of the particles and to calculate the corresponding distributions. Fig. 2 shows $P(t_p)$ measured for different values of the driving frequency ω and keeping constant the amplitude of the applied field. We find two different types of behaviour depending on ω which reflect the presence in the system of the underlying magnetic domain walls. For small frequencies, namely $\omega < 6.3 \text{ rad s}^{-1}$, clogging events are rare, and the distribution P displays an exponential decay. This effect can be understood by considering the particle trajectories which are characterized by a sequence of discrete jumps between the domain walls during each driving period. These jumps emerge in the system as periodic oscillations of the particles which are superimposed to the net drift velocity. The presence of such vibrations significantly reduces the clogging probability and the eventual formation of particle bridges. Such effect can be considered as an additional AC signal superimposed to the DC drift and allows to break the formation of a close packed monolayer of particles close to the constriction.¹⁹ We note that a similar strategy, namely the use of an additional AC field to fluidize the system, was recently introduced in numerical

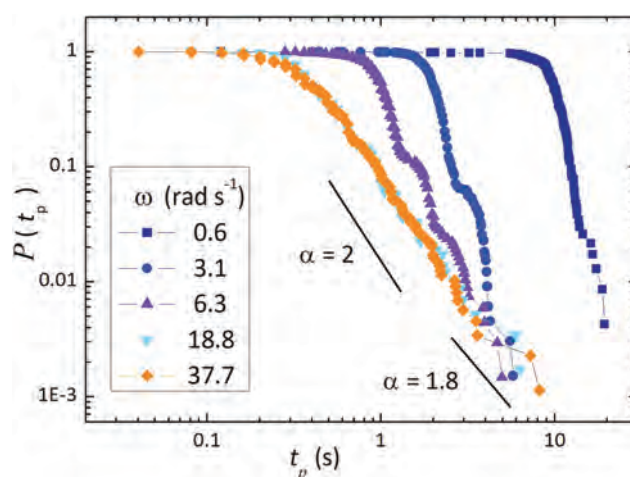


Fig. 2 Experiments: the distribution function $P(t_p)$ of time lapses $t > t_p$ for magnetic particles passing through a single constriction and at different driving frequencies. The continuous black line indicates the slope $\alpha = 2$ of the power-law $P \sim t_p^{-\alpha}$ which is used to distinguish clogged state ($\alpha < 2$) and unclogged ones ($\alpha > 2$).

simulations to maximize flow in a random array of obstacles.²³ In contrast, at high frequencies, the particles still move across the domain walls but their trajectories are continuous and the discrete jump are smeared out. As a consequence, the vibrations of the domain walls are not influencing the particle movement and cannot fluidize the system close to the constriction. Thus, we find that P becomes a power law, $P \sim t_p^{-\alpha}$ and the system is more prone to display clogging behavior. For these situations, we determine a common exponent $\alpha = 1.8$ for the tails of the high frequency distributions.³⁴ Such value is slightly higher as compared to pedestrian or granular systems that display stable arches at the constriction.^{15,20} The specificity of the colloidal system, and the role that the hydrodynamic interactions may have among the relative motion of the colloids close to the constriction may explain that the observed clogged states are more fragile than those observed on systems composed by larger constituents. Moreover, we find that all curves above $\omega = 6.3 \text{ rad s}^{-1}$ collapse, and clogging becomes independent on the particle speed. We note that experimental limitations impeded us to have enough statistical data, and thus to precisely determine the exponent of the distribution tails. Such limitations result from the unavoidable sticking of the particles to the FGF film after relatively long recording periods.

Simulation results: fixed obstacles

Fig. 3(a) and (b) display the results from the numerical simulations for fixed obstacles. In Fig. 3(a) we show how the distribution function $P(t_p)$ changes by varying the distance between the obstacles forming the constriction, at fixed driving frequency. As expected, a narrower constriction increases the particle mean passing time. Similar to the experimental data, we also observe a periodic decrease of the distributions followed by a series of characteristic plateaus which result from the external sinusoidal forcing. Indeed the time between two consecutive decays is proportional to the period of the applied field, $T = 1/f$. These plateaus are more evident in the simulations than in the experiments (Fig. 2), due to the higher temporal resolution achieved numerically. In the plateaus, the colloids have a higher probability to pass through the constriction, since they are located in a place where the potential is steeper, and thus feel a maximum positive force along the direction of motion. As the opening associated to a pair of obstacles decreases, these plateaus become narrow and the corresponding distributions smoother. Further, we find that for all the cases considered here, the system never develops a power law decay. Thus, no clogged states are present in the synchronous regime, in contrast to the experimental case where $\alpha = 1.8$ was observed for large ω but still slightly lower than ω_c .

As shown in Fig. 3(b), the speed of the paramagnetic particles, proportional to the driving frequency ω in the synchronous regime, strongly influences the distribution of t_p . In fact, increasing ω shifts the time lapse distribution towards shorter times, with a decay that may be characterized by an exponential law similar to the experimental results in Fig. 2. Interestingly, this trend reverses after $\omega = 37.7 \text{ rad s}^{-1}$ as the tails of the distributions flatten and become power law but with

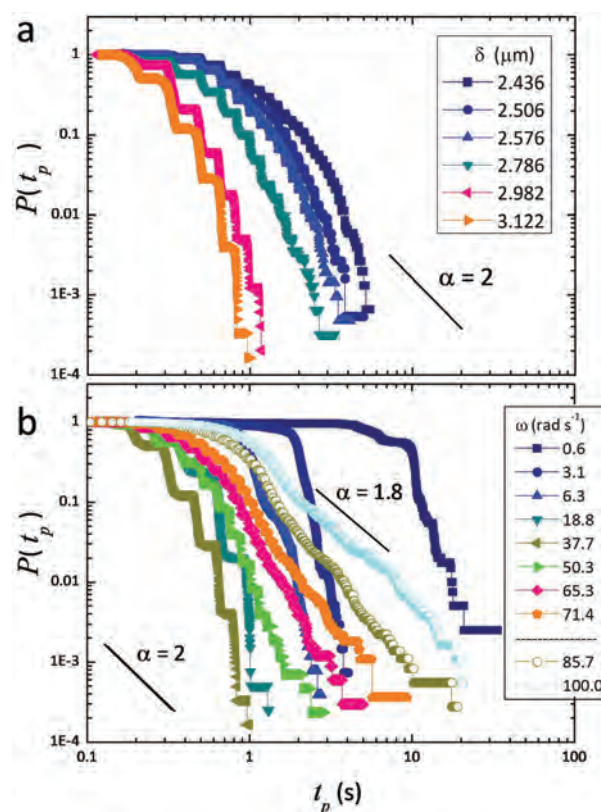


Fig. 3 (a and b) Numerical simulation results: (a) Distribution functions $P(t_p)$ of time lapses t_p for different values of the constriction width δ in the synchronous regime ($\omega = 37.7 \text{ rad s}^{-1}$). (b) Distribution functions $P(t_p)$ of time lapses t_p for different values of driving frequency ω , with $\delta = 2.98 \mu\text{m}$. The results are shown with filled symbols for particles driven in the synchronous regime for $\omega \leq 71.4 \text{ rad s}^{-1}$, and with empty symbols in the asynchronous regime.

no signature of clogging, $\alpha > 2$. Above $\omega = 85.7 \text{ rad s}^{-1}$, as the particles reach the asynchronous region, the $P(t_p)$ develop power law tails with $\alpha \sim 1.8$ signaling clogging. This results shows that losing synchrony promotes clogging.

Simulation results: harmonic spring and hydrodynamic interactions

The results obtained by fixing the positions of the obstacles show the emergence of clogging at high frequencies, however they did not capture all the effects observed in the experiments as, for example, the collapse of the distributions at high frequencies in the synchronous regime. In order to analyze the origin of such discrepancy, we consider the impact that moving obstacles and hydrodynamic interactions have on the system dynamics. To this end, we first introduce a small flexibility in the obstacle location and show in Fig. 4(a) the corresponding results. The presence of another vibration frequency resulting from the obstacle mobility can have relevant effects and contribute directly to clogging. To find the optimal spring constant k , we have performed different simulations and compare them directly with the experimental results in order to optimize the comparison. We find very similar distributions for

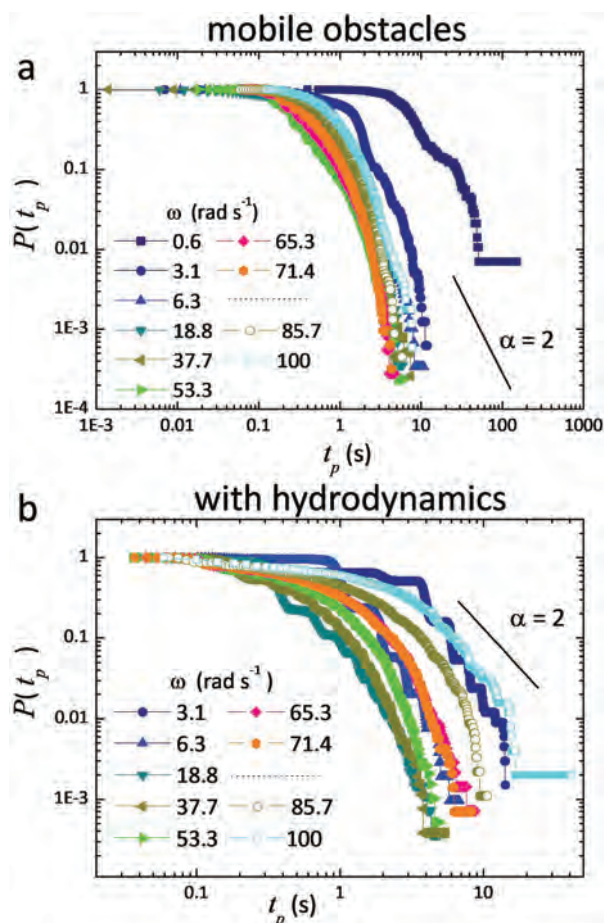


Fig. 4 (a) Distribution functions $P(t_p)$ of time lapses t_p for different values of the driving frequency ω both in the synchronous (filled symbols) and asynchronous (empty symbols) regimes from numerical simulations. The simulations were performed by considering mobile obstacles with a spring constant $k = 0.593 \mu\text{N m}^{-1}$. The black segment indicates the slope $\alpha = 2$ of the power law $P \sim t^{-\alpha}$. (b) Distribution functions $P(t_p)$ of time lapses t_p versus ω from numerical simulations with hydrodynamic interactions. The channel width for all data has been fixed to $\delta = 2.576 \mu\text{m}$.

a spring constant $k = 0.593 \mu\text{N m}^{-1}$. Moreover, in agreement with the experiments we also observe the collapse of the distributions at high frequencies by keeping fixed k and varying ω , Fig. 4(a). Thus, the presence of slightly mobile obstacles favors clogging, while using the same constriction width with no harmonic spring gives a completely unclogged state and a large exponent $\alpha > 2$ in the distribution $P(t_p)$. Further, as shown in Fig. 4(a), we find that there are no visible plateaus as in Fig. 3. Moreover, smaller spring constants can lead to states that are more prone to clogging than higher ones. The latter effect is unexpected, since smaller frequencies could induce longer period of time when the obstacles are more deformed and the width of the opening wider, which should favor unclogging. However, the results obtained in Fig. 4(a) point out to an interplay between the frequency of the external magnetic field and the frequency of oscillation of the obstacles which favor clogging. Thus, the obstacle mobility leads to an interaction with other constrictions because of particles passing through nearby

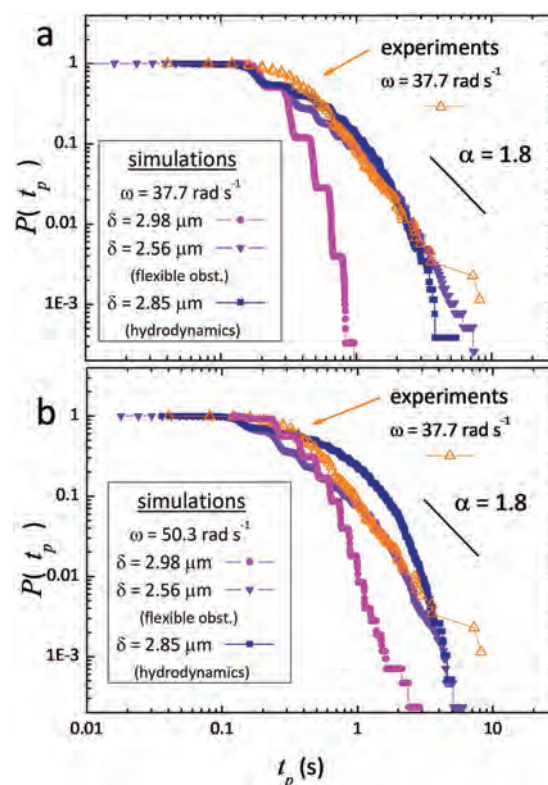


Fig. 5 (a and b) Comparison between the experimental data (open symbols, frequency $\omega = 37.7 \text{ rad s}^{-1}$) and the numerical simulations (filled symbols) the latter with driving frequencies: (a) $\omega = 37.7 \text{ rad s}^{-1}$ and (b) $\omega = 50.3 \text{ rad s}^{-1}$. In both images the black segment denotes the slope $\alpha = 1.8$ of the power law $P(t_p)$.

openings, see Fig. 1(b), can also indirectly exert additional pressure on the obstacles of the opening of interest, affecting the passage times of the particles.

Experimentally, the paramagnetic colloids move above the FGF film generating a net flux between them and close to the constriction. We use the extended Brownian dynamics model described in the Method section to analyze the impact that hydrodynamic interactions (HIs) have in the distribution functions. As shown in Fig. 4(b), we also explore the effect of HIs by varying the driving frequency from the synchronous ($\omega < 85.7 \text{ rad s}^{-1}$) to the asynchronous regime. The emergence of the finite plateaus is also observed at low frequency, while raising ω smooths the curves and produces power law tails, see Fig. 4(b).

The direct comparison with the experimental data taken at $\omega = 37.7 \text{ rad s}^{-1}$ is shown in Fig. 5(a) and (b) for two frequencies both in the synchronous regime. The numerical simulations show that the introduction both of obstacle mobility and HI smooth significantly the plateaus, to the extent that they are barely visible when HI are introduced with fixed obstacles. Moreover, flexible obstacles induce distribution functions which have dependence with frequency closer to the one observed experimentally.

Simulation results: planar wall

The geometry analyzed in the previous section with numerical simulation was designed to match the experimental system, thus featuring obstacles with the same positions and degrees

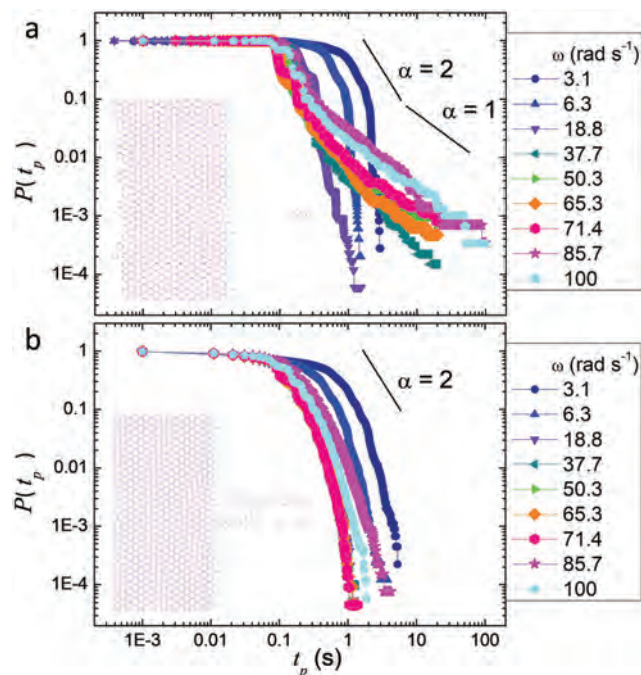


Fig. 6 (a and b) Distribution functions $P(t_p)$ of time lapses, t_p , for different frequencies of a straight wall of non magnetic colloids with: (a) a single constriction of width $\delta = 2.982 \mu\text{m}$ and (b), two small constrictions both with widths $\delta = 2.982 \mu\text{m}$ and separated by a single particle. The small insets on the left of both images show a fraction of the simulation box with a close packed monolayer of particles. The inset at the top shows channel clogging, while the inset at the bottom shows the particle flow.

of disorder. Such disorder results from the procedure to prepare the obstacles, since the silica particles were left sediment above the substrate and forced to stick there by addition of salt. Thus, adapting the simulation to the experimental system implies a random distribution of the particles and an opening characterized by a small inclination with respect to the driving direction, as shown in Fig. 1(c). However, it is also interesting to analyze the generic features of the probability of elapsed times on a simplified geometry, when the silica obstacles form a perfect planar wall with a small opening at the center. This geometry is depicted in the inset of Fig. 6(a), for a width $\delta = 2.982 \mu\text{m}$, while the main figure shows the variation of $P(t_p)$ as a function of ω . At very low frequencies, $\omega < 18.8 \text{ rad s}^{-1}$, the distributions are exponential and the particles easily flow through the aperture. Increasing ω we observe the emergence of the steps as in the previous case, however we find that clogging may be observed even within the synchronous regime ($\omega = 65.3 \text{ rad s}^{-1}$) where the power law distributions feature a very small exponent $\alpha \sim 1.2$. The reason is that, in contrast to the disordered geometry, the planar wall may act as a template for crystallization (see inset Fig. 6(a)) and create arches and bridges which easily impeded further motion, producing an intermittent flow at the opening. In contrast, at low frequency the particle oscillations due to the moving landscape are able to break these bridges and to avoid the crystallization process.

Further, the numerical system allows to explore the effect that an additional opening in the straight wall will have on the global

particle flow. An interesting question is whether adding a second aperture separated by only one silica obstacle, could favor the system fluidization and avoid clogging. We effectively report this effect in Fig. 6(b), where two apertures of widths $\delta = 2.982 \mu\text{m}$ are able to avoid the particle crystallization at the opening for all driving frequencies. The measured distribution functions $P(t_p)$ for both apertures are almost identical, and in both cases (in Fig. 6(b) we show their average) display a smooth and almost exponential decay. We note that the effect of two openings may be considered analogous to placing a single obstacle at the exit of one large aperture. This situation has been used in the past in other macroscopic systems as an efficient means to fluidize a system.^{35–37} However, in most cases the obstacle was placed close to the opening, but not exactly at the exit. Another interesting avenue for future study is to investigate how the distributions function may change upon variation of the different parameters, such as the location and size of the central obstacle, or when the two opening are asymmetric, namely with different width.

Conclusions

We have studied both experimentally and theoretically the dynamics of paramagnetic colloidal particles driven through a single aperture above a periodic magnetic substrate. We combine experiments with numerical simulations and analyze the distribution of displacements of the particles. We find that in the experiments clogging occurs when the particles are driven close to the asynchronous regime, while in the simulations they always occur deep in this regime. Further we unveil the role played by the obstacle movement due to flexibility and by hydrodynamic interactions. The comparison between experimental and simulation results on analogous geometries indicate that HIs play a relevant role in the clogging dynamics of forced colloids and that obstacle compliance hinders the dependence of particle motion on the frequency of the driving field.

While the experimental system is based on the use of a specially prepared ferrite garnet film, we observe a very good agreement between the experimental data and the results from numerical simulations by using a very generic model. The latter neglect dipolar interactions between the particles while considering an effective short range repulsive interaction potential. Thus our findings may be used to explore clogging in other driven many particle systems two dimensionally confined to a plate, not limited to magnetic ones. On the other hand, the possibility of increasing the dipolar interactions between the particles *via* the ellipticity of the applied field could be further used as an effective tool to switch on attractive interactions and induce chaining.

Moreover, our findings invite future explorations of the system, as considering two, three or several openings in different geometric arrangements. Another interesting avenue would be to explore how the overall dynamics changes for anisotropic magnetic particles driven through the aperture.^{38–43} On the application side, the possibility of transporting paramagnetic colloidal particles close to a surface, and localize their position by simply switching off the applied field may be of interest for

microfluidics⁴⁴ and lab-on-a-chip⁴⁵ systems. In particular, these particles can be used to pick up and mobilize a chemical or biological cargo *via* surface functionalization.⁴⁶

Conflicts of interest

There are no conflicts to declare.

Acknowledgements

We thank Tom H. Johansen for providing us with the FGF film. S.G-L and I.P. acknowledge support from Horizon 2020 program through 766972-FET-OPEN-NANOPHLOW. R. L. S. acknowledges support from the Swiss National Science Foundation Grant 180729. R. L. S. and P. T. acknowledge support from the ERC consolidator grant Enforce (No. 811234). P. T. acknowledges support from the Ministerio de Ciencia, Innovación y Universidades (Grant no. ERC2018-092827) and the Generalitat de Catalunya (2017SGR1061 and program ICREA Acadèmia). I. P. acknowledges support from Ministerio de Ciencia, Innovación y Universidades (Grant No. PGC2018-098373-B-100 AEI/FEDER-EU) and from Generalitat de Catalunya under project 2017SGR-884, and Swiss National Science Foundation Project No. 200021-175719.

Notes and references

- M. B. Isichenko, *Rev. Mod. Phys.*, 1992, **64**, 961–1043.
- A. A. Snarskii, I. V. Bezsudnov, V. A. Sevryukov, A. Morozovskiy and J. Malinsky, *Transport Processes in Macroscopically Disordered Media: From Mean Field Theory to Percolation*, Springer, New York, 2016.
- S. Redner and S. Datta, *Phys. Rev. Lett.*, 2000, **84**, 6018–6021.
- N. Roussel, T. L. H. Nguyen and P. Coussot, *Phys. Rev. Lett.*, 2007, **98**, 114502.
- M. P. MacDonald, G. C. Spalding and K. Dholaki, *Nature*, 2003, **426**, 421.
- F. Martinez-Pedrero, H. Massana-Cid, T. Ziegler, T. H. Johansen, A. V. Straube and P. Tierno, *Phys. Chem. Chem. Phys.*, 2016, **18**, 26353.
- T. M. Squires and S. R. Quake, *Rev. Mod. Phys.*, 2005, **77**, 977–1026.
- G. Whitesides, *Nature*, 2006, **442**, 368–373.
- C. Reichhardt and C. J. O. Reichhardt, *Rep. Prog. Phys.*, 2017, **80**, 026501.
- L. F. Cohen and H. J. Jensen, *Rep. Prog. Phys.*, 1997, **60**, 1581.
- D. G. Rees, H. Totsuji and K. Kono, *Phys. Rev. Lett.*, 2012, **108**, 176801.
- C. Bechinger, R. Di Leonardo, H. Löwen, C. Reichhardt, G. Volpe and G. Volpe, *Rev. Mod. Phys.*, 2016, **88**, 045006.
- D. R. Parisi, R. C. Hidalgo and I. Zuriguel, *Sci. Rep.*, 2018, **8**, 9133.
- C. Reichhardt, D. Ray and C. J. O. Reichhardt, *Phys. Rev. Lett.*, 2015, **114**, 217202.
- C. Lozano, G. Lumay, I. Zuriguel, R. C. Hidalgo and A. Garcimartín, *Phys. Rev. Lett.*, 2012, **109**, 068001.
- I. Zuriguel, D. R. Parisi, R. C. Hidalgo, C. Lozano, A. Janda, P. A. Gago, J. P. Peralta, L. M. Ferrer, L. A. Pugnali, E. Clément, D. Maza, I. Pagonabarraga and A. Garcimartín, *Sci. Rep.*, 2015, **4**, 7324.
- D. Helbing and P. Molnár, *Phys. Rev. E: Stat., Nonlinear, Soft Matter Phys.*, 1995, **51**, 4282–4286.
- A. Garcimartín, J. M. Pastor, L. M. Ferrer, J. J. Ramos, C. Martín-Gómez and I. Zuriguel, *Phys. Rev. E: Stat., Nonlinear, Soft Matter Phys.*, 2015, **91**, 022808.
- A. Janda, D. Maza, A. Garcimartín, E. Kolb, J. Lanuza and E. Clément, *Europhys. Lett.*, 2009, **87**, 24002.
- K. To, P.-Y. Lai and H. K. Pak, *Phys. Rev. Lett.*, 2001, **86**, 71–74.
- P. Galajda, J. Keymer, P. Chaikin and R. Austin, *J. Bacteriol.*, 2007, **189**, 8704–8707.
- N. Koumakis, A. Lepore, C. Maggi and R. Di Leonardo, *Nat. Commun.*, 2013, **4**, 2588.
- C. Reichhardt and C. J. O. Reichhardt, *Phys. Rev. Lett.*, 2018, **121**, 068001.
- M. D. Haw, *Phys. Rev. Lett.*, 2004, **92**, 185506.
- A. Marin, H. Lhuissier, M. Rossi and C. J. Kähler, *Phys. Rev. E*, 2018, **97**, 021102.
- R. L. Stoop and P. Tierno, *Commun. Phys.*, 2018, **1**, 68.
- P. Tierno, F. Sagués, T. H. Johansen and T. M. Fischer, *Phys. Chem. Chem. Phys.*, 2009, **11**, 9615–9625.
- P. Tierno, *Phys. Rev. Lett.*, 2012, **109**, 198304.
- A. V. Straube and P. Tierno, *Soft Matter*, 2014, **10**, 3915.
- A. V. Straube and P. Tierno, *Europhys. Lett.*, 2013, **103**, 28001.
- P. Tierno, R. Muruganathan and T. M. Fischer, *Phys. Rev. Lett.*, 2007, **98**, 028301.
- J. R. Blake and A. T. Chwang, *J. Eng. Math.*, 1974, **8**, 23.
- C. Saloma, G. J. Perez, G. Tapang, M. Lim and C. Palmes-Saloma, *Proc. Natl. Acad. Sci. U. S. A.*, 2003, **100**, 11947.
- A. Clauset, C. R. Shalizi and M. E. J. Newman, *SIAM Rev.*, 2009, **51**, 661.
- I. Zuriguel, A. Janda, A. Garcimartín, C. Lozano, R. Arévalo and D. Maza, *Phys. Rev. Lett.*, 2011, **107**, 278001.
- K. Endo, K. A. Reddy and H. Katsuragi, *Phys. Rev. Fluids*, 2017, **2**, 094302.
- M. G. Areán, A. Boschan, M. A. Cachile and M. A. Aguirre, *Phys. Rev. E*, 2020, **101**, 022901.
- D. Zerrouki, J. Baudry, D. Pine, P. Chaikin and J. Bibette, *Nature*, 2008, **455**, 380.
- S. H. Lee and C. M. Liddell, *Small*, 2009, **5**, 1957.
- J. Yan, M. Bloom, S. C. Bae, E. Luijten and S. Granick, *Nature*, 2012, **491**, 578.
- J. Palacci, S. Sacanna, A. Vatchinsky, P. M. Chaikin and D. J. Pine, *J. Am. Chem. Soc.*, 2013, **135**, 15978.
- P. Tierno, *Phys. Chem. Chem. Phys.*, 2014, **16**, 23515.
- F. Martinez-Pedrero, E. Navarro-Argemí, A. Ortiz-Ambriz, I. Pagonabarraga and P. Tierno, *Sci. Adv.*, 2018, **4**, 9379.
- A. Terray, J. Oakey and D. W. Marr, *Science*, 2002, **296**, 1841.
- L. Wang, M. Zhang, J. Li, X. Gong and W. Wen, *Lab Chip*, 2010, **10**, 2869.
- T. Garg, G. Rath and A. K. Goyal, *Crit. Rev. Ther. Drug Carrier Syst.*, 2015, **32**, 89.

Publication 4:
Clogging transition and anomalous transport in driven
suspensions in a disordered medium

Sergi G. Leyva^{1,2} and Ignacio Pagonabarraga^{1,2}

¹Departament de Física de la Matèria Condensada, Universitat de Barcelona, 08028 Barcelona,
Spain

²Universitat de Barcelona Institute of Complex Systems (UBICS), Universitat de Barcelona,
08028 Barcelona, Spain

Physical Review E, (2024), Accepted

Clogging transition and anomalous transport in driven suspensions in a disordered medium

Sergi G. Leyva^{1,2,*} and Ignacio Pagonabarraga^{1,2,†}

¹*Departament de Física de la Matèria Condensada, Universitat de Barcelona,
Carrer de Martí i Franqués 1, 08028 Barcelona, Spain*

²*Universitat de Barcelona Institute of Complex Systems (UBICS),
Universitat de Barcelona, 08028 Barcelona, Spain*

(Dated: January 16, 2024)

We study computationally the dynamics of forced, Brownian particles through a disordered system. As the concentration of mobile particles and/or fixed obstacles increase, we characterize the different regimes of flow and address how clogging develops. We show that clogging is preceded by a wide region of anomalous transport, characterized by a power law decay of intermittent bursts. We analyze the velocity distribution of the moving particles and show that this abnormal flow region is characterized by a coexistence between mobile and arrested particles, and their relative populations change smoothly as clogging is approached. The comparison of the regimes of anomalous transport and clogging with the corresponding scenarios of particles pushed through a single bottleneck show qualitatively the same trends highlighting the generality of the transport regimes leading to clogging.

I. INTRODUCTION

Transport in disordered media can lead to a rich phenomenology, where particles dynamically move freely, get trapped, and are eventually released [1]. Understanding the foundations and controlling the characteristics of clogging and its effects is an outstanding challenge with a large number of practical implications as diverse as human pedestrian crowds [2–6], sheep herds, [7, 8], silo discharges [9–11], and bottlenecks in microfluidic devices [12–15]. In microfluidics, much effort has been taken to understand how clogging can be prevented to avoid blocking of capillaries and develop efficient biological and medical applications in the microscale [16, 17]. Clogging is typically characterised when particles are forced to pass through a bottleneck consisting of a narrow constriction [18]. The role of the geometry, the particle shape, and the hydrodynamic coupling to the induced flows [19] has started to be analyzed systematically [20, 21]. Quantitative analysis of clogging in single bottlenecks can be successfully carried out by measuring the difference of the passage times between consecutive particles [22]. Its complementary cumulative distribution function (CCDF) follows a power law decay, and the tail gives the information of whether the average time of passing particles is diverging, depending on the tail exponent, $\tau^{-\alpha}$; specifically $\alpha < 2$ corresponds to clogged, and $\alpha > 2$ unclogged regimes. This exponent, hence, predicts the possibility that a bottleneck develops a clog for an indefinite period of time. A well-known, counterintuitive observation in the passage through a constriction, and that can be quantified with this methodology is the Faster is Slower effect, in which faster entities rushing into a bottleneck results in a more persistent clogged

state [23]. Experimental results using this approach to clogging show that the coupling of the moving particles to the environment, e.g. through hydrodynamics, may affect the nature of the clogging transition [24].

Clogging can also take place in a disordered system consisting of a landscape of pinned obstacles and free moving particles [25–29]. The characterisation of the filtration properties of granular media [30] constitutes a relevant problem in clogging, where the goal is to minimise the flow of suspensions to filtrate a fluid, or to selectively target some specific component of the solute through a disordered medium. In heterogeneous environments, Péter *et al.* [31] showed that a completely clogged disordered landscape is characterised by a critical obstacle density, ϕ_{pin}^c , independent of the density of moving obstacles, ϕ_{mov} , indicating that the transition to clogging is controlled by an average obstacles spacing, l_c . Furthermore, compared to jamming, clogging is characterized by a long transient in which particles reorganize in clogged regions of different size, leading to heterogeneous spatial morphologies, characterized by large concentration fluctuations.

The transition of the system from regular flow to the fully clogged regime, where there is strictly no flow, is characterized by a wide regime where flows are intermittent. This intermediate region is specific of the clogging transition. When clogging happens in local regions around an obstacle configuration, burst-like dynamics will also eventually appear and affect the flow before the whole system is clogged. Even if the average flow measured in the landscape does not vanish, locally clogged regions will coexist with free flows around other obstacles. In such intermediate states the flow is locally ill-defined, since the average time to leave a certain bottleneck may diverge. Linking the dynamics of particles travelling across a disordered landscape and local clogging requires specific measurements that quantify whether clogs exist in a certain landscape before the average velocity vanishes and the system is fully arrested.

* sergi.granados@ub.edu

† ipagonabarraga@ub.edu

Understanding clogging in a disordered heterogeneous medium will benefit from a perspective based in the adopted methodology for a single bottleneck. In this paper we focus on the dynamical properties of steady states of moving particles driven through an heterogeneous landscape. Our scope lays in identifying what these dynamical states consist of, and how to locally identify clogged regions when these coexist with free flow regions, bridging two complementary perspectives on the same phenomenon. For this purpose, we define a temporal quantity that follows the standard methodology developed for the determination of clogged states in single bottlenecks introduced in Ref.[22]. This temporal quantity allows us to determine whether a general landscape contains local clogs or not. We refer to these states with local clogs and non-vanishing average velocities in the landscape as abnormal flow states. We demonstrate that in such anomalous flows, structural properties of the system such as the cluster distribution, or the velocity distribution of particles in clusters change qualitatively. By describing these dynamical and structural properties we provide a framework to understand how local clogs rise in disordered landscape and eventually lead to total clogging of the system with increasing obstacle density. Similarly to fully clogged states, abnormal flow appears at a rather constant density of obstacles ϕ_{pin}^c , which suggests the existence of an additional lengthscale that favours local clog formation. We focus on steady states of the system, where that average velocity and average cluster size have reached a steady value. This is crucial since clogging characterisation requires of long simulation runs to accurately capture the tails of power law distributions. This corresponds to relevant experimental situations, where clogs persist for arbitrarily long times compared to an initial transient state. We also demonstrate that power law exponents measured through single particle characteristic times are correlated to local measures of clogging as defined in the usual way [22].

We structure the paper as follows: In section II the simulation procedure is introduced, and the magnitudes of interest are defined. In section III the flow states are quantified as a function of the concentrations of moving and obstacle particles, by calculating the complementary cumulative distribution function of passing times of moving particles, building on the procedure introduced to analyze clogging through a single constriction [22]. This methodology allows to introduce a general notion of abnormal flow, where localised flow of particles coexist with persistently clogged regions where the flow is not well defined. This new flowing regime allows to build a state diagram that distinguishes between normal flow, abnormal flow, and clogged states, where the average velocity is zero. In section IV we compare the developed methodology with a local measure of clogging and establish a clear correlation between both approaches. Thus, we confirm the intuition that the abnormal region is a consequence of locally constricted regions, and identify the same trends and clogging exponents for both methodologies. In sec-

tion V, the dynamic and structural features of normal and anomalous flows are compared. We characterise the distribution of clusters size and the probability distribution functions of the velocity of particles belonging to clusters interacting with obstacles, which show that such quantities depend strongly on the system density. We finish with the main conclusions and implications of the obtained results in section VI.

II. SIMULATION METHODOLOGY

We carry out Brownian dynamics simulations of a 2D system of area L^2 with periodic boundary conditions, composed by a total number of $N = N_{\text{mov}} + N_{\text{pin}}$ disks of radius σ . N_{mov} disks move under the action of forces, while N_{pin} remain pinned at their initial positions. Both moving and pinned particles interact sterically with a force that derives from a Yukawa potential [32]

$$\mathbf{F}^{\text{int}}(\mathbf{r}_{ij}) = \frac{U_0}{\lambda} \frac{\sigma}{r_{ij}} \left(\frac{\sigma}{r_{ij}} + \frac{\sigma}{\lambda} e^{-\frac{r_{ij}}{\lambda}} - B \right) \hat{\mathbf{r}}_{ij}, \quad (1)$$

where $\mathbf{r}_{ij} = \mathbf{r}_i - \mathbf{r}_j$, $r_{ij} = |\mathbf{r}_i - \mathbf{r}_j|$ and $\hat{\mathbf{r}}_{ij} = \mathbf{r}_{ij}/r_{ij}$, where i and j refer to both moving and pinned particles. The parameter λ characterises the decay range of the steric interaction, while U_0 is the interaction strength.

Moving particle i evolves according to an overdamped dynamics

$$\frac{1}{\mu} \frac{d\mathbf{r}_i}{dt} = \sum_{j \neq i}^N \mathbf{F}^{\text{int}}(\mathbf{r}_{ij}) + \mathbf{F}^{\text{ext}} + \mathbf{F}^{\text{T}}(\mathbf{r}_i). \quad (2)$$

where, μ is the disk mobility and relates the short time diffusion coefficient and the temperature through the Boltzmann constant, $D_0 = \mu k_B T$.

The driving force has a constant value and without loss of generality, is chosen to act on the x-direction so that $\mathbf{F}^{\text{ext}} = F_D \hat{\mathbf{x}}$, where $\hat{\mathbf{x}}$. The last term in Eq. 2 accounts for the thermal bath, and its integration over a time step describes a Gaussian random displacement with second moment $\Delta \mathbf{r} = \mu \mathbf{F}_i^{\text{T}} \Delta t$ such that $\langle (\Delta r^T)^2 \rangle = 2D_0 \Delta t$ and zero mean.

The dynamics can be expressed in dimensionless form scaling distance and time by appropriate reference quantities. We consider the particle radius, σ , as the characteristic distance, and the characteristic time as the time required for a particle dragged by the driving force to move its own radius, $\tau_D = \sigma/(\mu F_D)$. Accordingly, Eq. (2) reads

$$\frac{d\bar{\mathbf{r}}_i}{dt} = \frac{U_0}{\lambda F_D} \bar{\psi}(\bar{\mathbf{r}}_i/\sigma, \lambda/\sigma) \hat{\mathbf{r}}_{ij} + \hat{\mathbf{x}} + \sqrt{\frac{2\tau_D}{Pe}} \bar{\xi}, \quad (3)$$

where bar indicates that the magnitudes have no dimensions. The term $\bar{\psi}(\bar{\mathbf{r}}_i/\sigma, \lambda/\sigma)$ is the Yukawa force in

Eq. (1) divided by U_0/λ . The term $\bar{\xi}$ describes a Gaussian stochastic function with $\langle \bar{\xi} \rangle = 0$ and $\langle (\bar{\xi})^2 \rangle = 1$. The Péclet number, $Pe = v_0\sigma/D_0$, quantifies the ratio between the velocity and the thermal contribution to the particle motion.

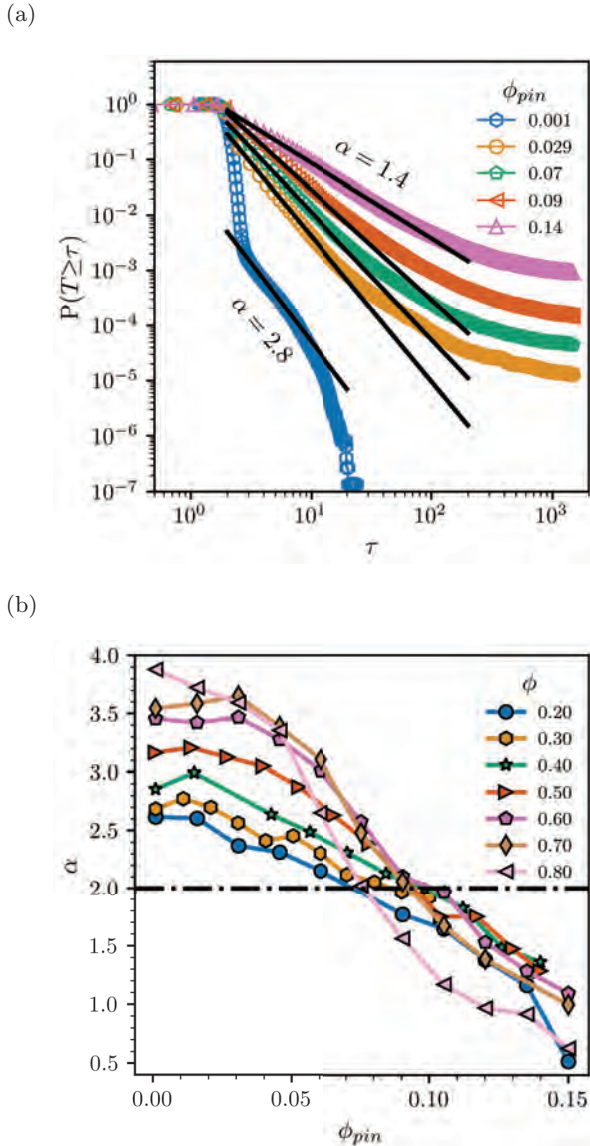


FIG. 1. (a) Computed complementary cumulative distribution function (CCDF) for $\phi = 0.40$. Black lines corresponds to the power law fit, and the calculated exponent, α is shown for the two extreme cases considered. The decay typically starts for $T > 2$, since it is the minimum moving time of a free particle, according to our definition of an event. Depending on the fraction of obstacles, one can observe a fast decay region produced by a majority of moving particles, or a power law region, where particles often interact with obstacles, which can lead to clogging events. (b) Characterisation of α as a function of the immobile particle packing fraction, ϕ_{pin} , for different total packing fractions, ϕ .

We are interested in the regime where driving and inter-particle forces dominate over thermal fluctuations. Accordingly, we consider $U_0/\lambda F_D = 300$, $Pe = 100$ and $\lambda/\sigma = 1$. The time step, Δt , is chosen small enough to avoid particle overlapping, $\Delta t/\tau_D = 1 \cdot 10^{-3}$. Both moving and pinned particles are initialized following a growing algorithm in which particles and obstacles are placed randomly in space and then evolved in time to grow to its size to reach the desired area fraction [31].

The number of moving particles in the simulation is constant and large enough to provide reliable statistics, $N_{mov} = 10000$. Simulations are performed fixing the total packing fraction, $\phi = (N_{mov} + N_{pin})\pi\sigma^2/L^2$, and varying the pinned packing fraction of particles, $\phi_{pin} = N_{pin}\phi\sigma^2/L^2$. Hence, the state of the flow will be characterized as a function of ϕ_{pin} and ϕ .

The simulation is first run until the average velocity of moving particles becomes constant $\langle v_x \rangle = cte$. After this initialisation, the tendency of particles to flow is captured by means of a characteristic time quantity, τ , that we explain below. In order to compare with standard clogging measurements, we will also measure the average particle velocity, and identify a state as clogged if it exhibits a zero average velocity in the direction of the driving force, thus $\langle v_x \rangle = \sum_i v_{i,x} \simeq 0$. Computationally, we never observe $\langle v_x \rangle \simeq 10^{-5}$ due to the thermal fluctuations. Thus, we take this threshold to identify a fully clogged state.

III. FLOWING STATES

We characterize the state of flow of the system computing the CCDF of disk displacement times. This function is constructed by quantifying the time, τ , it takes a disk to displace its own diameter, $d = 2\sigma$, in the direction of the driving force. We identify such intervals through dynamical measurements (DM), where we identify all events in which any given disk has moved a distance d through the numerical integration of Eq. (3) [33]. These events allow to determine the dynamic regimes of the moving disks. For example, free flowing particles have passing times close to $\tau \sim 2\tau_D$, while particles that interact with obstacles will exhibit larger τ . The flow regimes of the forced suspension are then analyzed using the CCDF, $P(T > \tau)$ that quantifies the fraction of all events that take a time T larger than a prescribed value τ . Later we will also characterise such events with static measurements (SM), a procedure that is equivalent to the standard local characterisation of clogging through bottlenecks.

Fig. 1a displays the CCDFs for a given overall area fraction, $\phi = 0.4$ as a function of the fraction of pinned disks, ϕ_{pin} . One can identify three different dynamical regimes. A first region of fast decay near $T = 2$ is observed for small fraction of obstacles, which corresponds to particles which do not interact strongly with the obstacles and are essentially driven by the applied force at

constant velocity. At larger times, a second region generally appears, characterized by larger displacement times, which is due to the interaction of the driven particles with fixed obstacles. This region can be characterized by a power law decay: Moving particles interact with obstacles, become trapped and may be able to move eventually. These interactions with constrictions and other free particles can give rise to clogging events that persist in time in certain bottlenecks of the system. For increasing obstacle fraction, the decay of the CCDF can start with this second region, as observed in Fig. 1a. Finally, a third region appears at largest times, produced by obstacles, in which the power law behaviour is lost. For such large times, the deviation is produced by particles that remain blocked most of the simulation run, typically due to a geometric confinement that hinders the flow, with no unclogging possibility. The saturation of the CCDF observed for increasing ϕ_{pin} is due to such blockage of free particles.

As shown in Fig. 1a, the second region can be adjusted by a power law, and the corresponding clogging exponent α can be systematically obtained following the procedure stated in Ref. [34], as a function of ϕ_{pin} . If $\alpha \leq 2$, the average passing of particles diverges, which means that in some regions of the landscape a clog can exist for an indefinite period of time, and will thus result in a local accumulation of particles. In such cases, the system may not be fully clogged and its average velocity may not be zero, but clogs coexists with flowing states of particles. Thus, in general, in this regime the average flow of particles can be well defined only locally in some regions of the landscape; accordingly, we refer to this flowing regime as abnormal flow.

By calculating the ϕ_{pin} at which the power law diverges, $\alpha(\phi_{pin}^a) = 2$, we can characterize the fraction of obstacles at which such abnormal flows are developed. Fig. 1b), displays the value of α as a function of ϕ_{pin} for different ϕ , and we find an important feature of clogging of colloidal suspensions in disordered media: The fraction of obstacles where normal flow becomes abnormal remains roughly constant $\phi_{pin}^a \simeq 0.09$, with a weak dependence on the overall area fraction ϕ .

The different dynamical regimes that control the transition from normal flow to complete clogging for the driven disks in a system composed by a random distribution of non-overlapping obstacles can be summarized in the state diagram of Fig. 2 that identifies the region of normal flow ($\alpha > 2, \langle v_x \rangle > 0$), abnormal flow ($\alpha < 2, \langle v_x \rangle > 0$), and clogging ($\alpha < 2, \langle v_x \rangle = 0$), as a function of ϕ and ϕ_{pin} . This diagram is similar to that shown by Péter *et al.* [31]: We see that flow vanishes at a constant critical obstacle density ϕ_{pin}^c . This constant ϕ_{pin}^c indicates the existence of a characteristic distance l_c between obstacles that impedes particle flows. Introducing in the diagram the notion of abnormal flow, we observe an additional anomalous region where the average velocity is not strictly zero, yet we observe that the distribution of times required for a particle to move

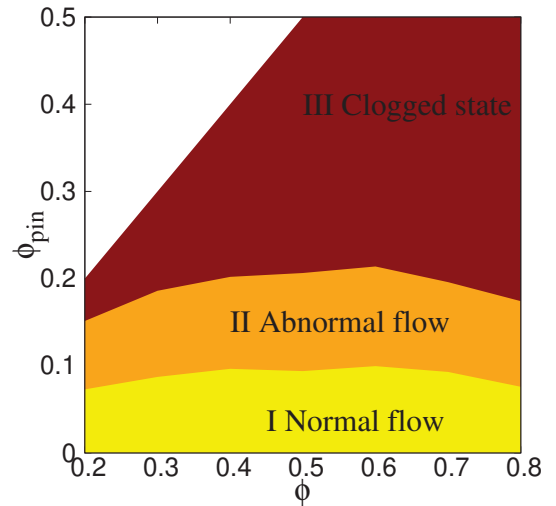


FIG. 2. State diagram, which identifies the three regimes of collective particle displacement of normal flow, abnormal flow, and clogging. The maximum width of the normal region is observed for intermediate densities, while it decreases for small ϕ , where isolated particles get trapped easily in constrictions, or for large ϕ , where when we approach the jamming transition.

its own diameter τ is diverging. In these states, clogs can locally develop for an indefinite period of time, dramatically altering the flowing properties of the moving particles in the landscape. Furthermore, we observe that similar to ϕ_{pin}^c , the critical abnormal flow density ϕ_{pin}^a also depends weakly on the obstacle density, suggesting an additional characteristic distance between obstacles l_a that sets the appearance of local clogs in the landscape. Different steric potentials will affect these characteristic sizes, l_c and l_a , that sets the diagram width, but will not affect the observed phenomenology. It is true that significant changes in the character of the potential, e.g. its range and attractive nature, can affect the stability of the clusters and clogs significantly. Nonetheless, these aspects complement the main message of this piece of work and may be the subject of subsequent research.

The average height of the of the normal flow region is around $\phi_{pin} = 0.09$, which is a relatively small area fraction. The normal and abnormal regions are comparable in width, showing that anomalous flow is not a marginal feature that takes place right before reaching a completely clogged state. Additionally, in the diagram, we find evidence of cooperation, as for increasing density ϕ , the normal region becomes thicker: For a constant ϕ_{pin} we can eliminate local clogs by means of increasing the fraction of moving particles.

At high densities, $\phi \geq 0.65$, we expect that increasing ϕ_{pin} the system exhibits jamming [31]. Some features indeed point towards the existence of the jamming transition in these regions: Both ϕ_{pin}^a and ϕ_{pin}^c slightly decrease for increasing ϕ . Even before the jamming transition, a

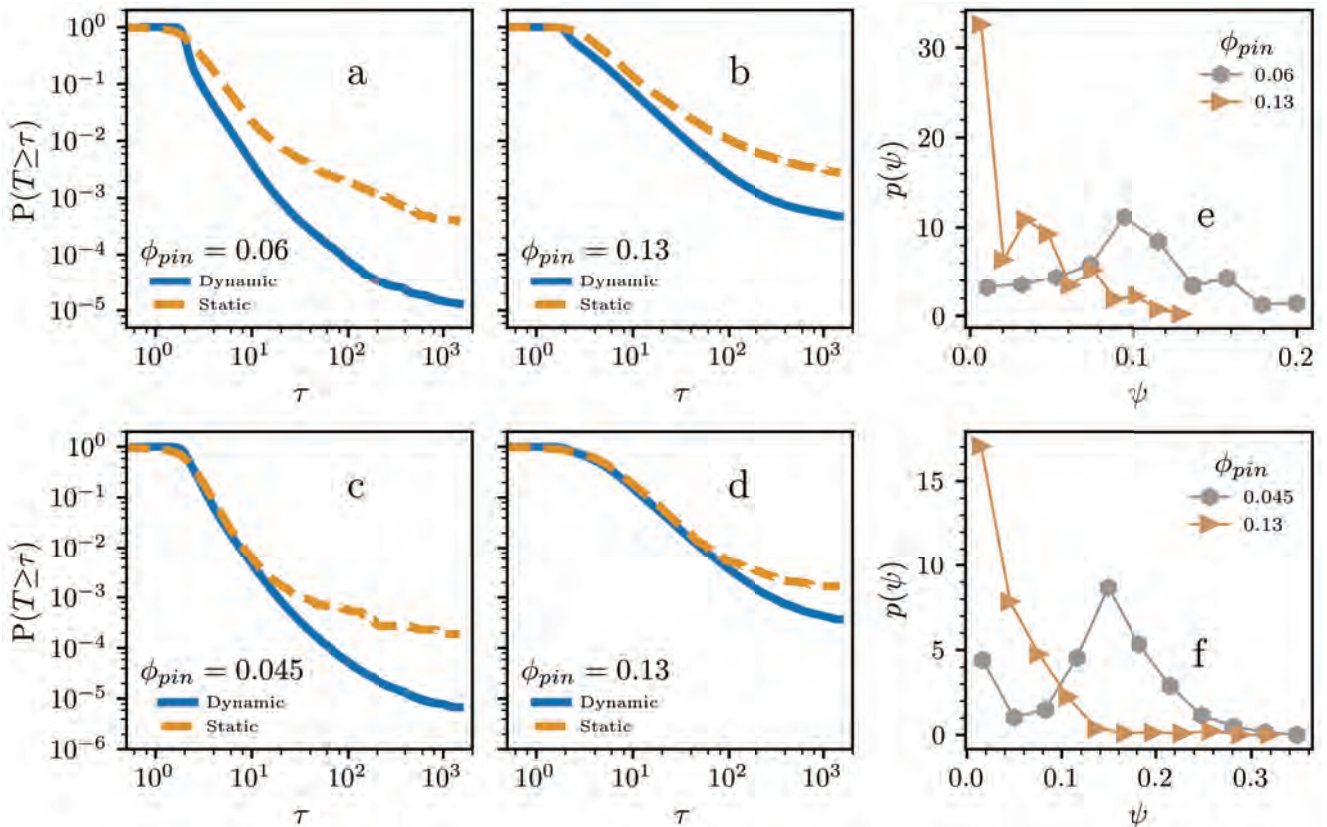


FIG. 3. SM and DM comparison for $\phi = 0.4$ (a,b,e) and $\phi = 0.6$ (c,d,f), in the normal region (a,c) and abnormal region (b,d). Our results show how SM and DM are not independent of each other and correlate in the characteristic algebraic decaying exponent. (e) and (f) show how both densities exhibit the same tendency: In the normal region, the flow pdfs peaks at a maximum value at the center, while in the abnormal region the flow pdfs has a maximum value at 0 and decreases with increasing flow rate.

region of abnormal flow develops before the average velocity decreases to zero $\langle v_x \rangle = 0$. Hence, the anomalous flow regimes are a general, strong feature of disordered landscapes, that can smoothly lead to fully clogged states as the fraction of obstacles increase.

In the next section we will establish the connection between clogging measured as previously described, and clogging measured in local regions of the landscape, which play a similar role of a bottleneck.

IV. LOCAL FLOW PROPERTIES

To provide further insight on the implications of the local spatial organization of abnormal flowing events, we analyse the flow of particles and compare the clogging measurements as typically measured locally through bottlenecks [22]. For this purpose, we divide the simulation box in the y direction in sections of a characteristic width l_s . We choose $l_s = 2.5\sigma$ comparable to l_c , which is of the order of magnitude of particle dimension. We measure the time interval it takes two consecutive particles to

cross the region defined by l_s [22]. We shall refer here to this procedure as static measurement (SM), as opposed to the previously DM protocol.

Fig. 3.a-d displays the CCDF obtained using the SM and DM protocols. The curves show similar trends, and indicates that SM systematically overestimates the events that require larger times, hence underestimating the value of α . In general, this deviation decreases with increasing ϕ_{pin} and ϕ , as can be appreciated in Fig. 4. The underestimation of α using SM is due to its sensitivity to flow disturbances due to large passing times produced by density fluctuations. For $\phi = 0.6$ we observe that both methods give quantitatively similar exponents. Thus, we find that SM and DM provide complementary methods to analyze the emergence of abnormal flow in suspensions of forced particles in a disordered system. In other words, locally measuring the flow along the disordered obstacle at a certain definite locations, is akin to following the flow of individual particles. However, the DM method, when characterising the dynamic properties of a certain disordered medium consisting of an arbitrary array of constrictions, provides a more robust characterisation because it is less sensitive to obstacle

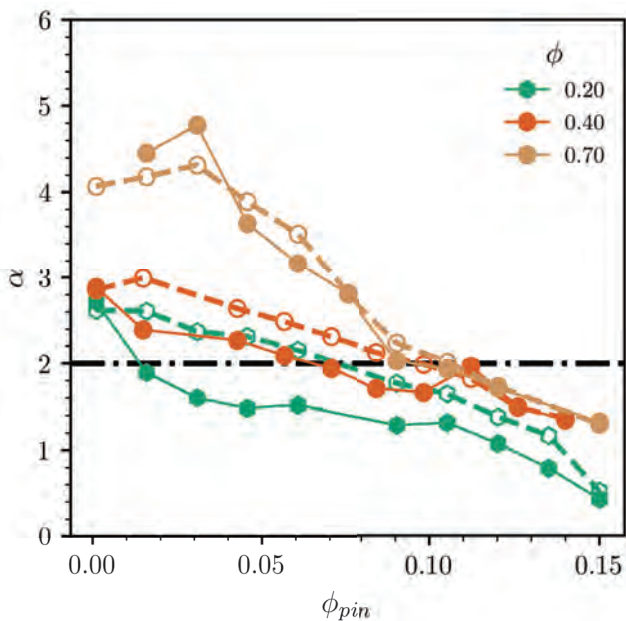


FIG. 4. Static measurements (filled markers with continuous lines) vs dynamic measurements (dashed lines and empty markers), for different total area fractions. Both methods exhibit qualitatively similar exponents. The SM method tends to overestimate α compared to DM. This tendency weakens as ϕ increases, and all the moving particles connect forming a large continuous cluster.

density fluctuations.

The robustness of the measured exponent α suggests that the state diagram, and the presence of an abnormal flow regime initially identified for the flow through isolated bottlenecks is a generic feature of the clogging transition. The comparison between DM and SM provides complementary strategies to analyze the transition when clogging does not take place through a unique obstacle.

We can also quantify the local particle flow using SM. To this end, we count the number of particles crossing a prescribed segment of length l_s perpendicular to the direction of the driving force during a prescribed time interval Δt . We choose $\Delta t = 20d\tau_D$, as a compromise to analyse the flow during a relevant amount of time minimising the impact of dispersion due to individual particle motion. The flow in each cross section, defined by l_c , is then calculated as $\psi = n_{mov}/l_c\Delta t$, where n_{mov} is the number of moving particles across the line defined by l_c in a time Δt . Fig. 3e,f shows that in the normal regime, the flow peaks around a certain value that depends on ϕ_{mov} . In the abnormal regime, the flow distribution decreases monotonously and has its maximum at $\phi = 0$, providing a complementary perspective on the properties of the abnormal flow as opposed to normal flow.

In this section we have explored the clog dynamics in local regions of the landscape, in a similar way as it is typically characterised in single bottlenecks [22]. Our analy-

sis demonstrates that the anomalous dynamics observed is directly correlated to clog development in localised regions of the system. The picture that emerges is that of a disordered system with heterogeneous dynamics, where bottlenecks with diverging distributions of characteristic passing times, τ , coexist with free flow paths [35]. These bottlenecks tend to accumulate particles, forming large dense clogs, and flow will tend to be localised around these bottleneck zones or regions where fluctuations of obstacles density have allowed a constant flow. To complete this picture, we now turn to study the distribution of particle velocities in clusters, and cluster distributions, in order to map this description to a geometrical and dynamical picture of the properties of moving particles in these anomalous flow regimes.

V. NORMAL AND ABNORMAL DYNAMICS

To gain insight on the particle dynamics that gives rise to abnormal flow and the related emergent properties, we analyze the disk cluster distribution and the relation to the velocity distribution at the steady state. We use a distance criterion, and consider that all particles with a separation smaller than $\sigma + \delta$ belong to the same cluster [36]. Fig. 3a shows the cluster probability distribution function (pdf) in the different flowing regimes. The decay of the pdfs is generically compatible with an algebraic decay. For small densities, e.g. $\phi = 0.2$, moving from the normal (dashed line, pink triangles) to the abnormal (continuous line, pink pentagons) flow regime results in a slower decay of the pdf, with an effective exponent of the algebraic tail that increases from $\xi < -2$ to $\xi > -2$. This implies that for small clogging densities, in the anomalous regime, the average number of clusters diverges and there is no characteristic cluster size. Instead, for arbitrarily large systems, and thus increasing N with the same ϕ_{pin} and ϕ_{mov} , we will find arbitrarily large clusters in the anomalous regime.

At higher concentrations, e.g. $\phi = 0.6$, in the normal flow regime (dashed line, silver triangles), in both normal and abnormal regions $\xi > -2$, implying that the mean cluster size is always diverging. The difference remains in the fact that now, arbitrarily large clusters will appear too in the normal flow regime, but these clusters do not induce clogging. This change of trend translates into qualitative differences in the morphology and flowing characteristics of the system depending on the total fraction of particles. To further understand how the area fraction affects the distribution of particles in the system, in Fig. 3b we show the average number of particles in clusters $\langle N_c \rangle$ for different ϕ , as a function of ϕ_{pin} . Indeed, it shows a strong qualitative dependence of $\langle N_c \rangle$ for the different curves, depending on ϕ . At small ϕ , flowing particles remain in small clusters. Keeping ϕ constant, as ϕ_{pin} increases, particles increase their probability to accumulate in small groups near obstacles, which explains the increase in $\langle N_c \rangle$. For larger ϕ , already at

small ϕ_{pin} particles display a strong probability to accumulate near obstacles while still being able to flow. By increasing ϕ_{pin} starting in the normal regime, obstacles initially divide the flow in disconnected regions of normal flow, sharply decreasing the average cluster size. Eventually, when $\phi_{pin} > \phi_{pin}^a$ flow is interrupted and results in clogs, as depicted in Fig. 6a-b, changing the decreasing trend, since now particles are not only divided in disconnected regions but also accumulate in clogs, as shown in Fig. 5b. Hence, in this case local clogs appear, and $\langle N_c \rangle$ decreases more smoothly, since such local clogs arise in spatially uncorrelated regions of the system disconnecting flow regions, but still favouring accumulation of particles in bottlenecks. Even if the dependence of $\langle N_c \rangle$ with ϕ_{pin} differs qualitatively for large and small ϕ , the resulting states are the same: Particles separate in regions of high density near bottlenecks and regions of small density between bottlenecks.

To quantify the impact of the dynamic properties of the clusters on these different scenarios we compute the velocity pdfs of particles belonging to clusters larger and smaller than the average cluster size, $\langle N_c \rangle$, and for two different densities. Fig. 6 displays a series of snapshots of the clustering of disks in the normal, Fig. 6.a, and abnormal, Fig. 6.b and Fig. 6.c, regimes. The plots show that abnormal flow correlates with the development of large clusters seeded around regions with a local enhancement in the concentration of obstacles. As the overall packing fraction increases, Fig. 6.e, the clusters grow towards a jammed state.

Fig. 6.d-f displays the velocity pdfs for particles interacting with obstacles and belonging to small and large clusters. For normal flow, Fig. 6.d, most particles displace at the velocity corresponding to free flow, $v_f = d/2 \simeq 1$, driven by the external force. Only a small fraction of the particles are trapped by an obstacle, displaying a velocity close to zero. This fraction is slightly larger for the small fraction of disks which belong to large clusters.

Entering the abnormal flow regime, the velocity pdfs for particles in small and large clusters show some qualitative differences. In the abnormal flow regime, far from the clogging transition, the velocity distribution of moving particles shows a characteristic two-peaked bimodal distribution, as observed in Fig. 6e. Local clogs coexist with normal flows, as appreciated in Fig. 6.b. Particles belonging to small clusters exhibit clearly this two-peaked bimodal distribution, with a finite fraction of particles displacing in reaction to the applied force, v_f , corresponding to localised particle free flow. Particles released from clogged states contribute to this peak, as they form trails moving freely until reaching the next clogged region. The other peak correspond essentially to arrested particles, with a velocity close to zero. Small clusters of particles accumulating at clog regions in specific bottlenecks of the system, temporarily or spatially isolated from flowing regions contribute to this peak. All these events can be observed in the snapshots of Fig. 6.b. In

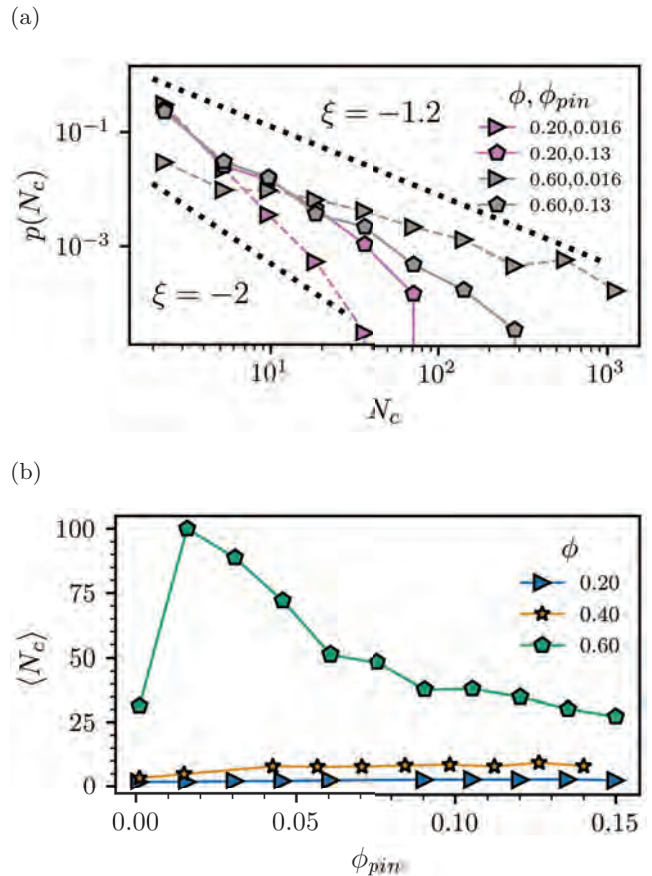


FIG. 5. (a) Probability distribution function of number of particles in clusters, in the normal region (dashed lines, triangles) and abnormal region (continuous lines, pentagons), for two different densities, 0.2 (pink) and 0.6 (silver). For $\phi = 0.2$, entering the abnormal region implies an increase of algebraic exponent ξ , while for $\phi = 0.6$ it implies a decrease of ξ . This highlights qualitatively different flowing properties for small and large concentrations. (b) Cluster size as a function of ϕ_{pin} for different ϕ . For $\phi < 0.5$, the average number of clusters increases gradually with increasing ϕ_{pin} , while for $\phi > 0.5$ it decreases, showing how in this case interrupting the flow translates into smaller clusters.

large clusters, the largest peak appears at $v_x \sim 0$, produced by large regions where clogs persist in time, giving rise to intermittent flows, but also in coexistence with paths where particles can flow. Such mixed state highlights the key ingredient of abnormal flows in disordered mediums: Intermittent flows and temporary blockages arise locally throughout the disordered system as particles are dynamically trapped and released from local constrictions.

As shown in Fig. 6.f, at higher ϕ , as we approach the clogging transition, a smaller fraction of disks are contained within small clusters and the bimodal velocity distribution is barely visible. Increasing ϕ decreases the regions of locally small density, as can be seen in

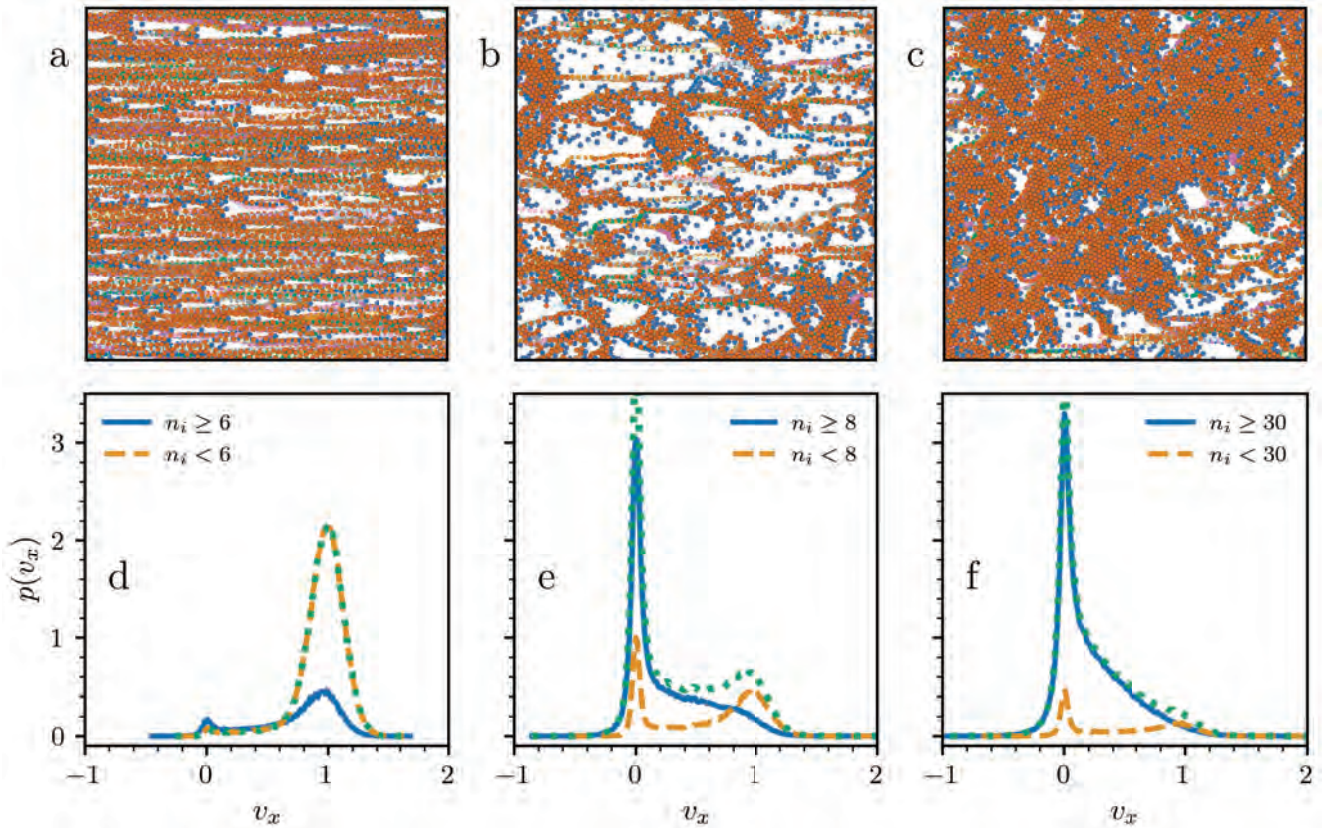


FIG. 6. (a,d) Shows a state of normal flow with $\phi = 0.4$, $\phi_{pin} = 0.03$ (b,e) Shows a state of abnormal flow with $\phi = 0.4$, $\phi_{pin} = 0.13$ (c,f) Shows a state of abnormal flow with $\phi = 0.6$, $\phi_{pin} = 0.13$, respectively. Figs (a,b,c) show snapshots of the simulations, different coloured lines correspond to different particle trajectories, showing where the flow typically takes place in the landscape. Figures (d, e, f) show the velocity distribution for clusters with n_i particles smaller than the average size $\langle N_c \rangle$ (dashed line), clusters larger than $\langle N_c \rangle$ (continuous line), and the probability distribution of all the particles (dotted line). The velocity is calculated for all particles as $v_x = d\langle \bar{r}_x \rangle / d\bar{t}$. For $\phi < 0.5$ the abnormal region exhibits a bimodal distribution, where big clusters have the most particles at $v_x = 0$, and small ones the largest velocities peaking at $v_x = 1$. For $\phi > 0.5$, the doubled peaked distribution disappears, and the total pdfs almost coincide with those belonging to large clusters.

Fig. 6b, favouring that all particles belong to few large clusters that dominate the system. For such large densities, instead of having a large number of small clusters distributed in uncorrelated bottlenecks, now we find a small number of big clusters, where the velocities inside the same cluster are correlated. The resulting velocity distribution corresponds to the attenuation of the bimodal two-peak distribution of velocities as seen in Fig. 6f. Large clusters exhibit a strong peak at $v_x \sim 0$, which corresponds to particles in clogs. The pdf decreases monotonously after the peak, exhibiting a broad range of intermediate velocities, and a marked depletion of particles moving at $v_x \simeq 1$. Hence, almost all particles are slowed down or trapped in a small number of larger clusters, containing a wide distribution of velocities.

To summarize, the velocity distributions highlight the nature of the abnormal flow and helps understand how for a given area fraction increasing ϕ_{pin} local clogs arise and affect the flow and system morphology. Typically, for $\phi < \phi_{pin}^a$ disks flow freely, either in big or small clus-

ters. Above ϕ_{pin}^a large clusters peak in the distribution around $v_x = 0$ due to constrictions and bottlenecks hindering the flow and leading to intermittent flows. Small ϕ results in a landscape of uncorrelated clogs and free particles, characterised by a bimodal distribution of velocities. Increasing ϕ weakens the bimodal distribution of velocities. Instead, large, dense clusters contribute to increase the correlation of clogging events, resulting in a mixed distribution of velocities that peak at $v_x \sim 0$

VI. CONCLUSIONS

We have carried out a thorough study on how forced particles move and give rise to flow in a randomly disordered obstacle landscape. The methodology put forward has allowed us to identify and quantify a regime of abnormal flow, where locally clogged regions persist in time and intermittent motion emerges, from the normal flow regime, where generally, the flow is well defined in the

whole disordered system. We have classified the properties of these two regimes at small and large densities, characterized by the development of a bimodal velocity distribution for small densities, and a large region of coexistence of particles with mixed velocities in large clusters for large densities. The weak dependence of the critical anomalous flow regime shows that different area fractions may reach the abnormal regime at different obstacle densities due to cooperation between flowing particles, which fluidize the system and hinder clogged states. The flowing behavior of the forced disks is also altered in the abnormal regime, where the distribution of flow through local regions of the landscape is maximum for arrested clusters and decreases monotonously, in comparison to a non-zero maximum peak in the normal regime.

We have characterized some of the structural features related to the anomalous flow regime by analysis the morphologies of particle clusters. We have observed that, independently to the total density, anomalous flows always exhibit a diverging average cluster size, which indicates that there is no characteristic cluster size scale. This contrasts with the fact that the abnormal flow density of obstacles, ϕ_{pin}^a , depends weakly on ϕ , meaning that there is a characteristic obstacle space, l_a , which results in clog formation, favouring large densities in bottlenecks and small densities in other regions. It is for this reason that we observe different dynamical and structural features for small and large local densities: Small densities start with disconnected flows, and large densities starts with connected flows, but both of them separate in large and small density regions in the anomalous regime as ϕ_{pin} increases, translating into an increase of the average cluster size in the first case and a decrease in the second case.

The study performed has shown that the transition

from normal flow to clogging is complex, and it is controlled by a broad region of abnormal flow where local clogging events coexist with the underlying flow imposed by the external driving. The nature and magnitude of these events strongly correlates with the distribution of particle clusters that nucleate and develop around local constrictions. This correlation is not trivial, since clogs in bottlenecks depend on very specific structural and dynamic properties, such as the bottleneck inclination with respect the force, the number of particles instantaneously arriving to a specific bottleneck and the size of the bottleneck. However, there is still generic features in the abnormal flow, such as the constant ϕ_{pin}^a or separation in large and small density regions. Therefore, the abnormal regime, initially identified in systems that undergo a clogging transition through a single obstruction, is also present in a disordered system, characterized by a spatial distribution of bottlenecks, unifying our understanding of the transition toward clogging.

The flexible methodology developed here can be applied to a wide variety of systems. from heterogeneous mixtures of particles to interacting active matter, to gain insight of how cooperation can be maximised to avoid local clogged states or, inversely, achieve locally spatial flows at some regions of the landscape.

ACKNOWLEDGMENTS

I.P. acknowledges support from Ministerio de Ciencia e Innovación MICIN/AEI/FEDER for financial support under grant agreement PID2021-126570NB-I00 AEI/FEDER-EU, and from Generalitat de Catalunya under Program Icrea Acadèmia and project 2021SGR-673.

-
- [1] N. A. M. Araújo, L. M. C. Janssen, T. Barois, G. Boffetta, I. Cohen, A. Corbetta, O. Dauchot, M. Dijkstra, W. M. Durham, A. Dussutour, S. Garnier, H. Gelderblom, R. Golestanian, L. Isa, G. H. Koenderink, H. Löwen, R. Metzler, M. Polin, C. P. Royall, A. Šarić, A. Sengupta, C. Sykes, V. Trianni, I. Tuval, N. Vogel, J. M. Yeomans, I. Zuriguel, A. Marin, and G. Volpe, *Steering self-organisation through confinement*, *Soft Matter* **19**, 1695 (2023).
 - [2] A. Corbetta and F. Toschi, *Physics of human crowds*, *Annual Review of Condensed Matter Physics* **14**, 311 (2023).
 - [3] A. Nicolas, S. Ibáñez, M. N. Kuperman, and S. Bouzat, *A counterintuitive way to speed up pedestrian and granular bottleneck flows prone to clogging: can ‘more’ escape faster?*, *Journal of Statistical Mechanics: Theory and Experiment* **2018**, 083403 (2018).
 - [4] R. Yano, *Crowd evacuation of pairs of pedestrians*, *Communications in Theoretical Physics* **74**, 045601 (2022).
 - [5] M. Haghani and M. Sarvi, *Crowd behaviour and motion: Empirical methods*, *Transportation Research Part B: Methodological* **107**, 253 (2018).
 - [6] C. von Krüchten and A. Schadschneider, *Empirical study on social groups in pedestrian evacuation dynamics*, *Physica A: Statistical Mechanics and its Applications* **475**, 129 (2017).
 - [7] A. Garcimartín, J. M. Pastor, L. M. Ferrer, J. J. Ramos, C. Martín-Gómez, and I. Zuriguel, *Flow and clogging of a sheep herd passing through a bottleneck*, *Phys. Rev. E* **91**, 022808 (2015).
 - [8] I. Zuriguel, J. Olivares, J. M. Pastor, C. Martín-Gómez, L. M. Ferrer, J. J. Ramos, and A. Garcimartín, *Effect of obstacle position in the flow of sheep through a narrow door*, *Phys. Rev. E* **94**, 032302 (2016).
 - [9] S. M. Rubio-Largo, A. Janda, D. Maza, I. Zuriguel, and R. C. Hidalgo, *Disentangling the free-fall arch paradox in silo discharge*, *Phys. Rev. Lett.* **114**, 238002 (2015).
 - [10] T. Borzsonyi, E. Somfai, B. Szabo, S. Wegner, P. Mier, G. Rose, and R. Stannarius, *Packing, alignment and flow of shape-anisotropic grains in a 3d silo experiment*, *New. J. Phys* **18**, 093017 (2016).
 - [11] B. V. Guerrero, L. A. Pugnali, C. Lozano, I. Zuriguel, and A. Garcimartín, *Slow relaxation dynamics of clogs in*

- a vibrated granular silo, *Phys. Rev. E* **97**, 042904 (2018).
- [12] O. Chepizhko and T. Franosch, Ideal circle microswimmers in crowded media, *Soft Matter* **15**, 452 (2019).
- [13] Z. B. Sendekie and P. Bacchin, Colloidal jamming dynamics in microchannel bottlenecks, *Langmuir* **32**, 1478 (2016).
- [14] T. Laar, S. Klooster, K. Schroën, and J. Sprakel, Transition-state theory predicts clogging at the microscale, *Scientific Reports* **6**, 28450 (2016).
- [15] S. G. Leyva, R. L. Stoop, P. Tierno, and I. Pagonabarraga, Dynamics and clogging of colloidal monolayers magnetically driven through a heterogeneous landscape, *Soft Matter* **16**, 6985 (2020).
- [16] C. Duchene, V. Filipe, S. Huille, and A. Lindner, Clogging of microfluidic constrictions by monoclonal antibody aggregates: role of aggregate shape and deformability, *Soft Matter* **16**, 921 (2020).
- [17] A. Sauret, K. Somszor, E. Villermaux, and E. Dressaire, Growth of clogs in parallel microchannels, *Phys. Rev. Fluids* **3**, 104301 (2018).
- [18] B. Dersoir, M. R. de Saint Vincent, M. Abkarian, and H. Tabuteau, Clogging of a single pore by colloidal particles, *Microfluidics and Nanofluidics* **19**, 953 (2015).
- [19] R. C. Hidalgo, A. Goñi Arana, A. Hernández-Puerta, and I. Pagonabarraga, Flow of colloidal suspensions through small orifices, *Phys. Rev. E* **97**, 012611 (2018).
- [20] N. Delouche, B. Dersoir, A. B. Schofield, and H. Tabuteau, Flow decline during pore clogging by colloidal particles, *Phys. Rev. Fluids* **7**, 034304 (2022).
- [21] M. Souzy and A. Marin, Role of liquid driving on the clogging of constricted particle suspensions, *Journal of Fluid Mechanics* **953**, A40 (2022).
- [22] I. Zuriguel, D. R. Parisi, R. C. Hidalgo, C. Lozano, A. Janda, P. A. Gago, J. P. Peralta, L. M. Ferrer, L. A. Pugnali, E. Clément, D. Maza, I. Pagonabarraga, and A. Garcimartín, Clogging transition of many-particle systems flowing through bottlenecks, *Scientific Reports* **4**, 7324 (2014).
- [23] A. Garcimartín, I. Zuriguel, J. Pastor, C. Martín-Gómez, and D. Parisi, Experimental evidence of the “faster is slower” effect, *Transportation Research Procedia* **2**, 760 (2014), the Conference on Pedestrian and Evacuation Dynamics 2014 (PED 2014), 22-24 October 2014, Delft, The Netherlands.
- [24] M. Souzy, I. Zuriguel, and A. Marin, Transition from clogging to continuous flow in constricted particle suspensions, *Phys. Rev. E* **101**, 060901 (2020).
- [25] J. C. Bellizotti Souza, N. P. Vizarrim, C. J. O. Reichhardt, C. Reichhardt, and P. A. Venegas, Clogging, diode and collective effects of skyrmions in funnel geometries, *New. J. Phys* **24**, 103030 (2022).
- [26] C. Reichhardt and C. J. O. Reichhardt, Clogging, dynamics, and reentrant fluid for active matter on periodic substrates, *Phys. Rev. E* **103**, 062603 (2021).
- [27] C. Reichhardt and C. J. O. Reichhardt, Directional clogging and phase separation for disk flow through periodic and diluted obstacle arrays, *Soft Matter* **17**, 1548 (2021).
- [28] R. L. Stoop and P. Tierno, Clogging and jamming of colloidal monolayers driven across disordered landscapes, *Commun. Phys* **1**, 68 (2018).
- [29] C. Reichhardt and C. J. O. Reichhardt, Clogging and depinning of ballistic active matter systems in disordered media, *Phys. Rev. E* **97**, 052613 (2018).
- [30] A. Zamani and B. Maini, Flow of dispersed particles through porous media — deep bed filtration, *Journal of Petroleum Science and Engineering* **69**, 71 (2009).
- [31] H. Péter, A. Libál, C. Reichhardt, and C. Reichhardt, Crossover from jamming to clogging behaviors in heterogeneous environments, *Scientific Reports* **8** (2017).
- [32] H. Lowen and G. Szamel, Long-time self-diffusion coefficient in colloidal suspensions: theory versus simulation, *Journal of Physics: Condensed Matter* **5**, 2295 (1993).
- [33] Specifically, we follow the displacement of all particles and, when the displacement reaches d , we identify the associated time, τ , and reset the corresponding counter of the particle to 0.
- [34] M. Newman, Power laws, pareto distributions and zipf’s law, *Contemporary Physics* **46**, 323 (2005).
- [35] See Supplemental Material at [URL will be inserted by publisher] for visualisation of the simulation dynamics.
- [36] We choose $\delta = 0.1\sigma$, to minimize the impact of thermal displacements in the cluster characterization.
- [37] A. Guével, Y. Meng, C. Peco, R. Juanes, and J. E. Dolbow, A darcy-cahn-hilliard model of multiphase fluid-driven fracture, *Journal of the Mechanics and Physics of Solids* **181**, 105427 (2023).
- [38] A. Garcimartín, M. Pastor, C. Martín-Gómez, D. Parisi, and I. Zuriguel, Pedestrian collective motion in competitive room evacuation, *Scientific Reports* **7**, 1 (2017).
- [39] A. Garcimartín, D. R. Parisi, J. M. Pastor, C. Martín-Gómez, and I. Zuriguel, Flow of pedestrians through narrow doors with different competitiveness, *Journal of Statistical Mechanics: Theory and Experiment* **2016**, 043402 (2016).
- [40] B. Blanc, J.-C. Geminard, and L. Pugnali, On-and-off dynamics of a creeping frictional system, *The European physical journal. E, Soft matter* **37**, 67 (2014).
- [41] B. Widom, Random sequential filling of intervals on a line, *The Journal of Chemical Physics* **58**, 4043 (1973).

Publication 5:
Hydrodynamics is needed to explain propulsion in
chemophoretic colloids raft

Dolachai Boniface¹, Sergi G. Leyva^{1,2}, Ignacio Pagonabarraga^{1,2}, and Pietro
Tierno^{1,2,3}

¹Departament de Física de la Matèria Condensada, Universitat de Barcelona, 08028 Barcelona,
Spain

²Universitat de Barcelona Institute of Complex Systems (UBICS), Universitat de Barcelona,
08028 Barcelona, Spain

³Institut de Nanociència i Nanotecnologia, IN²UB, Universitat de Barcelona, 08028 Barcelona,
Spain

ArXiv: <https://doi.org/10.48550/arXiv.2309.11084>

Clustering induces switching between phoretic and osmotic propulsion in active colloidal rafts

Pietro Tierno (✉ ptierno@ub.edu)

University of Barcelona <https://orcid.org/0000-0002-0813-8683>

Dolachai Boniface

University of Barcelona <https://orcid.org/0000-0002-1035-5126>

Sergi Leyva

University of Barcelona <https://orcid.org/0000-0001-9176-9285>

Ignacio Pagonabarraga

University of Barcelona <https://orcid.org/0000-0002-6187-5025>

Article

Keywords:

Posted Date: January 26th, 2024

DOI: <https://doi.org/10.21203/rs.3.rs-3869680/v1>

License:   This work is licensed under a Creative Commons Attribution 4.0 International License.

[Read Full License](#)

Additional Declarations: There is **NO** Competing Interest.

Clustering induces switching between phoretic and osmotic propulsion in active colloidal rafts

Dolachai Boniface,^{1,*} Sergi G. Leyva,^{1,2,*} Ignacio Pagonabarraga,^{1,2} and Pietro Tierno^{1,2,3,†}

¹*Departament de Física de la Matèria Condensada, Universitat de Barcelona, 08028, Spain*

²*University of Barcelona Institute of Complex Systems (UBICS), 08028, Barcelona, Spain*

³*Institut de Nanociència i Nanotecnologia, Universitat de Barcelona (IN2UB), 08028, Barcelona, Spain*

(Dated: January 16, 2024)

Active particles driven by chemical reactions are the subject of intense research to date due to their rich physics, being intrinsically far from equilibrium, and their multiple technological applications. Recent attention in the field is now shifting towards exploring the fascinating dynamics of mixture of active and passive systems. Here we realize active colloidal rafts, composed of a single catalytic particle encircled by several shells of passive microspheres, and assembled via light activated chemophoresis. We show that the cluster propulsion mechanism switches from diffusiophoretic to diffusioosmotic by increasing the number of colloidal shells. Using the Lorenz reciprocal theorem, we demonstrate that in large clusters self-propulsion emerges by considering hydrodynamics via the diffusioosmotic response of the substrate. The dynamics in our active colloidal rafts are governed by the interplay between phoretic and osmotic effects. Thus, our work highlights their importance in understanding the rich physics of active catalytic systems.

In the past few years, active colloidal particles have led to several exciting developments in the field of non-equilibrium statistical mechanics [1–4] while being also used as simplified models to reproduce emerging phenomena in biological self-propelling systems [5–8]. Since the pioneering works of Ismagilov *et al.* [9] and Paxton *et al.* [10], chemical reactions have been routinely used to induce propulsion in asymmetric systems [11] including Janus particles [12–15], nanorods [16, 17], dimers [18, 19], mixtures [20, 21] and many others [22–24]. Besides the interest in the reaction mechanism that leads to net motion, these particles showed the capabilities to pick up, transport, and release microscopic cargoes on command [25–28]. Thus, they may find direct applications in different technological fields, including biomedicine [29], targeted drug delivery [30] and microfluidics [31].

In several catalytic systems, self-propulsion is usually explained in terms of electrophoresis [32] and/or chemophoresis [33], namely the particle motion in an electric field/concentration gradient generated by the chemical activity of the particle [34]. The release or consumption of chemical elements produces also a

concentration gradient along the surfaces in the vicinity of the catalytic system. The vast majority of the self-propelled catalytic systems evolve close to a substrate. Thus, one can expect the presence of a local osmotic flow, which may affect the system dynamics through viscous interactions [35]. Actually, the osmotic flows on the substrate may even oppose and compete with particle diffusiophoresis. This competition has already been used to concentrate passive nanoparticles in a capillary channel [36]. Because both phenomena have a similar osmotic origin [37], the contributions of diffusiophoresis and substrate diffusioosmosis are difficult to disentangle [33]. As a consequence, most of the theoretical and simulation models in the field do not consider the impact of hydrodynamic interactions associated with substrate diffusioosmosis, and used an "ad hoc", effective diffusiophoresis to describe the experimental results. In contrast, a recent theoretical work showed that the diffusioosmotic contribution can be used even to guide active Janus particles across a chemically patterned substrate [38].

Here, we combine experiments and theory to demonstrate that the diffusioosmotic flow induced by the catalytic particle due to the near surface is necessary to describe the motion of active particles driven by chemical reactions. We realize active colloidal rafts composed of several shells of passive spheres around a single catalytic apolar particle, and investigate the raft kinetics and dynamics during the illumination process. These clusters grow up to an area of 120 times the silica colloids, corresponding to 7 compact shells of passive spheres. We find that the clusters display self-propulsion despite being made of symmetric shells of passive spheres. We thus realize a singular catalytic self-propelled system, characterized by an evolving shape, with an aspect ratio progressing toward a flat disk. Numerical simulations based only on a purely diffusiophoretic system, without osmotic flow on the substrate, reproduce the raft kinetics but not the cluster direction of motion and its persistence length for large clusters. We show that the substrate osmotic flow is an essential feature that should be considered to explain the mechanism of motion of these composite clusters.

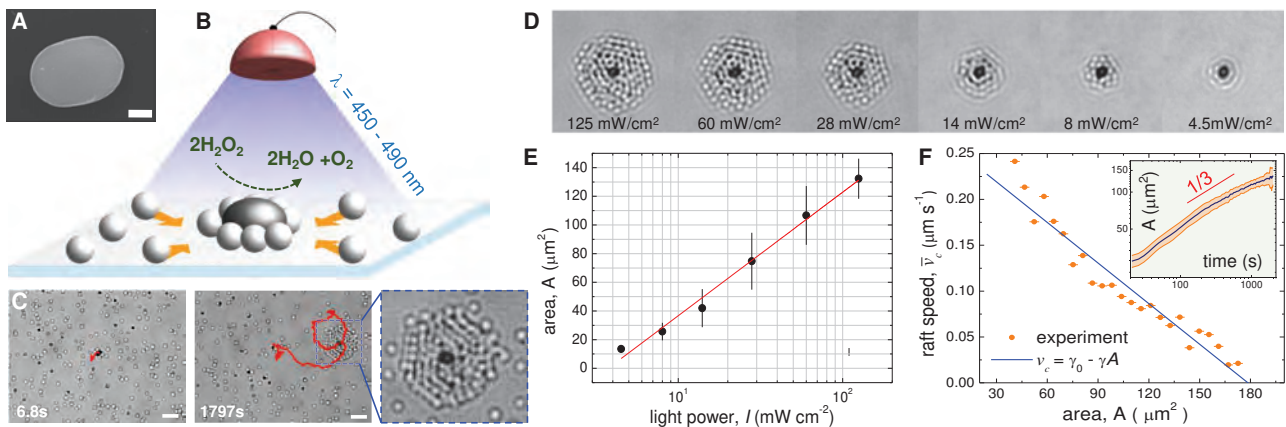


FIG. 1. **The active colloidal raft.** (A) Electron microscopy image of one hematite, scale bar is 500 nm. (B) Scheme showing the assembly of the colloidal raft under blue light in a water (H_2O) hydrogen peroxide (H_2O_2) mixture. (C) Sequence of two images of a growing raft with superimposed (red) the trajectory of the central active particle. Time $t = 0\text{s}$ corresponds to light application. Scale bar is $5\ \mu\text{m}$. Last image displays the final cluster size, see Supplementary Movie 1. (D) Sequence of average images showing the area occupied by the cluster at different light intensities. (E) Cluster area A at steady state versus light intensity I . Black dots are the average values. The error bars are the confidence interval for $P = 0.95$. Straight red line is the linear regression with the logarithm of the light intensity, $A(I) = A_0 \ln(I/I_0)$ with $A_0 = 37.4 \pm 1.9\ \mu\text{m}^2$ and $I_0 = 3.74 \pm 0.4\ \text{mWcm}^{-2}$. (F) Average raft velocity \bar{v}_c versus cluster area A showing the experimental data (black disk) and a linear regression with $\gamma_0 = 0.26 \pm 0.02\ \mu\text{ms}^{-1}$ and a negative slope $\gamma = (1.48 \pm 0.02) \cdot 10^{-3}\ \mu\text{m}^{-1}\text{s}^{-1}$. Inset shows a log-log plot of the area versus time for several rafts, error bars are indicated by the shaded orange region.

RESULTS

Colloidal rafts.

Our colloidal rafts are realized by illuminating with blue light (wavelength $\lambda = 450 - 490\text{nm}$) synthesized hematite ellipsoids with short and long axis equal to $1.3\ \mu\text{m}$ and $1.8\ \mu\text{m}$ resp., Fig. 1(A). These particles are dispersed with passive silica spheres ($1\ \mu\text{m}$ diameter) in an aqueous solution of hydrogen peroxide (3.6 % w/v). The pH solution is raised to ~ 9.2 by adding Trimethylphenylammonium to negatively charge the surfaces [39]. The electrostatic repulsion stabilizes the dispersion and prevents the colloids from sticking to the substrate. The colloidal dispersion is sediment over the bottom of a sealed rectangular capillary tube. The relative density is below 1 active particle for 2000 passive ones, with a total surface fraction of $\sim 6\%$. More details on the experimental protocol are given in the Materials and Method section.

Once the light is applied, the hematite particle starts the decomposition of hydrogen peroxide in water, following the chemical reaction: $2\text{H}_2\text{O}_{2(l)} \rightarrow \text{O}_{2(g)} + 2\text{H}_2\text{O}_{(l)}$. As a consequence, such particle becomes active and induces a strong phoretic attraction of the passive spheres, which assemble in the form of circular clusters as shown in the schematic in Fig. 1(B). During growth, the raft translates and rotates, and the association of both can result in looping trajectories, Fig. 1(C) and Supplementary Movie 1. The self-assembly process can be completely and re-

versibly controlled by the light intensity, as shown in the sequence of images in, Fig. 1(D) where one large cluster is disassembled by a step-wise reduction of the light power. At the maximum intensity $I = 125\ \text{mW cm}^{-2}$, corresponding to the standard experimental condition, one hematite accumulates up to 6 – 7 layers of passive particles, i.e more than 100 hundred colloids, for one-hour experiment. In contrast, at the minimal light intensity, which is ~ 28 times lower, there is only one layer. In terms of the light intensity, the cluster growth is characterized via a simple logarithmic relationship, as shown in Fig. 1(E). Further, we find that the rafts follow a sub-linear growth with a power law behavior up to $t = 2000\ \text{s}$ ($\simeq 0.6$ hours), inset in Fig. 1(F). The exponent $1/3$ is consistent with the Ostwald coarsening process, as described by the Lifshitz-Slyozov-Wagner theory [40]. Such exponent was predicted in scalar field theory of active systems [41] and recently experimental observed in clustering passive particles by active agents [42]. The mean cluster velocity, \bar{v}_c of the order of few micrometers per minute, linearly decreases with the cluster area A , reducing almost to zero for the largest size of $A = 175\ \mu\text{m}^2$, top inset in Fig. 1(F).

The aggregation process arises from chemophoresis, which is induced by the concentration gradient generated by the hematite particle [43]. However, more subtle is the emergence of self-propulsion in our system as it was not expected. Indeed, it was previously shown that the decomposition of hydrogen peroxide in water induce propulsion in Janus colloids with anisotropic coating [44, 45]. However our clusters ap-

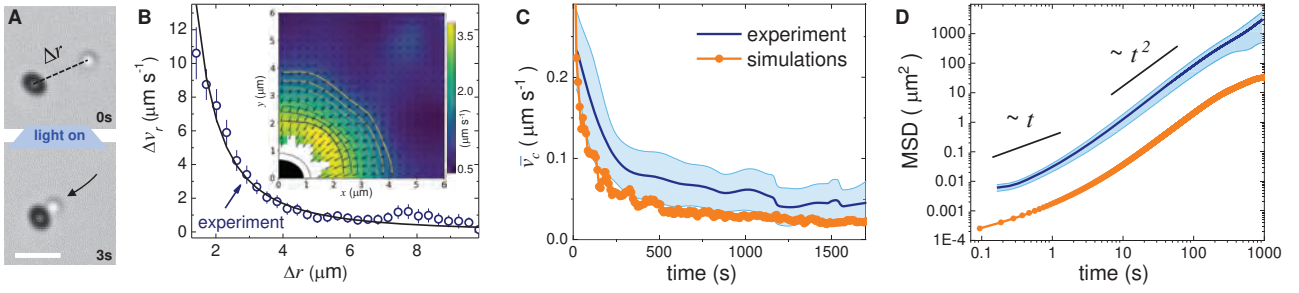


FIG. 2. **Raft dynamics.** (A) Sequence of images showing the attraction of a silica particle towards the hematite once blue light is applied ($t = 0$). (B) Relative speed Δv_r versus relative distance Δr : the solid line is fitted to the data (blue circles) following Eq. 3. Inset displays a heat map of the velocity and direction of a passive particle near the hematite. (C,D) Mean cluster speed \bar{v}_c (C) and mean square displacement (MSD) (D) versus time from experiments (blue line) and simulation (orange disks). In both graphs the shaded red regions denote experimental uncertainties.

pear symmetrically surrounded by shells of passive spheres, a situation that in principle would preclude the emergence of directed motion unless some spatial symmetries in the system are broken.

Numerical simulations.

To understand the kinetics and self-propulsion behavior, we first perform Brownian dynamic simulations using input parameters obtained from the experimental pair interaction between the hematite and the silica colloids. We assume a purely diffusiophoretic system and consider a bath of $i = 1..N$ passive particles at positions \mathbf{R}_i (diameter σ_p , surface mobility μ_p and diffusion coefficient D_p) with a single active particle. To model the aspect ratio of the experimental ellipsoids, the hematite is considered as a dumbbell of two active particles, $\alpha = 1, 2$, at positions \mathbf{r}_α (diameter $\sigma_a = 1.3 \mu\text{m}$, surface mobility μ_a , and diffusion coefficient D_a) joined by a spring with rest length $0.5 \mu\text{m}$, and force of magnitude F^h along the vector $\hat{\mathbf{n}}_i = (\mathbf{r}_i - \mathbf{r}_j)/r_{ij}$ joining the two beads. Accordingly, the motion of the active and passive colloids read:

$$\dot{\mathbf{r}}_\alpha = \mathbf{v}_\alpha + (F^h \hat{\mathbf{n}}_\alpha + \mathbf{F}_\alpha^c)/\gamma_\alpha + \sqrt{2D_a} \boldsymbol{\xi}_\alpha, \quad (1)$$

$$\dot{\mathbf{R}}_i = \mathbf{V}_i + \mathbf{F}_i^c/\gamma_p + \sqrt{2D_p} \boldsymbol{\xi}_i. \quad (2)$$

where γ_a and γ_p correspond to the active and passive friction coefficients, respectively, while \mathbf{F}_i^c and \mathbf{F}_α^c account for steric forces given by a Weeks-Chandler-Andersen potential, which prevents particles from overlapping. The term $\boldsymbol{\xi}_i$ is a random Gaussian forces noise that accounts for the thermal bath. Each bead constituting the dumbbell in the hematite acts as a source [22, 43, 46] of a chemical field, ϕ . A second particle with mobility μ_p (μ_a) will experience a slip velocity on its surface, $\mathbf{u}_s = \mu_p(\mu_a) \nabla_{\parallel} \phi$, that leads to a net diffusiophoretic velocity \mathbf{V}_i (\mathbf{v}_α), see the Materials and Methods section for the derivation. Accordingly, the relative speed of approach Δv_r between an active and a pas-

sive particle at a relative distance Δr reads,

$$\Delta v_r = v_\alpha + V = v_0 \left[\bar{\mu} \left(\frac{\sigma_a}{\Delta r} \right)^2 + \frac{1}{4} \left(\frac{\sigma_p}{\sigma_a} \right)^3 \left(\frac{\sigma_a}{\Delta r} \right)^5 \right], \quad (3)$$

where $\bar{\mu} = \mu_p/\mu_a$ is the mobility ratio, a detailed derivation is provided in the Materials and Methods section.

To determine Δv_r experimentally, we perform several experiments by measuring the approach distance Δr between an isolated pair of active and passive particles, Fig. 2(A). We then calculate Δv_r and use Eq. 3 to fit the experimental data, and extract a characteristic diffusiophoretic velocity $v_0 = 11.6 \pm 0.4 \mu\text{m s}^{-1}$, Fig. 2(B). The corresponding heat map of such field is shown in the inset of Fig. 2(B), and was measured by keeping fixed the orientation of the hematite with a constant magnetic field.

The simulations explain some of the experimental features: the growth of the raft size as $t^{1/3}$, the decrease of the raft velocity with the cluster area as shown in Fig. 2(C), and the emergence of self-propulsion behavior. This aspect is illustrated by Fig. 2(D), which displays the average translational mean square displacement $\text{MSD}(\tau) \equiv \langle (\mathbf{r}(t) - \mathbf{r}(t + \tau))^2 \rangle \sim \tau^\delta$, with τ the lag time and $\langle \dots \rangle$ a time average. The MSD computed from experimental and simulation data shows both diffusive ($\delta = 1$) dynamics at short time scale, followed by a sub-[super] diffusive ($\delta < 1$ [$\delta > 1$]) dynamics, very close to a ballistic one ($\delta = 2$). However, the non overlapping MSD curves in Fig. 2(D) show that the simulations do not recover all the experimental features of the raft dynamics. We further measure the trajectory persistence length l_p , i.e. the characteristic length over which the raft velocity orientation decorrelates. We calculate this quantity from the cluster trajectories as, $\langle \cos(\theta_v(d + \Delta l) - \theta_v(d)) \rangle_d \propto \exp(-\Delta l/l_p)$ being d the distance traveled by the cluster and θ_v the orientation of the velocity vector. From the experiment, we measure $l_p \simeq 20 \mu\text{m}$ which is signif-

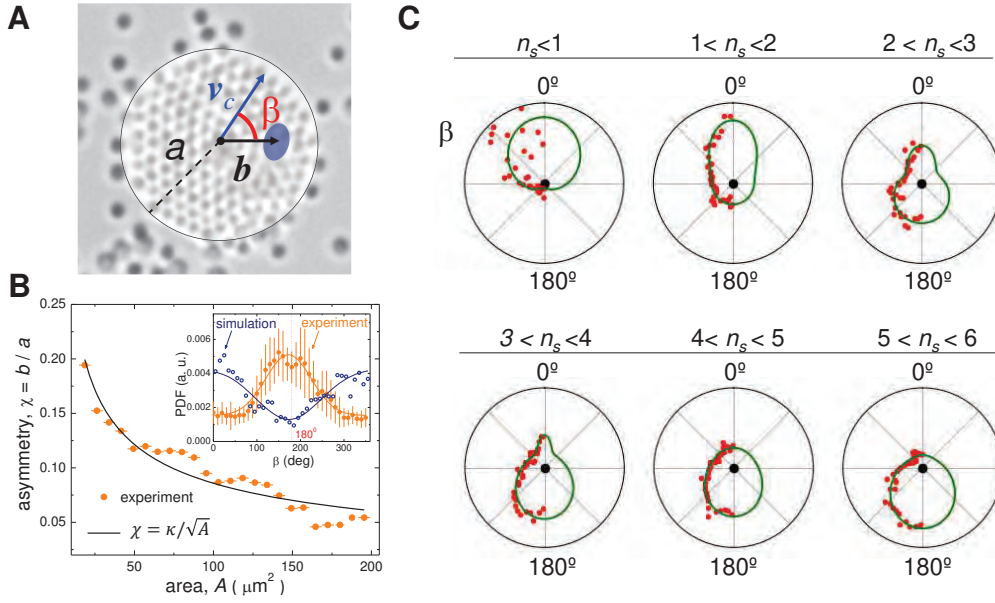


FIG. 3. **Raft Asymmetry.** (A) Schematic overlaid to a raft image indicating the asymmetry vector \mathbf{b} and the angle β between \mathbf{b} and the cluster velocity \mathbf{v}_c . The location of the hematite has been exaggerated (not on scale). (B) Experimentally measured asymmetry parameter $\chi = b/a$ versus cluster area A , being a the cluster radius. The continuous line is an inverse square root law from which we extract the prefactor $\kappa = 0.858 \pm 0.019 \mu\text{m}$. Top left inset shows the distribution of angles β between \mathbf{v}_c and the vector \mathbf{b} pointing from the cluster center to the hematite particle from experiments (filled symbols) and simulations (open circles). In both cases the continuous lines are wrapped normal distributions. (C) Polar plot showing the experimentally measured angle β (scattered red disks) for different clusters characterized by different number of shells n_s . each shell is made of passive particles encircling the active one. The continuous green line is a non-linear regression based on wrapped normal distributions.

icantly larger than the one predicted in the simulations, $l_p \simeq 2.5 \mu\text{m}$. As we show below, this discrepancy arises from the opposite self-propulsion direction observed in experiments and simulations.

Cluster asymmetry and self propulsion direction.

To better understand the origin of the raft propulsion, we have analyzed in detail the position of the hematite source within the cluster. During the growth process and at the steady state we find that the hematite is not exactly located in the cluster' geometric center, but it is displaced a small distance b from it, Fig. 3(A). Further, we find that the asymmetry parameter of the cluster, defined as $\chi = b/a$, decreases with the raft area A , being a the radius of the cluster. Such dependence can be well described by a power law, $\chi = \kappa A^{-1/2}$, Fig. 3(B), which indicates that the variations of b are rather small. Indeed, from the extracted prefactor κ , and taking into account that the radius of the cluster is $a = \sqrt{A/\pi}$ we find that $b = \kappa/\sqrt{\pi} = 0.48 \simeq \sigma_p/2$, i.e. the shifted distance between the hematite and the cluster center is of the order of the radius of the passive particle, consistent with the fact that the cluster is growing layer by layer.

The analysis of the distribution of angle β between the cluster velocity \mathbf{v}_c and the asymmetry vector \mathbf{b} gives

further insight on the propulsion direction. As shown in the top inset of Fig. 3(B), the global distribution is Gaussian (orange data and line) and centered around $\beta = 180^\circ$, meaning that the raft propels with the active particle at the rear. Numerical simulations show that the clusters instead tend to propel with the active particle at the front, as illustrated by the blue line and corresponding data in the same image, see also Supplementary Movie 2.

The hematite asymmetric location in the cluster controls its persistence length. This feature arises from the unfixed and evolving boundary that characterizes the self-propelled cluster of particles. Qualitatively, when a colloidal raft moves in a crowded environment of passive particles, they tend to accumulate at the front. Thus, a cluster moving with the hematite shifted toward the front has to change regularly its motion direction to maintain this configuration, as reported in the simulations. Instead, when a cluster moves with the hematite shifted towards its rear, the colloids accumulate at its front, preserving the asymmetry and the motion direction, as observed in the experiments. The two situations lead respectively to a system with a relatively low and high persistence length. To confirm this hypothesis, we have implemented a specific simulation by imposing that the cluster moves with the hematite at the

rear. As shown in Supplementary Movie 3, we observe a much longer persistence length, closer to the experimental results.

If we consider the distribution of the angle β for a given number of colloidal shells, n_s , we find that during the clustering process, the colloidal raft switches from a motion with the hematite at the front to the rear. As shown in Figure 3(C), for the smallest clusters, up to two shells $n_s = 2$, the probability distribution of the angle β has a peak around 0° . This observation is consistent with the simulation prediction, and previous experiments on smaller clusters [43]. For larger rafts, down to $n_s = 4$, the peak shifts to 180° . Due to the slow growing process, this orientation dominates the global dynamics described previously. For the intermediate sizes, $n_s = 2 - 4$, the two opposed peaks coexist in the distribution of angle β and show that the inversion in the direction of motion occurs within this size range.

The discrepancy between the numerical and experimental results arises from the assumption that the system is purely diffusiophoretic and neglects hydrodynamic interactions. The simulations do not consider the presence of the near wall, and the competition between diffusiophoresis and diffusioosmosis. In particular, the change in the direction of motion of the raft can be interpreted as a switch from a self-propulsion process dominated by diffusiophoresis to diffusioosmosis. For the small clusters at the early stage, diffusiophoresis dominates, leading to a motion direction consistent with the simulation prediction. However, the clustering process modifies the aspect ratio of the colloidal raft. The emerging configuration favor the viscous interaction between the raft and the substrate, with two mostly flat surfaces facing each other at a very short distance. Thus, due to clustering, the viscous interaction with the substrate increases, up to the point that the substrate diffusioosmotic flow overpass the diffusiophoresis and determine the direction of motion.

Theoretical model.

The competition between diffusiophoresis and diffusioosmosis is the key element to understand the raft propulsion. Indeed one can consider that arise from an osmotic effect, using the classical interpretation [47]. More precisely, the local diffusioosmotic flows occurring on mobile surfaces lead to a slip velocity making it move along the opposite direction [37]. On the contrary, an external flow, as the osmotic flow occurring on a nearby substrate, tends to drag the object in the same direction. Then if both surfaces generate a local osmotic flow along the same direction, their viscous interactions become opposite. Here we propose a more quantitative description illustrating the competition which occurs for the large rafts. To include the effect of hydrodynamics and the proximity of the wall, we approximate the colloidal raft by a disk of diameter $2a$ and the shifted hematite by a "semi-punctual"

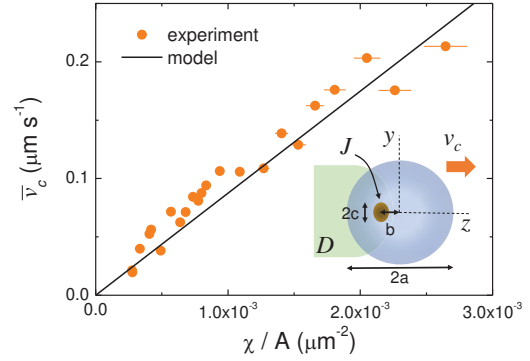


FIG. 4. **Mean raft speed.** Experimental data of the mean cluster velocity \bar{v}_c versus ratio χ/A being $\chi = b/a$. Scattered circles are experimental data while the continuous line is a linear fit from the model, see Eq. 35 in the text. Inset illustrates a schematic of the model: the cluster is considered as a thin disk of radius a with an active source of size σ_a and distance b from the center. J and D denote respectively the release rate of the source and solvent diffusion rate.

source, where the concentration field ϕ is similar to a punctual source except along the source surface, where ϕ is constant. We orient the system such that the unit vector e_z is diametrically opposed to the vector b linking the cluster centre to the source. The negative or positive sign of the cluster velocity v_c indicates a disk moving with the source at the front or the rear, respectively. We assume that the catalyzed product is released at the rate J , and diffuses in bulk with a diffusion coefficient D_c . We consider two parallel surfaces, the disk (p) and the substrate (S), separated by h , such as $h/a \ll 1$. To describe the disk dynamics we introduce two dimensionless numbers: the Péclet $\text{Pe}_c = \frac{v_c a}{D_c}$, the Damköhler number $\text{Da} = \frac{\mu_p J}{4\pi a D_c^2}$ which relates the reaction rate to the diffusive mass transport rate. Experimentally, $\text{Pe}_c \simeq 10^{-4} \ll 1$ thus solute transport is dominated by diffusion, and the source motion can be disregarded. Therefore at a distance r from the source the chemical gradient can be expressed as $\nabla\phi = -J/(4\pi D_c r^2)e_r$. The concentration gradient generates a slip osmotic flow $\mathbf{u}_S = \mu \nabla_S \phi$, along the relevant surfaces, namely the disk surface p and the substrate S , such that $\mathbf{u}|_p = v_c e_z + \mu_p \nabla \phi$, and $\mathbf{u}|_S = \mu_S \nabla \phi$. The disk motion is force-free, hence $\mathbf{F}_v + \mathbf{F}_p + \mathbf{F}_S = 0$, where \mathbf{F}_v is the damping force due to the motion of the disk, \mathbf{F}_p is the phoretic force associated with the slip velocity on the disk's surface, and \mathbf{F}_S the osmotic contribution coming from the slip velocity on the wall. The details of all terms employed and the extended model are given in the Materials and Methods section.

Using the Lorentz reciprocal theorem, we arrive at

$$\text{Pe}_c \simeq 2\text{Da}(1 - \mu_S/\mu_p)\chi + O(\chi^2) , \quad (4)$$

and, accordingly, the velocity of the disk at the first order in χ is given by

$$v_c \propto (\mu_p - \mu_S) \frac{\chi}{A} . \quad (5)$$

Note that if we remove the osmotic flow along the substrate, the term μ_S disappears from Eq. 35, and $v_c \propto \mu_p \frac{\chi}{A}$. Neglecting or taking into account this flow leads almost to the same dependencies with $\frac{\chi}{A}$ for the velocity of the disk which is consistent with the experimental observation, Fig. 4. The difference between the osmotic mobilities $\mu_p - \mu_S$ in Eq.35 marks the competition between diffusiophoresis and substrate diffusioosmosis because it controls the sign of v_c , i.e., the direction of motion of the raft. Since the passive colloid and the substrate are made of silica, it is reasonable to assume that μ_S is comparable to μ_p , and have the same sign. Thus, from the model and from the direction of motion of the large cluster the hematite at the rear, we deduce that $\mu_S/\mu_p > 1$. As a consequence, for the large cluster, diffusiophoresis acts against the motion, while the osmotic flow on the substrate induces the cluster propulsion.

Conclusion.

We have investigated the rich dynamics of active colloidal rafts composed of a central hematite particle and several shells of passive colloids. We have shown that this system displays a clustering phenomenon due to diffusiophoresis, and collective self-propulsion that result from the interplay between diffusiophoresis and diffusioosmosis on the nearby substrate. While for small clusters the first mechanism dominates, hydrodynamics become important and dominate for a number of shells $n_s > 3$. Indeed, simulations based only on diffusiophoresis describe well the clustering kinetics but cannot explain the direction of motion and persistence length for large clusters. Our model solves the discrepancy by considering the cluster asymmetry and the substrate diffusioosmotic flow. Thus, we have shown that there is a competition between the diffusiophoresis and osmosis, and the crucial role of the substrate diffusioosmotic flow on the raft dynamics. In line with these results, previous works in the field have also shown the importance of considering the osmotic flow generated by an active particle close to a wall [13, 48]. The theoretical approach, based on the Lorentz reciprocal theorem, could be extended to many other catalytic active systems close to a substrate, considering the proper boundary conditions. In our experiments, we approximate the raft to a disk allowing to reach an analytical expression that captures the underlying physics of this complex, yet rich hybrid active passive system.

METHODS

Experimental details. The active particles are hematite prolate ellipsoids synthesized following the "gel-sol" technique [49]. While maintaining the stirring, an iron chloride hexahydrate solution (54.00 g in 100 mL of water, Sigma-Aldrich 31232-M) is gradually added to a sodium hydroxide solution (19.48 g in 90 mL of water; Sigma-Aldrich S5881), followed by 5 minutes by a potassium sulfate solution (0.29 g in 10 mL of water; Sigma-Aldrich P0772). After being agitated for 5 more minutes, the mixture is hermetically sealed in a 1L bottle and left to age at 100 °C for 8 days. Afterwards, the reaction is stopped by completing the recipient with water and leaving it to cool down in a storage fridge. The hematite particles are concentrated and washed through multiple cycles involving centrifugation and a re-dilution in clean deionized water. The experimental system consists of a colloidal mix of synthesized hematite with silica sphere (diameter 1 μm ; Sigma-Aldrich) dispersed into an aqueous solution of hydrogen peroxide (3.6% w/v; Fisher BP2633). The quantity of active particles is much lower than passive ones, the ratio is below 1 active for 2000 passives. The solution is made basic (pH \sim 9.2) by adding TMAH (Sigma-Aldrich 328251), to see the attraction phenomena, and treated for 5 minutes with an ultrasound bath to break up the hematite chains. Right after, we introduce by capillarity the colloidal mixture into a rectangular glass micro-tube (inner dimension 2×0.1 mm; CMC Scientific) immediately sealed with wax at the atmospheric pressure. After a few minutes of rest, all the colloids are left sediment, and form a quasi-two-dimensional system. The high pH ensures dispersion stability and prevents colloids from sticking to the glass substrate. Contrary to a previous work [50], no surfactant is added to the solution since we have observed that SDS lowers the attraction phenomena. To record the colloid raft behavior, we use an upright optical microscope (Eclipse Ni; Nikon) equipped with a charge-coupled device camera (12 up to 50 frame per second; Basler Scout scA640-74f) and an epifluorescent tower. For the illumination, the light is provided by a commercial mercury fiber illumination system (C-HGFI Intensilight; Nikon) filtered with a band-pass filter (Nikon B-2A filter). The output after the objective (Nikon MRH01902) is a blue light (wavelength $\lambda = 450 - 490$ nm) with an intensity going from 4 up to 125 mWcm^{-2} .

Details of the numerical simulation. We start with the details on how we derive Eq.(3) in the main text. We consider that the active and passive particles of diameters σ_a and σ_p , respectively, are immersed in a concentration field $\phi(r)$. The concentration field obeys the Laplace equation $\Delta c(r, \theta) = 0$, where Neumann

boundary conditions are to hold $D_c \partial_r c(r, \theta)|_\phi \propto \alpha_r$ on each particle's surface. In the previous expression α_r is the production/consumption rate of the chemical, and D_c its diffusion coefficient. For passive particles $\alpha_r = 0$, as they do not consume or produce any chemical. We assume, for simplicity, that fuel depletion is negligible.

An active particle, i , located in the origin in the presence of a second particle, j at a distance $d_{ij} = |\mathbf{r}_i - \mathbf{r}_j|$, with the center-to-center direction parallel to \hat{z} , creates a concentration field

$$c_i(r, d, \theta) = \frac{\alpha_{r,i} \sigma_i^2}{4D_c} \frac{1}{r} + \phi_{i,j}(r, d_{ij}, \theta). \quad (6)$$

The first term on the right-hand side gives the production of chemical, while the second describes the disturbance of the chemical concentration produced by the j -th particle and guarantees that the boundary condition is satisfied on the i -th particle. The disturbance term $\phi_{i,j}$ can be expanded as a multipolar series with the axis of symmetry along \hat{z} .

The first contribution on particle i created by a particle j , $\phi_{i,j}^{(1)}(r, d_{ij}, \theta)$, corresponds to a dipole and depends on the activity $\alpha_{r,j}$ of the j -th particle, and the distance between the pair,

$$\phi_{i,j}^{(1)}(r, d, \theta) = -\frac{1}{2} \left(\frac{\sigma_i}{2}\right)^3 \frac{1}{d_{ij}^2} \frac{\alpha_{r,j} \sigma_j^2 \cos \theta}{4D_c r^2} \quad (7)$$

which for an active producing a concentration field in the presence of a passive corresponds to $\phi_{a,p}^{(1)} = 0$. The second dipolar contribution on particle i appears only on active particles. The monopolar field generated by i is reflected on particle j and gives, on i the dipolar term, $\phi_{i,j}^{(2)}$. As expected it depends on $\alpha_{r,i}$ as

$$\phi_{i,j}^{(2)}(r, d, \theta) = -\frac{1}{4} \left(\frac{\sigma_i}{2}\right)^3 \left(\frac{\sigma_j}{2}\right)^3 \frac{1}{d_{ij}^5} \frac{\alpha_{r,i} 2\sigma_i^2 \cos \theta}{4D_c r^2} \quad (8)$$

Note that this last contribution cancels for $i = p$, leading to the non-reciprocity of the interactions between active and passive particles. The gradient of the chemical concentration on the surface of a sphere generates a tangential diffusiophoretic velocity, $\mathbf{u} = \mu_d \nabla_{\parallel} c(r)$, of the fluid at the particle interface.

The particle velocity can be obtained from the diffusiophoretic velocity by imposing the momentum conservation

$$\mathbf{V} = -\frac{1}{\pi\sigma^2} \int d\Omega \mathbf{u}(r, \theta) = (\pi\sigma^2)^{-1} \mu_d \int d\Omega \nabla_{\parallel} c(r, \theta) \quad (9)$$

The integration of $\nabla_{\parallel} \phi$ for a multipolar expansion of the form $c(\theta, r) = \sum_l B_l P_l(\cos \theta) r^{-(l+1)}$ on a spherical shell of diameter σ results in a velocity in \hat{z} , the symmetry axis of the system.

$$\mathbf{V} = \frac{2}{3} \mu_d \left(\frac{2}{\sigma}\right)^3 B_1 \hat{z} \quad (10)$$

Hence, the diffusiophoretic velocity of the particle depends only on the $l = 1$ contribution of the multipolar expansion of the chemical field around the particle center.

Introducing Eqs. (7)-(8) into Eq. (10), we recover the relative velocities (Eq.(3) of the main text), with a characteristic velocity $V_0 = \alpha_r \sigma_a^2 / (12D_c)$. We have taken into account that active and passive particles have different diffusophoretic mobilities, μ_a, μ_p , and have introduced their ratio, $\bar{\mu} = \mu_p / \mu_a$.

Thus, the velocity of an active particle induced by the passive particle due to the diffusiophoresis reads

$$\mathbf{V}_i = \sum_{j \neq i} V_0 \bar{\mu} \left(\frac{\sigma_a}{d_{ij}}\right)^2 \hat{\mathbf{r}}_{ij} \quad (11)$$

while the passive particle velocity induced by an active particle is

$$\mathbf{v}_i = \sum_{j \neq i} \frac{V_0}{4} \left(\frac{\sigma_p}{\sigma_a}\right)^3 \left(\frac{\sigma_a}{d_{ij}}\right)^5 \hat{\mathbf{r}}_{ij} \quad (12)$$

Following the notation in the main text, we consider N passive particle of diameter σ_p and mobility μ_p in the presence of two active particles forming a dumbbell. The active particles have diameter σ_a , mobility μ_a , and consider σ_p a characteristic length and $\tau_c = \sigma_p / V_0 \bar{\mu}$ as a characteristic time. The equations of motion can be rewritten in terms of these dimensionless variables as

$$\dot{\mathbf{r}}_\alpha = \sum_j \frac{\hat{\mathbf{r}}_{\alpha j}}{\bar{\mu}} \left(\frac{\sigma_p^3 \sigma_a^2}{r_{\alpha j}^5}\right) + \frac{\mu_a (F^h \hat{\mathbf{r}}_\alpha + \mathbf{F}_\alpha^c)}{V_0 \bar{\mu}} + \sqrt{\frac{2\tau}{\text{Pe}_a}} \boldsymbol{\xi}_\alpha, \quad (13)$$

$$\dot{\mathbf{R}}_i = \sum_{j \neq i} \left(\frac{\sigma_a}{r_{ij}}\right)^2 \hat{\mathbf{r}}_{ij} + \frac{\mu_p}{V_0 \bar{\mu}} \mathbf{F}_i^c + \sqrt{\frac{2\tau}{\text{Pe}_p}} \boldsymbol{\xi}_i, \quad (14)$$

where $\text{Pe}_{a,p} = \sigma_p V_0 \bar{\mu} / D_{a,p}$ is the Péclet number, and subindices a and p distinguish between the active and passive Péclet, since they have different diffusion coefficients. Note also that the subindex $\alpha = 1, 2$ refers to each bead constituting the dumbbell joined by the harmonic spring interaction $F^h = -k|\mathbf{r}_1 - \mathbf{r}_2|$. We obtain the characteristic time that allows comparison between simulations and experiments from fitting the experimental velocity to the dependence in Eq. 14, $\tau_c \simeq 0.067$ s. The cluster dynamics are dominated by $\text{Pe}_{a,p}$ and $\bar{\mu}$. F_c and F_c^α follow a standard Weeks-Chandler-Andersen potential, such that $F_c^{(\alpha)} = 24(\epsilon/\sigma)[2(\sigma/r)^{13} - (\sigma/r)^7]$, being $\sigma = 0.5(\sigma_i + \sigma_j)$, where i, j stands for any combination pair of passive and active particles. Following the standard WCA force, we impose a cutoff at the minimum $2^{1/6}\sigma$, such that the force is purely repulsive. We choose $k = 50$ such that the active dumbbell remains essentially rigid. $\bar{\mu}$ is chosen high enough so that the relevant contribution to the

dynamics comes from the active particle, as suggested by the experiments. We can estimate the order of magnitude of the cluster radius ℓ_0 , by means of comparing the diffusion term of Eq. 13 with the diffusiophoretic velocity. From Eq. 11 and 12 we get

$$\ell_0 \sim \sqrt{\frac{V_0 \bar{\mu}}{\xi}} \frac{\sigma_a}{(2D_p)^{1/4}} \quad (15)$$

Taking the experimental values, $V_0 \bar{\mu} = 11.6 \mu\text{m/s}$, $\sigma_a \simeq 0.8 \mu\text{m}$, $D_p = 0.29 \mu\text{m}^2/\text{s}$ leads to $r \simeq 6 \mu\text{m}$, in agreement with simulations, and a good estimation of the experimental cluster radius. Thus, the growth rate of the cluster is compatible with an attraction $1/\Delta r^2$.

Supplementary Fig.2(a) shows how the cluster grows its area compared to an expression of the type $t^{1/3}$, similar to the experiments. In Supplementary Fig. 2(b) the cluster has a diffusive behavior at small times and moves ballistically at large ones, due to the non-reciprocal interactions. Supplementary Fig. 2(c) shows how the velocity decreases as a function of time. Supplementary Fig. 2(d) shows how the velocity follows approximately a linear behavior as a function of χ/A , as suggested by the theoretical results.

Details of the theoretical model.

Phoretic and osmotic force expression with the Lorentz reciprocal theorem In the context of phoretic/osmotic system, the main interest of the reciprocal theorem is to directly compute integral quantities such as the viscous flow force without solving the Stokes flows occurring in this type of system. The motion of an object in a concentration gradient is attributed to the osmotic flow \mathbf{u}_S along its surface S ,

$$\mathbf{u}_S = \mu \nabla_{\parallel} \phi, \quad (16)$$

with ϕ a chemical concentration and μ the osmotic mobility of the slip flow.

For the most general case, we imagine an object moving along a substrate at the velocity $v_c \mathbf{e}_z$ in a gradient of concentration $\nabla \phi$. The concentration gradient generated a slip osmotic flow Eq. 16 along the object surface p and the substrate S , such that:

$$\mathbf{u}|_p = v_c \mathbf{e}_z + \mu_p \nabla_{\parallel} \phi, \quad \mathbf{u}|_S = \mu_S \nabla_{\parallel} \phi. \quad (17)$$

The use of the Lorentz reciprocal theorem requires the introduction of a dual system. The dual system shares at any moment the same boundaries, but no osmotic phenomenon occurs, neither on the object surface nor on the substrate. In those conditions, we simply assume a no slip boundary condition:

$$\hat{\mathbf{u}}|_p = v_c \mathbf{e}_z, \quad \hat{\mathbf{u}}|_S = \mathbf{0}. \quad (18)$$

We add a hat “ $\hat{}$ ” to the quantities from the dual problem to distinguish them. According to the Lorentz reciprocal theorem [51], we have

$$\int_p (\mathbf{n} \cdot \boldsymbol{\epsilon}) \cdot \hat{\mathbf{u}} \, dS + \int_S (\mathbf{n} \cdot \boldsymbol{\epsilon}) \cdot \hat{\mathbf{u}} \, dS = \int_p (\mathbf{n} \cdot \boldsymbol{\epsilon}) \cdot \mathbf{u} \, dS + \int_S (\mathbf{n} \cdot \boldsymbol{\epsilon}) \cdot \mathbf{u} \, dS, \quad (19)$$

with \mathbf{n} the surface normal oriented toward the fluid and $\boldsymbol{\epsilon}$ the stress tensor, such that $\boldsymbol{\epsilon} = -p \mathbb{1} + \eta (\nabla \mathbf{u} + \nabla \mathbf{u}^T)$, with p the pressure and η the fluid viscosity. Knowing the boundary condition for the dual system, the left-hand side simplifies into $v_c F_v$. By injecting the boundary condition (18)(17) in the integrals of the left-hand side, we obtain an expression for the total viscous force F_v as a sum of three other forces,

$$\mathbf{F}_v = \hat{\mathbf{F}}_v + \mathbf{F}_p + \mathbf{F}_S, \quad (20)$$

$$\hat{\mathbf{F}}_v = \int_p \mathbf{n} \cdot \hat{\boldsymbol{\epsilon}} \, dS, \quad (21)$$

$$\mathbf{F}_p = \int_p \frac{\mathbf{n} \cdot \hat{\boldsymbol{\epsilon}}}{v_c} \cdot (\mu_p \nabla_{\parallel} \phi) \, dS \, \mathbf{e}_z, \quad (22)$$

$$\mathbf{F}_S = \int_S \frac{\mathbf{n} \cdot \hat{\boldsymbol{\epsilon}}}{v_c} \cdot (\mu_S \nabla_{\parallel} \phi) \, dS \, \mathbf{e}_z, \quad (23)$$

being \mathbf{u} the flow field, \mathbf{n} the surface normal oriented toward the fluid. $\hat{\mathbf{F}}_v$ is the viscous drag of the dual problem, aka damping force since $\hat{\mathbf{F}}_v \propto -v_c \mathbf{e}_z$, \mathbf{F}_p is the viscous force due to the osmotic flow along the moving object, aka the phoretic force, and \mathbf{F}_S is the viscous force due to the osmotic flow along the wall, aka the osmotic force.

For a system moving at a constant velocity, the force balance imposes that the total viscous force is null: $F_v = \mathbf{0}$. It leads to the dynamic equation,

$$\mathbf{0} = \hat{\mathbf{F}}_v + \mathbf{F}_p + \mathbf{F}_S. \quad (24)$$

Note for a diffusiophoretic spherical object far from any wall, the tangent stress is constant along the surface [52] for the dual problem. We deduce the well-known result [47] that the phoretic velocity is the opposite of the average slip velocity (16) over the object surface $v_c = -\langle \mathbf{u}_p \rangle_p = -\langle \mu_p \nabla_{\parallel} \phi \rangle_p$.

The raft motion. To model the cluster motion, we approximate the colloidal raft by a disk and the central hematite by an “semi-punctual” source with a radius size $\sigma_a/2$, i.e the concentration field is the same as a punctual source except along the source surface, in this case, the concentration is constant. We assume that the catalyzed product is released at the total rate $J = \alpha_r \pi \sigma_a^2$, and diffused in bulk at the diffusion rate D_c . The shift from the disk center is b , while the disk radius is a with an area A . We orient the system such that the unit vector \mathbf{e}_z is diametrically opposed to the vector \mathbf{b} linking the cluster center to the source. Thus, the disk velocity $v_c \mathbf{e}_z$ can be positive or negative, which indicates respectively a self-propulsion with the source at the rear or at the front.

We introduce the Péclet number $Pe_c = \frac{v_c a}{D_c}$, the Damköhler number $Da = \frac{\mu_p J}{4\pi a D_c^2}$, the asymmetry number $\chi = \frac{b}{a}$ and also the dimensionless substrate osmotic mobility $\bar{\mu}_S = \frac{\mu_S}{\mu_p}$. Experimentally $Pe_c \ll 1$, thus we assume that the motion of the source does not affect the chemical distribution ϕ , and by extension, the concentration gradient. For $r > \sigma_a/2$,

$$\phi = c_0 + \frac{J}{2\pi D_c r}, \quad \nabla \phi = -\frac{J}{2\pi D_c} \frac{1}{r^2} \mathbf{e}_r, \quad (25)$$

with r the distance from the source, and c_0 the concentration at the infinity. We neglect the terms in $O(h^2)$ due to the short distance h between the source and the impermeable substrate.

Because of the electrostatic interaction, the cluster is sliding at a distance h from the substrate, with h small compared to the cluster size. Two boundary conditions might be studied for the substrate, either no-slip as we consider in the *wall model*, or implementing an osmotic flow as we consider in the *osmotic model*. From the point of view of the Lorentz reciprocal theorem, both models are very similar to treat, since they share the same dual problem. The only difference is the osmotic force F_S , which is null for the *wall model*.

Surface stress in the dual problem. We seek analytical expression for the viscous stress $\hat{\boldsymbol{\epsilon}}$. The dual problem is a disk sliding at the distance h over a substrate. Even if the problem has already been solved analytically [53], the complexity of the expressions does not fit the objective of introducing analytical toy models with a simple view of the physics in play. We propose simple approximations for the viscous stress applying on the different surfaces:

-Disk upper side. We assume that the disk upper side facing the infinite half-space undergoes the same stress with or without the wall. Then, the tangential viscous stress on the disk surface is given by

$$\mathbf{n} \cdot \hat{\boldsymbol{\epsilon}} = -\eta \frac{v_c}{a} \frac{C}{2\pi} \frac{1}{\sqrt{1 - r^{*2}/a}} \mathbf{e}_z, \quad (26)$$

with r^* the distance from the disk center and $C = 16/3$. For an oblate the stress reaches its maximum intensity over the perimeter [51], for a disk it diverges over circumference $r^* = 1$.

-disk lower side and substrate right below the disk. For the lower disk side and the substrate straight below, we assume the velocity profile is a solution of the Stokes flow in the presence of a solid boundary. Thus, $\hat{\mathbf{u}}(x, y, z) = Ay^2 + By \mathbf{e}_z$, with two boundary conditions: $\hat{\mathbf{u}}(x, y = h, z) = v_c \mathbf{e}_z$ and $u(x, y = 0, z) = 0$. At the disk border, we impose that the pressure is equal to P_0 , therefore the only valid solution is a pure shear flow

$$\mathbf{u}(x, y, z) = v_c \frac{y}{h} \mathbf{e}_z, \quad \mathbf{n} \cdot \hat{\boldsymbol{\epsilon}} = (\mathbf{n} \cdot \mathbf{e}_z) \frac{v_c \eta}{h} \mathbf{e}_z, \quad (27)$$

with \mathbf{n} the normal to the surface considered.

-Remaining substrate. For the remaining surface of the substrate, we assume that its contribution in the osmotic force F_S is negligible compared to the contribution of the surface right below the disk, considering that $\mathbf{n} \cdot \hat{\boldsymbol{\epsilon}} \cdot \nabla_{\parallel} \phi \propto \frac{1}{r^4}$

Forces in the osmotic/phoretic problem. Knowing the stress over the surface in the dual problem and the chemical concentration gradient (25), we determine the forces applying on the disk.

-damping force:

$$\hat{\mathbf{F}}_v = -\eta v_c a \left(C + \frac{\pi}{h} \right) \mathbf{e}_z, \quad (28)$$

with $\bar{h} = h/a$. The drag formula proposed is computed from the rough stress estimation described above. Compared to the right variation, it becomes asymptotically accurate for $\bar{h} \ll 1$ [54], when the shear stress on the bottom side dominates.

-Phoretic force on the upper face:

$$\mathbf{F}_p^{up} = \frac{C}{\pi} D_c \eta Da \int_{\theta=-\pi}^{\theta=\pi} \cos \theta \int_{r=\bar{c}}^{r=\hat{a}} \frac{1}{\bar{r} \sqrt{1 - \bar{r}^{*2}}} d\bar{r} d\theta \mathbf{e}_z, \quad (29)$$

with $\hat{a} = \chi \cos \theta + \sqrt{1 - \chi^2 \sin^2 \theta}$, (30)

$$\bar{r}^{*2} = \bar{r}^2 \left(1 + \left(\frac{\chi}{\bar{r}} \right)^2 - 2 \frac{\chi}{\bar{r}} \cos \theta \right), \quad \text{and} \quad \bar{c} = \frac{c}{a}.$$

In the above expression, the surface integral is expressed in the cylindrical frame of reference centered on the source. Some quantities need to be rewritten in this frame, such as the radial position of the disk perimeter $\hat{a}(\theta, \chi)$ and the distance from the disk center $\bar{r}^*(\theta, \chi)$.

-Phoretic force on the lower face and osmotic force.

$$\mathbf{F}_p^{down} = 2D_c \eta \frac{Da}{h} \int_{\theta=-\pi}^{\theta=\pi} \cos \theta \int_{r=\bar{c}}^{r=\hat{a}} \frac{1}{\bar{r}} d\bar{r} d\theta \mathbf{e}_z, \quad (31)$$

$$\mathbf{F}_S = -2D_c \eta \frac{Da \bar{\mu}_S}{h} \int_{\theta=-\pi}^{\theta=\pi} \cos \theta \int_{r=\bar{c}}^{r=\hat{a}} \frac{1}{\bar{r}} d\bar{r} d\theta \mathbf{e}_z. \quad (32)$$

Finally, by using the dynamic equation (24), we obtain an equation involving the dimensionless numbers,

$$Pe_c = \frac{2Da}{hC + \pi} \int_{\theta=-\pi}^{\theta=\pi} \cos \theta \quad (33)$$

$$\int_{r=\bar{c}}^{r=\hat{a}} \frac{1}{\bar{r}} \left(\frac{\bar{h}C}{2\pi \sqrt{1 - \bar{r}^{*2}}} - \bar{\mu}_S + 1 \right) d\bar{r} d\theta. \quad (34)$$

If we assume $\bar{h} \ll 1$ and $\chi \ll 1$, the contribution of the upper face becomes negligible. We reach the formula:

$$Pe_c \simeq 2Da(1 - \bar{\mu}_S)\chi + O(\chi^2), \quad v_c \propto (\mu_p - \mu_S) \frac{\chi}{A}. \quad (35)$$

Note that if we remove the osmotic flow along the substrate, we have instead for the *wall model*

$$\text{Pe}_c \simeq 2\text{Da} \chi + O(\chi^2), \quad v_c \propto \mu_p \frac{\chi}{A}. \quad (36)$$

Data availability

The authors declare that all data supporting the findings of this study are available within the paper and SI or available from the corresponding author upon reasonable request.

Code availability

Computer codes are available from the corresponding authors upon reasonable request.

REFERENCES

-
- * Both authors equally contributed to this work.
 † ptierno@ub.edu
- [1] S. Ramaswamy, The mechanics and statistics of active matter, *Annu. Rev. Condens. Matter Phys.* **1**, 323 (2010).
 - [2] M. C. Marchetti, J. F. Joanny, S. Ramaswamy, T. B. Liverpool, J. Prost, M. Rao, and R. A. Simha, Hydrodynamics of soft active matter, *Rev. Mod. Phys.* **85**, 1143 (2013).
 - [3] E. Fodor, C. Nardini, M. E. Cates, J. Tailleur, P. Visco, and F. van Wijland, How far from equilibrium is active matter?, *Phys. Rev. Lett.* **117**, 038103 (2016).
 - [4] C. Nardini, E. Fodor, E. Tjhung, F. van Wijland, J. Tailleur, and M. E. Cates, Entropy production in field theories without time-reversal symmetry: Quantifying the non-equilibrium character of active matter, *Phys. Rev. X* **7**, 021007 (2017).
 - [5] J. Elgeti, R. G. Winkler, and G. Gompper, Physics of microswimmers-single particle motion and collective behavior: a review, *Rep. Prog. Phys.* **78**, 056601 (2015).
 - [6] C. Bechinger, R. Di Leonardo, H. Löwen, C. Reichardt, G. Volpe, and G. Volpe, Active particles in complex and crowded environments, *Rev. Mod. Phys.* **88**, 045006 (2016).
 - [7] A. Zöttl and H. Stark, Emergent behavior in active colloids, *J. Phys.: Condens. Matter* **28**, 253001 (2016).
 - [8] G. Gompper, R. G. Winkler, T. Speck, A. Solon, C. Nardini, F. Peruani, H. Löwen, R. Golestanian, U. B. Kaupp, L. Alvarez, T. Kiørboe, E. Lauga, W. C. K. Poon, A. DeSimone, S. Muiños-Landin, A. Fischer, N. A. Söker, F. Cichos, R. Kapral, P. Gaspard, M. Ripoll, F. Sagues, A. Doostmohammadi, J. M. Yeomans, I. S. Aranson, C. Bechinger, H. Stark, C. K. Hemelrijk, F. J. Nedelec, T. Sarkar, T. Aryaksama, M. Lacroix, G. Duclos, V. Yashunsky, P. Silberzan, M. Arroyo, and S. Kale, The 2020 motile active matter roadmap, *Journal of Physics: Condensed Matter* **32**, 193001 (2020).
 - [9] N. B. R. F. Ismagilov, A. Schwartz and G. M. Whitesides, Autonomous movement and self-assembly, *Angew. Chem. Int. Ed.* **41**, 652 (2002).
 - [10] W. F. Paxton, K. C. Kistler, C. C. Olmeda, A. Sen, S. K. S. Angelo, Y. Cao, T. E. Mallouk, P. E. Lammert, and V. H. Crespi, Catalytic nanomotors: autonomous movement of striped nanorods, *J. Am. Chem. Soc.* **126**, 13424 (2004).
 - [11] W. F. Paxton, S. Sundararajan, T. E. Mallouk, and A. Sen, Chemical locomotion, *Angew. Chem. Int. Ed.* **45**, 5420 (2006).
 - [12] J. R. Howse, R. A. L. Jones, A. J. Ryan, T. Gough, R. Vafabakhsh, and R. Golestanian, Self-motile colloidal particles: From directed propulsion to random walk, *Phys. Rev. Lett.* **99**, 048102 (2007).
 - [13] J. Simmchen, J. Katuri, W. E. Uspal, M. N. Popescu, M. Tasinkevych, and S. Sánchez, Topographical pathways guide chemical microswimmers, *Nat. Commun.* **7**, 10598 (2016).
 - [14] I. Theurkauff, C. Cottin-Bizonne, J. Palacci, C. Ybert, and L. Bocquet, Dynamic clustering in active colloidal suspensions with chemical signaling, *Phys. Rev. Lett.* **108**, 268303 (2012).
 - [15] S. Ketzetzi, J. de Graaf, R. P. Doherty, and D. J. Kraft, Slip length dependent propulsion speed of catalytic colloidal swimmers near walls, *Phys. Rev. Lett.* **124**, 048002 (2020).
 - [16] Y. Wang, R. M. Hernandez, D. J. Bartlett, J. M. Bingham, T. R. Kline, A. Sen, and T. E. Mallouk, Bipolar electrochemical mechanism for the propulsion of catalytic nanomotors in hydrogen peroxide solutions, *Langmuir* **22**, 10451–10456 (2006).
 - [17] W. Wang, W. Duan, A. Sen, and T. E. Mallouk, Catalytically powered dynamic assembly of rod-shaped nanomotors and passive tracer particles, *Proc. Nat. Acad. Sci. USA* **110**, 17744 (2013).
 - [18] G. Rückner and R. Kapral, Chemically powered nanodimers, *Phys. Rev. Lett.* **98**, 150603 (2007).
 - [19] L. F. Valadares, Y. G. Tao, N. S. Zacharia, V. Kitaev, F. Galembeck, R. Kapral, and G. A. Ozin, Catalytic nanomotors: Self-propelled sphere dimers, *Small* **6**, 565 (2010).
 - [20] R. Niu, T. Palberg, and T. Speck, Self-assembly of colloidal molecules due to self-generated flow, *Phys. Rev. Lett.* **119**, 028001 (2017).
 - [21] J. Agudo-Canalejo and R. Golestanian, Active phase separation in mixtures of chemically interacting particles, *Phys. Rev. Lett.* **123**, 018101 (2019).
 - [22] R. Soto and R. Golestanian, Self-assembly of catalytically active colloidal molecules: Tailoring activity through surface chemistry, *Phys. Rev. Lett.* **112**, 068301 (2014).
 - [23] O. Pohl and H. Stark, Dynamic clustering and chemotactic collapse of self-phoretic active particles, *Phys. Rev. Lett.* **112**, 238303 (2014).
 - [24] B. Jang, W. Wang, S. Wiget, A. J. Petruska, X. Chen, C. Hu, A. Hong, D. Folio, A. Ferreira, S. Pané, and B. J. Nelson, Catalytic locomotion of core-shell nanowire motors, *ACS Nano* **10**, 9983–9991 (2016).
 - [25] J. Burdick, R. Laocharoensuk, P. M. Wheat, J. D. Posner, and J. Wang, Synthetic nanomotors in microchannel networks: Directional microchip motion and controlled manipulation of cargo, *J. Am. Chem. Soc.* **130**, 8164 (2008).
 - [26] L. Baraban, D. Makarov, R. Streubel, I. Monch, D. Grimm, and S. Sanchez, Catalytic janus motors on microfluidic chip: deterministic motion for targeted cargo delivery, *ACS nano* **6**, 3383 (2012).
 - [27] J. Palacci, S. Sacanna, A. Vatchinsky, P. M. Chaikin, and D. J. Pine, Photoactivated colloidal dockers for cargo

- transportation, *J. Am. Chem. Soc.* **135**, 15978–15981 (2013).
- [28] A. Arslanova, V. R. Dugyala, E. K. Reichel, N. Reddy, J. Fransaer, and C. Clasen, ‘sweeping rods’: cargo transport by self-propelled bimetallic microrods moving perpendicular to their long axis, *Soft Matter* **17**, 2369 (2021).
- [29] B. J. Nelson, I. K. Kaliakatsos, and J. J. Abbott, Microrobots for minimally invasive medicine, *Annu. Rev. Biomed. Eng.* **12**, 55 (2010).
- [30] S. Kim, F. Qiu, S. Kim, A. Ghanbari, C. Moon, L. Zhang, B. J. Nelson, and H. Choi, Fabrication and characterization of magnetic microrobots for three-dimensional cell culture and targeted transportation, *Adv. Mater.* **25**, 5863 (2013).
- [31] S. Sanchez, A. A. Solovev, S. M. Harazim, and O. G. Schmidt, Microrobots swimming in the flowing streams of microfluidic channels, *J. Am. Chem. Soc.* **133**, 701 (2011).
- [32] J. L. Moran and J. D. Posner, Phoretic self-propulsion, *Annu. Rev. Fluid Mech.* **49**, 511 (2017).
- [33] B. Liebchen and A. K. Mukhopadhyay, Interactions in active colloids, *J. Phys.: Cond. Matt.* **34**, 083002 (2021).
- [34] J. Anderson, Colloid transport by interfacial forces., *Annu. Rev. Fluid Mech.* **21**, 61 (1989).
- [35] J. Palacci, S. Sacanna, A. P. Steinberg, D. J. Pine, and P. M. Chaikin, Living crystals of light-activated colloidal surfers, *Science* **339**, 936 (2013).
- [36] M. K. Rasmussen, J. N. Pedersen, and R. Marie, Size and surface charge characterization of nanoparticles with a salt gradient, *Nat. Comm.* **11**, 2337 (2020).
- [37] S. Marbach and L. Bocquet, Osmosis, from molecular insights to large-scale applications, *Chemical Society Reviews* **48**, 3102 (2019).
- [38] W. E. Uspal, M. N. Popescu, S. Dietrich, and M. Tasinkevych, Guiding catalytically active particles with chemically patterned surfaces, *Phys. Rev. Lett.* **117**, 048002 (2016).
- [39] G. Mériguet, E. Dubois, and R. Perzynski, Liquid–liquid phase-transfer of magnetic nanoparticles in organic solvents, *J. Colloid Interf. Sci.* **267**, 78 (2003).
- [40] A. J. Bray, Theory of phase-ordering kinetics, *Adv. Phys.* **43**, 357 (1994).
- [41] R. Wittkowski, A. Tiribocchi, J. Stenhammar, R. J. Allen, D. Marenduzzo, and M. E. Cates, Scalar ϕ^4 field theory for active-particle phase separation., *Nat. Communications* **5**, 4351 (2014).
- [42] J. Bouvard, F. Moisy, and H. Auradou, Ostwald-like ripening in the two-dimensional clustering of passive particles induced by swimming bacteria, *Phys. Rev. E* **107**, 044607 (2023).
- [43] J. Codina, H. Massana-Cid, P. Tierno, and I. Pagonabarraga, Breaking action–reaction with active apolar colloids: emergent transport and velocity inversion, *Soft Matter* **18**, 5371 (2022).
- [44] S. J. Ebbens and D. A. Gregory, Catalytic janus colloids: Controlling trajectories of chemical microswimmers, *Acc. Chem. Res.* **51**, 1931 (2018).
- [45] M. N. Popescu, W. E. Uspal, C. Bechinger, and P. Fischer, Chemotaxis of active janus nanoparticles, *Nano Letters* **8**, 5345 (2018).
- [46] R. Golestanian, T. B. Liverpool, and A. Ajdari, Designing phoretic micro-and nano-swimmers, *New J. Phys.* **9**, 126 (2007).
- [47] H. A. Stone and A. D. T. Samuel, Propulsion of microorganisms by surface distortions, *Phys. Rev. Lett.* **77**, 4102 (1996).
- [48] J. Katuri, W. E. Uspal, M. N. Popescu, and S. Sánchez, Inferring non-equilibrium interactions from tracer response near confined active janus particles, *Sci. Adv.* **7**, eabd0719 (2021).
- [49] T. Sugimoto and A. Muramatsu, Formation mechanism of monodispersed alpha-Fe₂O₃ particles in dilute FeCl₃ solutions, *J. Colloid Interf. Sci.* **184**, 626 (1996).
- [50] H. Massana-Cid, J. Codina, I. Pagonabarraga, and P. Tierno, Active apolar doping determines routes to colloidal clusters and gels, *Proc. Nat. Acad. Sci. USA* **10618**, 115 (2018).
- [51] M. Hassan and H. A. Stone, The reciprocal theorem in fluid dynamics and transport phenomena, *J. Fluid Mech.* **879**, P1 (2001).
- [52] J. Happel and H. Brenner, *Low Reynolds number hydrodynamics: with special applications to particulate media*, Vol. 1 (Springer Science & Business Media, 2012).
- [53] A. M. J. Davis, Some asymmetric stokes flows that are structurally similar, *Fluid Dynamics Research* **5**, 2086 (1993).
- [54] M.-U. Kim, K. W. Kim, Y.-H. Cho, and B. M. Kwak, Hydrodynamic force on a plate near the plane wall. part i: plate in sliding motion, *Fluid Dynamics Research* **29**, 137 (2001).

Acknowledgments

This work has received funding from the European Research Council (ERC) under the European Union’s Horizon 2020 Research and Innovation Programme (grant agreement no. 811234). S.G.L. and I.P. acknowledge support from Ministerio de Ciencia, Innovación y Universidades (grant no. PID2021-126570NB-I00 AEI/FEDER-EU) and from Generalitat de Catalunya under project 2021SGR-673. P.T. acknowledges support from the Ministerio de Ciencia e Innovación (Project No. PID2022-137713NBC22), the Agència de Gestió d’Ajuts Universitaris i de Recerca (Project No. 2021SGR 00450). P.T. and I.P. acknowledge support from the Generalitat de Catalunya (ICREA Acadèmia).

Author Contributions

D. B. performed the experiments and developed the theoretical model. S. G. ran the numerical simulations. I. P. and P.T. supervised the work. All authors discussed the results and commented on the manuscript at all stages.

Competing interests

The authors declare no competing interests.

Additional information

Supplementary Information is available in the on-line version of the paper. This material includes three supplementary movies illustrating the raft dynamics.

Correspondence and requests for materials should be addressed to P.T. (ptierno@ub.edu).

Supplementary Files

This is a list of supplementary files associated with this preprint. Click to download.

- [DescriptionofAdditionalSupplementaryFiles.pdf](#)
- [SupplementaryMovie1.mp4](#)
- [SupplementaryMovie2.mp4](#)
- [SupplementaryMovie3.mp4](#)

Publication 6:
Capillary imbibition in lubricant coated surfaces

Sergi G. Leyva^{1,2}, Ignacio Pagonabarraga^{1,2}, Aurora Hernández-Machado ^{1,3},
and Rodrigo Ledesma-Aguilar⁴

¹Departament de Física de la Matèria Condensada, Universitat de Barcelona, 08028 Barcelona,
Spain

²Universitat de Barcelona Institute of Complex Systems (UBICS), Universitat de Barcelona,
08028 Barcelona, Spain

³Institut de Nanociència i Nanotecnologia, IN²UB, Universitat de Barcelona, 08028 Barcelona,
Spain

⁴School of Engineering, University of Edinburgh, The King's Buildings, Mayfield Road, Edinburgh
EH9 3JL, UK

Capillary imbibition in lubricant coated channels

Sergi G. Leyva,^{1,2} Ignacio Pagonabarraga,^{1,2} Aurora Hernández-Machado,^{1,3} and Rodrigo Ledesma-Aguilar⁴

¹*Departament de Física de la Matèria Condensada, Universitat de Barcelona, 08028 Spain*

²*Universitat de Barcelona Institute of Complex Systems (UBICS), Universitat de Barcelona, 08028 Spain*

³*Institut de Nanociència i Nanotecnologia, Universitat de Barcelona, 08028 Spain*

⁴*School of Engineering, University of Edinburgh,*

The King's Buildings, Mayfield Road, Edinburgh EH9 3JL, UK

(Dated: January 16, 2024)

Capillary imbibition underpins many processes of fundamental and applied relevance in fluid mechanics. A limitation to the flow is the coupling to the confining solid, which induces friction forces. Our work proposes a general theoretical framework for the modeling of the transport of liquids in lubricant impregnated surfaces. We show that for sufficiently small lubricant viscosity, dissipation entirely occurs in the lubricant layer, resulting in a linear growth of the advancing front. As a result, an external force gives rise to an exponential front growth. This new capacity to control multiphase flows sets new experimental challenges that can be determinant for micro and nanofluidic devices.

Spontaneous imbibition, also known as capillary filling, occurs when one fluid displaces a second one from a solid porous medium due to its preferential affinity to wet the internal surfaces of the solid.

Applications can be found in nanofluidics [1], where elastocapillary forces support the self-assembly of arrays of carbon nanotubes [2]; biophysics, where capillary forces are known to influence protein folding [3–5]; and medical devices, where lateral flows, an example of capillary driven flows, are widely used to detect the presence of a target substance, and set the basis for antigen detection [6, 7].

Classical imbibition corresponds to a viscous fluid displacing a gas in a uniform porous medium, where the front position, $l(t)$, follows the “slowing-down” growth of Washburn’s law, $l(t) \propto t^\alpha$, with $\alpha = 1/2$ [?]. Understanding and controlling the exponent α , is therefore of both fundamental and practical interest. Pradas et al. [8, 9] and Queralt et al. [10] showed that the exponent can be lowered to $\alpha < 1/2$ by introducing disorder in the channel topography. On the other hand, Primkulov et al. [11] reported a larger exponent $\alpha = 1$, but lower imbibition speed, by capping the front with a slug of a viscous oil.

What happens if the solid walls of a porous medium are replaced by a liquid surface? Experimental realisations of lubricant impregnated surfaces, like Liquid-Infused Porous Surfaces (SLIPS) or Lubricant-Impregnated Surfaces (LIS) [12–16] have gained much attention in the recent years. These materials have outstanding properties for droplet manipulation due to their low friction, resistance to extreme conditions, and self-healing properties, as well as their ability to induce drag reduction in contact with a single liquid phase [17–19]. Here we address the fundamental question of how spontaneously invades a porous medium coated with a lubricant.

We show that the lubricant viscosity plays a determinant role to trigger a qualitative change in the dissipation mechanism where the liquid front advances at a constant rate, instead of slowing down, as would occur if the flu-

ids were in direct contact with the solid. We also identify the high sensitivity of the liquid front to external perturbations, which opens an avenue to new modes of liquid manipulation in the microscale.

To elucidate the front dynamics, we have carried out 2D lattice-Boltzmann (LB) numerical simulations of the imbibition into a solid channel coated with a liquid lubricant layer. We couple the LB method to a ternary free-energy model of three immiscible fluids, which we solve by using the Cahn-Hilliard equation. The ternary free-energy model [20], allows to independently choose the surface tensions of the liquids, and thus the Neumann angles at their intersection as well as the wettability of the solid. In our simulations, Fig. 1a, two reservoirs hold liquids of equal density but different viscosities, η_1 and η_2 . The reservoirs are connected by a solid channel of length L and width H , whose internal surfaces are coated by a thin film of a third liquid of viscosity η_s (the lubricant). The lubricant is kept in place by two small pillars located at the edges of the channel. This geometry mimics SLIPS, where the lubricant is locked into the surface by roughness [21]. Further details on the simulation methodology and choice of parameters are provided in the supplementary information [22].

As shown in the simulation snapshot of Fig. 1a, an appropriate choice of the surface tensions leads to the spontaneous imbibition of liquid 1 into the channel, displacing liquid 2. The displacing and displaced liquids form an advancing meniscus with a well-defined apparent angle relative to the solid, θ , suggesting a driving capillary force $F_c \propto \gamma \cos \theta$, where γ is the surface tension of the interface between liquids 1 and 2. Despite this similarity, the meniscus does not touch the solid, but moves on top of the lubricant layer.

We focus on the familiar case of a viscous liquid displacing a much less viscous fluid, $\eta_2/\eta_1 = 10^{-2}$, and analyse the motion of the meniscus at different lubricant viscosities, η_s . Fig. 1b shows the corresponding l vs t curves, where the penetration length is normalised by the length of the tube, and time is normalised using the filling time

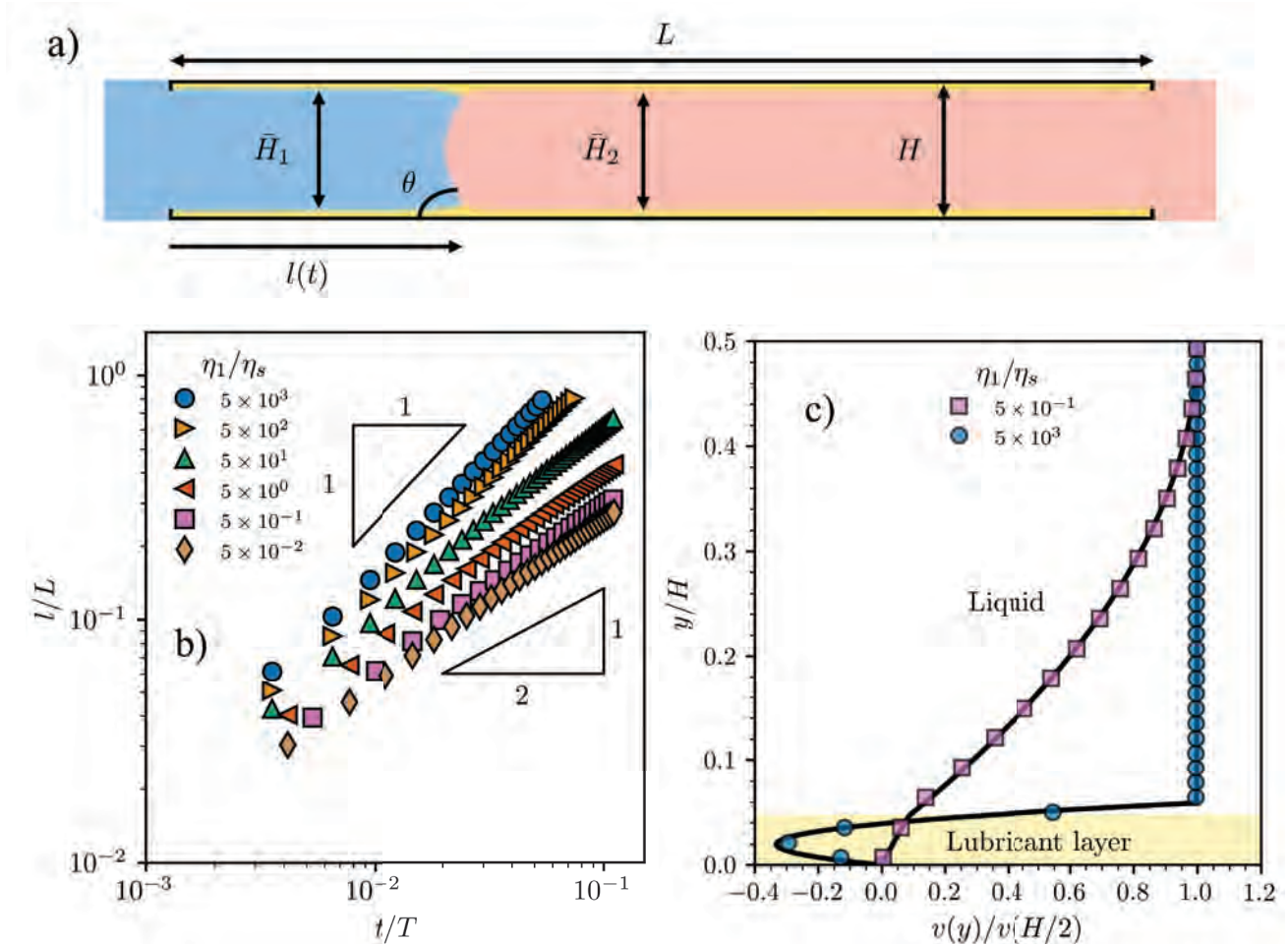


FIG. 1. Spontaneous imbibition in a lubricant coated channel. (a) Lattice-Boltzmann simulation snapshot. The liquid on the left, of width \bar{H}_1 , preferentially wets the surface of a thin lubricant layer of width h_1 , and displaces a resident fluid in a channel of width $H = \bar{H}_1 + 2h_1$, and length L . A meniscus, of apparent angle θ and position $l(t)$, advances within the channel. (b) Effect of the viscosity of the lubricant, η_s , on the imbibition curves at fixed viscosity contrast between the displaced and displacing liquids, $\eta_2/\eta_1 = 1 \times 10^{-2}$. (c) Velocity profile in the displacing fluid and in the lubricant layer, $v(y)$, for $\eta_1/\eta_s = 5 \times 10^{-1}$ (squares) and $\eta_1/\eta_s = 5 \times 10^3$ (circles). The solid lines show the theoretical prediction (see text). The velocity is made dimensionless by the velocity at the center of the channel, $v(H/2)$, while the y coordinate is normalised by the channel width, H .

predicted by Washburn's law, $T = 3\eta_1 L^2 / H\gamma \cos \theta$ [23]. For very large lubricant viscosity, the front advances following the scaling of Washburn's law, $l(t) \sim t^{1/2}$, indicating that the viscous force, F_v , increases with increasing l . Decreasing the lubricant viscosity leads to an unexpected result: The front grows linearly, $l(t) \sim t$, thus suggesting that F_v is independent of l . In addition, the filling time is significantly shorter than that predicted by Washburn's law. We shall show that these effects are not a transient due to inertia or dynamic-angle effects [23–26]. They correspond to a new long-time regime entirely dominated by the viscous dissipation in the lubricant film.

Fig. 1c shows profiles of the tangential velocity of the displacing phase and the lubricant far upstream of the meniscus. The expected parabolic flow profile of a forced

fluid [27] is approached for large η_s . The velocity in the lubricant layer becomes vanishingly small, which effectively behaves like a solid. In contrast, for small η_s , the flow profile resembles a plug flow in the displacing and displaced phases, while there is strong variation of the velocity in the lubricant layer, where shear stresses are sustained.

Building on these observations, we propose a simplified model of the flow in each fluid phase where we neglect the dynamics close to the meniscus and describe the flow profile in the four “bulk” flow regions depicted in Fig. 2a. The tangential velocity profiles in the displacing and displaced phases, $v_1(y)$ and $v_2(y)$, and in the adjacent regions of the lubricant layer, $v_{s1}(y)$ and $v_{s2}(y)$ are obtained from lubrication theory, assuming that the

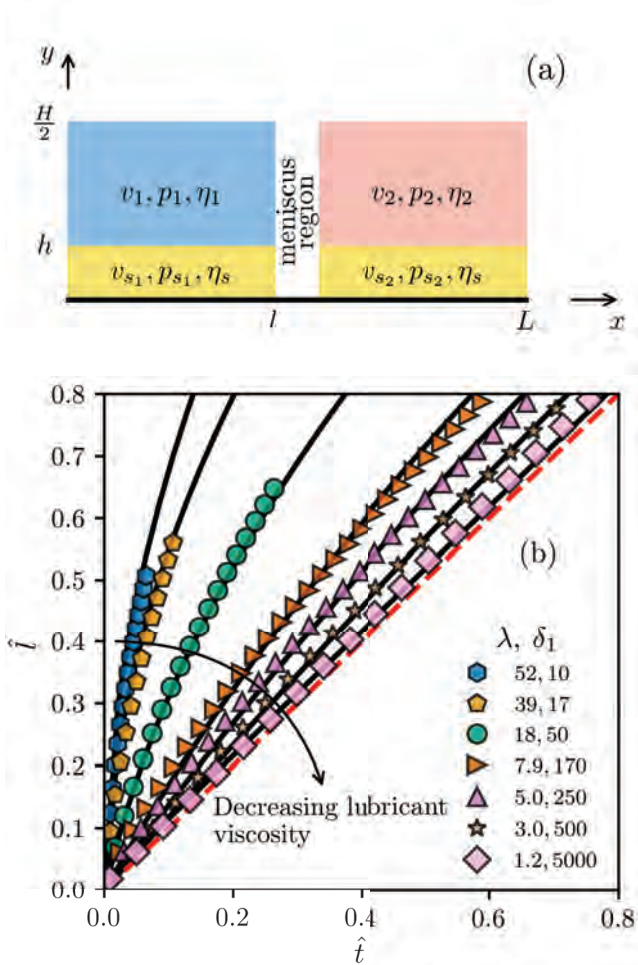


FIG. 2. (a) Schematics of the lubricant coated channel. The rectangular sections represent the bulk of the displacing and displaced liquids, and of the lubricant layer, which are separated by the meniscus region. (b) Theoretical imbibition curves (solid lines) vs simulation results (symbols) for different values of the parameter λ . For $\lambda \rightarrow 1$, corresponding to small lubricant viscosity, the imbibition curves approach the asymptotic limit $\hat{l} = \hat{t}$ (red dashed line). The values of Σ with decreasing lubricant viscosity correspond to 0.03, 0.01, 0.2, 0.9, 1.7, 3.2 and 24, respectively.

pressure profiles in each region, namely p_1 , p_2 , p_{s1} and p_{s2} , only vary along the longitudinal coordinate x . Accordingly, the flow profiles obey the Stokes equations. Four out of the eight integration constants are found by imposing continuity of the velocity and tangential stress at the interface with the lubricant layer. The remaining constants are determined by fixing the average velocities of the fluids and the lubricant, $\frac{1}{H/2-h} \int_h^{H/2} v_i dy = u$ and $\frac{1}{h} \int_0^h v_{s_i} dy = u_s$ [22].

In general, u and u_s are independent free parameters; however, for the imbibition geometry the lubricant layer responds to the capillary driving force that acts on the

meniscus. Therefore, we expect that if no external forces in the lubricant are present, the average velocity of the lubricant obeys $u_s = \alpha u$, with $0 \leq \alpha \leq 1$. This relationship allows us to eliminate the pressure gradient terms from the Stokes equations, and instead characterize the flow through u and α . Figure 1c shows the excellent agreement of the theoretical prediction with the simulation velocity profiles, where u_s and u are fixed to the measured liquid flow. The theoretical results show that a vanishing average lubricant velocity u_s leads to a negative derivative of the velocity profile close to the solid, indicating a recirculating flow in the lubricant layer, as reported in SLIPS/LIS simulations [18] (see analytical solution in the supplementary material [22]).

The model can be used to determine the viscous friction force (per unit length) exerted by the lubricant layer on the moving fluids, $F_v = 2l\tau_1 + 2(L-l)\tau_2$, where $\tau_i \equiv \eta_s dv_{s_i}(h)/dy$ is the shear stress. From the velocity profiles we obtain [22]

$$F_v = \frac{4(2-3\alpha)u\eta_s}{h} \left(\frac{l}{1 + \frac{2\bar{H}}{3\delta_1 h}} + \frac{L-l}{1 + \frac{2\bar{H}}{3\delta_2 h}} \right). \quad (1)$$

Here, $\bar{H}_i \equiv H - 2h = \bar{H}$ is the width of either liquid and $\delta_i \equiv \eta_i/\eta_s, i = 1, 2$ is the viscosity ratio between the displacing/displaced ($i = 1/2$) liquid and the lubricant. Letting $\delta_i h/\bar{H} \rightarrow 0$, $\eta_2/\eta_1 \rightarrow 0$ and setting $\alpha = 0$, this expression reduces to the classical result of the viscous force acting on a single liquid in contact with a solid channel i.e., $F_v = 12\eta_1 u l/H$. On the contrary, the limit of small lubricant viscosity is achieved by letting $\delta_i h/\bar{H} \rightarrow \infty$, where the friction force reduces to $F_v = 4(2-3\alpha)\eta_s u L/h$. In this regime the viscous force is dominated by the lubricant layer, despite being the *less* viscous phase, and the force does not depend on the position of the front; rather, its magnitude scales with the entire length of the channel, L . Comparing the energy dissipation rate in the bulk of the displacing and displaced liquids $\dot{E}_b = \int_0^l \int_h^{H/2} \eta_1 |\nabla v_1|^2 dy dx + \int_l^L \int_h^{H/2} \eta_2 |\nabla v_2|^2 dy dx$, to that of the lubricant $\dot{E}_s = \int_0^l \int_0^h \eta_s |\nabla v_{s1}|^2 dy dx + \int_l^L \int_0^h \eta_s |\nabla v_{s2}|^2 dy dx$, for $\delta_i h/\bar{H} \rightarrow \infty$, we find $\dot{E}_b/\dot{E}_s \rightarrow 0$ [22]. Therefore, in this limit the energy dissipation occurs in the lubricant, and not in the bulk of the displacing and displaced phases.

The imbibition growth law, $\hat{l}(t)$, is derived from the force balance, $F_c = F_v + F_m$, between the capillary (F_c), viscous (F_v) and contact-line friction (F_m) forces per unit length. The simulations show that the contact angle settles to a constant value, $\theta \approx \theta_e$ after a short transient. Accordingly, $F_c = 2\bar{H}\gamma \cos \theta_e/H$. The unbalanced interfacial stress close to the triple line is given by $\gamma \cos \theta(u)$. Since the contact angle is finite, for small velocities, one can expand this term $\gamma \cos \theta(u) \simeq \gamma \cos \theta(0) + ku$, resulting in $F_m = ku$, where k is a friction coefficient [23]. Independently, it has been reported that such a linear scaling holds in the limit $\eta_s/\eta_1 \rightarrow 0$ [28].

Using the dimensionless variables $\hat{l} \equiv l/L$, $\hat{t} \equiv$

$t\gamma \cos \theta \bar{H}/LH[4\eta_s L(2-3\alpha)/h+k]$ and $\hat{u} \equiv d\hat{l}/d\hat{t}$, we can integrate the equation of the front motion and obtain

$$\frac{\hat{l}^2}{2} \frac{(\lambda-1)}{1+\frac{2\bar{H}}{3h\delta_1}} + \hat{l} \left(\frac{1}{1+\frac{2\bar{H}}{3h\delta_1}} + \lambda\Sigma \right) = \lambda(1+\Sigma)\hat{t}, \quad (2)$$

where

$$\lambda \equiv \frac{\eta_1}{\eta_2} \frac{3\delta_2 h + 2\bar{H}}{3\delta_1 h + 2\bar{H}} \quad \text{and} \quad \Sigma \equiv \frac{kh}{4\eta_s L(2-3\alpha)}. \quad (3)$$

The parameter λ contains the relative effect of the viscosities of the three fluids together with the fraction of the channel occupied by the lubricant, and Σ quantifies the strength of the friction of the meniscus relative to the lubricant layer.

As shown in Fig. 2a, Eq. 2 agrees well with the simulations, with the contact-line friction coefficient, k , used as the only fitting parameter [29]. The classical, diffusive-like growth regime of Washburn's Law is recovered by imposing $\Sigma = 0$ and letting $\delta_i h/\bar{H} \rightarrow 0$. This eliminates the effect of the meniscus and reduces λ to the familiar viscosity contrast, i.e., $\lambda \rightarrow \eta_1/\eta_2$. Then, taking $\lambda \gg 1$ gives $\hat{l} \rightarrow \sqrt{4\bar{H}\eta_s \hat{t}/3h\eta_1}$.

On the other hand, for $\delta_i h/\bar{H} \gg 1$ and $\lambda \rightarrow 1$ equation (2) yields the linear growth law $\hat{l} \rightarrow \hat{t}$. After recovering dimensions we find

$$l(t) = \frac{\bar{H}h\gamma \cos \theta}{H[4\eta_s L(2-3\alpha) + kh]} t. \quad (4)$$

Remarkably, the velocity of the front depends only on the viscosity and thickness of the lubricant layer and on the channel length.

The linear growth regime identified in this letter occurs for $\delta_i h/\bar{H} \gg 1$, where energy dissipation occurs primarily in the lubricant layer. For intermediate regimes the asymptotic growth of the front will conform to Washburn's law. A cross-over length l_c can be estimated by comparing the magnitudes of quadratic and linear contributions in Eq. 2. We obtain $l_c \sim 2L(1+\lambda\Sigma[1+2\bar{H}/3h\delta_1])/(\lambda-1)$, which implies $l_c > L$ if $\lambda < 3/(1-2\Sigma[1+2\bar{H}/3h\delta_1])$. If the friction associated to the contact line is negligible compared to the lubricant dissipation $\Sigma = 0$, a crossover length $l_c > L$ requires $\lambda < 3$. However, increasing the contact line friction increases the crossover length, and when $\Sigma > 1/2$ Washburn's law will never be observed as the simulation results show in Fig. 2b.

Here we have focused on the case of spontaneous imbibition. However, a low-viscosity lubricant layer has a strong impact in the sensitivity of the front to perturbations, and leads to a significant modification of the front dynamics when the fluids are subject to external forces. Let us consider a uniform external force acting on the displacing liquid, $F_e = f\bar{H}l$, for small η_s . Fig. 3 shows a speed-up of the front as it advances in the channel, in sharp contrast to the classical result of forced imbibition, where the motion of the front is linear. This effect is also

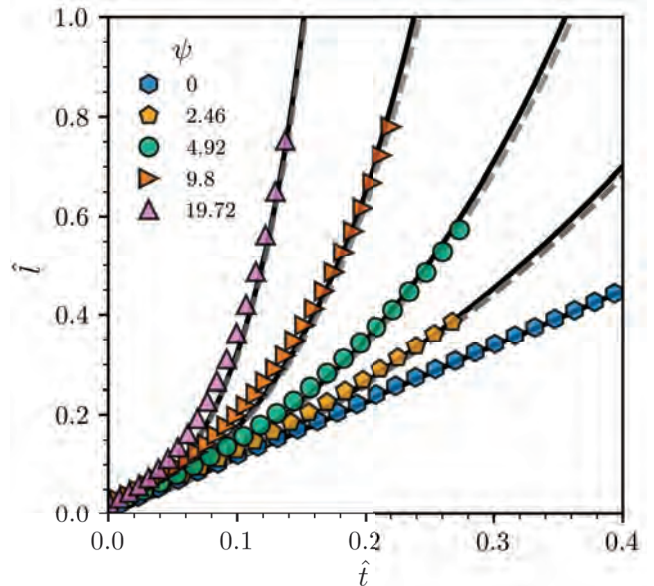


FIG. 3. Forced imbibition dynamics in a lubricant-coated channel. External forcing leads to an exponential growth of the position of the advancing front. The strength of the external force is quantified the forcing coefficient ψ . The simulation parameters correspond to $\Sigma = 24$, $\lambda = 1.2$ and $\delta_1 = 5000$. The symbols correspond to simulations, solid lines correspond to the numerical solution of the differential equation including the forcing term, and the dashed grey lines to the approximation in Eq. 5.

captured by the theoretical model upon adding an external force, which leads to the solid curves shown in Fig. 3 after numerical integration. An approximate expression of the growth law can be obtained in the regime $\lambda \rightarrow 1$ and $\delta_1 \rightarrow \infty$, which gives

$$\hat{l} = \frac{e^{\psi\hat{t}} - 1}{\psi} = \frac{e^{\hat{t}/t_i} - 1}{\psi}, \quad (5)$$

where $\psi = LHf/2\gamma \cos \theta$ is the forcing coefficient. Equation (5) predicts an exponential invasion of the channel in agreement with the simulation results (dashed curved in Fig. 3), with a characteristic time scale $t_i = \eta_s L/Hhf$ determined by the competition between viscous forces in the lubricant layer and the external forcing.

Our work can be used to design experimental setups that optimize imbibition in SLIPS/LIS channels. For example, using liquids with viscosities $\eta_1 = 1700$ mPas, $\eta_2 = 17$ mPas and $\eta_s = 10$ mPas [30], and a typical lubricant thickness of $1 \mu\text{m}$ in a channel of $H \simeq 20 \mu\text{m}$ would result in $\lambda \simeq 8$, thus making the linear regime reported here accessible in experiments. The analytical framework, validated with simulations, provides a starting point to characterise further effects that might be relevant in spontaneous imbibition processes in SLIPS and LIS, such as the precise role of the dissipation in the ridge, or the effect of the varying width of the lubricant in the channel.

Altogether, the ideas reported in this work will help rationalise the effect of a lubricant layer in naturally-occurring situations as well as inspire solutions to technological challenges. For example, in pitcher plants, which inspired SLIPS originally [12], the textured surface that supports the lubricant layer has corrugations which form semi-open channels, and such structures could sustain the capillary flows reported in this paper [31]. Binary liquid capillary bridges, which spontaneously move in confinement and can therefore be used for droplet transport applications, have been reported to spontaneously leave a thin film of liquid adhered to a channel wall [32]. In antifouling applications [28, 33–36], some studies suggest

that bacteria can accumulate in the lubricant layer, limiting its medical applications [37]. Controlling spontaneous flows could be a key solution to enhance LIS properties and make it a suitable material for medical applications [38].

I. P. acknowledges support from Ministerio de Ciencia, Innovación y Universidades (Grant No. PID2021-126570NB-I00 AEI/FEDER-EU), from Generalitat de Catalunya under Program Icrea Acadèmia and project 2021SGR-673DURSI (Grant No. 2017 SGR 884). A.H.-M. acknowledges support from Ministerio de Ciencia, Innovación y Universidades (Grant No. PID2019-106063GB-I00).

-
- [1] M. Rauscher and S. Dietrich, Wetting phenomena in nanofluidics, *Annual Review of Materials Research* **38**, 143 (2008).
- [2] M. De Volder, S. J. Park, S. Tawfick, D. Vidaud, and A. J. Hart, Fabrication and electrical integration of robust carbon nanotube micropillars by self-directed elastocapillary densification, *Journal of Micromechanics and Microengineering* **21** (2010).
- [3] J. Bico, E. Reyssat, and B. Roman, Elastocapillarity: When surface tension deforms elastic solids, *Annual Review of Fluid Mechanics* **50**, 629 (2018).
- [4] Y. Snir and R. D. Kamien, Entropically driven helix formation, *Science* **307**, 1067 (2005).
- [5] H. Hansen-Goos, R. Roth, K. Mecke, and S. Dietrich, Solvation of proteins: Linking thermodynamics to geometry, *Phys. Rev. Lett.* **99**, 128101 (2007).
- [6] X. Li, D. R. Ballerini, and W. Shen, A perspective on paper-based microfluidics: Current status and future trends, *Biomicrofluidics* **6**, 10.1063/1.3687398 (2012).
- [7] P. Estrela, K. Koczula, and A. Gallotta, Lateral flow assays, *Essays in Biochemistry* **60**, 111 (2016).
- [8] M. Pradas and A. Hernández-Machado, Intrinsic versus superrough anomalous scaling in spontaneous imbibition, *Phys. Rev. E* **74**, 041608 (2006).
- [9] M. Pradas, A. Hernández-Machado, and M. A. Rodríguez, Dynamical scaling of imbibition in columnar geometries, *Phys. Rev. E* **77**, 056305 (2008).
- [10] M. Queralt-Martín, M. Pradas, R. Rodríguez-Trujillo, M. Arundell, E. Corvera Poiré, and A. Hernández-Machado, Pinning and avalanches in hydrophobic microchannels, *Phys. Rev. Lett.* **106**, 194501 (2011).
- [11] B. K. Primkulov, J. Y. Y. Chui, A. A. Pahlavan, C. W. MacMinn, and R. Juanes, Characterizing dissipation in fluid-fluid displacement using constant-rate spontaneous imbibition, *Phys. Rev. Lett.* **125**, 174503 (2020).
- [12] T.-S. Wong, S. H. Kang, S. K. Y. Tang, E. J. Smythe, B. D. Hatton, A. Grinthal, and J. Aizenberg, Bioinspired self-repairing slippery surfaces with pressure-stable omniphobicity, *Nature*, 443.
- [13] J. D. Smith, R. Dhiman, S. Anand, E. Reza-Garduno, R. E. Cohen, G. H. McKinley, and K. K. Varanasi, Droplet mobility on lubricant-impregnated surfaces, *Soft Matter* **9**, 1772 (2013).
- [14] D. F. Miranda, C. Urata, B. Masheder, G. J. Dunderdale, M. Yagihashi, and A. Hozumi, Physically and chemically stable ionic liquid-infused textured surfaces showing excellent dynamic omniphobicity, *APL Materials* **2**, 056108 (2014).
- [15] C. Urata, G. J. Dunderdale, M. W. England, and A. Hozumi, Self-lubricating organogels (slugs) with exceptional syneresis-induced anti-sticking properties against viscous emulsions and ices, *J. Mater. Chem. A* **3**, 12626 (2015).
- [16] J. Cui, D. Daniel, A. Grinthal, K. Lin, and J. Aizenberg, Dynamic polymer systems with self-regulated secretion for the control of surface properties and material healing, *Nature materials* **14** (2015).
- [17] S. Kim, H. N. Kim, and S. Lee, A lubricant-infused slip surface for drag reduction, *Physics of Fluids* **32**, 091901 (2020).
- [18] C. Vega-Sánchez, S. Peppou-Chapman, L. Zhu, and C. Neto, Nanobubbles explain the large slip observed on lubricant-infused surfaces, *Nature Communications* **13**, 351 (2022).
- [19] P. A. Tsai, Slippery interfaces for drag reduction, *Journal of Fluid Mechanics* **736**, 1–4 (2013).
- [20] C. Sempregon, T. Krüger, and H. Kusumaatmaja, Ternary free-energy lattice boltzmann model with tunable surface tensions and contact angles, *Phys. Rev. E* **93**, 033305 (2016).
- [21] N. Gheraldi, J. Guan, L. Dodd, P. Maiello, B. Xu, D. Wood, M. Newton, G. Wells, and G. Mchale, Double-sided slippery liquid-infused porous materials using conformable mesh, *Scientific Reports* **9** (2019).
- [22] See EPAPS Document No.xxxx which includes further information on the model.
- [23] E. Ruiz-Gutiérrez, S. Armstrong, S. Lévêque, C. Michel, I. Pagonabarraga, G. G. Wells, A. Hernández-Machado, and R. Ledesma-Aguilar, The long cross-over dynamics of capillary imbibition, *Journal of Fluid Mechanics* **939**, A39 (2022).
- [24] The kinetics of wetting in a capillary, *Journal of Colloid and Interface Science* **136**, 189 (1990).
- [25] G. Martic, J. De Coninck, and T. Blake, Influence of the dynamic contact angle on the characterization of porous media, *Journal of colloid and interface science* **263**, 213–216 (2003).
- [26] D. Quéré, Inertial capillarity, *EPL (Europhysics Letters)* **39**, 533 (2007).
- [27] H. Bruus, *Theoretical Microfluidics*, Oxford Master Series

in Physics.

- [28] A. Keiser, L. Keiser, C. Clanet, and D. Quéré, Drop friction on liquid-infused materials, *Soft Matter* **13**, 6981 (2017).
- [29] The value of $k = 34$ simulation units, is computed once, which indicates it has a weak dependence on the lubricant properties and is controlled by the viscosities in the displacing and displaced fluids.
- [30] S. Peppou-Chapman, J. K. Hong, A. Waterhouse, and C. Neto, Life and death of liquid-infused surfaces: a review on the choice, analysis and fate of the infused liquid layer, *Chem. Soc. Rev.* **49**, 3688 (2020).
- [31] H. F. Bohn and W. Federle, Insect aquaplaning: Nepenthes pitcher plants capture prey with the peristome, a fully wettable water-lubricated anisotropic surface, *Proceedings of the National Academy of Sciences* **101**, 14138 (2004).
- [32] J. Bico and D. Quéré, Self-propelling slugs, *Journal of Fluid Mechanics* **467**, 101 (2002).
- [33] M. Kratochvil, M. Welsh, U. Manna, B. Ortiz, H. Blackwell, and D. Lynn, Slippery liquid-infused porous surfaces that prevent bacterial surface fouling and inhibit virulence phenotypes in surrounding planktonic cells, *ACS Infectious Diseases* **2** (2016).
- [34] M.-S. Lee, H. Hussein, S.-W. Chang, C.-Y. Chang, Y.-Y. Lin, Y. Chien, Y.-P. Yang, C.-Y. Chen, S.-H. Chiou, R. Jih, R. Hwu, V. Charushin, S. Bachurin, M.-S. Lee, H. Hussein, S.-W. Chang, C.-Y. Chang, Y.-Y. Lin, and C.-C. Chang, International journal of molecular sciences nature-inspired surface structures design for antimicrobial applications, *International Journal of Molecular Sciences* **24**, 1348 (2023).
- [35] Y. Yang, Q. Zhu, L. Xu, and X. Zhang, Bioinspired liquid-infused surface for biomedical and biosensing applications, *Frontiers in Bioengineering and Biotechnology* **10** (2022).
- [36] Y. Xie, J. Li, D. Bu, X. Xie, X. He, L. Wang, and Z. Zhou, Nepenthes-inspired multifunctional nanoblades with mechanical bactericidal, self-cleaning and insect anti-adhesive characteristics, *RSC Adv.* **9**, 27904 (2019).
- [37] Nanostructure-based wettability modification of tial6v4 alloy surface for modulating biofilm production: Superhydrophilic, superhydrophobic, and slippery surfaces, *Journal of Alloys and Compounds* **923**, 166492 (2022).
- [38] Y. Zhu, G. Mchale, J. Dawson, S. Armstrong, G. Wells, R. Han, H. Liu, W. Vollmer, P. Stoodley, N. Jakubovics, and J. Chen, Slippery liquid-like solid surfaces with promising antibiofilm performance under both static and flow conditions, *ACS Applied Materials Interfaces* **14** (2022).

Supplementary Material for: Capillary imbibition in lubricant coated channels

Sergi G. Leyva,^{1,2,*} Ignacio Pagonabarraga,^{1,2,3} Aurora Hernández-Machado,^{1,4} and Rodrigo Ledesma-Aguilar⁵

¹*Departament de Física de la Matèria Condensada, Universitat de Barcelona, 08028 Spain*

²*Universitat de Barcelona Institute of Complex Systems (UBICS), Universitat de Barcelona, 08028 Spain*

³*Centre Européen de Calcul Atomique et Moléculaire (CECAM),*

École Polytechnique Fédérale de Lausanne (EPFL), 1015 Lausanne, Switzerland

⁴*Institut de Nanociència i Nanotecnologia, Universitat de Barcelona, 08028 Spain*

⁵*School of Engineering, University of Edinburgh,*

The King's Buildings, Mayfield Road, Edinburgh EH9 3JL, UK

(Dated: January 16, 2024)

DETAILS OF THE SIMULATIONS

The simulations are based in the Lattice-Boltzmann (LB) method, where the discretised distribution function f_i defined at each node of a regular mesh, and each velocity i of a set of velocities follows

$$f_i(\mathbf{r}+\mathbf{c}_i\Delta t; t+\Delta t) = f_i(\mathbf{r}; t) + \sum_j L_{ij}(f_i(\mathbf{r}; t) - f_i^{eq}(\mathbf{r}; t)), \quad (1)$$

where \mathbf{c}_i is the discrete velocity basis and Δt is the discrete time step. L_{ij} is the collision operator that provides the way by which the distribution function evolves towards its equilibrium value. Given a velocity set the discrete distribution function provides a series of moments that relate to physical quantities of the model $\rho(\mathbf{r}; t) = \sum_i f_i(\mathbf{r}; t)$, $\rho u_\alpha(\mathbf{r}; t) = \sum_i f_i(\mathbf{r}; t)c_{i\alpha}$, $\Pi_{\alpha\beta}(\mathbf{r}; t) = \sum_i f_i(\mathbf{r}; t)c_{i\alpha}c_{i\beta}$. The summation takes place over the discrete set of velocities that corresponds to a certain basis, and the number of each basis depends on the basis election. The number of discrete velocities is called N_{vel} . In our method we will generally use three dimensions and 19 discrete velocities, which is widely known as the D3Q19 set. Further details on the collision operator and implementation can be found in the documentation of the implementation we used, Ludwig, which is an open access code [1]. The three liquid phases are implemented by means of a ternary free energy [2]

$$F = \int_{\Omega} \frac{\kappa_1}{2} C_1^2 (1 - C_1)^2 + \frac{\kappa_2}{2} C_2^2 (1 - C_2)^2 + \frac{\kappa_s}{2} C_3^2 (1 - C_s)^2 + \frac{\kappa'_1}{2} (\nabla C_1)^2 + \frac{\kappa'_2}{2} (\nabla C_2)^2 + \frac{\kappa'_s}{2} (\nabla C_s)^2, \quad (2)$$

where the subindex s refers to the fluid phase we use as the lubricant.

In our current implementation, the order parameters representing each phase are evolved following the Cahn-Hilliard equation

$$\partial_t C_i = \partial_\alpha (C_i u_\alpha - M \partial_\alpha \mu_i) \quad (3)$$

which involves calculation of the advection of the order parameter, and the gradient of the chemical potential for each phase i . We set $\kappa_i = \beta \kappa'_i$ to impose that all interfaces have the same width. The solid-liquid surface tension can be tuned by means of introducing a boundary condition of the gradient of the order parameters normal to solid boundaries, through the wetting parameters h_1 and h_2 . With this model, one can tune the equilibrium contact angles between the different fluids θ_1 , θ_2 and θ_s , through κ_i and α , and each combination of fluids and solid through the wetting parameters h_1 and h_2 , θ_{12} , θ_{1s} , θ_{s2} . All the details of this calculations relating the contact angles and the free energy parameters can be found in Ref. [2].

We briefly introduce the set of parameters used for the simulations. The total length and width of the channel are $L = 500$ and $H = 70$, respectively. We add two large reservoirs, of displacing (fluid 1, left) and displaced (fluid 2, right) phases, to allow for the displacing phase to invade the whole length of the capillary (from left to right). The upper and lower lubricant layers (fluid s) are initialised with a uniform width of $h = 4$ fluid nodes, and the displacing-displaced interface is set at an initial front position $l(0) = 0.02L$. The viscosity contrast is $\eta_2 = \eta_1/100$, and we choose a viscosity $\eta_1 = 5$, which in our simulations ensures stability in a range of η_s of orders of magnitude $\eta_s \in (0.001, 50)$. We choose the surface tension of the lubricant liquid with the other two to lead to contact angle close to 180 degrees, to minimize the effect of the curvature of the interface when the three liquids meet. More specifically, we choose $\kappa_1 = 0.002$, and $\kappa_2 = \kappa_3 = 0.007$, which leads to an equilibrium angles between fluids of 77.8° , 141.1° and 141.1° for fluids 1, s , and 2, respectively. For stabilising the lubricant layer, we choose complete wetting of the lubricant respect the displacing and displaced fluids by means of satisfying the relations $S_{1s} = \cos \theta_{1s} - \gamma_{1s} > 1$ and $S_{s2} = \cos \theta_{s2} - \gamma_{s2} < -1$.

*Electronic address: sergi.granados@ub.edu

This is achieved by a set of wetting parameters $h_1 = 1.75 \cdot 10^{-4}$ and $h_1 = 1.75 \cdot 10^{-3}$. Furthermore, this wetting parameters lead to an equilibrium contact angle $\theta_{12} = 51^\circ$ that is hydrophilic in order to enhance spontaneous imbibition of the pore. When the lubricant is introduced, the interaction of the front between the lubricant and the solid leads to a measured contact equilibrium angle of $\theta = 49^\circ$, which is the angle that sets the pressure drop.

ANALYTICAL SOLUTION

Our theoretical model consists in solving the Stokes equation

$$\eta_i \frac{\partial^2 v_i}{\partial y^2} = \frac{dp_i}{dx}, \quad i = 1, 2, \quad (4)$$

and

$$\eta_s \frac{\partial^2 v_{s_i}}{\partial y^2} = \frac{dp_{s_i}}{dx}, \quad i = 1, 2, \quad (5)$$

for the displacing and displaced phases, 1 and 2 respectively, and the corresponding lubricant velocity profile. The boundary conditions, already introduced in the paper, consist on imposing the continuity of the velocity and tangential stress at the interface with the lubricant layer, i.e., $v_i(h) = v_{s_i}(h)$ and $\eta_i dv_i(h)/dy = \eta_s dv_{s_i}(h)/dy$. and fixing the average velocities of the fluids and the lubricant, $\frac{1}{H/2-h} \int_h^{H/2} v_i dy = u$ and $\frac{1}{h} \int_0^h v_{s_i} dy = u_s$. With these boundary conditions, we obtain the velocity profiles

$$v_{s_i}(y) = a_i y + c_i y^2 \quad \text{for} \quad 0 \leq y \leq h, \quad (6)$$

and

$$v_i(y) = b_i + d_i (y - H/2)^2 \quad \text{for} \quad h \leq y \leq H/2. \quad (7)$$

where the coefficients can be determined analytically

$$a = \frac{3u_s}{h} + \frac{3(3u_s - 2u)\delta}{3h\delta + 2\bar{H}}$$

$$b = \frac{6u\delta h + 3\bar{H}(2u - u_s)}{2(3e\delta + 2\bar{H})}$$

$$c = \frac{9u\delta h - 3u_s(6h\delta + \bar{H})}{h^2(3e\delta + 2\bar{H})}$$

$$d = \frac{6(2u - 3u_s)\delta}{\bar{H}(3h\delta) + 2\bar{H}}$$

From Eq. 6, it becomes clear that an average lubricant velocity $u_s = 0$ results in recirculation of fluid, since $a = -6u\delta/(3h\delta + 2\bar{H}) < 0$, thus resulting in a

negative derivative of the flow profile at $y=0$. Even for small average lubricant velocities, some recirculation is expected. It can be shown that a becomes zero when $u_s = uh\delta/(3h\delta + \bar{H})$, taking a positive value. For lower u_s , we expect some lubricant going towards the opposite direction of the front close to the solid.

For calculating the dissipation rate between the lubricant and the bulk fluids, we note that $\dot{E}_b = \int_0^l \int_h^{H/2} \eta_1 |\nabla v_1|^2 dy dx + \int_l^L \int_h^{H/2} \eta_2 |\nabla v_2|^2 dy dx$, to that of the lubricant, $\dot{E}_s = \int_0^l \int_0^h \eta_s |\nabla v_{s_1}|^2 dy dx + \int_l^L \int_0^h \eta_s |\nabla v_{s_2}|^2 dy dx$.

Using this expressions and the analytical solution leads to

$$\frac{\dot{E}_b}{\dot{E}_s} = \frac{2\bar{H}}{3h} \frac{\left(\frac{3h\delta_1 + 2\bar{H}}{3h\delta_2 + 2\bar{H}}\right)^2 + 1}{\delta_2^2 \left(\frac{3h\delta_1 + 2\bar{H}}{3h\delta_2 + 2\bar{H}}\right)^2 + \delta_1^2}. \quad (8)$$

For adimensionalising curves in Fig. 2b, we use the equilibrium angle $\theta = 49^\circ$, and fit k to the curve of smallest lubricant viscosity, which has a value of $k = 34$ simulation units. Then we use this same value for all the curves. For each simulation, we measure the average slip width in the channel and calculate the Σ variable to obtain the solutions from our model.

The force balance, $F_v + F_m = F_c + F_e$ leads to the equation of motion

$$\frac{d\hat{l}}{d\hat{t}} \left[\frac{\hat{l}(\lambda - 1) + 1}{1 + \frac{2\bar{H}}{3h\delta_1}} + \lambda\Sigma \right] = (1 + \Sigma + \hat{l}\psi) \lambda, \quad (9)$$

where ψ contains the external forcing, as defined in the paper. If ψ is set to 0, we obtain Eq. 2 of the manuscript. If ψ is not zero, an analytical solution can be obtained in the case $\lambda = 1$, which corresponds to Eq. 5 in the article. In Fig. 3, we plot the numerical solution to Eq. 9 here (solid line), and compare it to the approximate solution Eq. 5 of the article (dashed lines) to check its validity.

COMPARING SIMULATIONS AND THEORETICAL RESULTS

Here we report the values of the parameters we used for reproducing the curves in Fig. 3b). The initial lubricant width corresponds to a width $h_0 = 4$ and relaxes to an average constant value h , which we measure in the simulations and always remains close to h_0 . The steady lubricant width is typically a smaller than h_0 , since some lubricant is accumulated in the meniscus due to the surface tensions and the resulting forces acting in the Neumann triangle. Since the channel width is $H=70$, this results in a $\bar{H} = H - 2h \simeq 62$ LB units. In the simulations, the average velocity of the lubricant, characterised

by α , is negligible compared to that of fluids 1 and 2. For example, for the largest lubricant viscosity η_s , we measure the largest $\alpha \simeq 0.06$. In this case, the influence of this small flux turns out to be negligible and the curves fit using $\alpha = 0$. As the lubricant viscosity decreases, for $\eta_s < 1$, the lubricant flux vanishes $\alpha = 0$. In the imbibition curves, In Fig. 3b), the values of δ_2 correspond, from large to small lubricant viscosities to 0.1, 0.83, 0.5, 1.7, 2.5, 5 and 50 respectively. With these parameters we can obtain the values of λ . In our simulations, the meniscous friction is characterised by a parameter $k=34$,

which remains constant as η_s is varied, in our simulation range, for δ_2 as small as 0.1. This allows to obtain the Σ 's reported in the caption of Fig 3.

-
- [1] J.-C. Desplat, I. Pagonabarraga and P. Bladon, *Computer Physics Communications* **134**, 273 (2001)
 - [2] C. Semperebon, T. Krüger, and H. Kusumaatmaja, *Phys. Rev. E* **93**, 033305 (2016).

Publication 7:
Discontinuous transition in electrolyte flow through
charge-patterned nanochannels

Tine Curk¹, Sergi G. Leyva^{2,3}, and Ignacio Pagonabarraga^{2,3}

¹Department of Materials Science & Engineering, Johns Hopkins University, Baltimore, Maryland
21218, USA

²Departament de Física de la Matèria Condensada, Universitat de Barcelona, 08028 Barcelona,
Spain

³Universitat de Barcelona Institute of Complex Systems (UBICS), Universitat de Barcelona,
08028 Barcelona, Spain

ArXiv: <https://doi.org/10.48550/arXiv.2401.03666>

Discontinuous transition in electrolyte flow through charge-patterned nanochannels

Tine Curk,^{1,*} Sergi G. Leyva,^{2,3} and Ignacio Paganobarraga^{2,3}

¹*Department of Materials Science & Engineering,
Johns Hopkins University, Baltimore, Maryland 21218, USA*

²*Departament de Física de la Matèria Condensada, Universitat de Barcelona, 08028 Spain*

³*Universitat de Barcelona Institute of Complex Systems (UBICS), Universitat de Barcelona, 08028 Spain*

We investigate the flow of an electrolyte through a rigid nanochannel decorated with a surface charge pattern. Employing lattice Boltzmann and dissipative particle dynamics methods, as well as analytical theory, we show that electro-hydrodynamic coupling leads to two distinct flow profiles. The accompanying discontinuous transition between slow, ionic, and fast, Poiseuille regimes is observed at intermediate ion concentrations, channel widths, and electrostatic coupling strengths. These findings indicate routes to design nanochannels containing a typical aqueous electrolyte that exhibits a digital on/off flux response, which could be useful for nanofluidics and ionotronic applications.

Ion transport through nanochannels often exhibits non-linear effects such as gating and pressure sensing [1–3]. These mechanisms are generically present in biological nanochannels, for example, channels can adapt their shape in response to mechanical stresses and act as emergency safety valves to avoid cellular damage [4], or changes in the fluid flows trigger electrochemical signals [5]. Much effort has been made to mimic the capabilities of such biological mechanisms. For example, conical nanopores with constant surface charge exhibit gating as a function of the exerted pressure, and have been extensively characterized, both experimentally and theoretically [6–12]. Such geometrical asymmetries can result in rectification [6, 7] and particle separation due to entropic transport [13]. Both molecular sized pores and nanochannels can give rise to gating and rectification, but the precise response and the physical mechanisms at play may change drastically [8–11, 14–16].

An alternative avenue to obtain non-linear response is by introducing charge heterogeneities. Theoretical investigations indicate that a discontinuity in the surface charge causes a disturbance in the flow profile that can extend a distance from the surface an order of magnitude larger than the Debye screening length λ_D [17]. Indeed, surface charge patterns in micron-sized channels can result in intricate electroosmotic flows [18], and complex flow patterns such as vortex formation that enhance fluid mixing [19–21]. Hence, surface charge patterns can qualitatively alter electrokinetic flows, opening up the possibility to exploit this feature to control ionic transport in nanochannels.

Here we investigate the flow of an electrolyte through a nanochannel slit of width w at low Reynolds numbers ($\text{Re} \ll 1$). In the absence of charge, the flow through a channel with slip length ℓ_s attains the parabolic, Poiseuille velocity profile

$$v_x^P(y) = \frac{G_x}{2\eta} (w^2/4 - y^2 + w\ell_s) , \quad (1)$$

where G_x is the pressure gradient in the x -coordinate,

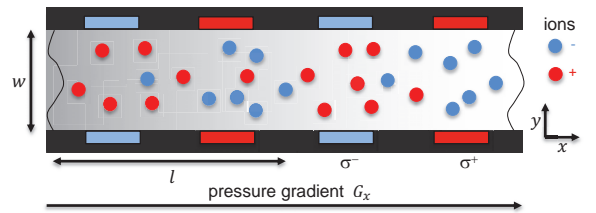


FIG. 1: Schematic of an electrolyte flow through a charge-patterned nanochannel under a pressure gradient G_x . Channel width w with a charge pattern of size l of alternating positive σ^+ and negative σ^- charge density.

η the dynamic viscosity and the channel walls are positioned at $y = \pm w/2$. Introduction of surface charge modifies this flow profile due to electrokinetic coupling between the hydrodynamic flow and electrostatic interactions. The electrostatic interaction strength is controlled by the Bjerrum length $l_B = e_0^2 / (4\pi\epsilon_0\epsilon_r k_B T)$, with e_0 the elementary charge, ϵ_0 and ϵ_r the vacuum and relative permittivity, k_B the Boltzmann constant and T the absolute temperature, which yields a typical length $l_B = 0.71$ nm for an aqueous solution at room temperature. We employ the simplest charge pattern that preserves the charge neutrality; an alternating pattern of positive and negative charged sections with pattern size l and fraction of the surface f with symmetric surface charge density, $\sigma^+ = -\sigma^- = \sigma$ (Fig. 1). The channel contains an electrolyte solution at density ρ and monovalent ion concentration c_{ion} . To investigate how the surface charge affects the flow we employ two independent computational methods that combine hydrodynamics with electrostatics, Lattice Boltzmann (LB) with electrokinetics [22] and Dissipative-particle dynamics (DPD) [23] with explicit ions. Analysis is further supported by analytical mean-field theory.

We initially focus on the parameters corresponding to channel width $w = 5.16$ nm, containing an aqueous salt solution ($\rho = 10^3$ kg/m³, $\eta = 10^{-3}$ Pa s, $T = 293$ K) and consider a typical slip length ℓ_s for electrolytes on

surfaces with different degree of polarity is generically finite and small, $\ell_s \approx 20$ nm [24]. The surface charge pattern length is $l = 10w$ with $f = 0.5$, which makes the width of each charged strip comparable to the width of the channel (Fig. 1). The pattern charge density is $\sigma \approx \pm 0.5e_0/\text{nm}^2$, which is typical of, e.g., silica or iron oxide surfaces [25].

The Lattice-Boltzmann (LB) method combined with convection-diffusion solver for ions [22] allows us to analyze the steady-state flow of an electrolyte as a function of pressure gradient G_x and ion concentration c_{ion} (Fig. 2). To model small ion diffusion with typical diffusion constant $D \approx 10^{-9}\text{m}^2/\text{s}$ we set $D = 10^{-3}\nu$, with the kinematic viscosity $\nu = \eta/\rho$. The slip length is introduced using a fractional bounce-back boundary condition at the walls [26]. The lattice size is set to $\Delta x = w/16$, which is sufficiently small to avoid finite size effects (see SI), and the reduced viscosity is set to $\eta^* = 0.2$, which determines the LB time unit $\Delta t = \Delta x^2 \eta^* / \nu$.

Surprisingly, we find that at a threshold pressure gradient G_t , the flow velocity exhibits a discontinuous transition characterized by nearly an order of magnitude change in the average flow velocity (Fig. 2a). This transition is associated with a discontinuous change in the ion distribution measured by the net charge density ρ_q in the channel. The slow flow regime shows localized counterion clouds that reflect the surface charge pattern (Fig. 2b), whereas the charge density is largely uniform in the fast flow regime with only a scant signature of the counterion layer (Fig. 2c). This suggests that at $G_x < G_t$ the counterions are localized in a pattern reflecting the surface charge, which results in a high drag on the fluid and thus a distinct slow flow regime. Conversely, at $G_x > G_t$, the drag becomes sufficiently large to pull the counterion away from the patterned surface charge, leading to ion mixing and associated reduction in local net charge density, which in turn substantially reduces the ion drag and results in a discontinuous transition. For $G \gg G_t$, electrokinetic effects become negligible and the average flow velocity is determined by the Poiseuille flow,

$$v_P = \langle v_x^P(y) \rangle = \frac{G_x w^2}{12\eta} \left(1 + \frac{6\ell_s}{w} \right). \quad (2)$$

The discontinuous transition is only observed at intermediate ion concentrations, whereas both higher and lower salt concentrations result in a non-linear, but continuous flow dependence on G_x . This peculiar behavior is a consequence of many-body electrokinetic effects. At low ion concentrations, $c_{\text{ion}} \rightarrow 0$, electrostatic interactions become irrelevant and the flow attains the Poiseuille profile. In the opposite limit the electrostatic effects become confined to a narrow boundary layer since $\lambda_D \propto c_{\text{ion}}^{-1/2}$ and thus the flow again approximately follows a Poiseuille profile. Conversely, at intermediate ion concentrations the electrokinetic effects can qualitatively change the flow, leading to a discontinuous transition

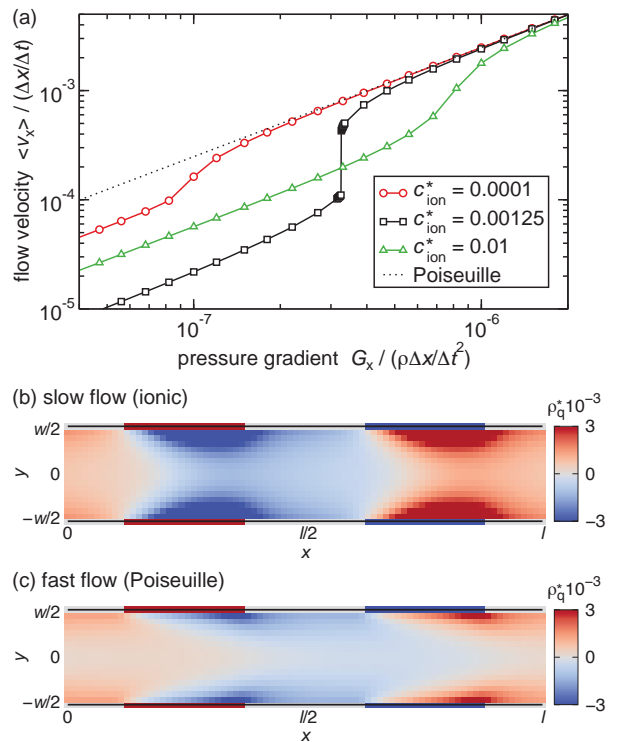


FIG. 2: Steady-state flow velocity obtained from LB simulations. (a) average velocity at different ion concentrations, $c_{\text{ion}}^* = c_{\text{ion}} \Delta x^3$. The dashed line corresponds to ideal Poiseuille flow [Eq. (2)]. (b,c) net charge density, $\rho_q^* = \rho_q \Delta x^3 / e_0$, at coexistence conditions for the (b) slow and (c) fast flow profiles at $G = 3.25 \cdot 10^{-7} \rho \Delta x / \Delta t^2$ and $G = 3.26 \cdot 10^{-7} \rho \Delta x / \Delta t^2$, respectively, and $c_{\text{ion}}^* = 0.00125$.

that separates the fast and slow flow regimes. The same argument implies the transition only occurs at intermediate Bjerrum lengths since $\lambda_D \propto l_B^{-1/2}$.

Although the LB calculations clearly point to a discontinuous transition in the flow, the method does not include thermal fluctuations and assumes a continuous charge distribution. To establish whether the observed transition is affected by thermal fluctuations or unit charge discretization, we turn to DPD, which is an off-lattice method that models the solvent as a fluid of soft particles and allows the introduction of explicit ions.

We use standard DPD parameters corresponding to an aqueous solution [23, 27] with DPD particle density $\rho_s = 3/\lambda^2$, at $\lambda = 0.645$ nm and hydrodynamic coupling $\gamma = 4.5k_B T \tau / \lambda^2$. We introduce electrolyte ions as charged spheres with diameter $\lambda_{\text{ion}} = \lambda$ (Fig. 3a). The short-range ion-ion and ion-wall repulsion is modeled using the standard WCA potential with strength $\varepsilon = k_B T$. The same WCA form is used to describe the smooth channel wall interaction with DPD particles and ions. To separate thermodynamic and hydrodynamic parameters, ions and DPD particles have no conservative

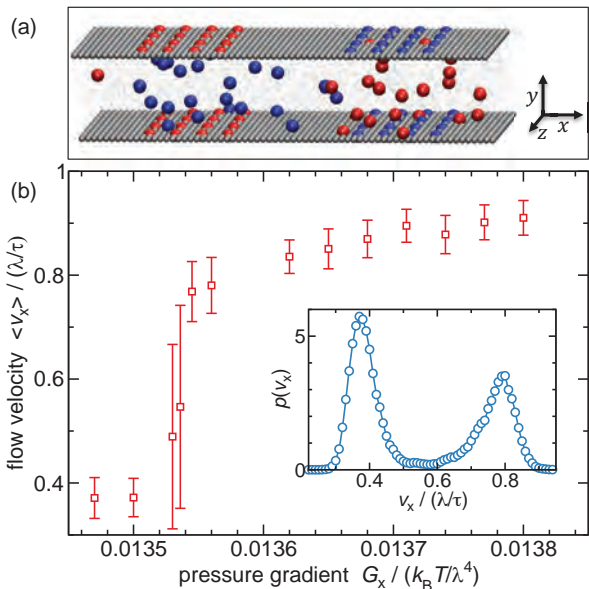


FIG. 3: Steady state flow from DPD simulations. (a) Nanochannel configuration where cations and anions are shown as red and blue spheres, respectively while channel walls are shown in grey with embedded surface charges (at $G = 0.003k_B T/\lambda^4$). DPD particles are represented as small black dots. (b) Average velocity, error bars mark the standard deviation of the velocity distribution. Inset shows the velocity distribution at coexistence ($G = 0.004512k_B T/\lambda^4$). System size $L/\lambda = [40, 8, 8]$ and $c_{\text{ion}} = 0.01\lambda^{-3}$.

pair-interaction and interact only through the DPD thermostat [28]. The ion-DPD hydrodynamic coupling is set to $\gamma_{\text{ion}} = 5\gamma$, which yields the desired diffusion constant of ions, $D \approx \text{nm}^2/\text{ns}$, where the time unit, $\tau = 0.077 \text{ ns}$, is determined from reduced viscosity $\eta_{\text{dpd}}^* = 0.85$ [27] via $\eta = \eta_{\text{dpd}}^* k_B T \tau \lambda^{-3}$. The pressure gradient is introduced as an external body-force on the solvent DPD particles. The partial-slip boundary condition at the walls is implemented by introducing immobilized particles at the wall with surface density $\rho_w = \rho_s \lambda$ that interact with DPD particles only via the thermostat with coupling γ_w , which is determined by the desired slip-length ℓ_s . Electrostatic interaction are calculated using PPPM Ewald summation (see SI for details).

Using this DPD model we find that the steady-state flow in a charge-patterned nanochannel exhibits a doubly-peaked velocity distribution (Fig. 3b) which implies a discontinuous transition between slow and fast flow regimes. Moreover, the transition becomes sharper at higher surface charge densities, which is in quantitative agreement with LB (Fig. 4). The agreement is remarkable given that LB does not account for either thermal fluctuations or discrete charges. This indicates that the existence and the location of the discontinuous transition is robust and is not sensitive to the details of the model.

Based on the simulation results, we propose a mean-

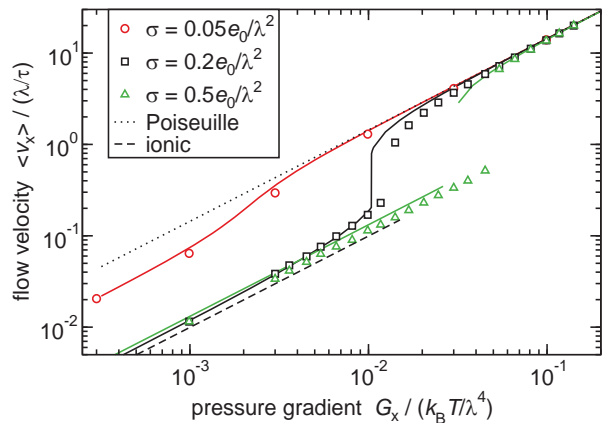


FIG. 4: Steady state flow at different surface charge densities σ . Comparison between DPD (symbols), LB (solid lines), and analytical prediction for the Poiseuille regime (dotted line, Eq. (2)) and ionic regime at $\sigma = 0.2e_0/\lambda^2$ (dashed line, Eqs. (6) and (7)). Parameters: $c_{\text{ion}} = 0.01\lambda^{-3}$.

field theory that captures the essential features of the electro-hydrodynamic coupling. The flow velocity is determined by both the drag of ions localized in the channel and the viscous drag of the walls. Specifically, the viscous drag force of the two confining walls F_w is determined by the shear rate at the walls,

$$F_w = \pm 2A\eta \left(\frac{\partial v_x}{\partial y} \right)_{y=\mp w/2}, \quad (3)$$

with A the surface area of the wall. The Stokes drag per ion is $f_i = -3\pi\eta\lambda_{\text{ion}}v_i$, where v_i is the velocity of the ion relative to the surrounding fluid and λ_{ion} is the hydrodynamic diameter of the ions. At small pressure gradients, ions are confined to the charged regions (Fig. 3a) thus the relative velocity is, $v_i = -v_x(y)$. The total ion drag F_i on the fluid is obtained by integrating over all counterions in the charged channel section. Approximating that the counter-ion charge density ρ_q does not vary with x within each charged section,

$$F_i = 3\pi\eta\lambda_{\text{ion}}fA \int_{-w/2}^{w/2} v_x(y) \frac{\rho_q(y)}{e_0} dy, \quad (4)$$

where $\rho_q(y)/e_0$ is the counterion concentration profile. For $\lambda_D \geq w/2$ the two screening layers from the opposite walls overlap and $\rho_q(y)$ is approximately uniform and determined by the surface charge density for $c_{\text{ion}} > f\sigma/(we_0)$ or the overall ion concentration for $c_{\text{ion}} < f\sigma/(we_0)$, $\rho_q(y) = \min[2\sigma/w, c_{\text{ion}}e_0]$. Conversely, for $\lambda_D < w/2$ and $c_{\text{ion}} > f\sigma/(we_0)$, the surface charge pattern is screened (Fig. 2) and the ion contribution becomes negligible, $F_i \sim 0$.

We can now analytically determine the ratio of drag forces due to bound counterions and the channel walls.

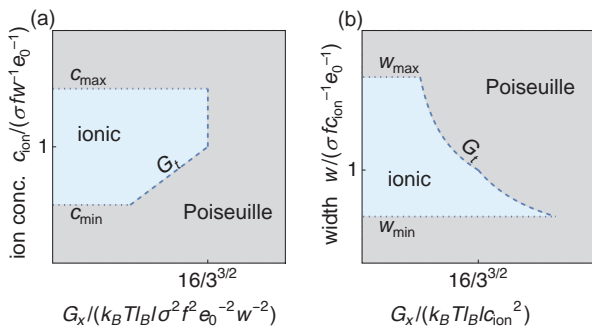


FIG. 5: Diagrams delineating the Poiseuille and diffusive flow regimes: (a) constant c_{ion} , (b) constant w . The upper bounds c_{max} and w_{max} are determined by $w = 2\lambda_{\text{D}}$, while the lower bounds c_{min} and w_{min} are determined by $R = 1$ [Eq. (5)] and shown as dotted lines. The transition at G_t (dashed line) is determined by Eq. (7).

Assuming the profile remains parabolic,

$$R = \frac{F_i}{F_w} = \frac{\pi \lambda_{\text{ion}} w}{2} \min[\sigma f, w c_{\text{ion}} e_0] \left(1 + \frac{6\ell_s}{w}\right), \quad (5)$$

which is independent of the pressure gradient. The average flow velocity in the channel $\langle v_x \rangle \propto G_x / (F_w + F_{\text{ion}})$ can be written as,

$$\langle v_x \rangle = \frac{v_{\text{P}}}{1 + R}. \quad (6)$$

For $R \ll 1$ the ion contribution is negligible and the flow attains the Poiseuille profile [Eqs. (1) and (2)], whereas for $R > 1$ the ion drag dominates and we call this regime “ionic”.

The transition between the two flow profiles will occur when the drag force is sufficiently large to pull the ions away from the charge pattern. This force can be estimated analytically by approximating the charge distribution with a point charge Q_s per surface patch depth w (the relevant lengthscale), $Q_s = \sigma w l$ (Fig 1), and a corresponding point charge Q_i for the counterions in the center of the channel, while neglecting interactions beyond w . The net counterion charge is determined by either the surface charge, or the ion concentration if ions cannot fully compensate the surface charge, $Q_i = \min[Q_s, c_{\text{ion}} w^2 l e_0]$. The resulting maximum restoring force is $F_{\text{max}} = k_B T \frac{8Q_s Q_i l_B}{3\sqrt{3}w^2 e_0^2}$ and the transition between the diffusive and Poiseuille flow regimes occurs at a pressure gradient that can overcome this force, $G_t = 2F_{\text{max}} / (w^2 l)$, which equals to

$$G_t = \frac{16k_B T l_B \sigma f l c_{\text{ion}} \min[1, f\sigma / (c_{\text{ion}} w e_0)]}{3^{\frac{3}{2}} w e_0}. \quad (7)$$

This theory is able to semi-quantitatively predict both the flow velocity $\langle v_x \rangle$ and the location of the transition G_t (Fig. 4). Moreover, the theory predicts general regions

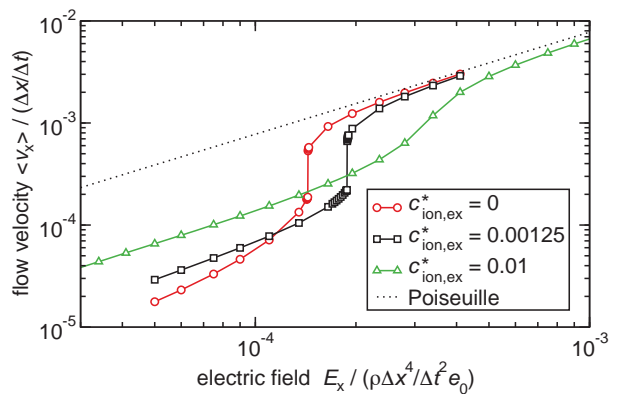


FIG. 6: Steady-state flow velocity for el. field-driven flow at $\sigma = 0.1e_0/\Delta x^2$. The channel configuration is the same as shown in Fig. 2], but without the negative surface charge. The dashed line corresponds to ideal Poiseuille flow [Eq. (2)] at force density $G_x = E_x \langle \rho_q \rangle$. Theory [Eq. (7)] predicts the transition at $E_t \approx 2 \cdot 10^{-4} \rho \Delta x^4 / (\Delta t^2 e_0)$.

of parameter space where different flow regimes are expected to be observed (Fig. 5). The ionic regime is found only at intermediate c_{ion} and w , while its extent depends on the surface charge σ and slip length ℓ_s . The larger the slip length, the larger the relative drag of ions [Eq. (5)] and thus the larger the jump at the transition [Eq. (6)].

For non-neutral charge patterns the fluid attains a net charge and the electroosmotic flow can be induced by an external electric field E_x instead of a pressure gradient. For a pattern consisting of only one polarity we again observe a discontinuous transition (Fig. 6). The only notable difference is a lower limit for the counterion concentration $\langle \rho_q \rangle = 2f\sigma/w$, at which the transition remains discontinuous even in the absence of extra salt density $c_{\text{ion,ex}}$. The net body force, $G_x = E_x \langle \rho_q \rangle$, is determined by the net charge density $\langle \rho_q \rangle$ and the location of the transition, $E_t = G_t / \langle \rho_q \rangle$, is semi-quantitatively determined by the theory [Eq. (7)]. Thus, we expect the flow-regime-diagrams (Fig. 5) are qualitatively applicable to flows driven by electric fields.

The sharp flow transition is reminiscent of the ionic Coulomb blockade effect that occurs at the level of individual ions or electrons at small channel widths $w \lesssim l_B$ and leads to sharp changes in the ionic current depending on the surface charge density. However, Coulomb blockade is limited to strong electrostatic coupling and does not predict a discontinuous transition as a function of electrostatic field [29]. Therefore, we conclude that the observed phenomenon (Fig. 6) is distinct from the Coulomb blockade effect.

In summary, we have investigated the flow of an electrolyte solution through a rigid nanochannel decorated with a surface charge pattern and demonstrated the capability of effective gating for overall electroneutral channels. Simulation results and analytical theory predict two

distinct flow regimes, a slow ion-drag dominated flow, and a faster Poiseuille flow, separated by a discontinuous transition. This transition occurs only at intermediate ion concentrations, channel widths, and electrostatic coupling strengths and appears to be qualitatively different both from the Coulomb blockade effect [29] in nanochannels and the continuous laminar–turbulent transition in pipe flow [30].

While mechanosensitive nanochannels are common in biology, their non-linear response is typically coupled to structural changes in the channel such as protein conformational changes [31]. Our findings imply that such structural changes are not necessary to obtain two distinct (on/off) flow profiles. Moreover, the principles that drive the discontinuous flow transition open venues for the design of nanochannel devices, an alternative to those based on conical pores [9, 12] and angstrom-scale slits [32], that could also result in a memristive response. Hence, the possibility to control ionic transport through charge-patterned nanochannels make them potential components in iontronics and the design of brain-inspired neuronal circuits. [12].

T.C. thanks Erik Luijten for enlightening discussions and acknowledges support from Whiting School of Engineering (JHU) through startup funds, and from Advanced Research Computing at Hopkins (rockfish.jhu.edu), which is supported by the National Science Foundation (NSF) grant number OAC 1920103. I.P. acknowledges support from Ministerio de Ciencia e Innovación MICIN/AEI/FEDER for financial support under grant agreement PID2021-126570NB-100 AEI/FEDER-EU, and from Generalitat de Catalunya under Program Icrea Acadèmia and project 2021SGR-673.

* Electronic address: tcurk@jhu.edu

- [1] E. Perozo, M. C. Cortes, P. Sompornpisut, A. Kloda, and B. Martinac, *Nature* **418**, 942 (2002).
- [2] S. Sukharev and D. Corey, *Sci STKE* **219**, 1 (2004).
- [3] N. Bavi, M. C. Cortes, C. Cox, P. Rohde, W. Liu, J. Deitmer, O. Bavi, P. Strop, A. Hill, D. Rees, et al., *Nat Commun* **7** (2016).
- [4] E. Haswell, R. Phillips, and D. Rees, *Structure (London, England : 1993)* **19**, 1356 (2011).
- [5] B. Martinac and O. Hamill, *Proceedings of the National Academy of Sciences of the United States of America* **99**, 4308 (2002).
- [6] Z. Siwy, E. Heins, C. Harrell, P. Kohli, and C. Martin, *Journal of the American Chemical Society* **126**, 10850 (2004).
- [7] C. C. Harrell, P. Kohli, Z. Siwy, and C. R. Martin, *Journal of the American Chemical Society* **126**, 15646 (2004), URL <https://doi.org/10.1021/ja044948v>.
- [8] J. Cervera, B. Schiedt, and P. Ramirez, *EPL (Europhysics Letters)* **71**, 35 (2007).
- [9] L. Jubin, A. Poggioli, A. Siria, and L. Bocquet, *Proceedings of the National Academy of Sciences* **115**, 4063 (2018), URL <https://www.pnas.org/doi/abs/10.1073/pnas.1721987115>.
- [10] T.-W. Lin and J.-P. Hsu, *Journal of Colloid and Interface Science* **564** (2019).
- [11] S. Dal Cengio and I. Pagonabarraga, *The Journal of Chemical Physics* **151**, 044707 (2019), ISSN 0021-9606, URL <https://doi.org/10.1063/1.5108723>.
- [12] T. M. Kamsma, W. Q. Boon, T. ter Rele, C. Spiti, and R. van Roij, *Phys. Rev. Lett.* **130**, 268401 (2023), URL <https://link.aps.org/doi/10.1103/PhysRevLett.130.268401>.
- [13] P. Margaretti, I. Pagonabarraga, and J. M. Rubi, *Phys. Rev. Lett.* **113**, 128301 (2014), URL <https://link.aps.org/doi/10.1103/PhysRevLett.113.128301>.
- [14] M. Ghosh, K. F. A. Jorissen, J. A. Wood, and R. G. H. Lammertink, *The Journal of Physical Chemistry Letters* **9**, 6339 (2018), URL <https://doi.org/10.1021/acs.jpcllett.8b02771>.
- [15] L. Xie, J. Tang, R. Qin, Q. Zhang, J. Liu, Y. Jin, and H. Wang, *Advanced Functional Materials* **33**, 2208959 (2023), URL <https://onlinelibrary.wiley.com/doi/abs/10.1002/adfm.202208959>.
- [16] Z. Zhu, D. Wang, Y. Tian, and L. Jiang, *Journal of the American Chemical Society* **141**, 8658 (2019), URL <https://doi.org/10.1021/jacs.9b00086>.
- [17] A. S. Khair and T. M. Squires, *Journal of fluid mechanics* **615**, 323 (2008).
- [18] A. D. Stroock, M. Weck, D. T. Chiu, W. T. S. Huck, P. J. A. Kenis, R. F. Ismagilov, and G. M. Whitesides, *Phys. Rev. Lett.* **84**, 3314 (2000), URL <https://link.aps.org/doi/10.1103/PhysRevLett.84.3314>.
- [19] S. Datta and J. N. Choudhary, *Fluid Dynamics Research* **45**, 055502 (2013), URL <https://dx.doi.org/10.1088/0169-5983/45/5/055502>.
- [20] L. M. Lee, W. L. W. Hau, Y.-K. Lee, and Y. Zohar, *Journal of Micromechanics and Microengineering* **16**, 17 (2005), URL <https://dx.doi.org/10.1088/0960-1317/16/1/003>.
- [21] U. Ghosh and S. Chakraborty, *Phys. Rev. E* **85**, 046304 (2012), URL <https://link.aps.org/doi/10.1103/PhysRevE.85.046304>.
- [22] F. Capuani, I. Pagonabarraga, and D. Frenkel, *The Journal of Chemical Physics* **121**, 973 (2004), URL <https://doi.org/10.1063/1.1760739>.
- [23] R. D. Groot and P. B. Warren, *The Journal of Chemical Physics* **107**, 4423 (1997), URL <https://doi.org/10.1063/1.474784>.
- [24] P. Joseph and P. Tabeling, *Phys. Rev. E* **71**, 035303 (2005), URL <https://link.aps.org/doi/10.1103/PhysRevE.71.035303>.
- [25] G. Trefalt, S. H. Behrens, and M. Borkovec, *Langmuir* **32**, 380 (2016), URL <https://doi.org/10.1021/acs.langmuir.5b03611>.
- [26] K. Wolff, D. Marenduzzo, and M. E. Cates, *Journal of The Royal Society Interface* **9**, 1398 (2012), URL <https://royalsocietypublishing.org/doi/abs/10.1098/rsif.2011.0868>.
- [27] A. Boromand, S. Jamali, and J. M. Maia, *Computer Physics Communications* **196**, 149 (2015), ISSN 0010-4655, URL <https://www.sciencedirect.com/science/article/pii/S0010465515002076>.
- [28] T. Curk, ArXiv preprint (2024).
- [29] N. Kavokine, S. Marbach, A. Siria, and L. Bocquet, *Nature Nanotechnology* **14**, 573 (2019), ISSN 1748-3395,

- URL <https://doi.org/10.1038/s41565-019-0425-y>.
- [30] M. Sano and K. Tamai, *Nature Physics* **12**, 249 (2016), ISSN 1745-2481, URL <https://doi.org/10.1038/nphys3659>.
- [31] C. D. Cox, N. Bavi, and B. Martinac, *Cell Reports* **29**, 1 (2019), ISSN 2211-1247, URL <https://www.sciencedirect.com/science/article/pii/S2211124719311301>.
- [32] P. Robin, N. Kavokine, and L. Bocquet, *Science* **373**, 687 (2021), URL <https://www.science.org/doi/abs/10.1126/science.abf7923>.

Supplemental Material: Discontinuous transition in electrolyte flow through charge-patterned nanochannels

Tine Curk,^{1,*} Sergi G. Leyva,^{2,3} and Ignacio Paganobarraga^{2,3}

¹*Department of Materials Science & Engineering,
Johns Hopkins University, Baltimore, Maryland 21218, USA*

²*Departament de Física de la Matèria Condensada, Universitat de Barcelona, 08028 Spain*

³*Universitat de Barcelona Institute of Complex Systems (UBICS), Universitat de Barcelona, 08028 Spain*

This Supplemental Material provides details on the simulations models and supporting results.

LATTICE BOLTZMANN

The lattice Boltzmann calculations are performed using the open-source package Ludwig [1]. The fluid contains monovalent cations and anions at initial concentration $c^+ = c^- = c$. Ions are initially uniformly distributed with net zero charge density at every position. Initial fluid velocity is zero. With this initial configuration, the LB simulations run for $N_t = 10000000$ time steps with step $\Delta t = \eta^*(\Delta x)^2/\nu$. Mapping to an aqueous solution with dynamic viscosity $\mu = 10^{-3} \text{ Pa} \cdot \text{s}$, kinematic viscosity $\nu = \mu/\rho$, density $\rho = 10^3 \text{ kg/m}^3$, at lattice size $\Delta x = \lambda/2$, the time step is $\Delta t \approx 2.1 \cdot 10^{-14} \text{ s}$. The diffusion constant of ions is set to $D = 10^{-3}\nu$, which models small ions in an aqueous solution with typical diffusion constant $D \approx \text{nm}^2/\text{ns}$. The reduced diffusion constants of ions is thus set to $D^* = D\eta^*/\nu = 0.0002$. The temperature is $T = 293\text{K}$, with a unit of temperature in LB units is $T_0 = \rho_0(\Delta x)^5(\Delta t)^{-2}/k_B$, the reduced temperature is set to $T^* = T/T_0 = k_B T(\eta^*)^2/(\nu^2 \rho_0 \Delta x)$. For the parameters used in $(\eta^*)^2$ and $\Delta x = \lambda/2$ we find $T^* = 0.0005$. The slip length L_s is introduced using a fractional bounce-back boundary condition at the walls [2],

$$\ell_s/\Delta x = 3\eta^* \frac{p}{1-p} \quad (\text{S1})$$

We use $p = 0.99$ at $\Delta x = w/16$ resulting in $\ell_s = 59.4\Delta x$. Since we set $w = 5.16 \text{ nm}$, this corresponds to $\ell_s = 19.2 \text{ nm}$.

Lattice-Boltzmann reduces to the Navier-Stokes in the limit of a small lattice size. Finite-size scaling shows that reducing the lattice size beyond $\Delta x = w/16$ has no noticeable effect on the results, see Fig. S1.

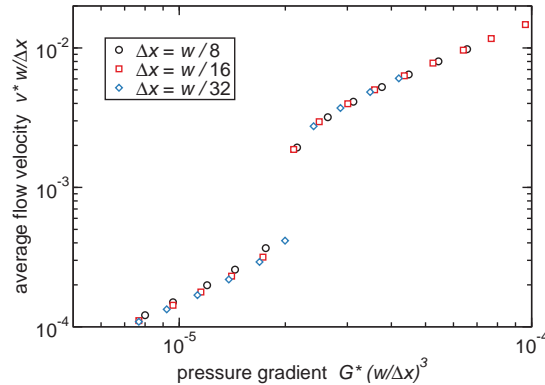


FIG. S1. Finite-size effects at the transition in the flow. Parameters correspond to the plot in Fig 1 in the main text: $w = 8\lambda$, $\rho_q = 0.01e_0/\lambda^3$, $\sigma = 0.2e_0/\lambda^2$, $f = 0.5$, $l_B = 1.1\lambda$, $\eta^* = 0.2$ at a time-point $t = 2.4 \cdot 10^5 (w/32\Delta x)^2 \Delta t$

DPD

Dissipative Particle Dynamics simulations are performed in a slit geometry using standard parameters corresponding to an aqueous solution [$r_c = 0.645$ nm, $A = 25k_B T$, $\rho_s = 3/r_c^3$, $\gamma = 4.5$] [3, 4]. Free ions are modeled as charged spheres with diameter $\lambda_{\text{ion}} = 0.645$ nm. The short-range ion-ion repulsion is modeled using WCA potential with $\varepsilon = k_B T$. The same WCA interaction is used between ions and wall particles. Ions and DPD particles have no pair-interactions. Instead, ions and DPD particles only interact through the dpd thermostat with coupling $\gamma_{\text{ion}} = 5\gamma$. This ensures that the presence of DPD particles does not affect equilibrium properties of ion distributions in the channel and only affects hydrodynamics. Electrostatic interactions are calculated using PPPM Ewald summation with real-space cutoff $r_{\text{ewald}} = 4r_c$ and relative force accuracy of 10^{-3} . Slab correction with ratio 3 is used for periodic boundaries in the y-axis. The external force acts only on the solvent (dpd particles) and does not directly affect ions. This is to ensure that local ion concentration would not alter the local external force density.

This implementation of walls enables simulations at variable slip length. Changing the damping parameter γ_w between the immobile particles and the dpd particles allows tuning of the slip length at the wall (Fig. S2). The slip length is defined as

$$\ell_s = \Delta v \left[\left(\frac{\partial v}{\partial y} \right)_{y=-w/2} \right]^{-1}, \quad (\text{S2})$$

where Δv is the velocity at the wall. Since the numerical accuracy of an average is much higher than that of a derivative, the slip length calculation is determined from the average velocity $\langle v_x \rangle$ rather than derivatives. Since the velocity profile follows the Poiseuille profile, Fig. S2, the slip length can be calculated as

$$\ell_s = \left(\frac{\langle v_x \rangle}{v_{P,0}} - 1 \right) \frac{w}{6}, \quad (\text{S3})$$

where $v_{P,0}$ is the average velocity at no slip, $v_{P,0} = \frac{Gw^2}{12\eta}$. Thus, we measure $\langle v_x \rangle$ as a function of γ_w and determine the slip length ℓ_s . We find $\ell_s \approx 30\lambda$ at $\gamma_w = 0.005\gamma$ which is used for comparison with LB data.

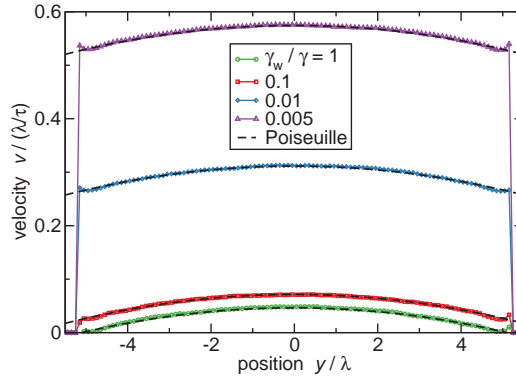


FIG. S2. Velocity flow profile from DPD simulations at different wall-DPD damping γ_w (symbols) and comparison to Poiseuille profiles (dashed lines). $G = 0.003\rho\Delta x/\Delta t^2$.

* tcurk@jhu.edu

- [1] K. Stratford, O. Henrich, and et. al., ludwig-cf/ludwig: Ludwig 0.20.1 (2023).
- [2] K. Wolff, D. Marenduzzo, and M. E. Cates, Cytoplasmic streaming in plant cells: the role of wall slip, *Journal of The Royal Society Interface* **9**, 1398 (2012), <https://royalsocietypublishing.org/doi/pdf/10.1098/rsif.2011.0868>.
- [3] R. D. Groot and P. B. Warren, Dissipative particle dynamics: Bridging the gap between atomistic and mesoscopic simulation, *The Journal of Chemical Physics* **107**, 4423 (1997).

- [4] A. Boromand, S. Jamali, and J. M. Maia, Viscosity measurement techniques in dissipative particle dynamics, *Computer Physics Communications* **196**, 149 (2015).

PART V

Conclusions

CHAPTER 5

Conclusions and perspectives

We conclude this work with a general view of the publications presented in this thesis and the methodologies employed to model soft matter at the nanoscale. We have modelled particles and fluids in different fashions, some of which share a common background. Between the simulation models presented in the two main parts of the thesis, there is a huge methodological gap. This gap is a consequence of the rich and complex phenomena that can be found in soft matter. We have studied systems as diverse as paramagnetic solid particles and electrolyte solutions in confined media. The key for employing this different techniques lays in identifying which are the aspects of the problems that needs to be understood. For example, one can imagine that the full solution to the velocity field in Pub. 4.2 is very intricated, specially when particles move in the asynchronous region. Solving the full numerical Navier-Stokes equation coupled to the colloids would only result in a very complicated solution, where the different contributions to the resynchronisation would be very difficult to disentangle. Using the Blake tensor coupled to Brownian Dynamics, we proved that far-field hydrodynamics lead to resynchronisation. At the same time, this allowed us to rationalise that thermal fluctuations and lubrication forces were not relevant for the problem. Thinking in terms of simple models can provide simple explanations, resulting in a solid framework for building an analytical theory that explains the desired response. This way of thinking can be extrapolated to all the publications from part one.

As we sketched in the introduction, part two has rather the opposite way of thinking. The research performed in these second part was entirely novel, in the sense that experiments were lacking, and no theoretical results existed prior to the publications. This second part was more focused on the direction of exploring the experimental viability of certain designs, based in principles contained in the simulations. In this case, simple models can be tricky, since there is a risk that effects not considered in the simple model might be important. In Pub. 4.6 we used a Lattice-Boltzmann approach, since we knew that this method reproduces accurately the dynamics of spontaneous imbibition and also the dynamics of ternary fluid with tunable contact angles. The simulations were used to set the viability of a experimental set-ups, to prove the dynamical properties of a front advancing on a lubricant.

In Pub. 4.7, we explored the properties of electrolyte solutions in charge-patterned confined channels. The lengthscale considered for this system was the nanoscale, meaning that thermal fluctuations can be determinant.

Furthermore, at the nanoscale the sizes of ions can be commensurate to the width of the channel, which might result in strong deviations from the Nernst-Planck equation, which considers ions in a continuous fashion. That is why we collaborated combining LB continuous-based simulations with DPD simulations, where ions are explicitly considered. Combining this two powerful simulation methodologies and obtaining the same result gave a confirmation that not only thermal fluctuations were not determinant in the discontinuous transition, but furthermore the transition did not depend on the explicit ion-ion interaction. This evidence paved the way towards a mean field theory that predicted the onset of the transition. Hence, this latter publication is also a solid example of how simulation models can be employed to build strong experimental evidence that a response exists in a experimental setup.

As for the scientific works presented here, we have significantly contributed to several different research topics in soft matter that open perspectives for other related works. Overall, the first part is inclined towards investigating collective effects that take place in colloidal suspensions. In the research topic of microswimmers, we have reported a swimming mechanism which allows to direct a swimmer to any direction of a plane, only by switching the magnetic field polarisation and one of the components of the magnetic field. This allows to control the movement of the swimmer without further alteration of the experimental setup. We have identified the mechanism that leads to this rectification mechanism, making possible other similar microswimmers can be designed with this idea in mind, with the hope of controlling microscopic object in the future near solid boundaries. We have reported novel results on the hydrodynamics of colloidal suspensions, both supported by experiments, theory and simulations. These will help understand and rationalise similar effects in other driven colloidal suspensions. We have also characterised clogging in the microscale in different conditions. Our work reports for the first time the effect that a modulated ratchet potential has on the clogging transition through a narrow constriction. Furthermore, we have developed a methodology to quantify clogging in a arbitrary landscape. This methodology relates the clogging that takes place locally with the emergence of an anomalous flow regime. In this regime particles flow in localised regions of the landscape and present a rich phenomenology, like a bimodal distribution of velocities for small densities that changes to a unique broad peak for large densities. This methodology will allow to report how prone to clogging are different types of active particles, and understand which parameters could enhance or hinder the anomalous flow region.

The second part has been more focused into posing experimental challenges and predicting responses of interest. We have unveiled a new dynamic regime of capillary driven spontaneous imbibition, based in lubricant coated surfaces. Our studies demonstrate the capability of lubricant coated surfaces to speed up an imbibition process, even resulting in a linear front advance. This could have huge implications for transport of flows, since it opens the possibility to obtain a constant flux of fluid without any need of an external pump or external field. We have further investigated on how the lubricant affects the deformation of the interface and obtained some analytical solutions that capture the observed trend. This reported results are very easy to test experimentally, contributing to capture the effect of the dissipation due to the deformation of the interface. Furthermore, we have also characterised a novel mechanism for controlling

electrolyte flows in confinement. Our studies clearly indicate that charge-patterned nanochannel can result in a discontinuous flow transition, where the average flow increases several orders of magnitude. This transition also can also take place with increasing the electric field, which suggests that potentially charge-patterned nanochannels could be suitable for designing devices suitable for iontronics.

Taken together, we hope that this thesis can be read as a collection of challenges, the effort of which has been put in choosing and developing the correct simulation approach to the problem at hand and advance each respective research topic. There is no ultimate simulation method that will solve all problems, and there is not even a correct single way of approaching a challenge by computational means. Instead, one needs to stop and think what is the problem at hand and try to use a simulation model accordingly, as rigorously as possible for the desired outcome. This way of modelling and solving scientific challenges does not come out of nowhere. It is the result of a continuous effort of the scientific community, for more than fifty years, to develop, test and validate methodologies so we can use them today, knowing their advantages and disadvantages. It is thanks to those efforts and those pioneers that developed and used simulation models, that today we can use them to comprehend better nature, make accurate predictions even when there is a lack of previous experiments and analytical theories, and face new challenges we wouldn't have imagined some decades ago. That is why the last lines of this thesis are dedicated to them.

Bibliography

- [1] Safa Jamali, Arman Boromand, Norman Wagner, and Joao Maia. Microstructure and rheology of soft to rigid shear-thickening colloidal suspensions. *JOURNAL OF RHEOLOGY*, 59(6):1377–1395, NOV-DEC 2015.
- [2] V Trappe, V Prasad, L Cipelletti, PN Segre, and DA Weitz. Jamming phase diagram for attractive particles. *NATURE*, 411(6839):772–775, JUN 14 2001.
- [3] Yves Chevalier and Marie-Alexandrine Bolzinger. Emulsions stabilized with solid nanoparticles: Pickering emulsions. *COLLOIDS AND SURFACES A-PHYSICOCHEMICAL AND ENGINEERING ASPECTS*, 439(SI):23–34, DEC 20 2013.
- [4] PN PUSEY and W VANMEGEN. Phase-behavior of concentrated suspensions of nearly hard colloidal spheres. *NATURE*, 320(6060):340–342, MAR 27 1986.
- [5] P. G. de Gennes. Wetting: statics and dynamics. *Rev. Mod. Phys.*, 57:827–863, Jul 1985.
- [6] Daniel Bonn, Jens Eggers, Joseph Indekeu, Jacques Meunier, and Etienne Rolley. Wetting and spreading. *Rev. Mod. Phys.*, 81:739–805, May 2009.
- [7] A.L. Yarin. Drop impact dynamics: Splashing, spreading, receding, bouncing. . . . *Annual Review of Fluid Mechanics*, 38(1):159–192, 2006.
- [8] A.L. Yarin. Drop impact dynamics: Splashing, spreading, receding, bouncing. . . . *Annual Review of Fluid Mechanics*, 38(1):159–192, 2006.
- [9] Pierre-Gilles Gennes, Françoise Brochard-Wyart, David Quéré, Axel Reisinger, and Benjamin Widom. Capillarity and wetting phenomena: Drops, bubbles, pearls, waves. *Physics Today - PHYS TODAY*, 57:66–67, 12 2004.
- [10] P. G. de Gennes. Wetting: statics and dynamics. *Rev. Mod. Phys.*, 57:827–863, Jul 1985.
- [11] Edward W. Washburn. The dynamics of capillary flow. *Phys. Rev.*, 17:273–283, Mar 1921.

-
- [12] Élfego Ruiz-Gutiérrez, Steven Armstrong, Simon Lévêque, Célestin Michel, Ignacio Pagonabarraga, Gary G. Wells, Aurora Hernández-Machado, and Rodrigo Ledesma-Aguilar. The long cross-over dynamics of capillary imbibition. *Journal of Fluid Mechanics*, 939:A39, 2022.
- [13] C. Josserand and S. T. Thoroddsen. Drop impact on a solid surface. In SH Davis and P Moin, editors, *ANNUAL REVIEW OF FLUID MECHANICS, VOL 48*, volume 48 of *Annual Review of Fluid Mechanics*, pages 365–391. 2016.
- [14] Shabina Ashraf, Ganesh Visavale, and Jyoti Phirani. Spontaneous imbibition in randomly arranged interacting capillaries. *CHEMICAL ENGINEERING SCIENCE*, 192:218–234, DEC 31 2018.
- [15] Elizabeth Haswell, Rob Phillips, and Douglas Rees. Mechanosensitive channels: What can they do and how do they do it? *Structure (London, England : 1993)*, 19:1356–69, 10 2011.
- [16] Laetitia Jubin, Anthony Poggioli, Alessandro Siria, and Lyderic Bocquet. Dramatic pressure-sensitive ion conduction in conical nanopores. *PROCEEDINGS OF THE NATIONAL ACADEMY OF SCIENCES OF THE UNITED STATES OF AMERICA*, 115(16):4063–4068, APR 17 2018.
- [17] Frank H J van der Heyden, Douwe Jan Bonthuis, Derek Stein, Christine Meyer, and Cees Dekker. Power generation by pressure-driven transport of ions in nanofluidic channels. *Nano letters*, 7 4:1022–5, 2007.
- [18] T. M. Kamsma, W. Q. Boon, T. ter Rele, C. Spitoni, and R. van Roij. Iontronic neuromorphic signaling with conical microfluidic memristors. *Phys. Rev. Lett.*, 130:268401, Jun 2023.
- [19] Carla Fernández-Rico, Massimiliano Chiappini, Taiki Yanagishima, Heidi de Sousa, Dirk G. A. L. Aarts, Marjolein Dijkstra, and Roel P. A. Dullens. Shaping colloidal bananas to reveal biaxial, splay-bend nematic, and smectic phases. *Science*, 369(6506):950–955, 2020.
- [20] D Frenkel. Soft condensed matter. *PHYSICA A-STATISTICAL MECHANICS AND ITS APPLICATIONS*, 313(1-2):1–31, OCT 1 2002. 10th International Summer School on Fundamental Problems in Statistical Physics, ALTENBERG, GERMANY, AUG 20-SEP 02, 2001.
- [21] J. Tailleur and M. E. Cates. Statistical mechanics of interacting run-and-tumble bacteria. *PHYSICAL REVIEW LETTERS*, 100(21), MAY 30 2008.
- [22] Nicholas C. Darnton, Linda Turner, Svetlana Rojevsky, and Howard C. Berg. Dynamics of bacterial swarming. *BIOPHYSICAL JOURNAL*, 98(10):2082–2090, MAY 19 2010.
- [23] A. P. Solon, M. E. Cates, and J. Tailleur. Active brownian particles and run-and-tumble particles: A comparative study. *EUROPEAN PHYSICAL JOURNAL-SPECIAL TOPICS*, 224(7):1231–1262, JUL 2015.

-
- [24] Bezia Lemma, Noah P. Mitchell, Radhika Subramanian, Daniel J. Needleman, and Zvonimir Dogic. Active microphase separation in mixtures of microtubules and tip-accumulating molecular motors. *Phys. Rev. X*, 12:031006, Jul 2022.
- [25] John Toner and Yuhai Tu. Long-range order in a two-dimensional dynamical XY model: How birds fly together. *Phys. Rev. Lett.*, 75:4326–4329, Dec 1995.
- [26] Julia Múgica, Jordi Torrents, Javier Cristin, Andreu Puy, M. Carmen Miguel, and Romualdo Pastor-Satorras. Scale-free behavioral cascades and effective leadership in schooling fish. *Scientific Reports*, 12:10783, 06 2022.
- [27] Macià-Esteve Pallarès, Irina Pi-Jaumà, Isabela Fortunato, Valeria Grazu, Manuel Gómez-González, Pere Roca-Cusachs, Jesús Fuente, Ricard Alert, Raimon Sunyer, Jaume Casademunt, and Xavier Trepát. Stiffness-dependent active wetting enables optimal collective cell durotaxis, 07 2022.
- [28] Yaohua Li, Nolan W. Kennedy, Siyu Li, Carolyn E. Mills, Danielle Tullman-Ercek, and Monica Olvera de la Cruz. Computational and experimental approaches to controlling bacterial microcompartment assembly. *ACS Central Science*, 7(4):658–670, 2021. PMID: 34056096.
- [29] Curt Waltmann, Nolan W. W. Kennedy, Carolyn E. E. Mills, Eric W. W. Roth, Svetlana P. P. Ikonomova, Danielle Tullman-Ercek, and Monica Olvera de la Cruz. Kinetic growth of multicomponent microcompartment shells. *ACS NANO*, 17(16):15751–15762, AUG 8 2023.
- [30] Clemens Bechinger, Roberto Di Leonardo, Hartmut Loewen, Charles Reichhardt, Giorgio Volpe, and Giovanni Volpe. Active particles in complex and crowded environments. *REVIEWS OF MODERN PHYSICS*, 88(4), NOV 23 2016.
- [31] Tamás Vicsek, András Czirók, Eshel Ben-Jacob, Inon Cohen, and Ofer Shochet. Novel type of phase transition in a system of self-driven particles. *Phys. Rev. Lett.*, 75:1226–1229, Aug 1995.
- [32] Daan Frenkel and Berend Smit. *Understanding Molecular Simulation*. Academic Press, Inc., USA, 2nd edition, 2001.
- [33] WK den Otter and JHR Clarke. A new algorithm for dissipative particle dynamics. *EUROPHYSICS LETTERS*, 53(4):426–431, FEB 2001.
- [34] WK den Otter and JHR Clarke. A new algorithm for dissipative particle dynamics. *EUROPHYSICS LETTERS*, 53(4):426–431, FEB 2001.
- [35] MB Liu, P Meakin, and H Huang. Dissipative particle dynamics with attractive and repulsive particle-particle interactions. *PHYSICS OF FLUIDS*, 18(1), JAN 2006.

-
- [36] C. M. Pooley, H. Kusumaatmaja, and J. M. Yeomans. Contact line dynamics in binary lattice boltzmann simulations. *PHYSICAL REVIEW E*, 78(5, 2), NOV 2008.
- [37] Kathrin Eisenschmidt, Moritz Ertl, Hassan Gomaa, Corine Kieffer-Roth, Christian Meister, Philipp Rauschenberger, Martin Reitzle, Karin Schlottke, and Bernhard Weigand. Direct numerical simulations for multiphase flows: An overview of the multiphase code fs3d. *APPLIED MATHEMATICS AND COMPUTATION*, 272(2):508–517, JAN 1 2016.
- [38] JC Phillips, R Braun, W Wang, J Gumbart, E Tajkhorshid, E Villa, C Chipot, RD Skeel, L Kalé, and K Schulten. Scalable molecular dynamics with namd. *JOURNAL OF COMPUTATIONAL CHEMISTRY*, 26(16):1781–1802, DEC 2005.
- [39] D Van der Spoel, E Lindahl, B Hess, G Groenhof, AE Mark, and HJC Berendsen. Gromacs: Fast, flexible, and free. *JOURNAL OF COMPUTATIONAL CHEMISTRY*, 26(16):1701–1718, DEC 2005.
- [40] Aidan P. Thompson, H. Metin Aktulga, Richard Berger, Dan S. Bolintineanu, W. Michael Brown, Paul S. Crozier, Pieter J. in ‘t Veld, Axel Kohlmeyer, Stan G. Moore, Trung Dac Nguyen, Ray Shan, Mark J. Stevens, Julien Tranchida, Christian Trott, and Steven J. Plimpton. Lammmps—a flexible simulation tool for particle-based materials modeling at the atomic, meso, and continuum scales. *COMPUTER PHYSICS COMMUNICATIONS*, 271, FEB 2022.
- [41] PR tenWolde and D Frenkel. Enhancement of protein crystal nucleation by critical density fluctuations. *SCIENCE*, 277(5334):1975–1978, SEP 26 1997.
- [42] Miguel X. Fernandes and José García de la Torre. Brownian dynamics simulation of rigid particles of arbitrary shape in external fields. *Biophysical Journal*, 83(6):3039–3048, 2002.
- [43] Ana Mateos-Maroto, Francisco Ortega, Ramón G. Rubio, Carles Calero, and Fernando Martínez-Pedrero. Modular interfacial microswimmers. *Phys. Rev. Appl.*, 16:064045, Dec 2021.
- [44] Carles Calero, José García-Torres, Antonio Ortiz-Ambriz, Francesc Sagués, Ignacio Pagonabarraga, and Pietro Tierno. Propulsion and energetics of a minimal magnetic microswimmer. *Soft Matter*, 16:6673–6682, 2020.
- [45] Carles Calero, José García-Torres, Antonio Ortiz-Ambriz, Francesc Sagués, Ignacio Pagonabarraga, and Pietro Tierno. Direct measurement of lighthill’s energetic efficiency of a minimal magnetic microswimmer. *Nanoscale*, 11:18723–18729, 2019.
- [46] A. G. Bailey, C. P. Lowe, I. Pagonabarraga, and M. Cosentino Lagomarsino. Accurate simulation dynamics of microscopic filaments using “caterpillar” oseen hydrodynamics. *Phys. Rev. E*, 80:046707, Oct 2009.

-
- [47] Sergi G. Leyva, Ralph L. Stoop, Ignacio Pagonabarraga, and Pietro Tierno. Hydrodynamic synchronization and clustering in ratcheting colloidal matter. *Science Advances*, 8(23):eabo4546, 2022.
- [48] Mikhail R. Stukan, Patrice Ligneul, John P. Crawshaw, and Edo S. Boek. Spontaneous imbibition in nanopores of different roughness and wettability. *LANGMUIR*, 26(16):13342–13352, AUG 17 2010.
- [49] Dong Feng, Xiangfang Li, Keliu Wu, Jing Li, and Wen Zhao. Capillary dynamic under nanoconfinement: Coupling the energy dissipation of contact line and confined water. *INTERNATIONAL JOURNAL OF HEAT AND MASS TRANSFER*, 127(B):329–338, DEC 2018.
- [50] Yuying Wang, Junbo Xu, Huajian Zhu, Steven Wang, and Chao Yang. Mechanism and regulation of spontaneous water transport in graphene-based nanoslits. *ADVANCED THEORY AND SIMULATIONS*, 1(9), SEP 2018.
- [51] S. Chibbaro. Capillary filling with pseudo-potential binary lattice-boltzmann model. *EUROPEAN PHYSICAL JOURNAL E*, 27(1):99–106, SEP 2008.
- [52] F. Diotallevi, L. Biferale, S. Chibbaro, A. Lamura, G. Pontrelli, M. Sbragaglia, S. Succi, and F. Toschi. Capillary filling using lattice boltzmann equations: The case of multi-phase flows. *EUROPEAN PHYSICAL JOURNAL-SPECIAL TOPICS*, 166:111–116, JAN 2009. 7th Biannual European Coating Symposium, Paris, FRANCE, SEP 12-14, 2007.
- [53] C. M. Pooley, H. Kusumaatmaja, and J. M. Yeomans. Modelling capillary filling dynamics using lattice boltzmann simulations. *EUROPEAN PHYSICAL JOURNAL-SPECIAL TOPICS*, 171:63–71, APR 2009. 16th Discrete Simulation of Fluid Dynamics International Conference, Univ Calgary, Schulich Sch Engn, Banff, CANADA, JUL 23-27, 2007.
- [54] Philseok Kim, Tak-Sing Wong, Jack Alvarenga, Michael J. Kreder, Wilmer E Adorno-Martinez, and J. Aizenberg. Liquid-infused nanostructured surfaces with extreme anti-ice and anti-frost performance. *ACS nano*, 6 8:6569–77, 2012.
- [55] Tak-Sing Wong, Sung Hoon Kang, Sindy K. Y. Tang, Elizabeth J. Smythe, Benjamin D. Hatton, Alison Grinthal, and Joanna Aizenberg. Bioinspired self-repairing slippery surfaces with pressure-stable omniphobicity. *Nature*, (7365):443–447.
- [56] Armelle Keiser, Ludovic Keiser, Christophe Clanet, and David Quéré. Drop friction on liquid-infused materials. *Soft Matter*, 13:6981–6987, 2017.
- [57] Kevin Stratford, Oliver Henrich, and et. al. ludwig-cf/ludwig: Ludwig 0.20.1, 2023.
- [58] R. G. Cox. The dynamics of the spreading of liquids on a solid surface. part 1. viscous flow. *Journal of Fluid Mechanics*, 168:169–194, 1986.

-
- [59] Oleg V. Voinov. Hydrodynamics of wetting. *Fluid Dynamics*, 11:714–721, 1976.
- [60] Jie Sheng Gan, Hao Yu, Ming Kwang Tan, Ai Kah Soh, Heng An Wu, and Yew Mun Hung. Performance enhancement of graphene-coated micro heat pipes for light-emitting diode cooling. *INTERNATIONAL JOURNAL OF HEAT AND MASS TRANSFER*, 154, JUN 2020.
- [61] JF Brady and G Bossis. Stokesian dynamics. *Annual review of Fluid Mechanics*, 20:111–157, 1988.
- [62] A. G. Bailey, C. P. Lowe, and A. P. Sutton. Efficient constraint dynamics using MILC SHAKE. *Journal of Computational Physics*, 227(20):8949–8959, October 2008.
- [63] E. M. Purcell. Life at low reynolds number. *American Journal of Physics*, 45(1):3–11, 1977.
- [64] E. A. Gaffney, H. Gadelha, D. J. Smith, J. R. Blake, and J. C. Kirkman-Brown. Mammalian sperm motility: Observation and theory. In SH Davis and P Moin, editors, *ANNUAL REVIEW OF FLUID MECHANICS, VOL 43*, volume 43 of *Annual Review of Fluid Mechanics*, pages 501–528. 2011.
- [65] Eric Lauga and Thomas R Powers. The hydrodynamics of swimming microorganisms. *Reports on Progress in Physics*, 72(9):096601, aug 2009.
- [66] Eric E. Keaveny and Martin R. Maxey. Spiral swimming of an artificial micro-swimmer. *JOURNAL OF FLUID MECHANICS*, 598:293–319, MAR 10 2008.
- [67] Rémi Dreyfus, Jean Baudry, Marcus Roper, Marc Fermigier, Howard Stone, and Jérôme Bibette. Microscopic artificial swimmers. *Nature*, 437:862–5, 11 2005.
- [68] Pietro Tierno, Ramin Golestanian, Ignacio Pagonabarraga, and Francesc Sagués. Controlled swimming in confined fluids of magnetically actuated colloidal rotors. *Phys. Rev. Lett.*, 101:218304, Nov 2008.
- [69] On Shun Pak, Wei Gao, Joseph Wang, and Eric Lauga. High-speed propulsion of flexible nanowire motors: Theory and experiments. *Soft Matter*, 7:8169–8181, 2011.
- [70] A. G. Bailey, C. P. Lowe, I. Pagonabarraga, and M. Cosentino Lagomarsino. Accurate simulation dynamics of microscopic filaments using “caterpillar” oseen hydrodynamics. *Phys. Rev. E*, 80:046707, Oct 2009.
- [71] William H. Press, Saul A. Teukolsky, William T. Vetterling, and Brian P. Flannery. *Numerical Recipes in C*. Cambridge University Press, Cambridge, USA, second edition, 1992.
- [72] John R. Blake and Allen T. Chwang. Fundamental singularities of viscous flow. *Journal of Engineering Mathematics*, 8:23–29, 1974.

-
- [73] Erik M. Gauger, Matthew T. Downton, and Holger Stark. Fluid transport at low reynolds number with magnetically actuated artificial cilia. *The European Physical Journal E*, 28:231–242, 2009.
- [74] Volker Schaller, Christoph Weber, Erwin Frey, and Andreas R. Bausch. Polar pattern formation: hydrodynamic coupling of driven filaments. *SOFT MATTER*, 7(7):3213–3218, 2011.
- [75] Arthur V. Straube and Pietro Tierno. Synchronous vs. asynchronous transport of a paramagnetic particle in a modulated ratchet potential. *Europhysics Letters*, 103(2):28001, jul 2013.
- [76] A. Garcimartín, J. M. Pastor, L. M. Ferrer, J. J. Ramos, C. Martín-Gómez, and I. Zuriguel. Flow and clogging of a sheep herd passing through a bottleneck. *Phys. Rev. E*, 91:022808, Feb 2015.
- [77] Iker Zuriguel, Jorge Olivares, Jose M. Pastor, Cesar Martin-Gomez, Luis M. Ferrer, Juan J. Ramos, and Angel Garcimartin. Effect of obstacle position in the flow of sheep through a narrow door. *Phys. Rev. E*, 94(3):032302, SEP 1 2016.
- [78] Alessandro Corbetta and Federico Toschi. Physics of human crowds. *Annual Review of Condensed Matter Physics*, 14(1):311–333, 2023.
- [79] Iker Zuriguel, Daniel Ricardo Parisi, Raúl Cruz Hidalgo, Celia Lozano, Alvaro Janda, Paula Alejandra Gago, Juan Pablo Peralta, Luis Miguel Ferrer, Luis Ariel Pugnaroni, Eric Clément, Diego Maza, Ignacio Pagonabarraga, and Angel Garcimartín. Clogging transition of many-particle systems flowing through bottlenecks. *Scientific Reports*, 4(1):7324, 2014.
- [80] Amir Zamani and Brij Maini. Flow of dispersed particles through porous media — deep bed filtration. *Journal of Petroleum Science and Engineering*, 69(1):71–88, 2009.
- [81] C. Reichhardt and C. J. O. Reichhardt. Clogging and depinning of ballistic active matter systems in disordered media. *Phys. Rev. E*, 97:052613, May 2018.
- [82] C. Reichhardt and C. J. O. Reichhardt. Directional clogging and phase separation for disk flow through periodic and diluted obstacle arrays. *Soft Matter*, 17(6):1548–1557, FEB 14 2021.
- [83] Sriram Ramaswamy. Active matter. *JOURNAL OF STATISTICAL MECHANICS-THEORY AND EXPERIMENT*, MAY 2017.
- [84] M. Reza Shaebani, Adam Wysocki, Roland G. Winkler, Gerhard Gompper, and Heiko Rieger. Computational models for active matter. *NATURE REVIEWS PHYSICS*, 2(4):181–199, APR 2020.
- [85] Giovanni Volpe, Ivo Buttinoni, Dominik Vogt, Hans-Jürgen Kümmerer, and Clemens Bechinger. Microswimmers in patterned environments. *Soft Matter*, 7:8810–8815, 2011.

-
- [86] Ivo Buttinoni, Julian Bialké, Felix Kümmel, Hartmut Löwen, Clemens Bechinger, and Thomas Speck. Dynamical clustering and phase separation in suspensions of self-propelled colloidal particles. *Phys. Rev. Lett.*, 110:238301, Jun 2013.
- [87] Michael E. Cates and Julien Tailleur. *Motility-Induced Phase Separation*, volume 6 of *Annual Review of Condensed Matter Physics*. Annual Reviews,, Palo Alto :, 2015.
- [88] Helena Massana-Cid, Joan Codina, Ignacio Pagonabarraga, and Pietro Tierno. Active apolar doping determines routes to colloidal clusters and gels. *Proceedings of the National Academy of Sciences*, 115(42):10618–10623, 2018.
- [89] D Quéré. Inertial capillarity. *Europhysics Letters (EPL)*, 39(5):533–538, sep 1997.
- [90] MARCUS HULTMARK, JEFFREY M. ARISTOFF, and HOWARD A. STONE. The influence of the gas phase on liquid imbibition in capillary tubes. *Journal of Fluid Mechanics*, 678:600–606, 2011.
- [91] MATHILDE REYSSAT, LAURENT COURBIN, ETIENNE REYSSAT, and HOWARD A. STONE. Imbibition in geometries with axial variations. *Journal of Fluid Mechanics*, 615:335–344, 2008.
- [92] José Bico, Étienne Reyssat, and Benoît Roman. Elastocapillarity: When surface tension deforms elastic solids. *Annual Review of Fluid Mechanics*, 50(1):629–659, 2018.
- [93] HO-YOUNG KIM and L. MAHADEVAN. Capillary rise between elastic sheets. *Journal of Fluid Mechanics*, 548:141–150, 2006.
- [94] CAMILLE DUPRAT, JEFFREY M. ARISTOFF, and HOWARD A. STONE. Dynamics of elastocapillary rise. *Journal of Fluid Mechanics*, 679:641–654, 2011.
- [95] Joël De Coninck, Fran çois Dunlop, and Thierry Huillet. Contact angles of a drop pinned on an incline. *Phys. Rev. E*, 95:052805, May 2017.
- [96] Kock-Yee Law. Contact angle hysteresis on smooth/flat and rough surfaces. interpretation, mechanism, and origin. *Accounts of Materials Research*, XXXX, 11 2021.
- [97] M. Pradas and A. Hernández-Machado. Intrinsic versus superrough anomalous scaling in spontaneous imbibition. *Phys. Rev. E*, 74:041608, Oct 2006.
- [98] M. Pradas, A. Hernández-Machado, and M. A. Rodríguez. Dynamical scaling of imbibition in columnar geometries. *Phys. Rev. E*, 77:056305, May 2008.
- [99] Periklis Papadopoulos, Lena Mammen, Xu Deng, Doris Vollmer, and Hans-Jürgen Butt. How superhydrophobicity breaks down. *Proceedings of the National Academy of Sciences*, 110(9):3254–3258, 2013.

-
- [100] Hernán Barrio-Zhang, Élfego Ruiz-Gutiérrez, Steven Armstrong, Glen McHale, Gary G. Wells, and Rodrigo Ledesma-Aguilar. Contact-angle hysteresis and contact-line friction on slippery liquid-like surfaces. *Langmuir*, 36(49):15094–15101, 2020. PMID: 33258609.
- [101] Holger F. Bohn and Walter Federle. Insect aquaplaning: Nepenthes pitcher plants capture prey with the peristome, a fully wetttable water-lubricated anisotropic surface. *Proceedings of the National Academy of Sciences*, 101(39):14138–14143, 2004.
- [102] Sydney Chapman, Thomas George Cowling, and David Park. The mathematical theory of non-uniform gases. 1939.
- [103] Timm Krüger, Halim Kusumaatmaja, Alexander Kuzmin, Orest Shardt, Goncalo Silva, and Erlend Magnus Viggen. *The Lattice Boltzmann Method - Principles and Practice*. 10 2016.
- [104] Sauro Succi. *The Lattice Boltzmann Equation: For Complex States of Flowing Matter*. 06 2018.
- [105] Junseok Kim. Phase field computations for ternary fluid flows. *Computer Methods in Applied Mechanics and Engineering*, 196(45):4779–4788, 2007.
- [106] Ciro Semprebon, Timm Krüger, and Halim Kusumaatmaja. Ternary free energy lattice boltzmann model with tunable surface tensions and contact angles. *Physical Review E*, 93, 11 2015.
- [107] Jan Guzowski, Piotr Korczyk, Sławomir Jakiela, and Piotr Garstecki. The structure and stability of multiple micro-droplets. *Soft Matter*, 8:3269–3278, 06 2012.
- [108] Zhaoli Guo, Chuguang Zheng, and Baochang Shi. Discrete lattice effects on the forcing term in the lattice boltzmann method. *Phys. Rev. E*, 65:046308, Apr 2002.
- [109] C. Pooley, Halim Kusumaatmaja, and Julia Yeomans. Modelling capillary filling dynamics using lattice boltzmann simulations. *European Physical Journal: Special Topics*, 171, 11 2009.
- [110] Chun Huh and L.E Scriven. Hydrodynamic model of steady movement of a solid/liquid/fluid contact line. *Journal of Colloid and Interface Science*, 35(1):85 – 101, 1971.
- [111] Richard L Hoffman. A study of the advancing interface. i. interface shape in liquid—gas systems. *Journal of Colloid and Interface Science*, 50(2):228 – 241, 1975.
- [112] Ping Sheng and Minyao Zhou. Immiscible-fluid displacement: Contact-line dynamics and the velocity-dependent capillary pressure. *Phys. Rev. A*, 45:5694–5708, Apr 1992.
- [113] A. J. Briant and J. M. Yeomans. Lattice boltzmann simulations of contact line motion. ii. binary fluids. *Phys. Rev. E*, 69:031603, Mar 2004.

-
- [114] Lewen Fan, Haiping Fang, and Zhifang Lin. Simulation of contact line dynamics in a two-dimensional capillary tube by the lattice boltzmann model. *Physical review. E, Statistical, nonlinear, and soft matter physics*, 63:051603, 06 2001.
- [115] M. Latva-Kokko and Daniel H. Rothman. Scaling of dynamic contact angles in a lattice-boltzmann model. *Phys. Rev. Lett.*, 98:254503, Jun 2007.
- [116] H. Kusumaatmaja, E. J. Hemingway, and S. M. Fielding. Moving contact line dynamics: from diffuse to sharp interfaces. *Journal of Fluid Mechanics*, 788:209–227, 2016.
- [117] AL Hodgkin and AF Huxley. Currents carried by sodium and potassium ions through the membrane of the giant axon of loligo. *Journal of Physiology-London*, 116(4):449–472, 1952.
- [118] Fabrizio Capuani, Ignacio Pagonabarraga, and Daan Frenkel. Discrete solution of the electrokinetic equations. *The Journal of Chemical Physics*, 121(2):973–986, 06 2004.
- [119] Patrick B. Warren. Electroviscous transport problems via lattice-boltzmann. *International Journal of Modern Physics C*, 08(04):889–898, 1997.
- [120] Mandakranta Ghosh, Koen F. A. Jorissen, Jeffery A. Wood, and Rob G. H. Lammertink. Ion transport through perforated graphene. *The Journal of Physical Chemistry Letters*, 9(21):6339–6344, 2018. PMID: 30351047.
- [121] Linhan Xie, Jiadong Tang, Runan Qin, Qianqian Zhang, Jingbing Liu, Yuhong Jin, and Hao Wang. Surface charge modification on 2d nanofluidic membrane for regulating ion transport. *Advanced Functional Materials*, 33(4):2208959, 2023.
- [122] Zhongpeng Zhu, Dianyu Wang, Ye Tian, and Lei Jiang. Ion/molecule transportation in nanopores and nanochannels: From critical principles to diverse functions. *Journal of the American Chemical Society*, 141(22):8658–8669, 2019. PMID: 31063693.
- [123] Laetitia Jubin, Anthony Poggioli, Alessandro Siria, and Lydéric Bocquet. Dramatic pressure-sensitive ion conduction in conical nanopores. *Proceedings of the National Academy of Sciences*, 115(16):4063–4068, 2018.
- [124] Tsai-Wei Lin and Jyh-Ping Hsu. Pressure-driven energy conversion of conical nanochannels: Anomalous dependence of power generated and efficiency on ph. *Journal of Colloid and Interface Science*, 564, 12 2019.
- [125] S. Dal Cengio and I. Pagonabarraga. Confinement-controlled rectification in a geometric nanofluidic diode. *The Journal of Chemical Physics*, 151(4):044707, 07 2019.

- [126] J. Cervera, B. Schiedt, and Patricio Ramírez. A poisson/nernst-planck model for ionic transport through synthetic conical nanopores. *EPL (Europhysics Letters)*, 71:35, 01 2007.
- [127] Zuzanna Siwy, Elizabeth Heins, C Harrell, Punit Kohli, and Charles Martin. Conical-nanotube ion-current rectifiers: The role of surface charge. *Journal of the American Chemical Society*, 126:10850–1, 10 2004.